ABSTRACT

Title of Dissertation: PHYSICAL CONDITIONS OF THE MULTI-PHASE INTERSTELLAR MEDIUM IN NEARBY GALAXIES FROM INFRARED AND MILLIMETER-WAVE SPECTROSCOPY

Elizabeth Tarantino
Doctor of Philosophy, 2022

Dissertation Directed by: Professor Alberto D. Bolatto
Department of Astronomy

Gas and dust in the interstellar medium (ISM) cools and condenses, gravitationally collapses, and forms stars. At the same time, stars can heat and ionize their surroundings, influencing the physical conditions of the nearby ISM. In this thesis, I take a multi-wavelength, spectroscopic approach to investigate the physical conditions of the multi-phase ISM in nearby galaxies.

The [CII] fine-structure transition at 158 μm is frequently the brightest far-infrared line in galaxies and can trace the ionized, atomic, and molecular phases of the ISM. I present velocity-resolved [CII] observations from SOFIA in the nearby galaxies M101 and NGC 6946 and determine that [CII] emission is associated with the atomic and molecular gas about equally, with little contribution from the ionized gas. Using the [CII] cooling function, I calculate the thermal pressure of the cold neutral medium and find that the high star formation rates in our sample can drive large thermal pressures, consistent with predictions from analytical theory.

Next, I investigate the properties of the ionized gas around one of the hottest and most luminous Wolf-Rayet (WR) stars in the Small Magellanic Cloud. I use spatially resolved mid-infrared Spitzer and far-infrared Herschel spectroscopy to establish the physical conditions of the ionized gas. Using the photoionization code `Cloudy`, I construct models with a range of constant densities between $\mathrm{n_H} = 4 - 12\ \mathrm{cm}^{-3}$ and a stellar wind-blown cavity of 15 pc that reproduce the intensity and spatial distribution of most ionized gas emission lines. The higher ionization lines cannot be produced by the models— however, I show that wind-driven shocks or a harder ionizing WR spectrum can explain their intensities.

Lastly, I explore the properties of molecular clouds in a large (170 $\times$ 350 pc) map of an active star-forming region in the Large Magellanic Cloud. Using $^{12}\mathrm{CO}(2-1)$ and $^{13}\mathrm{CO}(2-1)$ observations from the ALMA ACA, I decompose the emission into individual cloud structures and determine their sizes, linewidths, mass surface densities, and virial parameters. Almost all of the clouds are gravitationally bound or marginally bound and share size-linewidth relations to molecular clouds in the Milky Way and nearby dwarf galaxies. I do not find evidence that the surrounding star formation significantly influences the kinematic properties of the clouds through stellar feedback.

PHYSICAL CONDITIONS OF THE MULTI-PHASE INTERSTELLAR MEDIUM IN NEARBY GALAXIES FROM INFRARED AND MILLIMETER-WAVE SPECTROSCOPY

by

Elizabeth Tarantino

Dissertation submitted to the Faculty of the Graduate School of the
University of Maryland, College Park in partial fulfillment
of the requirements for the degree of
Doctor of Philosophy
2022

Advisory Committee:
Professor Alberto Bolatto, Chair/Advisor
Professor Andrew Harris
Dr. Mark Wolfire
Professor J.D. Smith, External Examiner
Professor Kara Hoffman, Dean's Representative

Preface

The research presented in this thesis is either published or in preparation for submission. Chapter 2 appears in *The Astrophysical Journal* (ApJ) as *"Characterizing the Mult-phase Origin of [CII] Emission in M101 and NGC 6946 with Velocity-resolved Spectroscopy"* and is presented here with minimal changes (Tarantino et al., 2021). Chapter 3 is in an advanced draft stage and will be submitted to *The Astrophysical Journal* at the same time as submission of this thesis. Chapter 4 is currently in preparation for submission to *The Astrophysical Journal*.

Acknowledgments

There are so many people that have influenced my development as a scientist over the years that I wish I could acknowledge them all by name. This section cannot be the length of a thesis, however, so I will attempt to make it brief.

First, I would like to express the utmost gratitude for my advisor, Alberto Bolatto. Thank you so much for taking me on as your student, guiding me through the process of a PhD, and never giving up on me. The dedication you have for your students, consistently prioritizing us with a very busy schedule, is incredibly admirable. You have helped me grow so much and made me a better astronomer throughout my time here. I'm going to miss our weekly meetings, but I'm excited to continue to collaborate in the future.

I want to thank my thesis committee– Andy Harris, Mark Wolfire, J.D. Smith, and Kara Hoffman– as well as Peter Teuben and Stuart Vogel, for providing valuable feedback that improved each one of these projects. Your advice, expertise and collaboration throughout my time here has helped me so much. It has been a joy to learn astronomy and how to be a good scientist from you all. To the administrative and front office staff– Olivia, Lauren, Barbara, Susan, Dorinda, Mona, and John– thank you for making this department run so smoothly.

To the grad students in the LMA research group– Carrie Rye Volpert, Vicente Villanueva, Jialu Li, Serena Cronin, and Ramsey Karim– thank you all for your unwavering support. You all are amazing friends and collaborating with you has been one of the best parts of graduate school. To Rebecca Levy and Laura Lenkíc, thank you for helping me along this journey. Not only are you both fantastic researchers, but you are some of the most generous and kind people I know. To my dear friend Carrie Holt, it's hard to put into words how much I appreciate your support and friendship. I'm so glad that we became instant friends in grad school and I will treasure every memory we've had together here. I also want to give a shoutout to my old roommates– Carrie Rye Volpert, Julian Marohnic, and Ben Hord– for making the uncertain times during the COVID pandemic not only bearable, but a lot of fun. Lastly, I want to thank *all* the graduate students and members of the department at UMD. Every single one of you has made a positive impact on my life and being around you all brings me so much joy. I am incredibly grateful for how special our community is and couldn't imagine being anywhere else. You have truly made this place my home.

I want to thank my parents, Joel and Angela, my stepfather James, and my grandparents, for instilling in me a love of learning at a young age. All of the trips to the planetarium, waking up early for a lunar eclipse, and spending your Saturday morning at a lecture on galaxies has culminated into me presenting this thesis. I also want to thank my brother, Brian, for instilling a sense of confidence and strength within me. You always encourage me to never give up and believe that I can do anything I put my mind to.

Next, I would like to thank the astronomy department at my undergraduate institution, Case Western Reserve University, and especially my research mentor there, Stacy McGaugh, for providing an excellent foundation in astronomical research. I also want to thank Grace Olivier, Nick Smith, and Emily Shelton for understanding the struggles of physics and supporting me in undergrad and beyond. To my other friends from Case– Sarah Mattson, James Hochadel, and Nick Schindler– thank you for listening to all of my rambles about JWST, the [CII] line, and being there to celebrate victories and comfort me when I was low. To my partner, Felix, thank you for making everything in my life better, from playing DnD together, to having fun dressing up in nerdy costumes, to knowing exactly what to say to comfort me. Your support and devotion has meant so much to me and my love for you is as big as the observable universe.

Lastly, I am eternally grateful for all the science educators and communicators that encourage little girls to study science, especially my father Joel. Fifteen years ago you gave me a gift of a telescope that sparked my interest in astronomy. Even before then, you were consistently inspiring me to reach for the stars. Thank you for supporting my lifelong love for the universe and encouraging me to pursue my dream.

Table of Contents

List of Tables

List of Figures

List of Abbreviations

ACA	Atacama Compact Array (part of the Atacama Large Millimeter/submillimeter Array)
ALMA	Atacama Large Millimeter/submillimeter Array
ANOVA	Analysis of variance
ASKAP	Australian Square Kilometre Array Pathfinder
BCD	Basic calibrated data
CASA	Common Astronomy Software Application
CLASS	Continuum and Line Analysis Single-dish Software
CNM	Cold neutral medium
DGR	Dust-to-gas ratio
FIR	Far infrared
FOV	Field of view
FWHM	Full-width-half-maximum
GMC	Giant molecular cloud
HERACLES	HERA CO-Line Extragalactic Survey
HIFI	Heterodyne Instrument for the Far-Infrared (onboard the Herschel Space Telescope)
HIPE	Herschel Interactive Process Environment
HST	Hubble Space Telescope
IGM	Intergalactic medium
IMF	Initial mass function
IR	Infrared
IRAC	Infrared ARray Camera (onboard the Spitzer Space Telescope)
IRS	InfraRed Spectrograph (onboard the Spitzer Space Telescope)
ISM	Interstellar medium
JWST	James Webb Space Telescope
KINGFISH	Key Insights on Nearby Galaxies: A Far-Infrared Survey with Herschel
LFA	Low Frequency Array
LL	Long Low module (on Spitzer IRS)
LMC	Large Magellanic Cloud
LSRK	Kinematic local standard of rest
LTE	Local thermodynamic equilibrium
MAD	Median absolute deviation

MW	Milky Way
NGC	New general catalogue
NIR	Near infrared
PACS	Photodetector Array Camera and Spectrometer (onboard the Herschel Space Telescope)
PAH	Polycyclic aromatic hydrocarbon
PDR	Photodissociation region (also sometimes called a photon-dominated region)
PRIMA	PRobe far-Infrared Mission for Astrophysics
PSF	Point spread function
rms	root-mean-square
S/N	Signal-to-noise ratio
S^4MC	Spitzer Spectroscopic Survey of the Small Magellanic Cloud
SED	Spectral energy distribution
SFE	Star formation efficiency
SFR	Star formation rate
SL	Short Low module (on Spitzer IRS)
SINGS	Spitzer Infrared Nearby Galaxies Survey
SMC	Small Magellanic Cloud
SN(e)	Supernova(e)
SNR	Signal-to-noise ratio
SOFIA	Stratospheric Observatory for Infrared Astronomy
SPIRE	Spectral and Photometric Imaging Receiver (onboard the Herschel Space Telescope)
SWB	Stellar Wind blown bubble
SVE	Simple virial equilibrium
THINGS	The HI Nearby Galaxy Survey
UGC	Uppsala General Catalogue
GREAT	German REceiver for Astronomy at Terahertz frequencies (onboard the Stratospheric Observatory for Infrared Astronomy)
UV	Ultraviolet
VLA	Very Large Array
WIM	Warm ionized medium
WNM	Warm neutral medium
WR	Wolf-Rayet
XFFTS	Fast fourier transform spectrometer

Symbols:

α_B	Recombination coefficient
α_{CO}	CO-toH_2 conversion factor
B_{nu}	Planck function
A_{ul}	Spontaneous emission rate coefficient
R_{ul}	Collisional de-excitation rate coefficient
G_0	FUV radiation field
N	Column density

τ	Optical depth
pc	parsec
kpc	kpc
Σ	Mass surface density
$n_{\rm crit}$	Critical density
$n_{\rm H}$	Hydrogen density
$M_\odot$	Solar mass
Z	Metallicity
$Z_\odot$	Solar metallicity

Lines, atoms, and molecules:

[CII]	Forbidden transition of singly-ionized carbon
[NII]	Forbidden transition of singly-ionized nitrogen
[SI]	Forbidden transition of atomic sulphur
[SIII]	Forbidden transition of doubly-ionized sulphur
[SIV]	Forbidden transition of triple-ionized sulphur
[OI]	Forbidden transition of atomic oxygen
[OIII]	Forbidden transition of doubly-ionized oxygen
[OIV]	Forbidden transition of triple-ionized oxygen
[NeII]	Forbidden transition of singly-ionized neon
[NeIII]	Forbidden transition of doubly-ionized neon
[NeV]	Forbidden transition of quadruple-ionized neon
[SiII]	Forbidden transition of singly-ionized silicon
HeII	Singly-ionized helium
CO	Carbon monoxide
H	Hydrogen
Hα	Hydrogen alpha emission at 6562 Å
H_2	Molecular hydrogen
HI	Atomic hydrogen, can also correspond to the 21-cm spin-flip hydrogen line
HII	Singly ionized hydrogen
C^+	Singly ionized carbon
N^+	Singly ionized nitrogen

Chapter 1: Introduction

"All of the rocky and metallic material we stand on, the iron in our blood, the calcium in our teeth, the carbon in our genes were produced billions of years ago in the interior of a red giant star. We are made of star-stuff."

– Dr. Carl Sagan

The universe is composed of mostly hydrogen and dark matter. With the help of gravity, hydrogen gas condenses, coalesces and forms stars. A galaxy is a collection of stars, gas, and dark matter gravitationally bound together. Our universe is made up of billions of galaxies, each containing billions of stars. Thus, understanding the relationship between stars and gas is fundamental to revealing the nature of our universe.

The matter between the stars, mostly composed of gas and dust, is called the interstellar medium (ISM). Even though the ISM constitutes only 10% of the observable matter in the universe, it plays a critical role in the formation of stars, galaxies, and planets. While stars form out of the ISM, they also impact their nearby environment through heating and ionizing the gas, imparting energy and momentum into the surrounding material, and enriching the gas with elements formed through nucleosyntheis. Understanding the complex interplay between these "cosmic ecoysystems" in galaxies is a key priority in the next decade of astronomical research (National Academies, 2021).

The universe began with the big bang, which created most of the hydrogen and helium we observe in the universe. Almost all other elements were produced through the evolution of stars. Astronomers refer to elements other than hydrogen and helium as *metals* and define the fraction of metals in a system as its *metallicity*. As stars form, evolve, and die they eject metals produced through nucleosynthesis into the surrounding ISM, thereby increasing the metallicity of the universe as a function of time. Metallicity directly affects many properties in the ISM, such as the availability of cooling lines and the amount of dust. Since galaxies at early times were much more metal-poor, it is important to study low metallicity systems to understand how this key environmental variable influences young star formation and galaxy evolution. The early galaxies are too distant to study in detail; therefore, we use nearby low metallicity analogues to investigate the effects on the ISM and star formation. The Large and Small Magellanic Clouds (LMC and SMC, respectively) are the prime laboratories to study low metallicity systems, due to their proximity (50 kpc and 63 kpc, Graczyk et al., 2020; Pietrzyński et al., 2019) and metallicities of $Z_{\mathrm{LMC}} \sim 1/2\ Z_{\odot}$ (Russell & Dopita, 1992) and $Z_{\mathrm{SMC}} \sim 1/5\ Z_{\odot}$ (Dufour, 1984).

1.1 The Multi-phase Interstellar Medium

This thesis focuses on understanding the properties of the multi-phase ISM in nearby galaxies. Since hydrogen is the most abundant molecule in the universe, the phases of the ISM are often defined by the state of hydrogen, i.e. whether hydrogen is in atomic (HI[1]), ionized (HII), or molecular (H_2) form. The states of the gas can be broken down further into phases of the gas through their density, n, and temperature, T. Figure 1.1 shows a graphical representation of the

[1]Astronomers often use spectroscopic notation when referring to the ionization state of an element. An atom followed by a roman numeral I is considered in the neutral state, while II refers to a singly-ionized atom, III refers to a doubly-ionized atom and so on. Spectroscopic notation is used throughout this thesis.

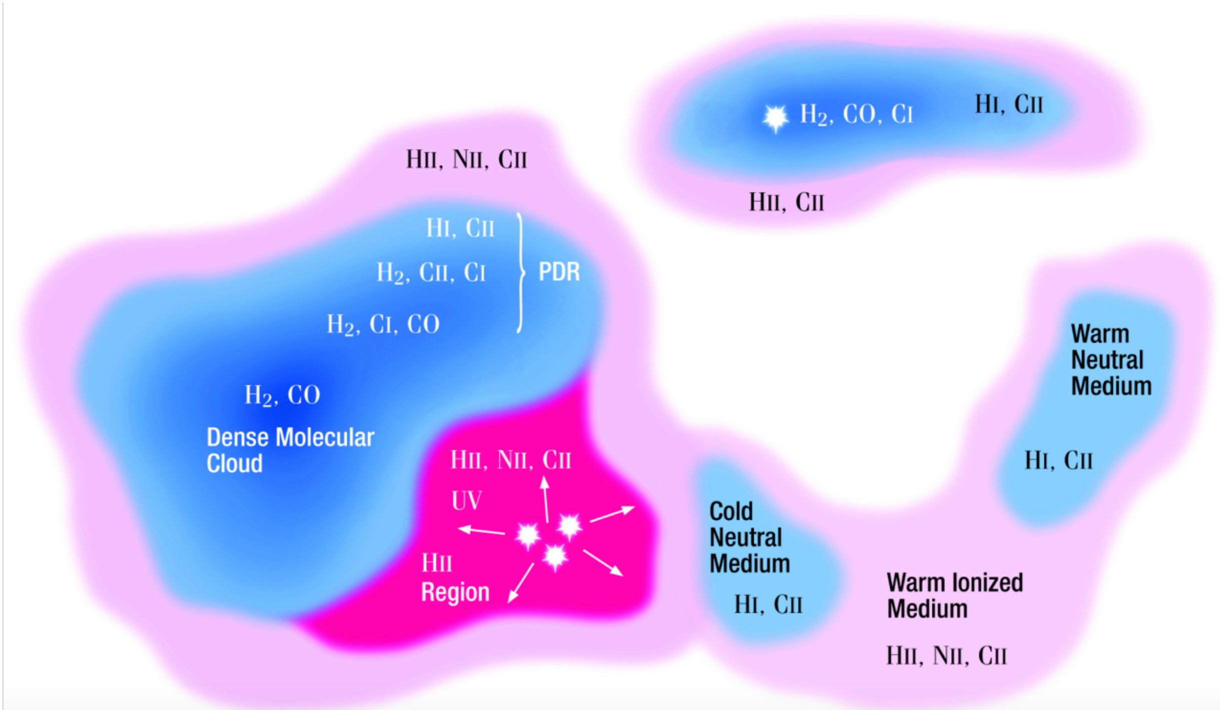

Figure 1.1: Pictorial representation of the multi-phase interstellar medium. The light blue regions show the atomic gas, in the form of the cold neutral medium and warm neutral medium (CNM and WNM, respectively). Cold, dense molecular gas regions (dark blue) can form out of the atomic gas and are the sites of star formation. An HII region, where massive stars ionize their surroundings, is shown in bright pink. The interface between the HII region and molecular gas is called a photodissociation region (PDR). The low density, warm ionized medium (WIM) permeates throughout in a light pink color. Various tracers, such as the [CII] emission, are labeled around the schematic. (Figure credit: Jorge Pineda)

multi-phase ISM that we will refer to throughout this introduction.

Various atoms, ions, and molecules besides hydrogen also exist in the multi-phase ISM and are used to determine the physical conditions of the gas. The variation of physical properties, such as a given atoms ionization energy, critical density ($n_{\rm crit}$), and radiative/collisional excitation of these tracers are used to determine the conditions of the gas. For example, ionized carbon ([CII] or C^+), an ion of one of the most abundant elements in the universe and a focus of this thesis, exists throughout the multi-phase ISM: in the atomic, molecular, and ionized gas. We use observations of C^+ in chapter 2 to quantify its multi-phase nature and calculate the thermal pressure in the

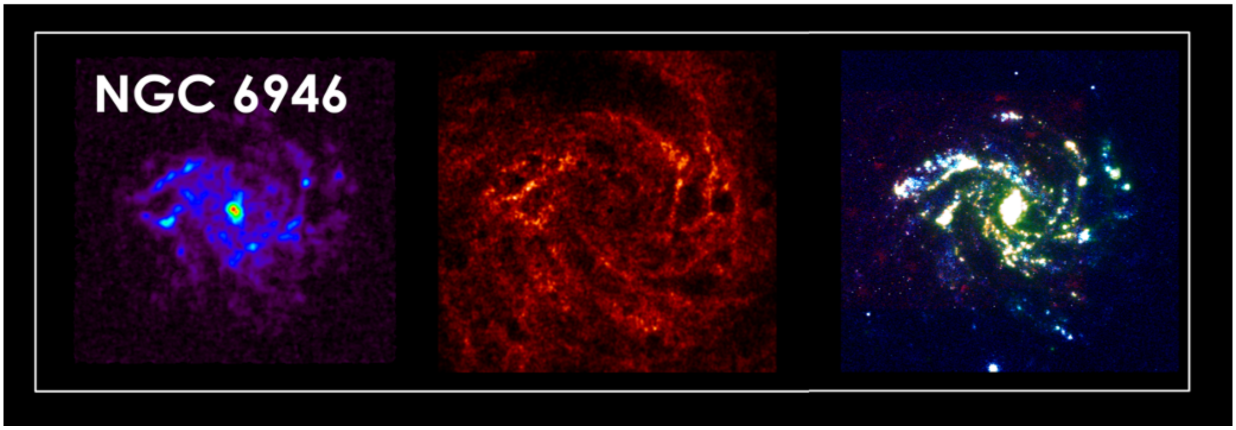

Figure 1.2: The multi-phase and multi-wavelength view of NGC 6946 from (Leroy et al., 2013). Left shows the cold, molecular gas from CO(2-1) emission, center is the atomic gas from 21 cm HI emission, and right is the ionized gas and HII regions from Hα and 24 μm dust emission.

atomic gas.

Many spectral lines found in the infrared, a focus of this thesis, are considered $fine-structure$ transitions and are due to the coupling between the spin and orbit of an electron. Fine structure lines tend to have small energy level changes, resulting in a $\Delta E \sim h\nu$ that corresponds to a photon at infrared wavelengths. Many of these transitions are also considered $forbidden$, which are denoted by square brackets, e.g. [CII]. A forbidden line is one that is not allowed through traditional selection rules and can have very low spontaneous decay rates, A, leading to long timescales. These lines are weaker but are relevant in astronomy because every atom and ion has excited states than only decay through forbidden transitions. At high densities, excited states could depopulate through collisions. However, in the low density of the ISM collisions are infrequency and the only pathway for decay is through a forbidden line, making forbidden lines relevant in astrophysics.

In the following subsections, I summarize the three different phases of the multi-phase ISM that are relevant for this thesis. For more detail, I refer the reader to (Draine, 2011) for an in-depth review of these phases.

1.1.1 Atomic gas

Neutral atomic gas, colored by the light blue regions in Figure 1.1, is traced by the 21-cm (1420 MHz) line through radio telescopes. This transition originates from the hyperfine splitting of the $1s$ ground state state of hydrogen and is called the *spin-flip* transition. Observations of the 21-cm HI emission are presented for NGC 6946 in the center panel of Figure 1.2. The HI gas establishes the spiral arms of the galaxy and traces more of the outskirts of the galaxy compared to the molecular or ionized gas.

The atomic gas consists of two phases, the dense cold component (Cold Neutral Medium, CNM; $n_{\rm H} \approx 50$ cm^{-3}, $T_{\rm kin} \approx 80$ K) and a diffuse warm component (Warm Neutral Medium, WNM; $n_{\rm H} \approx 0.5$ cm^{-3}, $T_{\rm kin} \approx 5000$ K) in approximate pressure equilibrium (Field et al., 1969; Wolfire et al., 1995, 2003). Observationally, it is challenging to distinguish between these two phases as they both contribute to the 21-cm emission. Absorption studies of the 21-cm line that that use bright background sources can disentangle the CNM and WNM by identifying the spin temperature of the gas. Studies in the Milky Way suggest that the CNM and WNM exist in a approximately 50/50 ratio (Dickey et al., 2009; Heiles & Troland, 2003). These two phases coexist in a multi-phase, pressure curve that is produced by the balance of heating and cooling of the atomic gas.

The dominant source of heating in the atomic gas is photoelectric heating from small dust grains and large molecules (Draine, 1978; Wolfire et al., 1995). A high energy photon can be absorbed by a dust grain, or a polycyclic aromatic hydrocarbon (PAH) compound, and through the photoelectric effect, the dust grain releases an electron that heats the gas. Cosmic rays (and to a lesser extent X-rays) also contribute to the heating of the atomic gas, especially for the lower density WNM. The major coolants of the atomic gas are [CII] 158 μm and [OI] 63 μm emission that are excited through collisions with H^0 and then spontaneously decay, releasing photons and energy out of the system. The WNM has a higher hydrogen ionization fraction ($X_e \sim 0.017$), leading to Lyman-α emission and recombination of electrons onto the dust grains also acting as a cooling channel.

The atomic gas is in thermal equilibrium when the cooling and heating rates are equal. When the pressure is constant, a curve is defined that identifies the temperature of the gas where the heating and cooling is balanced. Figure 1.3 shows an example of a pressure curve from Wolfire et al. (1995). For an interstellar radiation field (ISRF) at the solar neighborhood there is a stable pressure regime between $P_{\mathrm{th}} \sim 990 - 3600$ K cm^{-3} with a WNM density of $n \sim 0.1 - 0.6$ cm^{-3} in tandem with a CNM a density of $4.2 - 80$ cm^{-3}. Outside of these warm and cold regimes, the gas is unstable and while cool or heat to reach the stable conditions. These pressure curves are driven by the ISRF, which contributes to the heating rate of the region. As the ISRF increases, the thermal pressure curve is driven upwards. The pressure curve depends on a variety of parameters besides the ISRF that can impact the heating and cooling rates, such as the metallicity of the gas, gas column density, dust-to-gas ratio, and PAH abundance.

The thermal pressure plays a critical role in the process of star formation. The formation of giant molecular clouds (GMCs) is governed by the ratio of atomic to molecular hydrogen that the pressure balance can influence (Blitz & Rosolowsky, 2006). The cycle of self-regulation of star formation activity is also controlled by pressure (Kim et al., 2011; Ostriker et al., 2010). However, it is observationally challenging to measure the pressure directly and most previous work has

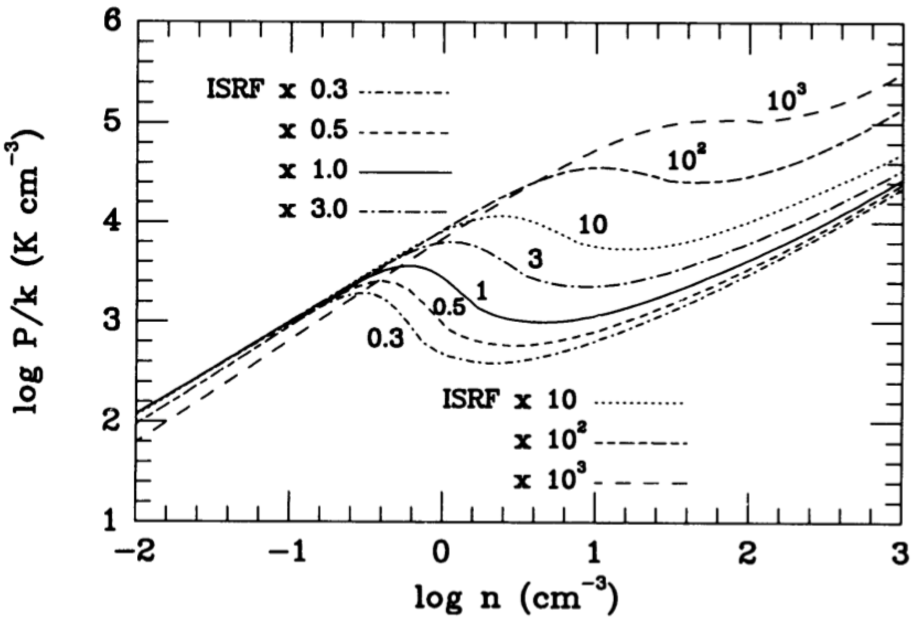

Figure 1.3: Pressure equilibrium of the atomic gas as a function of the interstellar radiation field (ISRF). In the two-phase model of atomic gas, the CNM and WNM can coexist at a given thermal pressure P/k. For ISRF = 1, the local interstellar radiation field, the stable pressure regime is between $P_{\mathrm{th}} \sim 990 - 3600\ \mathrm{K\ cm^{-3}}$ and the WNM can exist with a density $n \sim 0.1 - 0.6\ \mathrm{cm^{-3}}$ in tandem with the CNM that has a density of $4.2 - 80\ \mathrm{cm^{-3}}$. As the ISRF increases, the heating rate increases driving the thermal pressure curve upwards (Figure from Wolfire et al., 1995).

focused on measurements in the galactic plane (Gerin et al., 2015; Jenkins & Tripp, 2011) or quiescent regions in nearby galaxies (Herrera-Camus et al., 2017). In chapter 2, I demonstrate a technique of using velocity-resolved [CII] spectroscopy to determine the thermal pressure of the CNM near active, star-forming regions (Tarantino et al., 2021).

1.1.2 Ionized gas

Ionized gas, HII, consists of hydrogen that lost its electron, most often due to the absorption of photons greater than the ionization energy of hydrogen, 13.6 eV. Bright, massive stars that emit photons with $h\nu \gtrsim 13.6$ eV in the far-ultraviolet (FUV) region of the electromagnetic spectrum ionize their surroundings, producing an emission nebula called an HII regions. These stars have O and B spectral types and are the youngest and most massive stars in the universe. The most common way to trace HII regions is through the Balmer series of hydrogen recombination lines, in particular the Hα line that corresponds to the electronic transition of the $n = 3$ to the $n = 2$ level. This line has a an optical rest wavelength of 6562 Å and is bright, making Hα a great high-mass star formation tracer for galaxies near and far (e.g. Kennicutt, 1998; Lee et al., 2009). HII regions are represented in Figure 1.1 by the bright pink colored regions, where there is active star formation and UV radiation ionizing the surrounding gas. In Figure 1.2, the HII regions are visible as bright knots in the spiral arms of NGC 6946.

The simplest model of an HII region was developed by Strömgren (1939). In the steady state solution of HII regions, hydrogen recombination, $\mathrm{H}^+ + \mathrm{e}^- \rightarrow \mathrm{H}+\mathrm{h}\nu$ is balanced by photoionization, $h\nu \rightarrow \mathrm{H}^+ + \mathrm{e}^-$. Equating the rates of photoionization and radiative recombination for ionization balance leads to the relationship between the number of ionizing photons of a given star, Q_0, and the Stromgren radius of an HII region (R_{S0}):

$$Q_0 = \frac{4\pi}{3} R_{\mathrm{S0}}^3 \alpha_B n(H^+) n_e \tag{1.1}$$

where α_B is the case B recombination coefficient, $n(H^+)$ is the density of protons, and n_e is the density of electrons (generally, $n(H^+) = n_e \equiv n_H$ since all hydrogen is considered ionized). While this prescription of HII regions does not take into account complications such as dust, clumpiness, or radiative transfer, it is a useful framework for understanding the physics of HII regions.

While the Strömgren (1939) model of HII regions assumes they are perfectly confined spheres, in reality HII regions can "leak", i.e. ionizing photons can escape and permeate the surrounding ISM. This process produces another phase of ionized gas called the Warm Ionized Medium (WIM), that is characterized by low densities ($n \sim 0.01\ \mathrm{cm}^{-3}$) and hot temperatures ($T \sim 6000 - 10000$). The WIM is pictured by the light pink color in Figure 1.1 and constitutes a substantial fraction of a galaxies Hα emission (Haffner et al., 2009).

The main heating source in HII regions is the heating by photoionzation: photons that have ionization energies excess that of hydrogen $h\nu \sim 13.6$ eV can add thermal energy into the gas. For instance, after an atom absorbs a photon, the energy greater than the recombination energy can be transferred into excess kinetic energy in the atom. There are three main cooling pathways in HII regions, including 1) the radiation produced through recombination of electrons with an ion (for example, the emission from Hα), 2) free-free emission (also called bremsstrahlung), when electrons scatter off of an ion, decelerating and producing radiation, and 3) emission from collisionally excited spectral lines. The balance of the heating and cooling determines the temperature of HII region gas. There are a variety of atoms and ions of S, Ar, Ne and O that may be singly- or more more highly ionized in an HII region. Since these lines are important coolants, they also serve as diagnostics of the conditions in an HII region, such as the temperature or density of the gas. Figure 1.4 shows how ratios of infrared fine-structure lines can be used to determine the density of an HII region. Modeling the spectral lines together through computer codes that simulate the photoionization process is a very powerful way to estimate characteristic conditions of the ionized gas. I used the code `Cloudy` (Ferland et al., 2017) to investigate the properties of an HII region called N76 in chapter 4 of this thesis.

An important property I investigate in chapter 4 is how the metallicity of the the gas affects an HII region. Lower metallicity stars have harder[2], more high energy photons due to less line blanketing from overlapping lines in the stellar atmospheres (Martín-Hernández et al., 2002). The abundance of elements also decreases, leading to less cooling of the HII region through spectral lines. These two effects combine make low metallicity HII regions hotter, which I will investigate further in chapter 4.

The impact HII regions have on their surroundings is also substantial. The input of energy and momentum from stars is called *stellar feedback*. Besides ionizing the neighboring ISM, HII regions are not in pressure equilibrium with the adjacent gas and can expand, imparting momentum into the ISM. In addition to the ionizing radiation from HII regions, the stellar winds from massive stars may also influence the surround gas. There has been a substantial observational effort in the past decade to quantify the feedback effects associated with HII regions (Krumholz et al., 2019; Lopez et al., 2011, 2014; McLeod et al., 2019; Olivier et al., 2021; Pabst et al., 2019). In chapter 4, we investigate whether there is evidence of star formation feedback on molecular

[2] hardness is defined by the proportion of high energy photons in a radiation fields spectrum

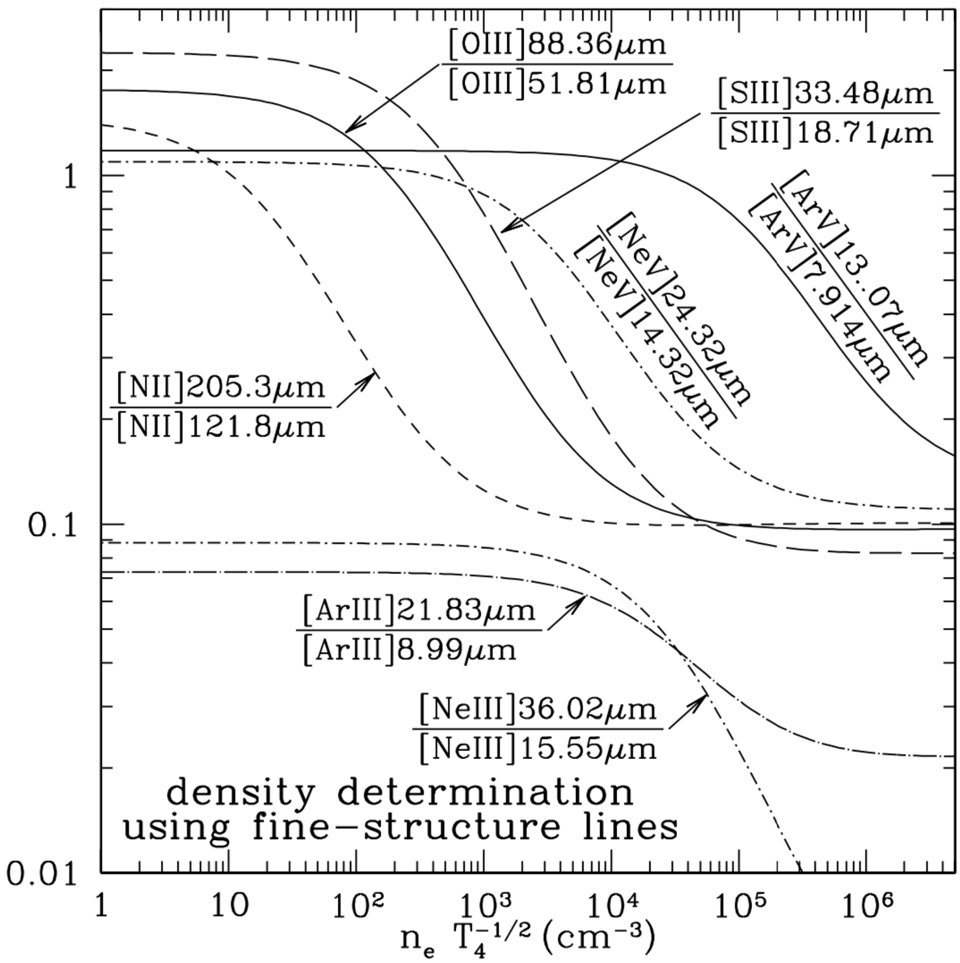

Figure 1.4: Fine-structure line ratios that can be used for density determination of ionized gas. Since the lines vary in their critical densities, the ratios can be used to determine the density of the ionized gas. (Figure 18.5 from Draine, 2011).

clouds in the LMC.

1.1.3 Molecular gas

Molecular gas, H_2, is the densest ($n \sim 10^3 - 10^6\ \mathrm{cm}^{-3}$) and coldest ($T \sim 10 - 50$ K) phase of the ISM. Molecular gas can condense and form coherent structures called molecular clouds that become the sites of star formation (McKee & Ostriker, 2007, and references therein). Thus, observations of the molecular gas are vital in understanding the cycle of star formation. Figure 1.1 presents the molecular gas in the dark blue color, showing that this material forms stars (upper center cloud) and is also influenced by the surrounding star formation (left cloud). Molecular hydrogen is a symmetric, diatomic molecule and does not have a permanent electric dipole moment to emit photons through rotational transitions. The lowest rotational transitions from the quadrupole moment of H_2 traces gas at temperatures $T > 100$K and therefore do not trace the bulk of the cold molecular gas. Instead, astronomers use the second most abundant molecule, carbon monoxide (CO), to observe the molecular gas. Figure 1.2 shows that the CO emission in NGC 6946 on the left panel spatially corresponds to the measures of star formation on the right panel, illustrating the connection between the molecular gas and star formation.

Direct observations of warm H_2, however, are possible through the rotational quadrupole transitions in the infrared, ranging from $\lambda = 28\ \mu$m to $\lambda = 2.2\ \mu$m. These lines are relatively weak, have a transition energies of $E_{\mathrm{upper}}/k \sim 500$ K, and trace gas that has a temperature of $T \gtrsim 100$ K (Dabrowski, 1984). Therefore, the electric quadrupole H_2 transitions will not trace the dense, cold gas that forms stars. Instead, the quadrupole H_2 transitions are an indicator of where molecular gas is heated by bright stars, which we investigate in chapter 3.

The ground transition of carbon monoxide molecule ($^{12}\mathrm{C}^{16}\mathrm{O},\ \mathrm{J}=1-0$) has a rest frequency of 115 GHz (2.6 mm) and an excitation energy of $E_{\mathrm{upper}}/k \sim 5K$, making it observable from the earth with millimeter/radio telescopes and easy to excite in molecular clouds. Other transitions of CO are also easily observable, such as the $\mathrm{J}=2-1$ transition (rest frequency of 230 GHz) that we study in this thesis. One challenge of using the CO emission to trace the molecular gas is the necessity to convert the luminosity of the CO line to a molecular hydrogen mass. This is called the "CO-to-H_2" conversion factor α_{CO} (Bolatto et al., 2013, and references therein). This factor relies on a variety of ISM conditions, such as the metallicity, temperature, and column density of the gas, making the adoption of a singular value uncertain. Nevertheless, for Milky Way clouds, we often use $\alpha_{\mathrm{CO}} = 4.3\ \mathrm{M}_{\odot}\ \mathrm{K\ km\ s^{-1}\ pc^{-2}}$.

The CO molecule is an imperfect tracer of molecular gas which can lead to complications in its interpretation. FUV fields can dissociate CO into C and O while H_2 remains in molecular form because H_2 can self shield from the radiation (e.g. Draine & Bertoldi, 1996). Dust particles can often protect the CO molecular from dissociation, but in low metallicity environments where the dust abundance is decreased, the FUV radiation can permeate deep into a cloud, creating a substantial layer of "CO-dark" or "CO-faint" molecular gas (Grenier et al., 2005; Langer et al., 2014; Lequeux et al., 1994; Madden et al., 1997; Maloney & Black, 1988; Wolfire et al., 2010). This CO-dark material can constitute a substantial fraction of the molecular gas; up to 75% of the molecular gas in the nearby Magellanic Clouds may be CO-dark (Chevance et al., 2020; Jameson et al., 2018).

While the most abundant $^{12}\mathrm{C}^{16}\mathrm{O}$ molecule of carbon monoxide is the workhorse molecule for measuring the molecular gas content, observations of less abundant CO isotopologues can reveal the properties of molecular clouds. In particular, we focus on the $^{13}\mathrm{C}^{16}\mathrm{O}$ molecule which is 30-70 times less abundant than $^{12}C^{16}O$ (e.g., Langer & Penzias, 1990). When the $^{12}C^{16}O$ and $^{13}C^{16}O$ are spatially co-located, the $^{13}C^{16}O$ line tracers more optically thin gas compared to the optically thick $^{12}C^{16}O$ line. After assuming local thermodynamic equilibrium, the intensity of ^{13}CO can reveal the column densities and masses of molecular clouds without having to assume an α_{CO} factor (e.g., Bourke et al., 1997; Garden et al., 1991). I use this method in chapter 4 to calculate the masses of molecular clouds and determine whether they are bound in the LMC.

1.1.4 Photodissociation regions

Photodissocation regions (PDRs)[3] are areas in the ISM where the gas is predominately neutral but the heating and chemistry is dominated by non-ionizing FUV radiation ($6\ \mathrm{eV} < \mathrm{h}\nu < 13.6\ \mathrm{eV}$, Hollenbach & Tielens, 1999; Tielens & Hollenbach, 1985; Wolfire et al., 2022). PDRs form the interface between molecular clouds and HII regions (labeled in Figure 1.1 as the transition between light blue and dark blue) and contribute a large amount of far-infrared emission from galaxies, including a substantial amount of [CII] emission. Figure 1.5 shows a slab schematic of a PDR where there is an ionization source on the left and the extinction increases towards the right. Beyond the ionization front (the transition from ionized to neutral gas), the hydrogen gas is neutral and cooled by [CII] and [OI] emission. The heating source is by photoelectrons from PAHs, similar to the heating source for the diffuse atomic gas described in §1.1.1. As the extinction increases, hydrogen becomes molecular because of the lower UV radiation. However, the carbon is still in an ionized state and cannot form CO, creating a portion of gas that is "CO-dark". At the final layer, the carbon combined with oxygen to form CO.

PDRs are very common throughout the universe, encompassing all of the atomic and ∼90%

[3]sometimes PDRs are referred to as photon-dominated regions, which conveniently share the same acronym

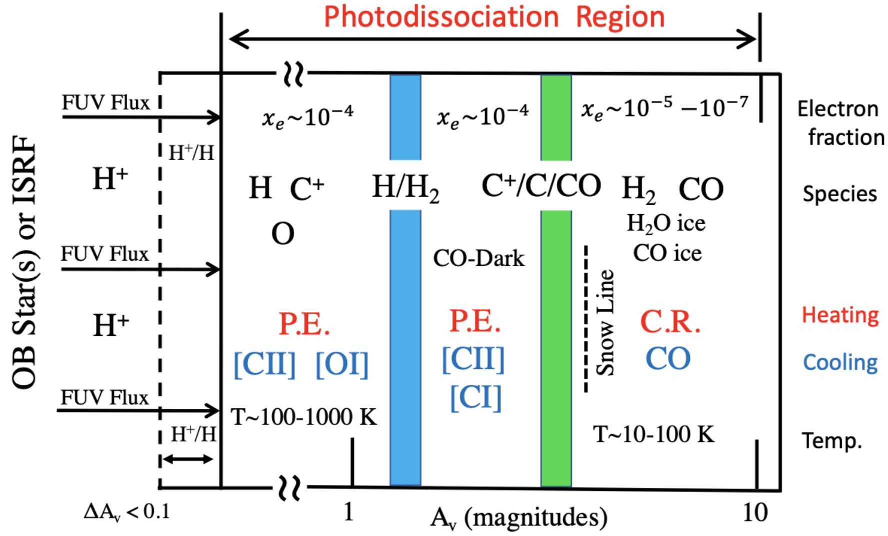

Figure 1.5: Structure of a PDR as a function of extinction increasing to the right. PDRs can harbor a significant portion of CO-dark gas (center region between blue and green bands). Here, [CII] can trace the neutral material, which can be a mixture of atomic gas and molecular (Figure 2 from Wolfire et al., 2022).

of the molecular gas by mass in the Galaxy (Hollenbach & Tielens, 1999). They are found not just in the transition between HII regions and molecular clouds, but also appear on the surfaces of molecular clouds because the ISRF contains substantial FUV radiation. As such, PDRs play an important role when discussing the ISM as a whole and are mentioned throughout this thesis.

1.2 Outline of Thesis

This thesis studies the multi-phase ISM in nearby galaxies through infrared and sub-millimeter spectroscopy. I am particularly interested in understanding the effect star formation and metallicity have on the surrounding ISM. Therefore, I conduct three studies that are focused on deriving the physical conditions of the multi-phase ISM through observations of spectral lines in various environments.

In chapter 2, I present velocity resolved observations of [CII] emission in the nearby disks of galaxies M101 and NGC 6946. With ancillary atomic and molecular gas data, I decompose the [CII] emission into components associated with each of these phases and find that the [CII] emission originates from the molecular and atomic gas about equally, with almost no contribution from the ionized gas. Then, I use the cooling function of [CII] to calculate the thermal pressure in CNM of these galaxies. The thermal pressure is relatively high, but consistent with the predictions of the CNM around star formation. This chapter is published in as "Characterizing the Multiphase Origin of [CII] Emission in M101 and NGC 6946 with Velocity-resolved Spectroscopy" in *The Astrophysical Journal* (Tarantino et al., 2021).

In chapter 3, I investigate the ionized gas in the the Wolf-Rayet (WR) emission nebula N76, caused by one of the most luminous WR stars in the low metallicity Small Magellanic Cloud. I use spatially-resolved mid-infrared Spitzer IRS and far-infrared Herschel PACS spectroscopy to establish the physical conditions of the ionized gas. I construct models with a range of constant densities between $\mathrm{n_H} = 4 - 12\ \mathrm{cm}^{-3}$ and a stellar wind-blown cavity of 15 pc which reproduces the intensity and shape of most ionized gas emission lines, including [SIII], [SIV], [OIII], and [NeIII]. The higher ionization lines, [OIV] and [NeV], cannot be produced by photoionization and require wind-driven shocks. Surprisingly, we detect a spectral line that appears to be due to neutral sulphur within the central regions of the nebula, which we cannot easily explain. The models suggest that the ionized gas in N76 makes a small ($< 5\%$) contribution to the neutral-dominated lines, [CII] and [OI], while producing most (96%) of the [SiII] emission. I have completed a final draft of the manuscript for this work and have received comments from all coauthors. I will submit the paper to the *The Astrophysical Journal* at the same time this thesis is submitted.

Chapter 4 focuses on the molecular phase of the ISM and whether the kinematics of molecular clouds are influenced by surrounding star formation. I analyze a large (170 × 350 pc) map of $^{12}\mathrm{CO}(2-1)$ and $^{13}\mathrm{CO}(2-1)$ emission at 1.7 pc resolution in the star-forming northern molecular ridge of the LMC. I decompose the CO emission into individual molecular clouds and measure their sizes, linewidths, mass surface densities, and virial parameters. I find a power law correlation between the size and linewidth of the clouds similar to that of the Milky Way. I then calculate the virial parameter to find most clouds are bound or marginally bound. I find no correlation between the 8 μm flux and the virial parameter for a cloud, indicating that there is no strong evidence of significant energy injection into the clouds due to star formation. This work is in preparation for submission to *The Astrophysical Journal*.

In chapter 5, I summarize and discuss the future work that builds off of this thesis.

Chapter 2: Characterizing the Multi-Phase Origin of [CII] Emission in M101 and NGC 6946 with Velocity Resolved Spectroscopy

2.1 Introduction

Emission from the far-infrared (FIR) [CII] 158 μm line is bright and ubiquitous in most star-forming galaxies. It is the ${}^2P^0_{3/2} \rightarrow {}^2P^0_{1/2}$ fine-structure, collisionally excited line of singly ionized carbon, C^+. The emission from [CII] provides a major cooling channel for the gas in the interstellar medium (ISM), specifically in the cold neutral medium (Wolfire et al., 2003), on the illuminated surfaces of molecular clouds, and, along with [OI], in dense photodissociation regions (PDRs) (Hollenbach & Tielens, 1999; Tielens & Hollenbach, 1985). [CII] is often the brightest emission line in the FIR from galaxies, amounting to about 0.1% - 1% of the integrated FIR continuum emission (Crawford et al., 1985; Stacey et al., 1991). Previous studies have also shown a correlation between [CII] emission strength and star formation rates (Boselli et al., 2002; De Looze et al., 2014; Herrera-Camus et al., 2015, 2018; Smith et al., 2017; Stacey et al., 1991). In low metallicity environments, the [CII] line is the only coolant necessary to form stars (Glover & Clark, 2012; Krumholz, 2012). Studying the nature of [CII] emission is thus vital to the understanding of star formation and cooling in the ISM.

Ionized carbon (C^+) can be present throughout the different phases of the ISM due to the low ionization potential of neutral carbon (11.26 eV, slightly less than that of hydrogen). Collisions with electrons (e^-), neutral hydrogen (HI), and molecular hydrogen (H_2) produce [CII] emission that is found in the warm ionized medium, the neutral atomic medium, and cold molecular gas, respectively (e.g., Heiles, 1994; Kim & Reach, 2002; Madden et al., 1993; Pineda et al., 2013). Identifying the contribution that each of the phases have to the overall [CII] intensity allows one to determine which phase is dominant. Such information can be used to determine the physical conditions of the ISM, such as the thermal pressure of the constituent phases (e.g., Cormier et al., 2019, 2015; Goldsmith et al., 2012; Lebouteiller et al., 2019; Pineda et al., 2013; Sutter et al., 2019).

The [CII] emission is partially associated with the tracer of molecular gas, CO, as seen in correlations between the intensity of [CII] and CO (Accurso et al., 2017; Stacey et al., 1991; Wolfire et al., 1989; Zanella et al., 2018). On the surfaces of molecular clouds, far ultra-violet (FUV) radiation fields can dissociate CO into C and O and photoionize C to C^+ while the hydrogen remains in molecular (H_2) form, producing [CII] emission associated with the CO-traced molecular cloud. These PDRs are very bright and will account for most of the [CII] emission close to massive star formation (e.g., Tielens & Hollenbach, 1985). Pineda et al. (2014, 2013) use velocity resolved *Herschel*/HIFI [CII] observations in the plane of the Milky Way to quantify the degree to which [CII] is associated with the CO and find that 30-47% of the total [CII] emission observed comes from the molecular gas near dense PDRs. The study by de Blok et al. (2016) compared *Herschel*/PACS [CII] observations of 10 galaxies to CO and HI data and found that the [CII] radial surface density profiles are shallower than CO but much steeper than the HI surface density profile. At low metallicities, however, the [CII] associated to the CO-emitting molecular gas can be more complex. A decrease in the dust abundance leads to less shielding of

CO clouds, creating regions of molecular material that produce [CII] emission but faint in CO, called "CO-dark" or "CO-faint" gas (Grenier et al., 2005; Jameson et al., 2018; Madden et al., 2020; Wolfire et al., 2010). For example, analysis of velocity resolved [CII] observations in the low metallicity dwarf galaxy NGC 4214 suggests that 79% of the molecular mass is traced by [CII] alone, whereas only 21% is traced by CO (Fahrion et al., 2017).

Ionized carbon fine-structure emission also arises from the atomic medium and plays an important role in the radiative heating and cooling balance of this phase (Wolfire et al., 2003). The atomic gas, as traced by the hyperfine 21 cm spin flip HI transition, has a dense cold component (Cold Neutral Medium, CNM; $n_{\rm H} \approx 50$ cm^{-3}, $T_{\rm kin} \approx 80$ K) and a diffuse warm component (Warm Neutral Medium, WNM; $n_{\rm H} \approx 0.5$ cm^{-3}, $T_{\rm kin} \approx 8000$ K) in approximate pressure equilibrium with one another (Field et al., 1969; Heiles & Troland, 2003; Wolfire et al., 1995). Because of the difference in volume densities, the contribution from the WNM to the overall [CII] emission is $\sim$20 times less than that of the CNM (Fahrion et al., 2017; Lebouteiller et al., 2019; Pineda et al., 2013; Wolfire et al., 2010). Thus the [CII] line can be used to directly probe the conditions of the CNM. Once the CNM is isolated, we can estimate the thermal pressure, which is related to the star formation rate, metallicity, and the thermal balance between the heating and cooling of the system (Ostriker et al., 2010; Wolfire et al., 2003). In observations of star forming regions with spatial resolutions of a few parsecs, the atomic gas contributes 5% - 15% to the overall [CII] emission (Lebouteiller et al., 2019; Okada et al., 2019, 2015; Requena-Torres et al., 2016). In contrast, [CII] observations of regions that are more quiescent or at larger resolutions of 50-200 parsecs, associate 20% - 46% of the [CII] emission to the atomic phase (Fahrion et al., 2017; Kramer et al., 2013; Pineda et al., 2013). The spatial resolution and star formation activity may therefore play a role when decomposing the [CII] emission.

The contribution the ionized gas has to the [CII] emission is usually found through observations of the [NII] line. Ionized nitrogen is only present in the ionized gas and its 205 μm transition has a critical density similar to [CII], enabling [NII] 205 μm observations to isolate the contribution of ionized gas to the [CII] emission (Oberst et al., 2006). Croxall et al. (2017) use observations of the [NII] and [CII] lines in a variety of galaxies to find that ionized gas contributes only $\sim$26% to the [CII] emission on average. Expanding on the sample of galaxies used by Croxall et al. (2017), Sutter et al. (2019) identify that $\sim$33% of the [CII] emission comes from ionized gas by comparing the [NII] and [CII] measurements in these galaxies. Both Lebouteiller et al. (2019) and Fahrion et al. (2017) find that the contribution ionized gas has to the [CII] emission is negligible through a combination of [NII] observations and modeling of the PDRs in each system. The ionized gas, however, makes a larger contribution of about 36% - 75% in the bright HII region M17 SW and in the center of the starburst galaxy IC 342 (Pérez-Beaupuits et al., 2015; Röllig et al., 2016). Overall, it appears that the ionized gas tends to contribute a small amount to the [CII] emission, except perhaps in areas of extended, dense ionized gas.

One method to identify the origin of the [CII] emission is to compare the velocity profiles of the [CII], CO, HI, and other tracers in order to quantify the contribution each phase has to the [CII] emission. This method can use velocity resolved observations of [CII] from the SOFIA/GREAT or *Herschel*/HIFI instruments, along with similar resolution data for the tracers of component data, such as 21 cm HI for the atomic gas and CO for the molecular gas. Previous studies use this method but mostly target individual star-forming regions in the Milky Way (Pérez-Beaupuits et al., 2015), Magellanic Clouds (Lebouteiller et al., 2019; Okada et al., 2019, 2015; Pineda et al., 2017), or the bright centers of nearby galaxies (Fahrion et al., 2017; Mookerjea et al., 2016; Röllig et al., 2016). There are few studies, however, that explore the origin of [CII] in both star-forming and quiescent regions, an important regime due to the multi-phase nature of [CII]. This work aims to spectrally decompose the [CII] emission in a variety of environments, including different star formation rate surface densities ($\Sigma_{\rm SFR}$) and metallicities, in the two galaxies M101 (NGC 5457) and NGC 6946 at a resolution of $\sim$500 pc. These galaxies are representative of spiral galaxies as a whole, are at distances of 6.8 Mpc for M101 (Fernández Arenas et al., 2018) and 7.8 Mpc for NGC 6946 (Anand et al., 2018; Murphy et al., 2018), and have a wealth of ancillary data available. We will also present an evaluation of the spectral profile decomposition technique.

The organization of this paper is as follows. In Section 2.2 we describe the data used in the decomposition. Section 2.3 we discuss the method used for the decomposition and evaluate its accuracy. Section 2.4 shows the results of the decomposition and describes limits on the contribution of the ionized gas to the [CII] emission. Section 2.5 computes the pressure of the CNM through the [CII] cooling function and compares the results of the decomposition to other works. Lastly, Section 2.6 summarizes our conclusions.

2.2 Observations

2.2.1 SOFIA Data

Observations of M101 and NGC 6946 were taken using the German REceiver for Astronomy at Terahertz Frequencies (GREAT and its improved successor upGREAT) on board the Stratospheric Observatory for Infrared Astronomy (SOFIA) in cycles 2 and 4 (Heyminck et al., 2012; Risacher et al., 2018, 2016). The cycle 2 (PI: Herrera-Camus, project 02_0098) data used the original GREAT instrument, consisting of a single element receiver, and targeted four regions in M101 and four in NGC 6946. Observations were taken May 20th and 21st of 2014, with

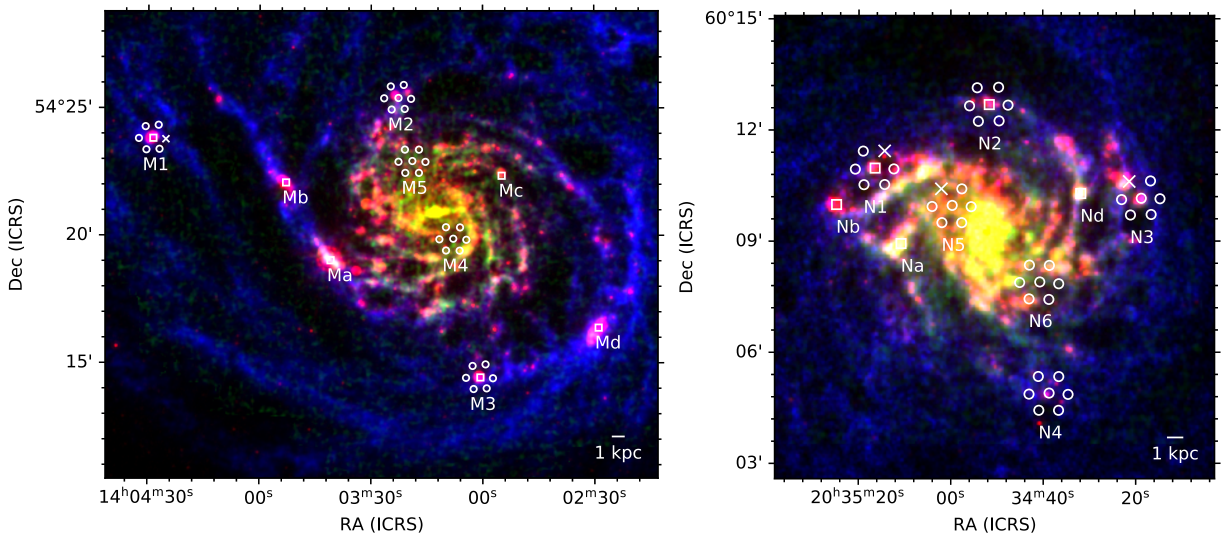

Figure 2.1: M101 (left) and NGC 6946 (right) three-color image with the SOFIA/GREAT pointings overlaid. The three-colors show the ancillary datasets used in this work: the 24 μm map from *Spitzer* (red), the HI column density map from the THINGS survey (blue), and the CO moment 0 map from the HERACLES survey (green). SOFIA cycle-4 observations (7 pixel upGREAT pointings) are labeled with numbers while the cycle 2 observations (single pointing with GREAT) are labeled with letters. Region Nc is not shown because the GREAT receiver was mistuned at that position and the region was re-observed as N1 in cycle 4. Pointing circles are the approximate beam of these data and correspond to the quiescent regions ($\Sigma_{\rm SFR} < 6 \times 10^{-2}$ M$_\odot$ yr^{-1} kpc^{-2}), squares represent the star-forming regions ($\Sigma_{\rm SFR} > 6 \times 10^{-2}$ M$_\odot$ yr^{-1} kpc^{-2}), and x are regions that were removed from the sample due to emission in the off-source chop-position contaminating the observed profile. Pointing selection shows a range of environments, probing the metallicity gradient in each galaxy and different levels of star formation rate.

receivers tuned to 1900.5 GHz ([CII] 158 μm) and 1461.1 GHz ([NII] 205 μm). The receiver was accidentally mis-tuned for the [CII] observations in one of the regions (labeled Nc) and was then re-observed with upGREAT in cycle 4 as region N1. We adopt a uniform beam size of 15$''$ for [CII] and 18$''$ for [NII]. The average sensitivity for [CII] in cycle 2 was T$_{\rm mb}$ = 0.11 K and T$_{\rm mb} = 0.05$ K for [NII] in a velocity channel width of 5.2 km s^{-1}.

The cycle 4 data (PI: Bolatto, project 04_0151) comprised of eleven total regions, five in M101 and six in NGC 6946, using the dual polarization upGREAT instrument on SOFIA. The upGREAT instrument consists of two seven-element hexagonal arrays, one for each polarization, and the two polarizations were averaged together for these data. The observations of M101 were taken during the upGREAT commissioning on December 9th and 10th, 2015 and the NGC 6946 observations were taken on May 12th, 18th, 19th, and 25th of 2016. For both galaxies, the Low Frequency Array (LFA) band was tuned to 1900.5 GHz ([CII] 158 μm) and the L1 band was tuned to 1461.1 GHz ([NII] 205 μm). The half-power beam widths were 15″ for [CII] and 18″ for [NII]. The average sensitivity for [CII] achieved with the integration time obtained for each observation in cycle 4 is $T_{\rm mb}$ = 0.05 K and $T_{\rm mb}$ = 0.04 K for [NII] in a velocity channel width of 5.2 $\rm km\,s^{-1}$. Cycle 4 pointings are referred to by their region name and a number denoting the pointing number in the array (e.g. N2-0 would be the cycle 4 NGC 6946 region N2 and the 0th, central pointing).

The single point chopped mode for SOFIA/GREAT was used for each cycle. We excluded pointings where the chop-off position showed weak emission, contaminating the on-source spectrum. The data in both cycles were processed with the eXtended bandwidth Fast Fourier Transform Spectrometer (XFFTS) and calibrated with the standard GREAT calibrator (Guan et al., 2012). The antenna efficiency for both cycles is $\eta_f = 0.97$ and the main beam efficiency varies between $\eta_{mb} = 0.65 - 0.71$, for the different elements in the array. The level 3 data products were produced through the CLASS/GILDAS software where a first order polynomial spectral baseline was removed.

2.2.1.1 Pointing selection

The placement of these pointings is shown in Figure 2.1. There are two types of regimes targeted in this study: areas that are coincident with high star formation rates (represented by squares in Figure 2.1) and the more quiescent regions found in the interarm of each galaxy (represented by circles in Figure 2.1). The star-forming regions are chosen for having strong star formation activity as traced by Hα, far-UV, and 24 μm emission. The diffuse ISM in these regions is exposed to about six times higher average radiation fields than the solar neighborhood (Aniano et al., 2020; Draine et al., 2007) when measured on large ($\sim$kpc) scales. The other category targeted are the quiescent interarm regions. These regions are selected for their low star formation activity, weak CO and HI emission, and have similar average radiation field strengths as the solar neighborhood (Aniano et al., 2020; Draine et al., 2007). We use a threshold value of $\Sigma_{\rm SFR} = 6 \times 10^{-2}$ $\mathrm{M_\odot}$ $\mathrm{yr^{-1}\,kpc^{-2}}$, which roughly bisects the sample, to distinguish between the star-forming and quiescent regions.

In addition to the star formation rate surface density ($\Sigma_{\rm SFR}$), we are also interested in studying the effect of metallicity on the [CII] decomposition. We use the abundance gradients published by Pilyugin et al. (2014), which employs the "strong-line method" of abundance determination on 130 nearby galaxies (including M101 and NGC 6946) to produce homogeneous gas phase oxygen abundance gradients from the HII regions in these galaxies. Although there are small azimuthal metallicity variation in similar spiral galaxies, the overwhelming metallicity change is due to these radial gradients (Kreckel et al., 2020). Similar to the $\Sigma_{\rm SFR}$, we use a threshold value of $12 + \log(\mathrm{O/H}) = 8.55$ to distinguish between high and low metallicities. We note that the pointings centered on star-forming regions extend to larger galactocentric distance and are consequently biased towards lower metallicities. We cannot separate the effect of the lower metallicity on the high star formation regions because the lack of integration time on quiescent pointings at low metallicity leads to little [CII] detections in this regime.

2.2.2 Herschel PACS [CII] data

[CII] observations of M101 and NGC 6946 were also made with the *Herschel*/PACS instrument as part of the KINGFISH program (Kennicutt et al., 2011). The KINGFISH program focused on deep spectroscopic imaging of ISM diagnostic lines, including [CII], at a resolution of $\sim$12″.

With an effective spectral resolution of about 220 km s^{-1}, PACS does not resolve the [CII] line, in contrast to the GREAT instrument. However, we can compare the integrated intensities of the [CII] line between the two instruments. The overlap between the *Herschel*/PACS observations and detected SOFIA/GREAT [CII] pointings includes all but three GREAT pointings.

To compare the GREAT and PACS [CII] intensities we use a convolution kernel to convert from the PACS 158 μm Point Spread Function (PSF) to the Gaussian 15″ beam of the GREAT data from the kernels provided in Aniano et al. (2011). These kernels are most appropriate for the PACS continuum camera, but are likely to result in a much better approximation than assuming a Gaussian PSF. Figure 2.2 shows the comparison between GREAT and PACS line integrated intensities with the black line representing the line of unity. We also show data from the literature for NGC 4214 and the Large Magellanic Cloud (LMC) for comparison (Fahrion et al., 2017; Lebouteiller et al., 2019). Error bars are reported where available and correspond to the 1σ rms noise of the given spectrum.

There is a small systematic difference of about 7% between the GREAT flux and the corresponding PACS [CII] flux. The expected absolute flux uncertainties for the PACS KINGFISH data are about 15%, making this discrepancy within the bounds of the PACS and GREAT calibration uncertainty (Croxall et al., 2013). The observations from the literature, by contrast, show

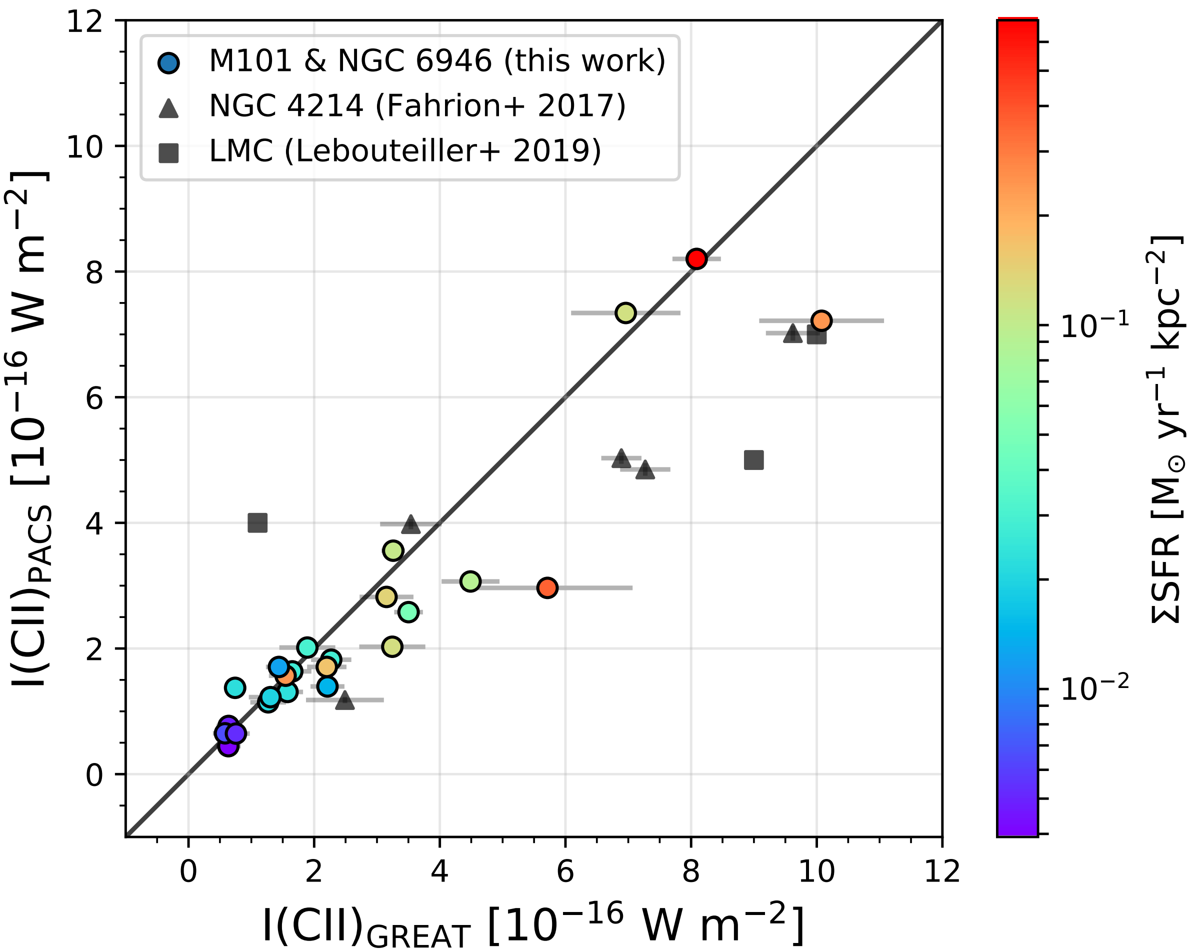

Figure 2.2: The line flux of the SOFIA/GREAT [CII] emission compared to the *Herschel* PACS [CII] flux. Circles are the data in this paper, triangles are from NGC 4214 (Fahrion et al., 2017), and squares are for the LMC (Lebouteiller et al., 2019). The black line represents the line of unity. Colorscale is the $\Sigma_{\rm SFR}$ calculated from 24μm data. The GREAT data in this work is $\sim$7% brighter than the PACS data on average, but this difference is within absolute flux accuracy bounds for the PACS instrument (15%, Croxall et al., 2013). The GREAT and PACS [CII] intensities from the literature have a larger discrepancy, likely due to approximating the PACS PSF as a Gaussian. Error bars reported are the statistical 1σ rms noise (PACS errorbars are smaller than the data points).

a much larger discrepancy, with GREAT data approximately 40% brighter than PACS. These studies, however, approximate the PACS PSF as a Gaussian beam instead of using the more accurate convolution kernels required to transform the PACS PSF into a Gaussian comparable to the GREAT beam. The native PACS spectrograph PSF at $158\,\mu$m is not Gaussian shaped: a significant portion of the total power resides in wide wings and a high pedestal that creates a halo around a point source (Geis & Lutz, 2010). When we do not use the proper PACs convolution kernel, we receive a similar discrepancy of $\sim 40\%$ that is seen in the observations from the literature. Therefore, we attribute their discrepancy to a beam mismatch.

2.2.3 HI 21 cm data

The HI data comes from The HI Nearby Galaxy Survey (THINGS, Walter et al. 2008), a 21 cm (1.4204 GHz) Very Large Array (VLA) survey of nearby galaxies that uses the same galaxy sample as SINGS, the Spitzer Infrared Nearby Galaxies Survey (Kennicutt et al., 2003). We use the THINGS naturally weighted cubes which have a half-power beam width of $10.8'' \times 10.2''$ for M101 and $6.0'' \times 5.6''$ for NGC 6946. We will use the HI data as the tracer for the atomic material in these galaxies.

Maps of extended objects made with interferometer data that are not combined with single dish data have missing flux on large scales, called the short spacings problem (Braun & Walterbos, 1985). This may manifest as a shallow negative bowl around the emission, caused by the interferometer filtering out the lowest spatial frequencies. The effect is seen in the HI THINGS data of these galaxies and is particularly strong in NGC 6946. We cannot properly correct for the lack of this information, but we can mitigate the effect of the negative portions of the spectrum

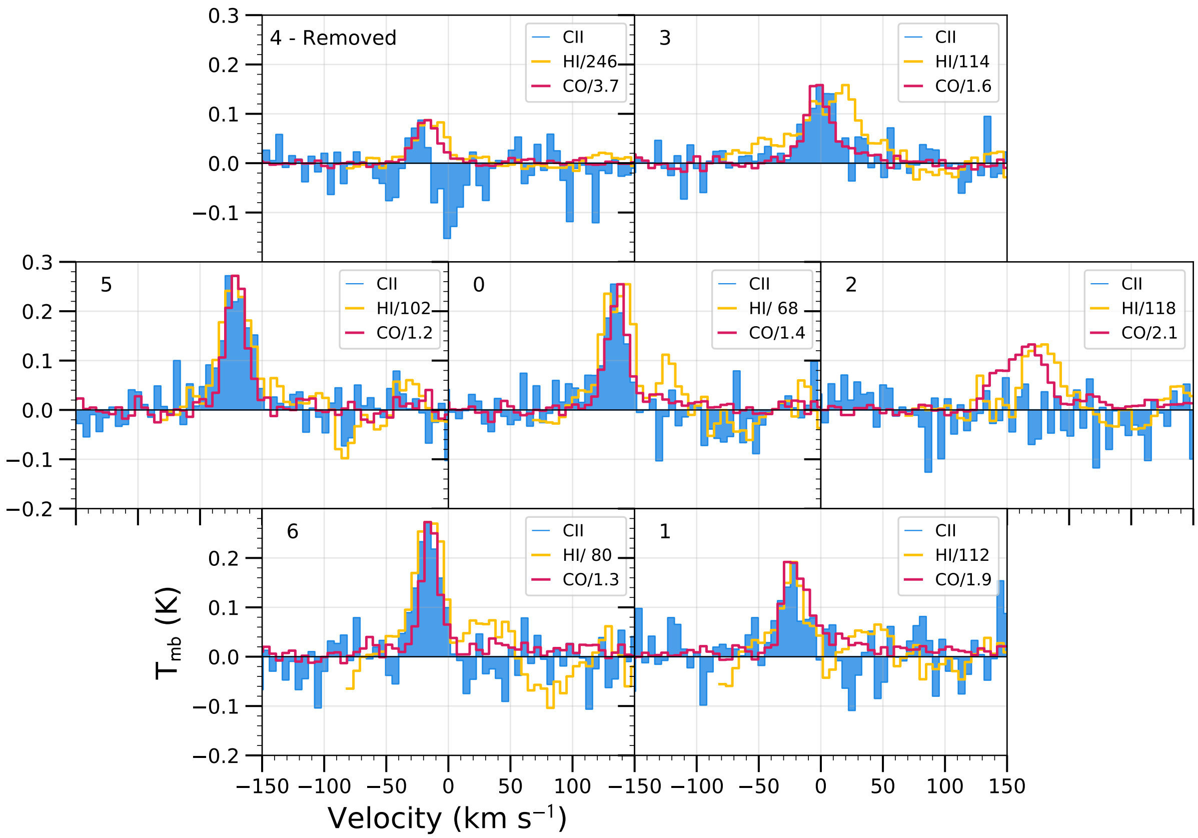

Figure 2.3: An example of spectra from the upGREAT receiver in NGC 6946 region N5. This region contains detected [CII] emission in most of the pointings. The HI and CO spectra are normalized to the maximum intensity of the [CII] spectra. The width of the [CII] profiles tend to lie in between the CO and HI profile widths, suggesting an origin from both the atomic and molecular gas. These offsets between the [CII], CO, and HI, are greater than the instrument's spectral resolution of 5.2 km s^{-1}. Pointing number is labeled in the top left corner of each spectrum. Region N5-4 contains negative emission from emission in the off during calibration and is an example of a spectrum that is removed from this analysis.

in our analysis. We fit the negative spectral region around the signal with a first order polynomial and add the resulting fit to the negative wings that border the signal. For our analysis, which focuses on the spectral shape of emission, this fairly small re-baselining correction is sufficient to avoid negative regions having a strong effect on the decomposition.

2.2.4 CO (2-1) data

The CO data are from the HERA CO-Line Extragalactic Survey (HERACLES, Leroy et al. 2009). This is a CO(2-1) (230.54 GHz) survey using the IRAM 30 m telescope, designed to complement the THINGS and SINGS surveys. The half-power beam width for both galaxies is $13''$. The CO data will be used as the tracer for the molecular material in these galaxies.

2.2.5 Star formation Rates

We use a combination of 24 μm and Hα data in order to trace the obscured and unobscured star formation activity in these galaxies. The 24 μm data were taken from the SINGS Survey (Kennicutt et al., 2003) and we use the convolution kernels provided by Aniano et al. (2011) to convert the MIPS 24 μm PSF into a Gaussian beam of $15''$. The Hα data were compiled and processed by Leroy et al. (2012), where the map for NGC 6946 came from the SINGS Survey (Kennicutt et al., 2003) and the map for M101 was retrieved from Hoopes et al. (2001). The contribution of [NII] to the Hα emission was removed (Kennicutt et al., 2009, 2008), the foreground stars were subtracted (Muñoz-Mateos et al., 2009), and the Hα data were corrected for Galactic extinction (Schlegel et al., 1998). We use the calibration from Calzetti et al. (2007) (Equation 7) and the combination of the 24 μm and Hα data to calculate the star formation rate surface densities ($\Sigma_{\rm SFR}$) in these galaxies. The $\Sigma_{\rm SFR}$ is corrected for inclination, assuming a value of 38° for NGC 6946 and 18° for M101.

This calibration adopts a truncated Salpeter IMF with a slope of 1.3 in the range of 0.1–0.5 $M_\odot$ and a slope of 2.3 in the range of 0.5–120 $M_\odot$. The distribution of $\Sigma_{\rm SFR}$ is shown in the colorscale of Figure 2.2, where there is a spread of about 3 orders of magnitude in $\Sigma_{\rm SFR}$ for our sample.

2.2.6 Matching the spectral and spatial resolution

In order to match the resolution of the SOFIA data, we convolved the CO and HI maps with a Gaussian to the GREAT beam size of 15″, which corresponds to 495 pc for M101 and 567 pc for NGC 6946.

We also resample the [CII], CO, and HI spectra to a common velocity resolution of 5.2 km s^{-1} by hanning smoothing (when applicable) and regrid each spectra to match that of the 5.2 km s^{-1} resolution CO data. All data were in the radio velocity convention and when necessary we converted the velocity reference to the kinematic local standard of rest (LSRK). An example of the three spectra after smoothing to the same resolution is shown in Figure 2.3.

2.2.7 Selecting the spectra for this study

We select the regions for the analysis by the integrated intensity of the [CII] line. First, we remove all spectra that exhibit features due to emission in the off position (see Figure 2.3, region N5-4) or spectra with noise spikes greater than 1 K. We calculate the [CII] integrated intensity and 1σ rms error by defining the bounds of integration from the HI data. We then select the spectra that have an integrated intensity greater than three times the calculated rms 1σ noise level as the main sample in this work (referred to as the 3σ sample). In addition, we use an integrated intensity cut, which includes all spectra greater than a given K km s^{-1} value, and a sample which uses all of the spectra, to test how the sample selection alters the results (see more in §2.4.3).

A summary of all the [CII] spectra, including the position of pointings, star formation rate surface density, and the [CII] integrated intensity are given in Table 2.1.

2.3 Methodology

2.3.1 [CII] emission decomposition description

The method of using the kinematic information to establish the origin of the [CII] is presented in several analyses (e.g., Fahrion et al., 2017; Lebouteiller et al., 2019; Okada et al., 2019, 2015). These approaches generally rely on decomposing the profiles into Gaussian components that can then be related with the HI or CO spectra. Here we present another approach, by creating a model [CII] spectrum that is comprised of a linear combination of the CO and HI spectra, and finding the coefficients that best reproduce the [CII] spectrum, similar to the work by Mookerjea et al. (2016). This has the advantage of being entirely non-parametric, and of presenting a mathematically well-posed problem with a unique solution that lends itself to a simple reliability analysis. The drawback is that components that are not represented in our model (besides the HI or the CO spectra) are not easily analyzed. To account for this, we show that the ionized gas has a negligible contribution to the [CII] emission in §2.4.2. Because HI has two phases that contribute equally to the 21 cm spectrum, but [CII] emission is thought to be predominately associated with one of them (the CNM), this method requires that we work on scales ($\sim$ 500 pc) that are large

Table 2.1: [CII] SOFIA/GREAT Spectra Summary

Galaxy	Region	Cycle	R.A. (J2000)	Decl. (J2000)	12+log(O/H)	$\Sigma_{\rm SFR}$ ($M_\odot$ yr^{-1} kpc^{-2})	$\int I_{[CII]}$ (K km s^{-1})	rms (K)
M101	Ma	2	14h03m41.0s	54d19m01.0s	8.43	6.88×10^{-1}	27.5 ± 1.3	0.06
M101	M3-0	4	14h03m00.8s	54d14m25.2s	8.31	1.06×10^{-1}	7.5 ± 1.1	0.05
NGC6946	Nd	2	20h34m32.0s	60d10m16.0s	8.53	1.18×10^{-1}	23.6 ± 3.0	0.12
NGC6946	N5-5	4	20h35m04.3s	60d09m55.1s	8.62	4.54×10^{-2}	8.0 ± 0.8	0.04
NGC6946	N1-4	4	20h35m19.2s	60d11m24.7s	8.48	4.93×10^{-3}	-0.3 ± 1.2	0.06

Description of [CII] spectra with examples given from the two different cycles and galaxies used in this work. Region N1-4 represents a "non-detected" [CII] spectra due to the negative integrated [CII] intensity. Divide by 1.43 $\times\ 10^5$ to convert $\int I_{[CII]}$ from K km s^{-1} to erg s^{-1} cm^{-2} sr^{-1} (Goldsmith et al., 2012). (This table in its entirety is available in a machine-readable form online.)

enough for the phases to be well-mixed so that the kinematics of the 21 cm emission represents well the CNM.

We use the Rayleigh-Jeans brightness temperatures as a measure of the flux for the [CII], CO, and HI spectra. The decomposition creates a model [CII] spectrum from a linear combination of the CO and HI spectra, where $w_{\rm CO}$ and $w_{\rm HI}$ are the constants for the linear combination:

$$T_{\rm [CII],model} = w_{\rm CO} T_{\rm CO} + w_{\rm HI} T_{\rm HI}. \tag{2.1}$$

We define $T_{\rm CO}$ and $T_{\rm HI}$ as the Rayleigh-Jeans brightness temperatures of the CO and HI data, respectively, and $T_{\rm [CII],model}$ is the model [CII] spectrum. We then use χ^2 minimization to estimate the values of $w_{\rm CO}$ and $w_{\rm HI}$ that best reproduce the observed [CII] spectrum given the noise of the observations:

$$\chi^2 = \sum_{n=1}^{n} \frac{(T_{\rm [CII]} - w_{\rm CO} T_{\rm CO} - w_{\rm HI} T_{\rm HI})^2}{\sigma^2_{\rm [CII]} + w^2_{\rm CO}\sigma^2_{\rm CO} + w^2_{\rm HI}\sigma^2_{\rm HI}} \tag{2.2}$$

where σ corresponds to the rms noise of each spectrum and the model is evaluated across the n channels in the given spectra.

With best fit $w_{\rm CO}$ and $w_{\rm HI}$ values, we then calculate the fraction of the integrated [CII] intensity associated with the molecular and atomic gas:

$$f_{\rm mol} = \frac{w_{\rm CO} \int T_{\rm CO} dv}{\int T_{\rm [CII]} dv};\ f_{\rm atomic} = \frac{w_{\rm HI} \int T_{\rm HI} dv}{\int T_{\rm [CII]} dv}. \tag{2.3}$$

By using the linear combination of CO and HI spectra as the model for the [CII] spectra, we maximize the contribution the CO-traced molecular gas and the HI-traced atomic gas have to the overall [CII] emission. Additional contributing ISM components to the [CII] emission will be seen in residuals of the fit if the velocity profiles have a different shape from the CO or HI profiles. ISM components that have similar velocity profiles as the CO or HI will therefore be attributed to the tracer with the most similar shape. For example, [CII] associated with the dense ionized gas from HII regions will likely share a similar spectral profile to the CO that is associated with the dense PDRs. Thus, this dense ionized gas may be assigned to the molecular component.

2.3.2 Evaluation of the decomposition method

In order to evaluate the accuracy of the method, we run a series of simulated [CII] decomposition cases to explore how this method changes with different parameters, such as the peak signal-to-noise ratio (SNR). We produce realistic CO and HI templates by averaging the spectral profiles of our existing CO and HI data, normalizing them to a peak of unity. Using a combination of these CO and HI template spectra, we create simulated [CII] spectra using different values of w_{CO} and w_{HI}, where $w_{\mathrm{CO}} + \mathrm{w}_{\mathrm{HI}} = 1$. We then add Gaussian distributed noise that correspond to the given [CII] SNR for that trial. The input w_{CO} parameter ranges from 0.0 - 1.0 in 0.1 increments and the peak SNR ranges from 5 - 30 in increments of 5. Lastly, we use the χ^2 minimization in Equation 2.2 to calculate best fit values for w_{CO} and repeat the process 5000 times.

We find the accuracy of the decomposition method by comparing the input w_{CO} parameter to the resulting fitted parameter (note that this is a one-parameter problem since $w_{\mathrm{CO}} + \mathrm{w}_{\mathrm{HI}} = 1$, so our results for the molecular fraction also apply to the atomic fraction). We calculate the standard deviation and median absolute deviation between the fitted w_{CO} and the respective input

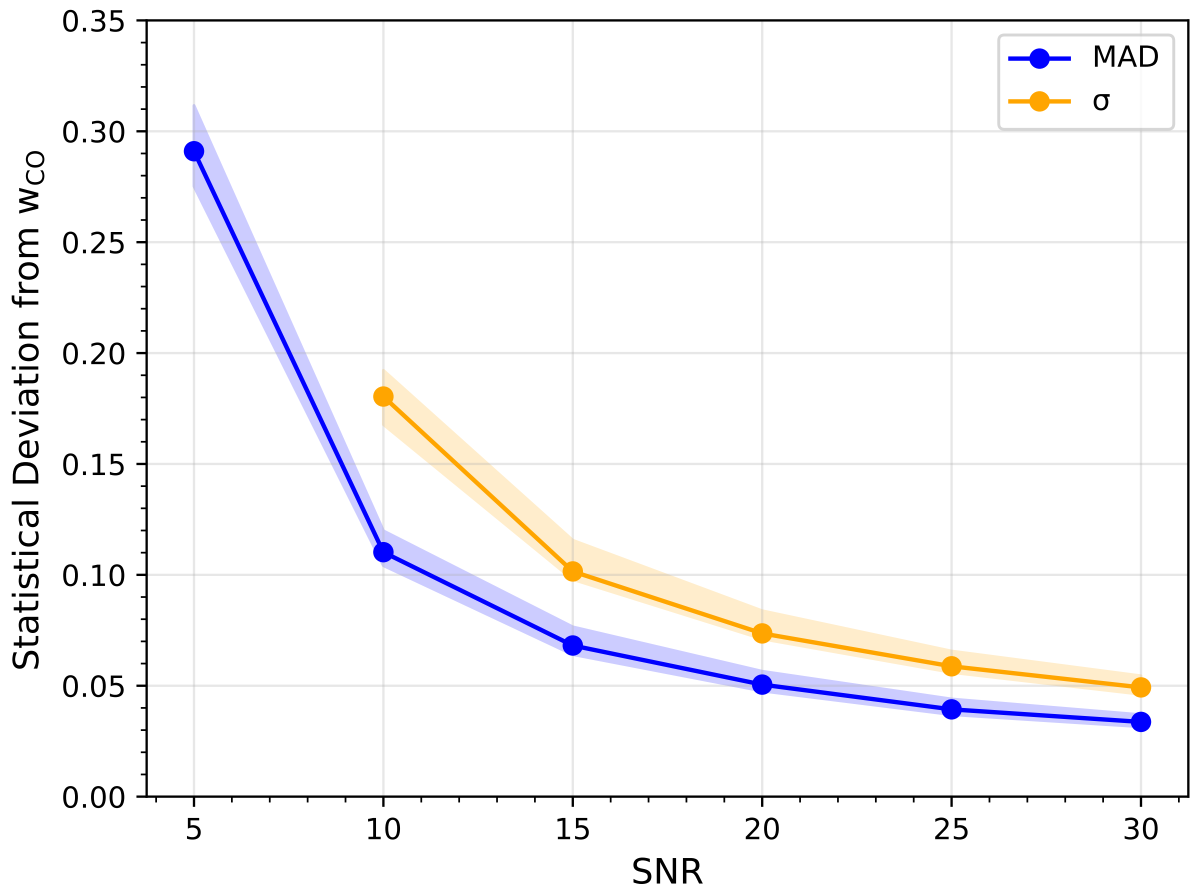

Figure 2.4: Accuracy of the [CII] decomposition method: error in the recovery of the input parameter in Monte Carlo realizations using realistic template spectra and varying SNR. The orange curve is the standard deviation of the fitted parameter with respect to the input. The blue curve is the median absolute deviation (MAD) of the fitted parameters. The shaded regions correspond to the variation of the statistical deviations from the w_{CO} value. A SNR of ~ 15 is necessary for recovering the fraction of emission from the molecular phase to an accuracy of $\Delta w_{CO} \approx \pm 0.10$ at 1σ.

$w_{\rm CO}$. Figure 2.4 shows both statistics averaged over all $w_{\rm CO}$ input parameters in a given SNR bin with the distribution of the $w_{\rm CO}$ input parameter represented by the shaded region. The standard deviation is more sensitive to outliers and consequently can have very large values, such as σ = 660 for the SNR = 5 bin (not shown on figure). The median absolute deviation is not as sensitive to outliers and returns a value of 0.29 for SNR = 5 (equivalent to 0.41 for standard deviation when assuming Gaussian distributed data). The MAD value for SNR = 5, however, is much larger than for other SNR values, indicating that spectra with SNR = 5 do not give accurate results.

The standard deviation represents the 1σ Gaussian distributed error expected on the parameter when decomposing a single spectrum. Thus a peak SNR of about 15 corresponds to a deviation or error of 0.1 on the fitted parameter when using this decomposition method. Over most observations in this sample, the [CII] data have the lowest peak SNR, and therefore their SNR is the main limit on the ability to decompose the [CII] spectra accurately.

In addition to the accuracy, we are also interested in determining whether a two-component model, using both the CO and HI spectra as templates, gives a statistically better result than a one-component model using either of the templates. This can be thought of as a *nested model*, as the one-component model is a subset of the two-component model (i.e., it is the two-component model with one parameter equal to zero). Adding more parameters to a nested model will always produce a lower χ^2, but the improvement may not be significant.

We compare the possible models through the *F-test* (Mendenhall & Sincich, 2011, § 4.6). While the F-test is often used in analysis of variance (ANOVA), it can also be used in regression analysis to test whether the simpler of two models provides a better fit. We calculate the F-statistic through:

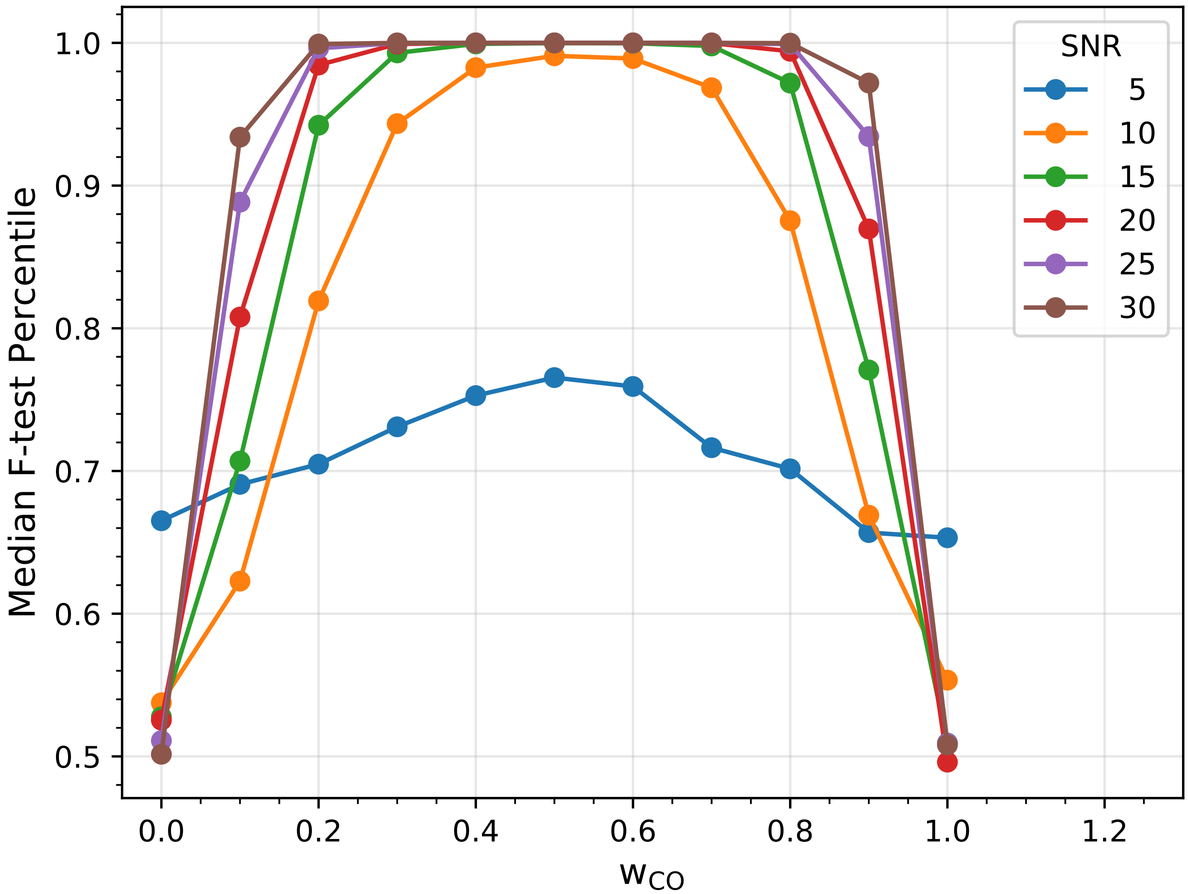

Figure 2.5: When is a two-component description statistically better than a one-component model? A high F-test value shows that the two-component model provides a better description of the data. In turn, the ability to make this distinction requires a minimum SNR from the data. A two-component model is also more easily distinguishable from a single-component when both components have similar weights (note that $w_{\rm CO} + w_{\rm HI} = 1$). This plot shows that in cases where one-component contributes 20% of the emission and the other 80% a SNR∼15 is necessary. For $40\% - 60\%$ contributions this can be relaxed to SNR~ 10, but to distinguish between one and two components when the lesser component contributes only 10% of the signal requires very high SNR$\gtrsim 30$.

$$F = \frac{(\chi^2_{1\mathrm{comp}} - \chi^2_{2\mathrm{comp}})/(q-p)}{\chi^2_{2\mathrm{comp}}/(N-q)} \tag{2.4}$$

where $\chi^2_{1\mathrm{comp}}$ is the χ^2 for the simpler model, p is the number of parameters in the simpler model, $\chi^2_{2\mathrm{comp}}$ is the χ^2 for the complex model, q is the number of parameters in the complex model, and N is the number of data points. The F statistic defined in Equation 2.4 follows the F-distribution with $(q-p, N-q) = (1, N-2)$ degrees of freedom. We define a null hypothesis that the more complex model does not provide a significantly better fit than the simpler model. We can reject this null hypothesis, implying that the complex model provides a better fit, when the F-statistic is greater than a given critical value from the corresponding F-distribution.

We show in Figure 2.5 the median F-statistic percentile for the same range of w_{CO} and peak SNR as used in the accuracy simulations. The one-component model is defined by fitting the CO and HI template to the simulated data and selecting the fit with the lowest χ^2 value. The F-statistic percentile is dependent on the value for w_{CO}, since it is easier to see the effect of both components when they contribute approximately equally (note that $w_{\mathrm{HI}} = 1 - w_{\mathrm{CO}}$). We cannot statistically distinguish between the two-component model and a one-component model with a peak SNR of five. A peak SNR of ten does a better job, but only for $w_{\mathrm{CO}} = 0.4 - 0.6$. The spectra therefore need to have a high SNR of at least fifteen to distinguish between a one-component and a two-component model for cases where the lesser component contributes 20% or more of the signal. The majority of the individual [CII] spectra from M101 and NGC 6946 have a peak SNR of less than ten. Combined with the simulations on the accuracy of the decomposition method, we conclude we need a higher peak [CII] SNR than that provided by most individual spectra in this sample: we achieve this through averaging the data (see §2.4.3).

2.4 Results

In order to identify the dominant phase of the ISM traced by [CII], we compare the velocity resolved profiles of [CII] from the SOFIA/GREAT data to the profiles of HI 21 cm emission, a tracer of the atomic phase, and to CO $\mathrm{J} = 2 - 1$ emission, a tracer of the molecular phase. The physical spatial resolution of the [CII], CO, and HI data is $\sim$500 pc for M101 and NGC 6946. The profiles carry information about the bulk motions of the given gas phase at this resolution, and we will use their shape to identify the origin of the [CII] emission. Early detections of [CII] emission from line-of-sight observations of the Milky Way revealed the multi-phase and extended nature of [CII] emission (Bennett et al., 1994; Madden et al., 1993; Makiuti et al., 2002; Shibai et al., 1991; Stacey et al., 1985; Wright et al., 1991). In order to quantify the amount of [CII] that is associated with each phase in the plane of the Milky Way, velocity resolved spectra are required, as performed by Pineda et al. (2013). We apply a similar velocity resolved approach to decompose the [CII] emission into the component phases in two nearby galaxies outside of the local group. The multi-phase nature of the [CII] emission can be inferred by inspection of Figure 2.3 (especially region N5-6), where the [CII] profile widths are intermediate between those for CO and HI.

2.4.1 Linewidth comparison

By fitting the spectral line profiles of the [CII], CO, and HI data, we can quantify how the [CII] emission is intermediate between the CO and HI emission. We fit each spectra with a Gaussian profile and compare the linewidths between the spectra by examining the fitted full width at half maximum (FWHM) of each line. Figure 2.6 shows the difference between the

FWHM of the [CII] and the CO profile (on the y-axis) or the HI profile (on the x-axis). Most points are found in the fourth quadrant, indicating that the [CII] FWHM lies between those of CO and HI. There are no strong trends with $\Sigma_{\rm SFR}$, shown through the colorscale, and the difference between the FWHM of the [CII], CO, and HI. The mean FWHM for the [CII] is 27.7 km s^{-1} while the mean FWHM for CO and HI are 22.1 km s^{-1} and 35.7 km s^{-1}, respectively. On average, the HI FWHM is 29% wider than the [CII] profile and the CO FWHM is 25% narrower than the [CII] profile. Other studies have also shown linewidth differences between the [CII], CO, and HI spectra, with up to a 50% difference between the CO and [CII] profiles (e.g. Lebouteiller et al., 2019; Requena-Torres et al., 2016; de Blok et al., 2016).

Gaussian curves fit most of these spectra well, but there are some instances where the fit is poor ($\chi^2_{\rm red} \simeq 2.5$), often when spectra are not symmetric or have a lower peak SNR. These asymmetries provide motivation for using a [CII] decomposition method that does not assume a line shape (see §2.3.1). Additionally, the poor Gaussian fits are the points in Figure 2.6 that have higher errorbars.

Note that the kinematic decomposition method would not be effective if the CO and HI profiles are too similar. The HI spectra, however, are on average 62% wider than the CO spectra. Thus the tracers of the molecular and atomic gas are sufficiently different to provide an accurate decomposition of the [CII] emission (see §2.3.2). Further, the difference between the spectral profiles of [CII], CO, and HI are also larger than the velocity resolution of these data.

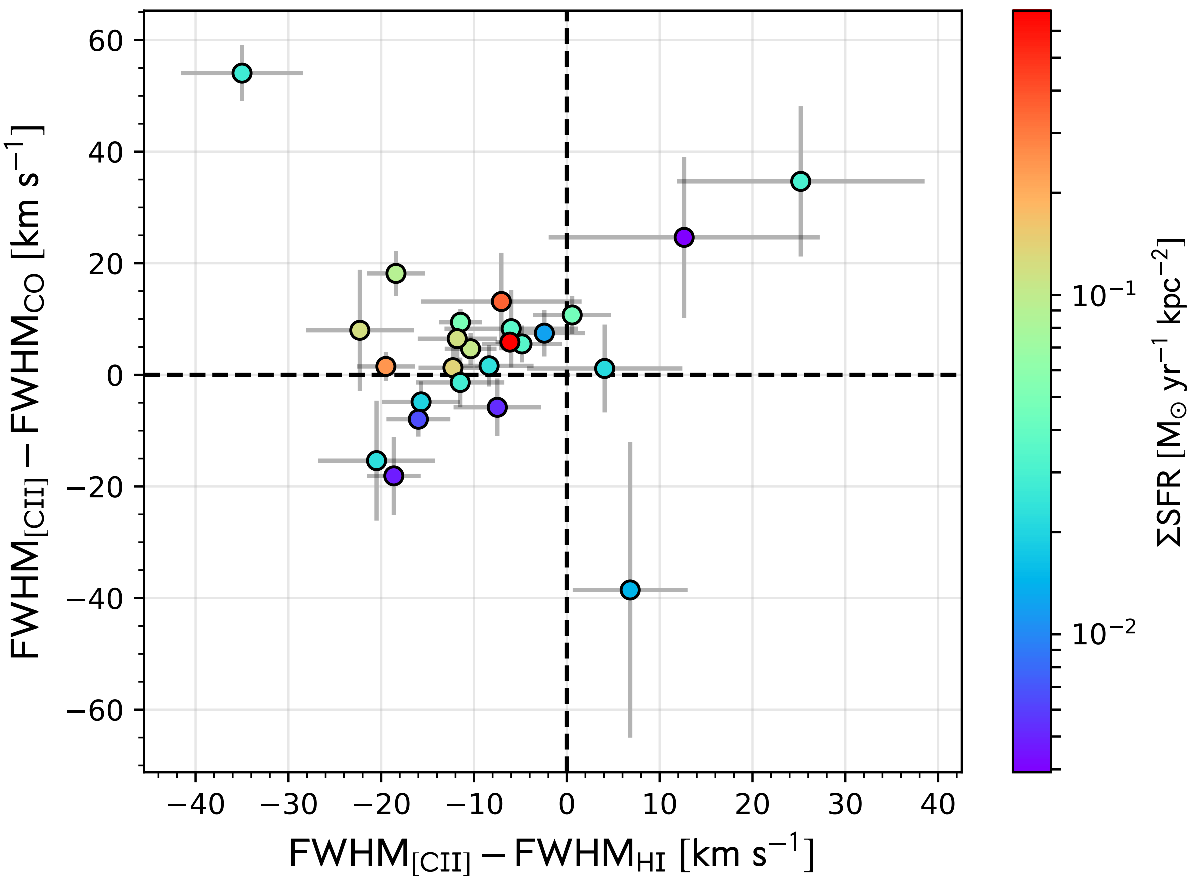

Figure 2.6: The linewidth of the fitted Gaussian curves for the HI, CO, and [CII] data as traced by the FWHM. Points to the left of the zero line mean that the HI line profiles are wider than the [CII] while points above the zero line show [CII] line profiles that are wider than the CO. Most of the [CII] profiles have a width in between the CO and HI (see upper left quadrant), suggesting a combined origin of the two.

Table 2.2: [CII] Gaussian Fits Summary

Galaxy	Region	A (K)	v_{peak} ($\mathrm{km\,s^{-1}}$)	FWHM ($\mathrm{km\,s^{-1}}$)
M101	Ma	0.95±0.04	273.6±0.6	27.4±1.3
M101	M3-0	0.20±0.03	201.6±2.0	31.1±4.8
NGC6946	Nd	0.61±0.06	110.5±1.7	33.1±4.0
NGC6946	N5-5	0.24±0.02	-21.7±1.4	30.1±3.3

The Gaussian fitted parameters of the [CII] lines for the 3σ sample. A represents the amplitude of the Gaussian, v_{peak} is the fitted peak velocity, and FWHM is the full width half maximum of the Gaussian fit. (This table in its entirety is available in a machine-readable form online.)

2.4.2 Contributions from ionized gas

The [NII] 205 μm transition arises from ionized gas because nitrogen has an ionization potential of 14.5 eV, greater than that of hydrogen, and can be used to isolate the contribution the ionized gas has on the [CII] emission. The similar critical densities for collisions with electrons, $n_e \approx 32\,\mathrm{cm^{-3}}$ for [NII] 205 μm and $n_e \approx 45\,\mathrm{cm^{-3}}$ for [CII] (Schöier et al., 2005), mean that the [CII]/[NII] line ratio has a weak dependence on the density and ionization state. Therefore, for a given $\mathrm{N^+/C^+}$ abundance ratio, the observed [CII]/[NII] line ratio gives a relatively density-independent estimate of the contribution of ionized gas on the total [CII] emission (Oberst et al., 2006).

[NII] 205 μm is a faint line compared to [CII], and consequently all the [NII] observations we have from SOFIA/GREAT are non-detections. We use the 3σ rms of [NII] to compute a lower limit on the [CII]/[NII] ratio. This ratio can then be used to find a lower limit on $f_{neutral}$, the fraction of molecular and atomic gas that contributes to the overall [CII] intensity (or, conversely, an upper limit to the fraction of emission contributed by the ionized gas). We compare the observed [CII]/[NII] ratio to the theoretical ratio derived from the ionic abundance of C^+/N^+ and attribute any excess to the contribution the neutral gas has to the [CII] emission. The theoretical [CII]158 μm/[NII]205 μm ratio does depend slightly on density, but ranges between 3.1 at low densities and 4.2 for high densities (Oberst et al., 2006). We use a [CII]158 μm/[NII]205 μm ratio of 4, the same as Croxall et al. (2017), in order to compare to their results. This value comes from calculations of the collision rates of e^- with C^+ (Tayal, 2008) and N^+ (Tayal, 2011) and assumes Galactic gas phase abundances for carbon ($X_{C/H} = 1.6\times\ 10^{-4}$, Sofia et al. 2004) and nitrogen ($X_{N/H} = 7.5\times\ 10^{-5}$, Meyer et al. 1997). We calculate $f_{neutral}$ by subtracting the ionized gas contribution to [CII]:

$$f_{\text{neutral}} = \frac{I_{\text{[CII]}} - R_{\text{ionized}} \times (3\sigma_{\text{rms,[NII]}})}{I_{\text{[CII]}}} \tag{2.5}$$

where R_{ionized} = 4, the approximate theoretical [CII]/[NII] ratio.

We present the $f_{neutral}$ lower limits in Figure 2.7, with the colorscale representing the oxygen abundance we estimate from the metallicity gradients found in Pilyugin et al. (2014). All of the limits show an $f_{neutral}$ greater than 70% with an average of $f_{neutral}$ = 88%. There is also a trend with the [CII] intensity, suggesting that the regions with brighter [CII] have a smaller possible contribution from the ionized gas.

The estimation of $f_{neutral}$ assumes a C^+/N^+ ratio, which we anchor to the Galactic $C/N = 2.13$ ratio at log(O/H) $\approx$ 8.65 (Simón-Díaz & Stasińska, 2011). There is an expected variation of the C/N ratio with metallicity (Nieva & Przybilla, 2012), but Croxall et al. (2017) show that $f_{neutral}$ varies by only 10% for a change of 0.8 dex in oxygen abundance. Therefore our original calculation using a Galactic abundance will only marginally change the already minimal

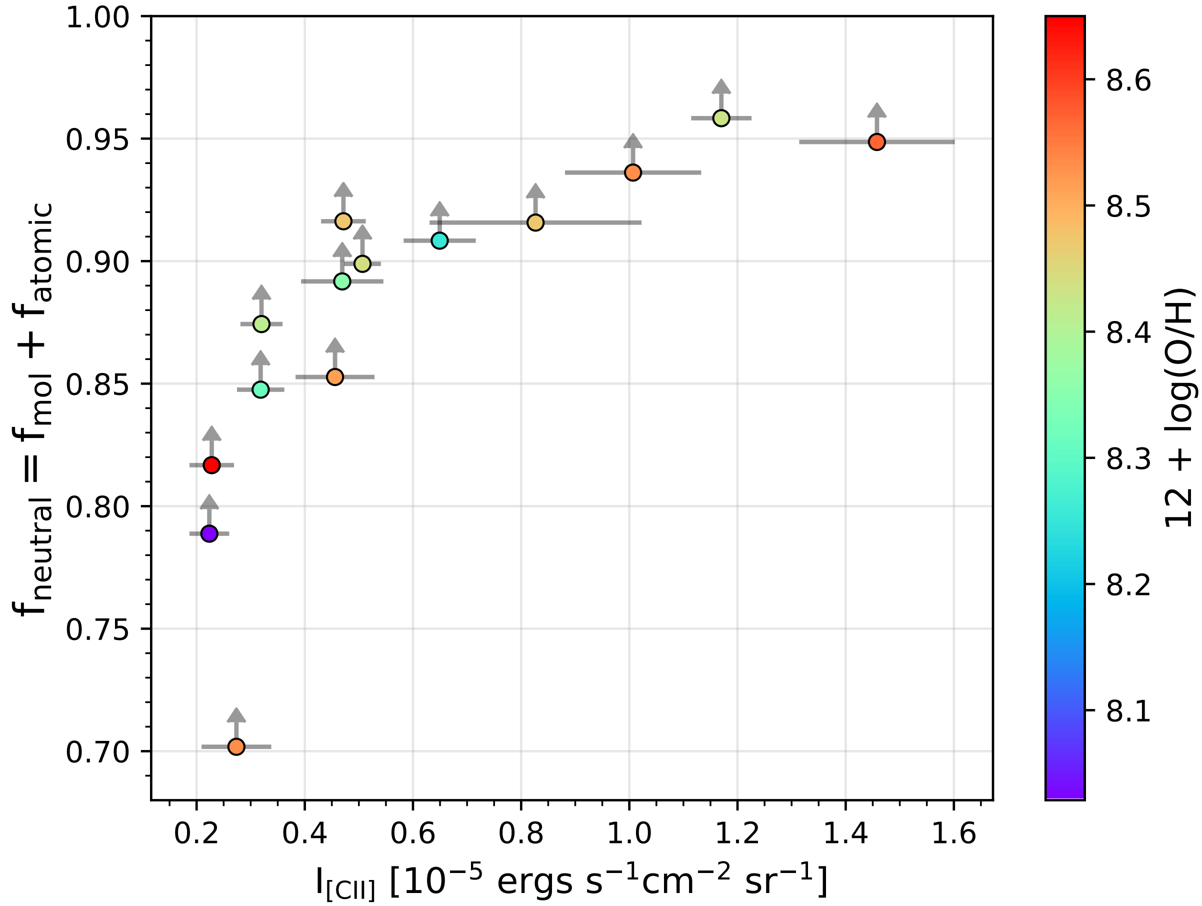

Figure 2.7: Lower limits of the contribution the neutral gas has to the [CII] emission found through 3σ rms [NII] 205 μm measurements. Colors represent the gas phase oxygen abundances. The average limit $f_{neutral} \gtrsim 88\%$, suggesting the the contribution of ionized gas to the [CII] emission is negligible.

contribution the ionized gas has to the [CII] emission.

The $f_{neutral}$ lower limits we compute are very similar to the work by Croxall et al. (2017), who find (74±8)% of the [CII] emission comes from the neutral gas in galaxies from KINGFISH (Kennicutt et al., 2011). A similar result is found for regions in the LMC, where $f_{neutral} \gtrsim 90\%$ (Lebouteiller et al., 2019), and in the measurements of low metallicity galaxies in the Dwarf Galaxy Survey, which estimate $f_{neutral} > 70\%$ (Cormier et al., 2019). According to these limits, we assume that the contribution of the ionized gas to the [CII] emission is negligible. This allows us to spectrally decompose the [CII] emission using only tracers for molecular and atomic gas.

2.4.3 Decomposition of spectrally averaged data

As discussed in §2.3.2, we need a high peak signal-to-noise ratio (SNR) of 10-15 to accurately spectrally decompose the [CII] emission. Only three spectra in this dataset have a peak SNR greater than 10, and these individual spectra are analyzed in §2.4.4. In order to achieve the SNR required to accurately decompose the [CII] spectra, we average the bulk of the data by combining similar spectra together through a process called stacking.

We stack the spectra by aligning them in velocity, with the HI data providing the velocity reference because the HI spectra have a higher SNR compared to the CO spectra. First, we shift all of the spectra to the center of the HI Gaussian-fitted peak velocity. We then interpolate over a velocity grid with a 150 $\mathrm{km\,s^{-1}}$ bandwidth and the 5.2 $\mathrm{km\,s^{-1}}$ velocity resolution. The centered, interpolated spectra for the [CII], CO, and HI are averaged together. This method reduces the noise of the final spectrum by a factor of $\sim \sqrt{N_{spec}}$, where N_{spec} is the number of spectra stacked in the given cut and sample. The peak SNR of the stacked [CII] spectra thus increases to about 10 or higher, making a meaningful spectral decomposition possible. For example, stacking 13 spectra together each with an average SNR $\sim$ 5 produces a stacked spectrum with an SNR $\sim$ 15.

In the process of stacking the data, we wish to preserve any relation between the environmental properties in a region and the results of the [CII] decomposition. For this study, we will stack spectra binning by star formation rate surface density ($\Sigma_{\rm SFR}$), metallicity (Z), and normalized galactocentric radius ($\rm R/R_{25}$). We bisect the data into a "low" $\Sigma_{\rm SFR}$ bin and a "high" $\Sigma_{\rm SFR}$ bin, with a cutoff value of $\Sigma_{\rm SFR} = 6 \times 10^{-2}$ $\rm M_\odot\ yr^{-1}\,kpc^{-2}$. We use the same process for metallicity by defining a cutoff value of 12 + log(O/H) = 8.55 and for the galactocentric radius with a cutoff value of $\mathrm{R/R_{25}}$ = 0.4. These values were chosen by splitting the 3σ sample of [CII] spectra into roughly equal numbered bins. The minimum metallicity for the 3σ sample is 12 + log(O/H) = 8.03 and the maximum is 12 + log(O/H) = 8.65. The Σ_{SFR} varies between 3.9×10^{-3} and 6.9×10^{-1} $\mathrm{M_{\odot}\ yr^{-1}\ kpc^{-2}}$. These spectra also span the distribution of galactocentric radii, with $\mathrm{R/R_{25}}$ ranging from 0.1 to 0.9. In addition, we stack all the spectra from M101 and NGC 6946 separately in order to identify whether there are differences in the results of the [CII] decomposition in a given galaxy. Lastly, we produce a stack of all spectra together regardless of the property or galaxy (labeled "all spec").

Because the results of the decomposition may depend on the sub-sample of [CII] spectra used, we produce different stacks with selections as described in §2.2.7. We include spectra by using three different criteria: a 3σ sub-sample (defined as including spectra where the [CII] integrated intensity of a given [CII] spectrum is 3 times the rms noise), an intensity sub-sample (defined as including spectra when the [CII] integrated intensity is greater than $5\,\mathrm{K\,km\,s^{-1}}$), and the sample where all the [CII] spectra are selected, including non-detections (labeled "no cuts"). The 3σ and I>$5\,\mathrm{K\,km\,s^{-1}}$ intensity sub-samples give similar results; therefore we present stacked data using just the 3σ and "no cut" samples.

We then fit the stacked spectra with a two-component model, defined as the linear combination of the CO and HI data, as well as a one-component model, which uses only the CO or HI data as templates. We compare the goodness of fit of the one-component model with the lowest χ^2 to the two-component model using the F-test, as described in §2.3.2. We find that a two-component model fits the data statistically better in most instances, except for stacks corresponding to the low Σ_{SFR} bin, which has a lower [CII] SNR than other stacks, and the stacks where both models

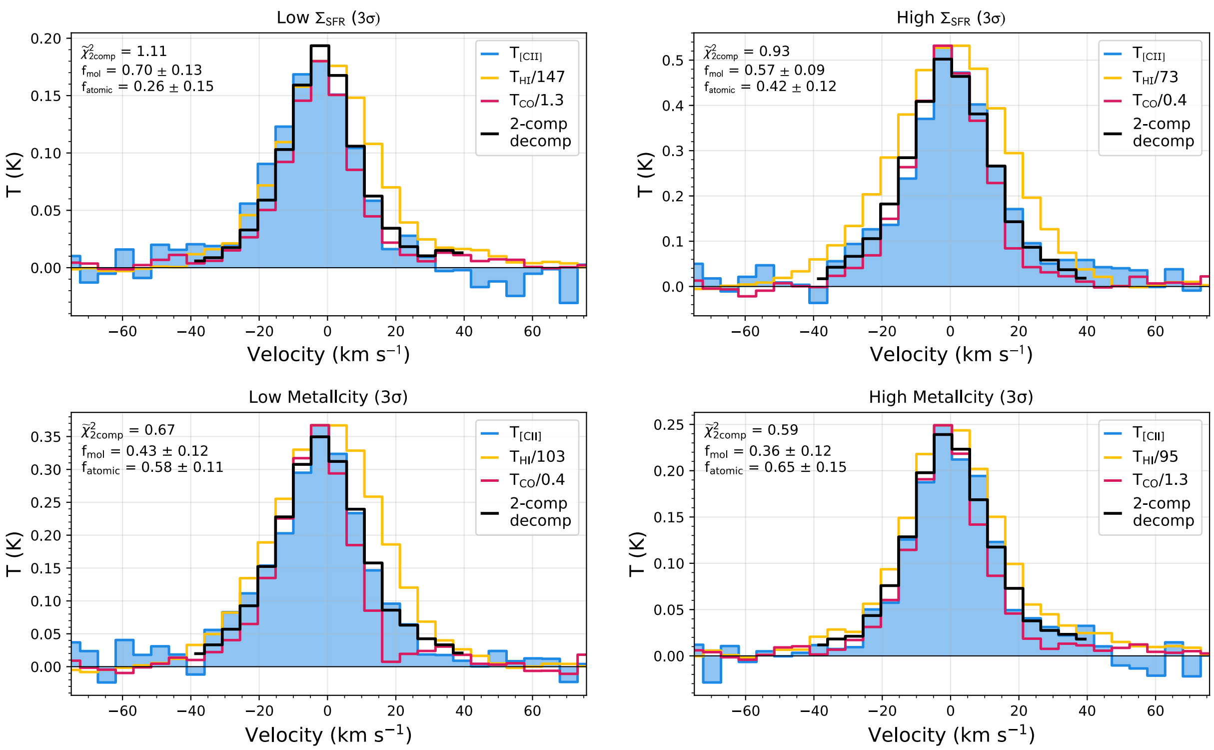

Figure 2.8: Decomposition of stacked spectra from the 3σ sub-sample (includes all regions with integrated [CII] intensities three times greater than the rms noise). The top two panels show the sample split by $\Sigma_{\rm SFR}$ where the division is $\Sigma_{\rm SFR} = 6 \times 10^{-2}$ M$_\odot$ yr^{-1} kpc^{-2}. The bottom two panels show the sample split by metallicity, where the division is 12 + log(O/H) = 8.55. Blue colors represent the stacked [CII] spectrum, yellow corresponds to the stacked HI spectrum, and red shows the stacked CO data. The CO and HI spectra are scaled to the amplitude of the [CII] spectrum. The black line is the two component decomposition using the scaled HI and CO data to best reproduce the [CII] spectrum. The reduced χ^2 of the two component fit and the results of the decomposition are shown in the upper left corner. The agreement between the decomposition fit (black) and the original [CII] spectrum (blue) are generally very good.

provide a bad fit ($\chi^2_{\rm red} \approx 3.2$).

Figure 2.8 shows an example of the stacked [CII], HI, and CO spectra for the $\Sigma_{\rm SFR}$ and metallicity property bins as well as the resulting [CII] spectral decomposition. The full results are given in Table 2.3 and a summary of the decomposition results for $\rm f_{mol}$ is plotted in Figure 2.9. We calculate the average $\Sigma_{\rm SFR}$, metallicity, $\rm R/R_{25}$, and total gas surface density for each bin and report the result in Table 2.3. We use the HI and CO line intensities at the ~500 pc resolution and Equations 1 and 2 from Herrera-Camus et al. (2017) to calculate the total gas surface density for these regions.

Most of the stacked spectra show that the atomic gas has an equal or larger contribution to the overall [CII] intensity. For example, the high metallicity (Z) bin yields values of $\rm f_{mol} = 0.36 \pm 0.12$ and $\rm f_{atomic} = 0.65 \pm 0.15$, suggesting that the high metallicity points have [CII] emission that is present slightly more in the atomic phase. Similarly, the high $\Sigma_{\rm SFR}$ bin contains [CII] emission that is equally distributed between the two phases, with a $\rm f_{mol} = 0.57 \pm 0.09$ and an $\rm f_{atomic} = 0.42 \pm 0.12$. When taking into account the uncertainties, all stacked bins are approximately consistent with a 50% or more contribution from the atomic phase to the [CII] decomposition.

We also find that the fraction of [CII] coming from the molecular phase decreases or remains the same when comparing the "no cuts" sample to the 3σ sub-sample. The "no cuts" sample uses all of the spectra in the dataset and consequently contains fainter and non-detected [CII] spectra. When there are more non-detections included in a stacked bin, the atomic gas tends to have a larger contribution to the [CII] emission. This trend is relatively consistent for the different properties studied, except in cases where $\rm f_{atomic}$ stays constant.

There is a clear trend when comparing the stacked bins between the two galaxies. The

Table 2.3: Results of the decomposition

Property	Sample	N_{spec}	$SNR_{[CII]}$	ΣSFR	12 + log(O/H)	R/R_{25}	Σ_{gas}	f_{mol}	f_{atomic}	$\widetilde{\chi}^2_{2c}$	$\widetilde{\chi}^2_{1c}$
High ΣSFR	3σ	10	16.62	20.01	8.42	0.52	58.31	0.57±0.09	0.42±0.12	0.93	1.57
High ΣSFR	No Cuts	10	16.62	20.01	8.42	0.52	58.31	0.57±0.09	0.42±0.12	0.93	1.57
Low ΣSFR	3σ	17	12.15	1.69	8.59	0.38	45.11	0.70±0.13	0.26±0.15	1.11	1.15
Low ΣSFR	No Cuts	68	10.89	0.77	8.50	0.46	27.27	0.43±0.15	0.57±0.17	1.63	1.80
High Z	3σ	13	15.71	1.66	8.62	0.25	48.51	0.36±0.12	0.65±0.15	0.59	0.80
High Z	No Cuts	27	15.73	1.01	8.62	0.23	36.84	0.36±0.15	0.65±0.19	0.47	0.67
Low Z	3σ	14	16.58	13.63	8.42	0.58	43.88	0.43±0.12	0.58±0.11	0.67	2.34
Low Z	No Cuts	51	18.43	4.10	8.40	0.59	26.24	0.21±0.10	0.81±0.14	3.29	3.27
High R/R_{25}	3σ	13	14.86	10.91	8.42	0.60	49.60	0.52±0.09	0.48±0.11	0.68	1.34
High R/R_{25}	No Cuts	45	14.84	3.49	8.40	0.64	28.03	0.47±0.14	0.53±0.13	0.76	1.21
Low R/R_{25}	3σ	14	12.89	6.38	8.61	0.26	49.84	0.47±0.14	0.53±0.16	0.60	1.01
Low R/R_{25}	No Cuts	33	10.13	2.97	8.58	0.25	35.97	0.47±0.23	0.53±0.26	1.39	1.44
M101	3σ	13	21.30	12.98	8.48	0.37	38.32	0.28±0.09	0.69±0.18	1.28	2.74
M101	No Cuts	40	11.40	3.73	8.45	0.37	23.65	-0.03±0.09	1.03±0.14	3.20	2.99
NGC 6946	3σ	21	15.66	5.96	8.56	0.51	56.44	0.59±0.10	0.41±0.11	0.32	0.74
NGC 6946	No Cuts	45	16.31	2.86	8.52	0.56	38.37	0.63±0.15	0.38±0.12	0.35	0.64
All Spec	3σ	27	23.04	8.56	8.53	0.46	49.73	0.48±0.07	0.52±0.07	0.40	1.97
All Spec	No Cuts	78	23.73	3.27	8.49	0.48	31.39	0.34±0.09	0.66±0.11	1.11	1.83

The results of the stacked decomposition. The $\Sigma_{\rm SFR}$ bin corresponds to the star formation rate surface density with a low/high cutoff value of $\Sigma_{\rm SFR} = 6 \times 10^{-2}$ $\rm M_\odot$ $\rm yr^{-1}\,kpc^{-2}$, the Z bin corresponds to the 12 + log(O/H) with a low/high cutoff value of 12 + log(O/H) = 8.55, and the R/R_{25} bin is the normalized galactocentric radius with a low/high cutoff value of $R/R_{25} = 0.4$. Sub-Sample represents how the regions were selected, with 3σ representing regions with integrated [CII] intensities three times greater than the RMS noise and No Cuts containing all of the spectra in the data. The average weighted $\Sigma_{\rm SFR}$ (in units of 10^{-2} $\rm M_\odot$ $\rm yr^{-1}$ $\rm kpc^2$), metallicity in 12 + log(O/H), normalized galactocentric radius (R/R_{25}), and the total gas surface density ($\Sigma_{\rm gas} = \Sigma_{\rm HI} + \Sigma_{\rm H_2}$) in units of $\rm M_\odot\ pc^{-2}$ of the stacked spectra are reported. $f_{\rm atomic}$ and $f_{\rm mol}$ are the fraction of the integrated [CII] intensity that is associated with the atomic and molecular gas, respectively. $\widetilde{\chi}^2_{\rm 2comp}$ is the reduced χ^2 for the model using both HI and CO while $\widetilde{\chi}^2_{\rm 1comp}$ is the reduced χ^2 for the CO or HI one-component model that has the smallest χ^2

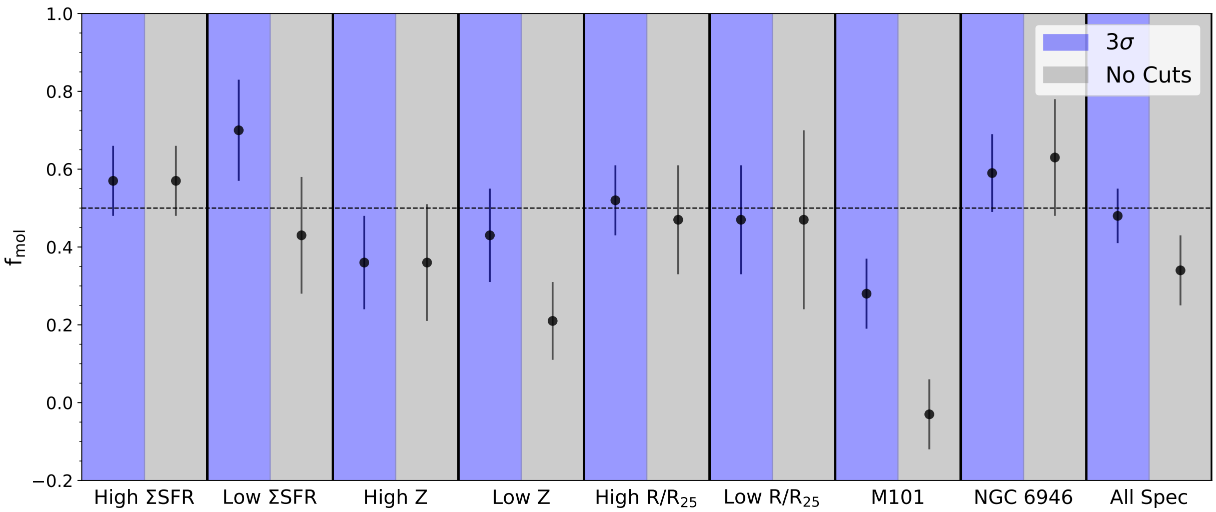

Figure 2.9: Summary of the [CII] decomposition of averaged spectra. The stacked property is named on the x-axis and the sub-sample used is colored in blue for the 3σ sample and gray for when no cuts are made. Most stacked bins contain [CII] with an equal or greater contribution from the atomic gas. There is also a slight trend of decreasing f_{mol} when the "no cuts" sub-sample is used. The spectra from NGC 6946 are more dominated by the molecular gas when compared to the spectra in M101.

molecular gas dominates the [CII] emission significantly more in NGC 6946 than M101. Additionally, the contribution of molecular gas to the [CII] emission stays consistent for the "no cut" sample in NGC 6946 but decreases for M101.

We find high χ^2 values of $\chi^2 = 3.29$ for the low metallicity bin and $\chi^2 = 3.20$ for the M101 bin in the "no cuts" sample, suggesting that the two component model does not fit these data well. Figure 2.10 shows the stacked spectrum for the low metallicity bin and there is excess [CII] emission not traced by the two-component model. This suggests that the underlying assumption, that the combination of an atomic phase (as traced by the HI data) and molecular phase (as traced by the CO data) can completely explain the [CII] emission profile, may not apply. An additional component, either ionized gas (which we think unlikely in view of the discussion in §2.4.2) or much more likely CO-faint molecular gas, may be needed to appropriately model the [CII] emission.

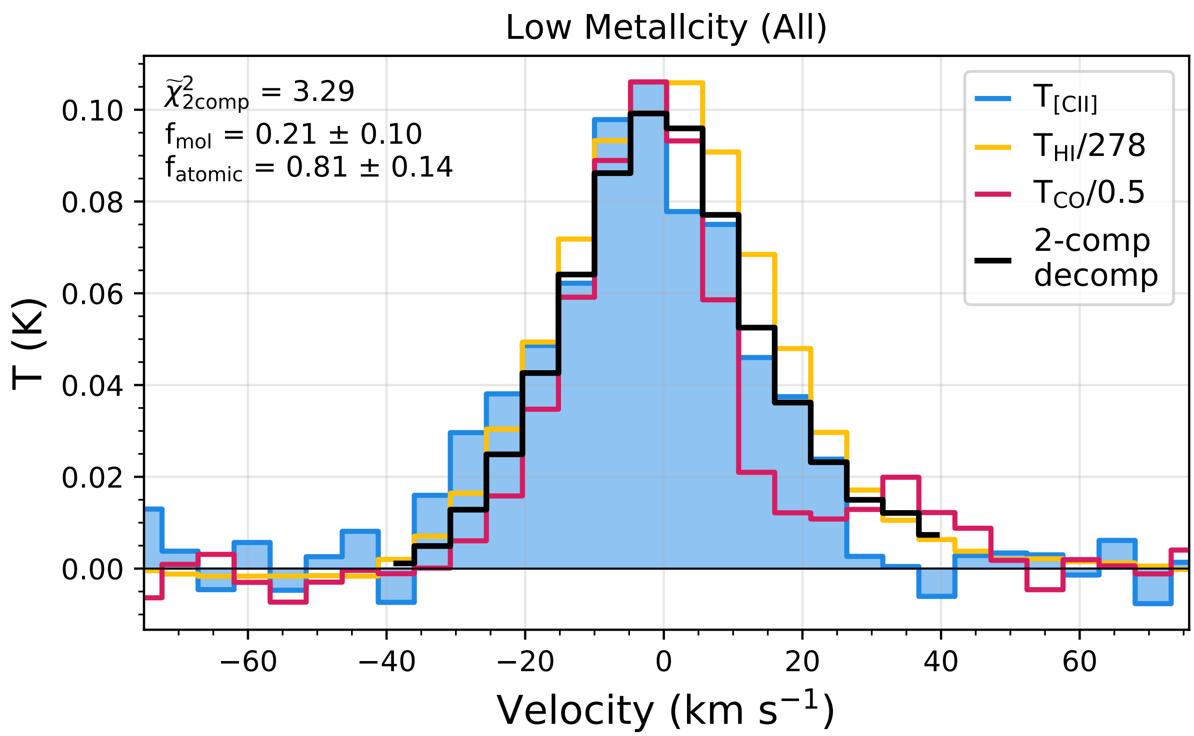

Figure 2.10: Spectra of the low metallicity stacked bin when making no cuts on the included regions. See Figure 2.8 for description of line colors and labels. There is [CII] emission on the left wing that isn't traced by the CO or HI data, leading to a high χ^2 for the two-component model. The excess emission may be from CO-dark gas or another contribution not traced in this work.

At low metallicities, CO-faint molecular gas can be a large contributor to the [CII] emission, hinting that the high χ^2 and additional [CII] emission in Figure 2.10 is likely CO-faint gas (e.g. Grenier et al., 2005; Jameson et al., 2018; Madden et al., 1997; Wolfire et al., 2010). Fahrion et al. (2017) also observe wider wings in their [CII] profiles, but their origin was not attributed to the CO or HI gas. Similar work using higher resolution data from the Small and Large Magellanic Clouds show wide [CII] profiles not associated with the atomic, molecular, or ionized gas (Lebouteiller et al., 2019; Okada et al., 2019, 2015; Requena-Torres et al., 2016). With the present data, however, we cannot ascertain the exact nature of this component.

There are no clear differences in the [CII] decomposition when comparing the high and low cuts of the $\Sigma_{\rm SFR}$ and metallicity. The spectra come from ∼500 pc regions, which may contain multiple PDR and HII complexes, and averaging over the 15″ beam can dilute trends with metallicity or star formation rate. The necessity to stack data may further weaken possible trends by averaging over multiple spectra from two different galaxies. Interestingly, the largest difference between the results of the [CII] decomposition comes from comparing the two galaxies. M101 contains [CII] emission dominated more by the atomic gas while the [CII] in NGC 6946 comes more from the molecular gas. The physical property driving the difference between these [CII] decomposition results is uncertain, but is likely not the aggregate star formation rate or metallicity of these galaxies.

We also investigate the dependence on galactocentric radius and the [CII] decomposition and find a similar value of $\rm f_{atomic} \approx 0.5$ for both the low and high $\rm R/R_{25}$ cuts. There is no difference in the distribution of galactocentric radius between NGC 6946 and M101, suggesting that $\rm R/R_{25}$ is not the reason for the varying [CII] decomposition results in these two galaxies. The galactocentric radius does slightly increase with the "no cuts" sample, but because there is no difference between the low and high $\mathrm{R}/\mathrm{R}_{25}$ bins, the small increase in $\mathrm{R}/\mathrm{R}_{25}$ is unlikely causing the larger contribution of atomic gas to the [CII] emission seen in the "no cuts" sample.

Lastly, we use bootstrapping techniques to confirm that the process of stacking the spectra is accurate. We randomize the regions included in each bin, then decompose the summed random combination of spectra for that bin, and repeat this process for 500 trials. The results of the bootstrap technique are very similar to the original results, suggesting that the uncertainties in the original decomposition are accurate and that one given spectrum in a bin does not dominate the [CII] decomposition. Additionally, we do not change the weighting of the original stacked spectra, which are by nature of summing the data fluxed-weighted. We do not use rms weighting because the brighter [CII] spectra tend to have shorter integration times and larger rms values.

2.4.4 Decomposition of individual spectra

There are three spectra in our dataset that have a sufficient SNR to produce a meaningful decomposition, as determined by our analysis in §2.3.2. We show the results in Table 2.4. Within the uncertainties, the results from these regions agree with those from stacked spectra.

All three data points are in the low metallicity property bin, but $\mathrm{f}_{\mathrm{atomic}}$ ranges from 0.65 to 0.46, suggesting there may be a fair amount of scatter in the decomposition of individual spectra that make up the bins described in §2.4.3. The individual variation is also seen in similar [CII] decomposition work by Mookerjea et al. (2016).

Table 2.4: Single Spectrum Decomposition

Galaxy	Region	Cycle	$SNR_{[CII]}$	ΣSFR	12 + log(O/H)	R/R_{25}	Σ_{gas}	f_{mol}	f_{atomic}	$\widetilde{\chi}^2_{2comp}$	$\widetilde{\chi}^2_{1comp}$
M101	Ma-0	2	14.84	68.80	8.43	0.33	131.84	0.39±0.13	0.65±0.12	1.61	2.25
NGC6946	N2-0	4	9.20	10.30	8.47	0.73	49.85	0.53±0.15	0.46±0.14	0.69	1.12
NGC6946	N3-0	4	11.16	4.84	8.44	0.83	44.37	0.44±0.11	0.54±0.08	1.05	2.51

The decomposition results for the three individual spectra with the highest $SNR_{[CII]}$. The table headers are the same as Table 2.3.

2.5 Discussion

2.5.1 Thermal Pressure in the Cold Neutral Medium

The spectral [CII] decomposition allows us to separate [CII] emission that is directly associated with the atomic gas. Using a method proposed by Kulkarni & Heiles (1987) and demonstrated by Herrera-Camus et al. (2017), we use the [CII] cooling rate to estimate the thermal pressure in the cold neutral medium (CNM). The thermal pressure is important in determining the cooling curve and pressure equilibrium in the atomic medium (Field et al., 1969), has consequences for the amount of cold dense material available for star formation, and it is part of the cycle of self-regulation of star formation activity in galaxies (Kim et al., 2011; Ostriker et al., 2010).

In order to estimate the thermal pressure in the CNM, we need to relate the observed [CII] emission to the physical properties of the gas that emits the [CII]. The integrated intensity of [CII] for collisional excitation in the optically thin limit with a given collisional partner is (Crawford et al., 1985; Goldsmith et al., 2012)

$$\begin{aligned} I_{[\mathrm{CII}]} = \left(\frac{2e^{-91.2/T}}{1 + 2e^{-91.2/T} + A_{ul}/(\Sigma R_{ul,i} n_i)} \right) N_{\mathrm{C}^+} \\ \times 2.3 \times 10^{-21} \,, \end{aligned} \tag{2.6}$$

where $I_{[\mathrm{CII}]}$ is the integrated [CII] intensity in units of erg s^{-1} cm^{-2} sr^{-1}, T is the kinetic temperature of the collisional partner in K, N_{C^+} is the column density of ionized carbon in the line of sight in units of cm^{-2}, A_{ul} is the spontaneous decay rate of the 158 μm [CII] transition (A_{ul} =

2.3$\times$ $10^{-6}\,\mathrm{s}^{-1}$), n is the number density of the collisional partner in units of cm^{-3}, and R_{ul} is the collisional de-excitation rate coefficient of a given partner at a kinetic temperature T. The sum in the denominator is over all the relevant collisional partners, including H^0, H_2, He, or e^-. The focus in this section is collisions with the atomic gas, H^0, where R_{ul} is calculated by Goldsmith et al. (2012)

$$R_{ul}(H^0) = 4.0 \times 10^{-11}(16 + 0.35T^{0.5} + 48T^{-1}) \tag{2.7}$$

and is in units of $\mathrm{cm}^3\,\mathrm{s}^{-1}$. For $T = 100\,\mathrm{K}$, the collisional de-excitation rate coefficient for atomic hydrogen is $R_{ul}(H^0) = 8 \times 10^{-10}\,\mathrm{cm}^3\,\mathrm{s}^{-1}$. The atomic gas will also contain helium, which has a collisional de-excitation rate coefficient equal to 0.38 times the rate for atomic hydrogen (Draine, 2011).

The total observed [CII] integrated intensity has components from the neutral gas (including the molecular and atomic phases) and the ionized gas.

$$I_{\mathrm{[CII]}}^{\mathrm{tot}} = I_{\mathrm{[CII]}}^{\mathrm{neutral}} + I_{\mathrm{[CII]}}^{\mathrm{ionized}}, \tag{2.8}$$

where $I_{\mathrm{[CII]}}^{\mathrm{neutral}} = I_{\mathrm{[CII]}}^{\mathrm{atomic}} + I_{\mathrm{[CII]}}^{\mathrm{mol}}$. We define f_{ion} as the fraction of $I_{\mathrm{[CII]}}^{\mathrm{tot}}$ that comes from the ionized gas. As part of the neutral phase there is diffuse "CO-dark" molecular gas phase that is mixed within the CNM (Grenier et al., 2005; Langer et al., 2014; Wolfire et al., 2010). The kinematics of the CO-dark gas may match those of the CNM and thus the contribution needs to be removed. We define f_{H_2} as the fraction of the [CII] intensity that originates in the CO-dark molecular gas. Therefore we can write

$$I_{\text{[CII]}}^{\text{atomic}} = (1 - f_{\text{H}_2})(1 - f_{\text{ion}})(1 - f_{\text{mol}}) I_{\text{[CII]}}^{\text{tot}}, \tag{2.9}$$

where we use f_{mol} calculated from the fitting described in §2.4.3 to find the fraction of the total [CII] intensity that originates from the atomic gas alone.

The warm neutral medium (WNM) in the atomic phase has a combination of physical conditions (T $\approx$ 8000 K, n $\approx$ 0.5 cm^{-3}) and an overall low mass fraction to not produce appreciable [CII] emission (see also Fahrion et al., 2017; Herrera-Camus et al., 2017; Pineda et al., 2013). Therefore the [CII] emission associated with the atomic gas is due to CNM. In the equation above $I_{\text{[CII]}}^{\text{atomic}} \cong I_{\text{[CII]}}^{\text{CNM}}$.

[CII] emission is the dominant cooling source in the CNM (Draine, 2011; Wolfire et al., 1995, 2003). The cooling rate per H nucleon is

$$\Lambda_{\text{[CII]}} = \frac{4\pi I_{\text{[CII]}}^{\text{tot}}}{N_{\text{HI}}} \tag{2.10}$$

where N_{HI} is the column density of the HI gas in cm^{-2} derived from the 21 cm spin-flip transition, to which both the WNM and CNM contribute. The fraction of HI column density in the CNM is $f_{\text{CNM}} = N_{\text{HI}}^{\text{CNM}}/N_{\text{HI}}$, with values likely in the range $f_{\text{CNM}} = 0.3 - 0.7$ (Heiles & Troland, 2003). Therefore,

$$\Lambda_{\text{[CII]}}^{\text{CNM}} = \frac{4\pi I_{\text{[CII]}}^{\text{CNM}}}{f_{\text{CNM}} N_{\text{HI}}}. \tag{2.11}$$

We can then relate the observed cooling rate as defined in Equation 2.10 to the CNM cooling rate using

$$\Lambda_{\text{[CII]}} = \Lambda_{\text{[CII]}}^{\text{CNM}} \frac{f_{\text{CNM}}}{(1-f_{\text{ion}})(1-f_{\text{mol}})(1-f_{\text{H}_2})}. \tag{2.12}$$

With Equation 2.6 as the expression for the [CII] intensity, we rewrite the cooling rate as

$$\Lambda_{\text{[CII]}}^{\text{CNM}} = \frac{2.9 \times 10^{-20} K N_{\text{C}^+}^{\text{CNM}}}{f_{\text{CNM}} N_{\text{HI}}}, \tag{2.13}$$

where K is

$$K = \frac{2e^{-91.2/T}}{1 + 2e^{-91.2/T} + A_{ul}/(\Sigma R_{ul,i} n_i)}. \tag{2.14}$$

Assuming the carbon abundance is the same for the CNM and WNM, and assuming all gas-phase carbon is C^+, then $N_{\text{C}^+}^{\text{CNM}}/(f_{\text{CNM}} N_{\text{HI}}) = (\text{C/H})^{\text{CNM}}$, and the final expression for the observed cooling rate is

$$\Lambda_{\text{[CII]}} = \frac{2.9 \times 10^{-20} K (\text{C/H})^{\text{CNM}} f_{\text{CNM}}}{(1-f_{\text{ion}})(1-f_{\text{mol}})(1-f_{\text{H}_2})}. \tag{2.15}$$

We then solve for the density, n_i, in Equation 2.14. The collisional partners with C^+ in the CNM will be atomic hydrogen and helium. Assuming the cosmic abundance ratio of 10 to 1 for hydrogen to helium, the sum over collisional partners in Equation 2.14 simplifies to $1.038 R_{ul}(H^0) n_{\text{CNM}}$ (Draine, 2011). The thermal pressure of the CNM is

$$P_{th} = n_{\text{CNM}} T \text{ K cm}^{-3} \tag{2.16}$$

To calculate P_{th} in the CNM, we assume a temperature of $T_{\text{CNM}} = 100\,K$ (e.g., Gerin et al., 2015). A variation of T_{CNM} of a factor of 2 will alter the thermal pressure by $\sim$30%. We obtain the gas-phase carbon abundance through the oxygen abundance gradients measured for these galaxies (Pilyugin et al., 2014) and convert these oxygen abundances into carbon abundances through the relation used in MAPPINGS (Nicholls et al., 2017)

$$\log(\mathrm{C/H}) = \log(\mathrm{O/H}) + \log(10^{-1.00} + 10^{2.72+\log(\mathrm{O/H})}). \tag{2.17}$$

Herrera-Camus et al. (2017) normalize the expression above to recover the local Galactic ISM gas phase carbon abundance of $\mathrm{C/H} = 1.5 \times 10^{-4}$ (Gerin et al., 2015) with an input oxygen gas phase abundance of 12 + log(O/H) = 8.65 (Simón-Díaz & Stasińska, 2011). We set the fraction of CNM in the atomic gas to $f_{\mathrm{CNM}} = 0.5$, which is consistent with the results of Heiles & Troland (2003) and Pineda et al. (2013). The fraction of H_2 is uncertain but we set it to $f_{\mathrm{H_2}} = 0.3$, motivated by Pineda et al. (2013) who use [CII] observations of the plane of the Milky Way to find that the CO-dark gas contributes $\sim 30\%$ of the total [CII] emission. Our [NII] SOFIA/GREAT observations have an average upper limit of $f_{\mathrm{ion}} = 0.12$ for the [CII] emission from ionized gas (c.f., Figure 2.7), although we also include the result of setting $f_{\mathrm{ion}} = 0.3$, as in Herrera-Camus et al. (2017).

In addition to the assumptions described above, we use the results in Table 2.3 for the value of f_{mol}. We then estimate the thermal pressure of the CNM for each stacked bin through the [CII] cooling rate given in Equation 2.15. Those results are compared to the calculated thermal pressures found in Herrera-Camus et al. (2017) and shown in Figure 2.11.

The thermal pressure of the CNM calculated in this study range from $\log(P_{th}/k) = 3.8 - 4.6$ [K cm^{-3}]. These pressures correspond to a density range of 75 cm^{-3} to 400 cm^{-3} when assuming $T_{\mathrm{CNM}} = 100\,\mathrm{K}$. The effect of increasing f_{ion} from 0.12 to 0.3, the value Herrera-

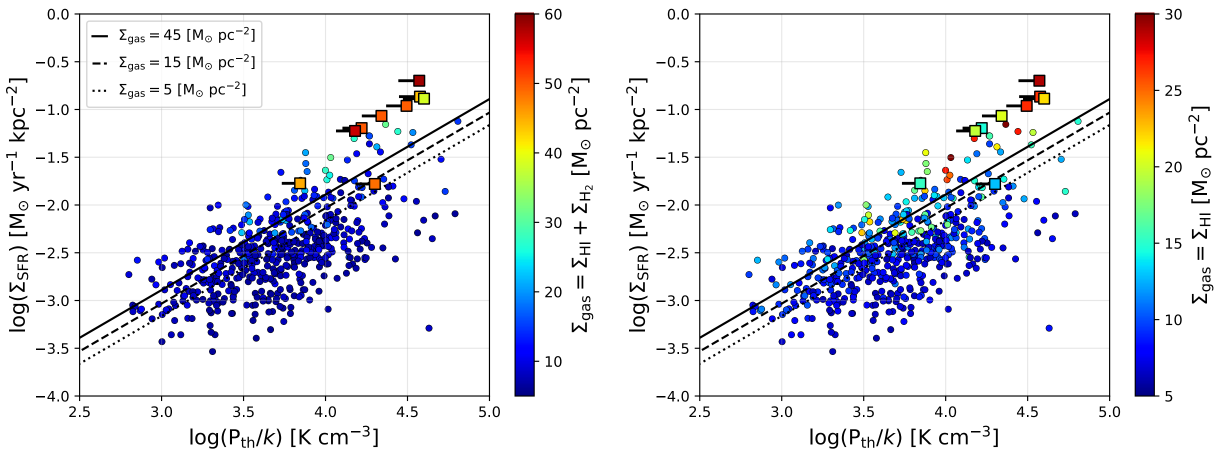

Figure 2.11: The thermal pressure vs. star formation rate where $f_{\text{ion}} = 0.12$ and $f_{\text{H}_2} = 0.3$. The KINGFISH data from Herrera-Camus et al. (2017) are circles and the 3σ stacked data bins in this study correspond to squares. The color coding represents the gas surface density, with the total presented ($\Sigma_{\text{gas}} = \Sigma_{\text{HI}} + \Sigma_{\text{H}_2}$) on the left panel and the HI gas surface density (Σ_{HI}) shown on the right. The horizontal lines to the left of the square points show how the pressure would change if $f_{\text{ion}} = 0.3$, as is set in the KINGFISH data. The vertical lines on the plot represent theortical predictions from Wolfire et al. (2003) for different values of Σ_{gas}. Our estimates follow the same trends as the KINGFISH data but they are localized on the higher pressure region rather than the median, likely due to the bias towards regions of higher Σ_{SFR} and Σ_{gas}.

Camus et al. (2017) uses for the KINGFISH sample, decreases the thermal pressure by 0.1 dex on average.

These pressures are slightly higher than those derived in the atomic disk for the KINGFISH sample, but broadly follow the same trends with gas surface density and Σ_{SFR}. Herrera-Camus et al. (2017) identify atomic-dominated regions by finding where the surface density of atomic gas is larger than that of molecular gas and thus are biased towards quiescent regions with lower gas surface densities (Σ_{gas}). The technique in this work spectrally identifies the [CII] coming only from the atomic gas and allows us to calculate $\text{P}_{\text{th}}/\text{k}$ for a wider range of regions with higher Σ_{SFR} and Σ_{gas}. Figure 2.11 shows that this work has much larger total gas surface density values due to the inclusion of regions with appreciable molecular gas. The atomic gas surface density values of these regions, however, are comparable to those in Herrera-Camus et al. (2017). The

KINGFISH data and analytic work by Wolfire et al. (2003) show that an increase in $\Sigma_{\rm SFR}$ leads to higher thermal pressures. At fixed $\Sigma_{\rm SFR}$, however, larger gas surface densities decrease the thermal pressure, leading to different predicted slopes for the relationship between the $\Sigma_{\rm SFR}$ and $\rm P_{th}/k$ as seen in Figure 2.11. Because the regions in this work have high $\Sigma_{\rm SFR}$ and $\Sigma_{\rm gas}$, these data are on the upper end of the trend between star formation rate and thermal pressure. Similar to Herrera-Camus et al. (2017), the trends here generally agree with the theory, but there is a wider dispersion in the relationship between $\Sigma_{\rm SFR}$, $\Sigma_{\rm gas}$, $\rm P_{th}/k$, possibly due to regions continuing to evolve to equilibrium or observational uncertainties in these measurements.

Gerin et al. (2015) compute thermal pressures in Milky Way star-forming regions using [CII] and [CI] far-infrared/sub-mm observations toward bright dust continuum regions on the Galactic plane, and find a median of $\log(P_{th}/k) = 3.8$ K cm^{-3} and a maximum of $\log(P_{th}/k) = 4.3$ K cm^{-3}, comparable to our result. Jenkins & Tripp (2011) use CI ultraviolet absorption measurements toward Milky Way stars within 3 kpc to estimate a median pressure of $\log(P_{th}/k) = 3.6$ K cm^{-3} with a log-normal distribution, although finding an excess of $\log(P_{th}/k) > 4.0$ K cm^{-3} of pressures and a positive correlation with radiation field (and star formation activity). Goldsmith et al. (2018) use velocity resolved [CII] observations and 21 cm absorption spectra and find a pressure range of $\log(P_{th}/k) = 3.3 - 4.0$ [K cm^{-3}] in atomic gas dominated lines of sight. Also using [CII] observations, Velusamy et al. (2017) compute the pressure by isolating the H_2 gas and find areas of higher pressure, $\log(P_{th}/k) > 4$ K cm^{-3}, in high star-forming regimes.

Outside of the Milky Way, Welty et al. (2016) use CI ultraviolet absorption measurements to identify the CNM thermal pressure in sight lines of Magellanic Clouds and compute pressures that range from $\log(P_{th}/k) = 3.6 - 5.1$ [K cm^{-3}], agreeing well with the range of thermal pressures we find for M101 and NGC 6946. The authors hypothesize that the higher pressures may be due to the enhanced radiation fields in the CNM of the Magellanic Clouds. Energetic feedback from stellar winds, supernova remnants, and star formation may also play a role in increasing the overall thermal pressure of in the Magellanic Clouds. It is possible that the same effects may be contributing to the higher thermal pressures found in M101 and NGC 6946.

The trends we find with $\Sigma_{\rm SFR}$ and gas surface density generally agree with the observational work of Herrera-Camus et al. (2017) and the analytic modeling work by Wolfire et al. (2003). The thermal pressure increases with increasing $\Sigma_{\rm SFR}$, possibly caused by the relation between $\Sigma_{\rm SFR}$ and G_0, the far-ultraviolet (FUV) intensity field (Dopita, 1985; Ostriker et al., 2010), or through stellar feedback from winds or supernovae (Barrera-Ballesteros et al., 2021; Hayward & Hopkins, 2017).

2.5.2 Origins of the [CII] emission

Studies that explored the multi-phase nature of [CII] emission in NGC 6946 did so initially based on spatial information rather than spectral profiles. Using the *Kuiper* Airborne Observatory, Madden et al. (1993) found an extended component of [CII] emission that they attribute to the atomic gas. Following up that study, measurements of NGC 6946 using the Infrared Space Observatory found that $\lessapprox$40% of the [CII] emission comes from the diffuse galaxy disk (Contursi et al., 2002). Through PDR modeling, these authors find that the majority of the [CII] emission associated with the HI gas arises from dense HI, likely from the photodissociation of H_2 on molecular cloud surfaces, and is consistent with the density and pressure computed in our study. More recently, Bigiel et al. (2020) use [CII] SOFIA/FIFI-LS data of NGC 6946 to find that 73% of the [CII] luminosity comes from the spiral arms, 19% is from the central regions, and 8% is in the interarm regions. It is difficult to compare directly to this work, because we separate our regions based on star formation rate and metallicity, but these spatial results are broadly consistent with what is measured here.

Previous work studying the origin of [CII] emission with velocity resolved [CII] data and some form of profile decomposition are broadly consistent with our conclusions. Fahrion et al. (2017) use SOFIA/GREAT observations of the dwarf galaxy NGC 4214 and a similar spectral decomposition method to identify the origin of [CII] emission in five regions at a resolution of $\sim$200 pc. They find on average that 54% of the [CII] emission is associated with the CO profiles and 46% is associated with the HI profiles, in agreement with our finding (see Table 2.3). The authors state, however, that only about 5 - 11% of the [CII] emission originates in the CNM because they take a narrower definition of the CNM than we use here. In order to reproduce the [CII] emission associated with the HI gas in NGC 4214, Fahrion et al. (2017) calculate a density of $\sim$1000 cm^{-3} at a temperature of 80 K, concluding there is a denser atomic phase than the classical CNM associated with the [CII] that has similar broad wings to the HI profile. Our pressures in fact suggest that this "high pressure CNM phase" is fairly common in star-forming regions.

Mookerjea et al. (2016) use *Herschel*/HIFI velocity resolved [CII] data of M33 at 50 pc resolutions and a method of combining the CO and HI profiles to reproduce the [CII] spectra that is identical to the method presented in this study. In 20 different regions that cover the center of M33 and one of its large HII regions, they find that 8-85% of the [CII] emission comes from the atomic gas. They calculate CNM densities that range from 150 cm^{-3} to 1500 cm^{-3}, depending on the given region in their sample. With these high densities, they conclude that the [CII] originating from the majority of the atomic medium comes from the atomic envelopes of molecular PDRs. Therefore, Mookerjea et al. (2016) is consistent with other studies (e.g. Contursi et al., 2002; Fahrion et al., 2017), including the work in this paper, that associate portions of the [CII] emission with a dense, high pressure, atomic phase.

Studies that focus on [CII] in the Magellanic Clouds have higher spatial resolutions, on the order of a few parsecs compared to the ∼500 pc regions in this work. Okada et al. (2019, 2015) use spectrally resolved SOFIA/GREAT observations of CO and [CII] in the LMC at spatial resolutions of ∼4 pc to show that the CO spectra alone cannot explain 30% - 60% of the [CII] emission in the LMC, suggesting the presence of CO-dark gas. By matching the wide wings in the [CII] spectra with the HI profile, they find that less than 15% of the [CII] emission comes from the atomic phase on average. Other studies in the SMC that use velocity resolved [CII] data also observe a small contribution from the atomic gas to the overall [CII] emission (Requena-Torres et al., 2016). Lebouteiller et al. (2019) use SOFIA/GREAT data of the LMC and employ a Bayesian approach to decompose the line profiles of each tracer into multiple components per region, which are analyzed individually. In order to find the contribution from atomic gas, they estimate the density using the HI column density and the average cloud sizes in the LMC found by Indebetouw et al. (2013), computing densities that range between a few cm^{-3} to 10^3 cm^{-3}. With this method, the atomic phase contributes about 30% of the total [CII] emission in regions with faint [CII] emission. In bright regions, CO-dark gas associated with [CII] dominates, contributing 95% to the emission.

In this study we find that the atomic gas contributes ∼50% or more to the overall [CII] emission, similar to the other spectral decomposition studies on scales between 50 and 200 pc (Fahrion et al., 2017; Mookerjea et al., 2016). At these resolutions, multiple HII regions, PDR complexes, and extended gas are averaged into one beam. It is likely that the discrepancy of the importance of the contribution from the atomic phase between the Magellanic Clouds (where atomic gas contributes less to the [CII] emission) and other studies is caused by the difference in spatial scales, as we would expect the more extended components to contribute more on the larger scales. In the literature, as well as in our study, there is a tendency to find that the contribution of the atomic gas to the [CII] emission increases in regions with fainter [CII] emission (Fahrion et al., 2017; Lebouteiller et al., 2019). Neither the literature nor this study finds that the origin of [CII] emission has a consistent dependence on the star formation rate, metallicity, or galactocentric radius of the region.

2.6 Summary & Conclusions

We present two cycles of SOFIA/GREAT velocity resolved 158 μm [CII] and 205 μm [NII] observations of the nearby galaxies M101 and NGC 6946. These observations have a spatial resolution of $\sim$500 pc and probe a variety of regions that range in star formation rate and metallicity. We compare the velocity resolved [CII] spectra to ancillary HI spectra from the THINGS survey and CO spectra from the HERACLES survey. The goal of this study is to determine the origin of the multi-phase [CII] emission through spectral decomposition using HI as a tracer of atomic gas and CO as a tracer of molecular gas. We model the [CII] emission as a linear combination of the HI and CO spectra and identify the fraction of the [CII] emission associated with each phase. After isolating only the [CII] emission coming from the atomic phase, we compute the cooling rate per hydrogen nucleus (Equation 2.15) in order to solve for the thermal pressure of the CNM. Our main results are as follows:

1. We find that the HI spectral profiles are on average 29% wider than the [CII] spectra, while

the CO spectra are 25% narrower than the [CII] spectra (Figure 2.6). The [CII] linewidths lie in between the CO and HI (see also Lebouteiller et al., 2019; Requena-Torres et al., 2016; de Blok et al., 2016), suggesting that the [CII] originates from both molecular and atomic gas.

2. We find that the neutral gas (atomic and molecular) contributes at least 88% to the [CII] emission on the average of our pointings, based on the [NII] 205 μm upper limit data acquired by GREAT (Figure 2.7). This agrees with other studies that use [NII] observations to model the ionized gas contribution (Croxall et al., 2013; Lebouteiller et al., 2019; Pineda et al., 2013). Thus the ionized gas has a negligible contribution to the [CII] emission.

3. To quantify the reliability and uniqueness of our [CII] decomposition methodology we use template spectra derived from our data to run a series of simulations. We find that a peak SNR$\sim 10 - 15$ is required to accurately decompose the [CII] emission into the atomic and molecular components using our linear combination methodology (§2.3.2, Figures 2.4 and 2.5).

4. We perform our analysis on spectra stacked in bins of $\Sigma_{\rm SFR}$, metallicity, and normalized galactocentric radius for different samples based on SNR and intensity. We find that over all the spectra the atomic phase contributes $\gtrsim$50% or more to the the [CII] emission ($f_{\rm mol} \simeq 48\%$, $f_{\rm atomic} \simeq 52\%$ when stacking all $\geq 3\sigma$ spectra), with a weak but consistent trend for the fainter [CII] emission to have an increasing contribution from the atomic medium (Table 2.3, Figure 2.9). We also perform our decomposition on the three individual spectra with sufficient SNR to produce meaningful results, and confirm this finding that on average $45\% - 55\%$ of emission arises from molecular and atomic gas, respectively (Table 2.4).

5. While the fraction of atomic or molecular gas associated with the [CII] emission has no

clear dependence with Σ_{SFR}, metallicity =or galactocentric radius, there is a significant difference in the results of the [CII] decomposition when comparing spectra in M101 and NGC 6946. The [CII] pointings in M101 are more dominated by the atomic gas ($\mathrm{f_{mol}} \simeq 0.28 \pm 0.09$) while those in NGC 6946 appear more associated with the molecular gas ($\mathrm{f_{mol}} \simeq 0.59 \pm 0.10$).

6. At the lowest metallicities probed and in the faintest [CII] spectra of M101 there is a tentative hint of an extra component in the [CII] emission which may be associated with a "CO-dark" phase (Figure 2.10). Evidence of [CII] tracing CO-dark gas is also seen in a variety of other [CII] studies, especially in regions with low metallicities (e.g. Fahrion et al., 2017; Lebouteiller et al., 2019; Pineda et al., 2013).

7. From the [CII] emission, we find a thermal pressure of $\log(P_{th}/k) = 3.8 - 4.6$ [K cm^{-3}] in the atomic gas in our pointings (Figure 2.11). This is somewhat higher than other estimates of the thermal pressure in the atomic phase (Gerin et al., 2015; Herrera-Camus et al., 2017; Jenkins & Tripp, 2011). We suspect this is likely due to the comparatively high Σ_{SFR} in our regions. Other studies of the origin of [CII] also report a significant contribution from atomic gas that is at higher densities and pressures than the traditional Cold Neutral Medium (Contursi et al., 2002; Fahrion et al., 2017; Mookerjea et al., 2016).

Because SNR $\gtrsim$ 10-15 are needed for a meaningful decomposition of the velocity resolved [CII] emission, we highlight the importance of acquiring high SNR observations of extragalactic [CII], which can be time-consuming. As demonstrated in this work, however, velocity resolved [CII] observations that enable kinematic decomposition of the emission are a useful tool for understanding the origin of [CII] and the physical conditions in the ISM.

Chapter 3: Modeling Ionized Gas at Low Metallicities: The Wolf-Rayet Nebula N76

3.1 Introduction

Massive stars inject energy into their surrounding gas, heating and influencing the chemistry of their nearby interstellar medium (ISM). The effects massive stars have on the ISM depend on a variety of factors, including the metallicity of the surrounding material. Lower metallicity stars have harder radiation fields and a decreased mass-loss rate (e.g. Hurley et al., 2000; Vink et al., 2001). At the same time, the low metallicity ISM contains less dust, which consequently leads to a more porous structure allowing radiation fields to penetrate deeper into the ISM (e.g. Cormier et al., 2015; Poglitsch et al., 1995). The chemistry and physical processes governing the interaction between massive stars is thus highly affected by the metallicity of the medium.

Investigation of ionized gas tracers are used to determine the properties of the ionized gas across galaxies. In particular, the infrared (IR) lines such as [NeII], [SIII], [OIII], [NeIII], and [SIV], accessed by the *Spitzer* and *Herschel* space telescopes (and now the *James Webb Space Telescope*) trace a variety of conditions in the ISM, including the ionizing radiation field strength and hardness, the ionization parameter, the density and temperature of the ionized gas, and the heating mechanism of the gas (e.g. Baldwin et al., 1981; Cormier et al., 2019, 2015; Kaufman et al., 2006; Polles et al., 2019). The IR fine-structure lines are less affected by extinction and dust attenuation and are therefore ideal for studying star-forming regions.

Previous studies of mostly spatially unresolved infrared spectroscopy in low metallicity star-forming galaxies find harder radiation fields, extended, bright [OIII] emission, and an overall more porous structure (Cormier et al., 2019, 2015; Hunt et al., 2010). Spatially resolved studies, on the other hand, bring additional information and can be considerably more powerful at constraining physical conditions. Of course, they can only be carried out in nearby sources. The Small Magellanic Cloud (SMC), at one-fifth solar metallicity and only 63 kpc away provides the ideal laboratory for studying the low metallicity ionized gas in spatially-resolved detail (Dufour, 1984; Russell & Dopita, 1992).

This paper focuses on studying the ionized gas emission around one of the hottest and most luminous stars in the local universe, a Wolf-Rayet (WR) star. After an O-type star loses its hydrogen-rich envelope (either from binary stripping and accretion, or via stellar winds removing the outer layers of the star), the inner, hot core is exposed and forms a WR star. WR stars are characterized by effective temperatures of $T_{*} \sim$ 50 - 110 kK, luminosities of $\log L \sim 5 - 6.2\,\mathrm{L}_{\odot}$, have strong stellar winds with velocities that range from $\mathrm{v}_{\infty} \sim 1500 - 5000\ \mathrm{km\,s^{-1}}$, and mass outflow rates of $\dot{\mathrm{M}} \sim 10^{-4} - 10^{-5}\,\mathrm{M}_{\odot}\ \mathrm{yr}^{-1}$ (Crowther & Hadfield, 2006). These stellar winds compress the surrounding material, forming a stellar wind blown bubble (Weaver et al., 1977). Simultaneously, the bright ultraviolet (UV) flux from the WR star creates a highly ionized HII region, forming a structure often called a WR nebula (e.g. Chu, 1981). Since WR stars inject massive amounts of energy into the surrounding medium, they can have a profound influence on shaping the nearby ISM and energy exchange in a galaxy (e.g. Sokal et al., 2016).

Observations of Milky Way WR nebulae show that they vary in morphology, but often appear as thin, bubble structures, or disrupted shells (Chu, 1981; Chu et al., 1983; Toalá et al., 2015). In particular, the well-studied WR nebula NGC 6888 shows a double shell model with a denser inner shell ($n_e \sim 400\,\mathrm{cm}^{-3}$) and a thinner outer shell ($n_e \sim 180\,\mathrm{cm}^{-3}$) (Fernández-Martín et al., 2012; Rubio et al., 2020). Due to the rarity of Wolf-Rayet nebulae, there have been few observations investigating the properties of WR nebulae at low metallicities. It is possible that the lower dust abundance and harder radiation fields at low metallicities will allow high energy photons to penetrate deeper into the low metallicity ISM, forming larger, lower density nebulae with high ionizing photon escape fractions. Further, understanding how WR stars directly affect their surrounding environment and host galaxies is essential to deciphering the nature of extreme emission line galaxies (EELGs). These are local analogues to galaxies during the Epoch of Reionization, characterized by bright emission lines from high ionization species (such as [O III], C III], C IV, and He II), low metallicities, and highly ionized gas (e.g. Atek et al., 2011; Berg et al., 2019; Maseda et al., 2013; Olivier et al., 2022; Rigby et al., 2015; Senchyna et al., 2017). The ionization source for the extreme emission found in these galaxies is unclear, but radiation from WR stars is a possible explanation. Investigating WR nebulae in low metallicity environments can help us gain insight on possible physical conditions in these EELGs, as well as enabling us to explore how the most extreme stars affect their surrounding environment.

This paper focuses on the WR nebula N76 that harbors one of the hottest, most luminous WR stars in the SMC (Shenar et al., 2016). First classified by Henize (1956) as an HII region, Garnett et al. (1991) identified broad He II emission in N76, indicative of a WR nebula. N76 is powered by a well-studied binary system consisting of a WN4 and a O6 I(f) star (Niemela et al., 2002; Shenar et al., 2016). The goal of this work is to model the physical conditions of the ionized gas in N76 using mid and far infrared spectroscopy and the `Cloudy` photoionization code. In Section 3.2, we describe the *Spitzer* and *Herschel* observations and the methods of producing line-integrated spatially resolved emission line maps. Section 3.3 describes the `Cloudy` photoionization model input conditions and N76 geometry. We then compare the photoionization models to the spatially resolved IR data in Section 3.4. We discuss the implications of these results, putting N76 in context with other low metallicity galaxies and WR nebulae in Section 3.5. Lastly, our conclusions are described in Section 3.6.

3.2 Observations

3.2.1 Spitzer IRS observations and spectral line images

The *Spitzer* data come from the InfRared Spectrograph (IRS) as part of the *Spitzer* Spectroscopic Survey of the Small Magellanic Cloud (S^4MC). The full observations are described by Sandstrom et al. (2012), but we summarize them briefly here. We downloaded the raw Basic Calibrated Data (BCD) files from the *Spitzer* Heritage Archive from project GO 30491 (PI: A. Bolatto) with pipeline version S18.18. We use the long-low (LL) and short-low (SL) modules of the IRS to cover the 5.2 μm - 38.4 μm range with a resolving power ranging from $R \sim 60 - 120$ (coverage of the modules is shown in Figure 3 of Sandstrom et al., 2012). The spatially resolved maps are produced by stepping the IRS slit perpendicular and parallel to the source in steps of half a slit width for the LL module (5$''$.08) and the full slit width for the SL module (3$''$.7). The LL maps for N76 had 75×6 steps (376$''\times$ 395$''$) with a 14 s integration time per position. The SL maps are created similarly, except the steps are using the full slit width in order to increase coverage and have 120×5 steps (220$''\times$ 208$''$).

Each set of observations has an associated background observation taken at R.A. $1^{\rm h}9^{\rm m}40^{\rm s}$

Dec. $-73°31'30''$ (J2000), a region chosen from the Multiband Imaging Photometer for Spitzer (MIPS) and Infrared Array Camera (IRAC) observations of the SMC to have negligible emission from the SMC itself (Bolatto et al., 2007; Leroy et al., 2007; Sandstrom et al., 2010). We subtract the background from the BCD files, which removes emission from the zodiacal light the Milky Way cirrus, and reduces the number of "hot" pixels that contaminate the IRS data.

3.2.1.1 Constructing the data cubes

The BCD files are assembled into cubes using the software CUBISM (Smith et al., 2007a, we use version 1.8). CUBISM processes the two-dimensional slit spectral images created by scanning the IRS slit across the source into three-dimensional spectral data cubes through polygon-clipping-based re-projection. This algorithm is flux-conserving and is specially adapted for the IRS on *Spitzer*. For the extended sources analyzed in this work, we apply a slit-loss correction when constructing the cubes to ensure that the extended source fluxes are not underestimated. The IRS is susceptible to hot, "rogue", or bad pixels that represent themselves on the cube images as repeating stripes, resulting from the bad pixel scanning across the image through the grid of positions. These pixels are often caused by the IRS CCD array malfuctioning due to interactions with solar wind particles. The positions and intensity of the rogue bad pixels can vary on scales of hours to days, making them unpredictable. Some bad pixels can be flagged automatically through CUBISM, but many must be flagged by hand. We perform extensive flagging of the bad pixels in each data cube ($\sim$ 7% of data), with particular focus on the emission from the spectral lines we plan to model, in order to produce the cleanest spectral line maps.

3.2.1.2 Fitting spectral line maps

We use the program PAHFIT (Smith et al., 2007b) to create integrated line maps for each emission line in the IRS bandpass. PAHFIT uses a physically motivated model to simultaneously fit multiple components in an IRS spectrum. Its model includes dust continuum in fixed equilibrium temperature bins, starlight background, bright emission lines, individual and blended PAH features, and extinction from silicate grains. In our fits we do not include extinction because the SMC has very low levels of mid-IR dust absorption, due to its low gas-to-dust ratio (Lee et al., 2009). The mapping strategy produces maps for both the SL and LL modules, but the placement of the slits creates an offset of the mapping area between the different modules and orders, resulting in different coverage for SL1, SL2, LL1, and LL2 (see Fig. 3 in Sandstrom et al., 2012, for an illustration of the coverage on N 76). To maximize the area of the line maps, we fit each IRS module and spectral order separately with PAHFIT.

In order to create the integrated emission line map, we first extract the spectrum for each pixel in the data cube. We pass the spectrum into PAHFIT with a custom emission line fitting list to ensure the fainter lines not included in the default fitting list are incorporated. Then we extract the result of the line fit and construct the resulting line map using the fits for the individual pixels. The line maps of all emission lines (excluding PAHs and quadrupole H_2 transitions) found in N76 are presented in Figure 3.1.

3.2.2 Herschel PACS observations and spectral line images

In addition to the *Spitzer* IRS data, we also report far-infrared observations from the *Herschel* Photodetector Array Camera and Spectrometer (PACS) project 1431 (PI: R. Indebetouw).

We downloaded the data from the ESA *Herschel* Science Archive and use the level 2 pipeline reduced data, which contains spectral data cubes of the [CII] 158 μm, [OI] 63 μm, and [OIII] 88 μm lines. To produce the spectral line maps, we fit a polynomial of order one to the baseline, remove the continuum, and integrate over the spectral line. This process was repeated pixel-by-pixel over the full datacube to produce a line intensity image for [CII], [OI], and [OIII]. Lastly, we convert to the same surface brightness units 10^{-8} W m^{-2} sr^{-1} used with the IRS. We compared this reduction to a independent reduction using the procedure in Cormier et al. (2015) and found excellent agreement within the uncertainties (priv comm, D. Cormier).

3.2.3 Estimation of uncertainty in emission line surface brightness

For the *Spitzer* IRS data, CUBISM provides a uncertainty cube that corresponds to the statistical uncertainty of the IRS measurement. These uncertainties are then propagated into the PAHFIT code, where they are used for the chi-squared minimization fitting. The resulting uncertainty from the PAHFIT output is propagated into our emission line images. These estimates of the uncertainties, however, are only statistical and do not include systematic errors. For the *Herschel* PACS data, we compute the RMS noise outside of the signal integration per each pixel as a 1σ statistical uncertainty for each channel. We then propagate the channel rms to calculate an uncertainty for the integrated signal. This process is repeated per pixel to create a map of the statistical uncertainties for [CII], [OI], and [OIII].

In addition to the statistical uncertainties, we also calculate a “background” level for each emission line. We concentrate on modeling the emission from the HII region created by the Wolf-Rayet/O star binary ionization source AB7. There are other ionization sources across the SMC

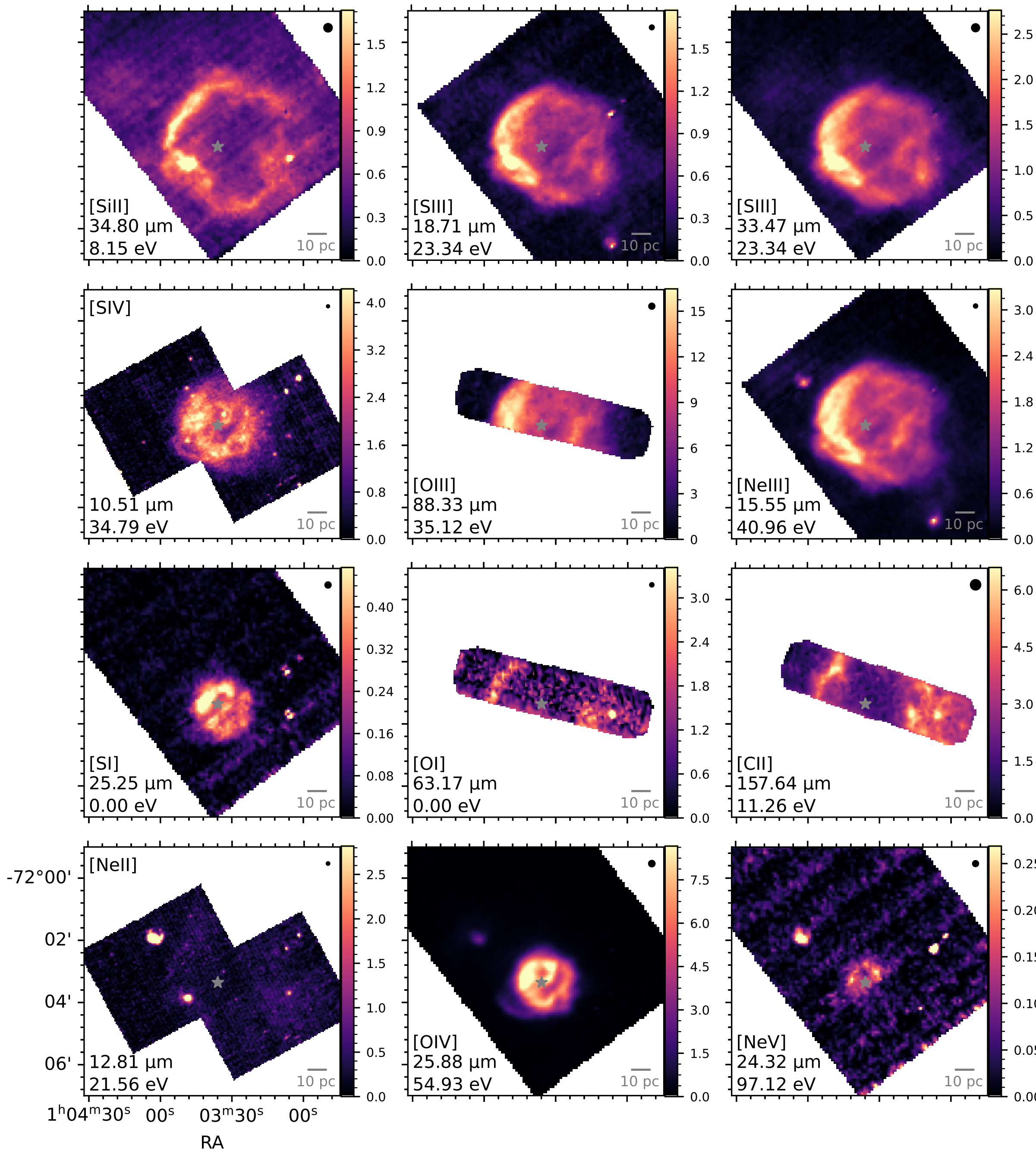

Figure 3.1: Images of infrared line emission in N76 where the color scale corresponds to the line brightness in 10^{-8} W m^{-2} sr^{-1}. The location of the WR-O star binary AB7, the ionization source of N76, is illustrated by a gray star in the center of each image. The supernova remnant (SNR) E0102-72 is located NE, on the upper left of N76, and is seen in some of the emission lines ([OIV], [NeV], [NeIII], [NeII]). The full width at half maximum (FWHM) of the point spread function (PSF) is shown in the upper right corner of each panel, and the ionization potential of the ion is displayed in the lower left corner together with the wavelength of each transition. These images show how the structure of N76 changes depending on the ion.

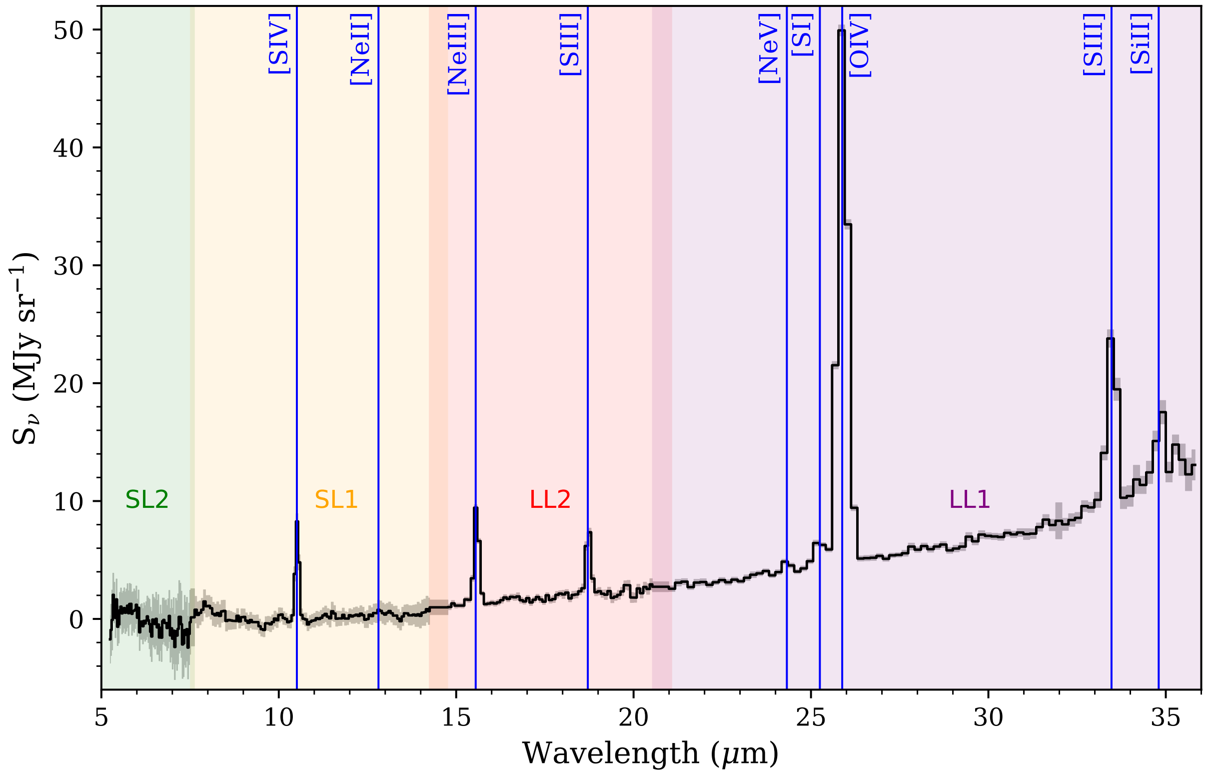

Figure 3.2: Example spectrum showing the ionized gas lines in N76 we model with `Cloudy`, at one line of sight towards 01h03m40s -72d03m20s in a singular pixel aperture. Line labels are in blue and the orders of the IRS instrument are presented through the background color. This position corresponds to the peak of the faintest lines in the N76 nebula, [NeV] and [SI], and is close to AB7 in an area of high ionization.

that can produce diffuse ionized gas throughout the galaxy (e.g. Haffner et al., 2009). In order to quantify and remove this extraneous emission, we identify a blank part of the map that is not contaminated by emission from the HII region (typically ~80 pc away from AB7). We calculate the median surface brightness in this patch of sky and consider it the "background" for the given emission line. The background is very low, typically $\lesssim 5\%$ of the emission line intensity.

3.2.4 PSF matching

The spatial resolution of the *Spitzer* IRS changes as a function of wavelength as the telescope is diffraction limited, with a point spread function (PSF) full width at half maximum

(FWHM) ranging from 7.6″at 34.8 μm for [SiII] to 2.4 ″at 10.5 μm for [SIV]. In order to properly model the spectra, we need to convolve the spectral line images to a common PSF (e.g. Sandstrom et al., 2009; Smith et al., 2009). We follow the procedure described by Aniano et al. (2011) to create custom convolution kernels that will transform an image with a narrower PSF to a broader PSF. Mathematically, we generate a kernel, K, that when convolved transforms Ψ_B, the narrower PSF, to Ψ_A, the broader PSF:

$$\Psi_A = \Psi_B * K(B \rightarrow A). \tag{3.1}$$

To calculate the convolution kernel, K, we take the Fourier Transform (FT) and solve:

$$K(B \rightarrow A) = \mathrm{FT}^{-1}\left(\mathrm{FT}(\Psi_\mathrm{B}) \times \frac{1}{\mathrm{FT}(\Psi_\mathrm{A})}\right). \tag{3.2}$$

Computing this kernel numerically while ensuring its accuracy and stability requires several steps outlined in Aniano et al. (2011) and are summarized below for completeness.

3.2.4.1 Preparing the PSFs

The IRS PSFs are from version 2.0 of the *Spitzer* Tiny Tim software[1]. We create model PSFs for the full wavelength range of IRS, 5 μm - 38 μm. We note that these are simulated PSFs and there are some differences between the predicted PSF for IRS and the measured PSF from calibration stars, but these differences are neglgible for our application (Pereira-Santaella et al., 2010). The PSFs range in pixel scale and image size, depending on the module. In order to

[1] https://irsa.ipac.caltech.edu/data/SPITZER/docs/dataanalysistools/tools/contributed/general/stinytim/

calculate the convolution kernel, K, we regrid all PSFs to a common pixel scale of $0.2''$ and an image size of 1859×1859 pixels. The PSF matching algorithm outlined in Aniano et al. (2011) works best when the PSFs are rotationally symmetric. We circularize the PSFs by rotating the PSF 14 times and averaging after each rotation in order to make the final PSF invariant for any angle that is a multiple of $360^o/2^{14} = 0.022^o$.

3.2.4.2 Creating the convolution kernel

We compute the Fourier Transform (FT) of the narrower PSF, Ψ_B, and the broader PSF, Ψ_A. We use the PYTHON package FFTPACK for all FT calculations. The FT of the target PSF is in the denominator (see Equation 3.2) and will amplify any small high-frequency components of the FT when creating the convolution kernel, K. We account for this by introducing a low-pass filter, f, in kernel construction:

$$f(k) = \begin{cases} 1 & \text{for } k \leq k_L \\ \frac{1}{2} \times \left[1 + \cos\left(\pi \times \frac{k-k_L}{k_H-k_L}\right)\right] & \text{for } k_L \leq k \leq k_H \\ 0 & \text{for } k_H \leq k \end{cases} \tag{3.3}$$

where k is the spatial frequency in the Fourier domain, k_H is the high frequency cutoff for the filter, and $k_L = 0.7 \times k_H$ is the low-frequency cutoff. We create the convolution kernel by modifying Equation 3.2 with the low-pass filter:

$$K(B \to A) = \mathrm{FT}^{-1}\left(\mathrm{FT}(\Psi_\mathrm{B}) \times \frac{1}{\mathrm{FT}(\Psi_\mathrm{A})} \times \mathrm{f(k)}\right). \tag{3.4}$$

repeating the process by looping over the narrower PSFs for Ψ_B. Lastly, we normalize the kernel to unity to ensure flux conservation.

3.2.4.3 Testing the kernel

We test the convolution kernel for accuracy and stability through the metrics defined by Aniano et al. (2011). The convolution of the narrower PSF, Ψ_B, and the kernel, $K(B \to A)$, should reproduce the broader PSF Ψ_A (see Equation 3.1). Further, kernels with many negative values, which redistribute flux, can be unstable. Aniano et al. (2011) define two parameters, D (their equation 20), the integral of the difference between the convolved PSF and the target PSF, and W^-, a sum of the negative values in the kernel, to evaluate the kernels. We calculate these metrics and find very low values for D (< 0.01 for all kernels) and satisfactory values for W^- (ranges between 0.2 - 1.0). Aniano et al. (2011) report that $W^- < 1.2$ are stable. Further, the value chosen for the filtering function k_H affects these metrics, where an increase in k leads to a lower D but a higher W^-. When constructing kernels for each wavelength, we use a range of k_H values and select a k_H with the minimum of both W^- and D. The k_H filtering value ranges from $0.7 - 1.0$ for the final convolution kernels.

3.2.4.4 The final PSF matched images

We produce two sets of PSF matched line images: one that provides maximum uniform resolution by matching to the PSF of the [SiII] transition (our longest wavelength line), and one that matches everything to a 12″ Gaussian for ease of comparison with other data. In our analysis we use the 12″ Gaussian PSF. The broadest PSF out of the spectral lines detected with *Spitzer*

IRS is the [SiII] 34.8 μm line with a FWHM of 7.6″. First, we match each narrower IRS PSF to the PSF of the [SiII] line. Then, we create and apply a convolution kernel to go from the [SiII] PSF to a 2D Gaussian PSF. We find that a 2D Gaussian with a FWHM of 12″ best matches the [SiII] PSF while balancing kernel stability.

Each emission line image is convolved with its custom kernel using the `ASTROPY` package `CONVOLUTION`. We then regrid each image to the coordinates of the [SiII] image to match its pixel scale and to simplify the analysis. For the analysis we also mask non-physical bright artifacts and the emission from the SNR E0102-72. We use 12″ Gaussian PSF-matched final images for the analysis in this work. Note that Figure 3.1 presents the original resolution images to show the maximum detail in the morphology of N76.

In addition to creating the PSF matched line maps that are described in §3.2.1, we also produce a PSF matched cube for the full IRS spectrum, including all orders: SL1, SL2, LL2, LL1. We follow the same procedure on each frame of the original data cubes. A spectrum of the PSF matched cube is presented in Figure 3.2.

We PSF match the IRS *Spitzer* data, but not the *Herschel* PACS images (see §3.2.2). The emission line images from PACS have larger PSFs that would degrade too much the resolution of the IRS maps if we were to match each image to the largest *Herschel* PSF.

3.2.5 Radial profiles

We utilize the spatial information in the infrared observations of N76 when modeling with the photoionization code `Cloudy` to best differentiate models. `Cloudy` simulates HII regions as 1-dimensional (1D) objects that are spherically symmetric. In order to properly compare with the models, we average the spectral line images to create surface brightness radial profiles. N76 is an ideal region for this method because it is approximately spherically symmetric and mostly isolated from other bright regions (see Figure 3.1). We use the location of AB7 as the center of N76 and compute an azimuthal average with a radial bin size corresponding to one pixel or $5''$. The radial profiles show how the line emission varies with distance away from the ionization source, thereby preserving some of the spatial information from the spectral line images but making it simple to compare to properly integrated 1D `Cloudy` models. The radial profiles measured for each line are shown in Figure 3.5, showing that higher ionization lines generally peak closer to AB7. We also report the standard deviation in a given azimuthal bin as the gray uncertainty bars in the profile.

3.2.6 Integrated Intensities

In addition to examining the resolved surface brightness of the infrared emission lines through radial profiles (§3.2.5), we also record the total intensities by integrating across the full size of the nebula. Since each line has a different morphology, we create independent regions for each map that isolate the flux coming from N76. The results are given in Table 3.2. The lines from *Herschel* PACS ([CII], [OI], and [OIII]) only cover a strip of the N76 nebula. We correct for the missing emission by identifying the *Spitzer* IRS emission line that has the most similar radial profile, and multiplying by the ratio of total flux to flux contained in the PACS footprint. For [CII] and [OI] we use [SiII], and for [OIII] we use [NeIII].

The uncertainties in the integrated intensities are derived from the statistical uncertainties propagated through the total intensity calculation (see §3.2.3). They are likely an underestimate of the uncertainty since they do not take into consideration how changing the integration region can affect measurements.

3.3 Photoionization models

3.3.1 `Cloudy` model parameters

We use version C17.01 of `Cloudy` (Ferland et al., 2017) to model the properties of the ionized gas in N76. `Cloudy` is a spectral synthesis code designed to simulate physical conditions and resulting spectrum from gas and dust that is exposed to an ionizing radiation field. In order to produce a model, a variety of input parameters are required and listed below.

Ionizing source SED: The shape of the source spectrum as a function of photon energy must be specified in `Cloudy`, which for N76 corresponds to the spectral energy distribution of the central binary. We use the spectral classification of the two stars in the AB7 binary from Shenar et al. (2016), which classifies them as a WN4 star and an O6 I(f) star. We take the SED of each star from the Potsdam Wolf Rayet (PoWR) database[2], which provides grids of hot stars with expanding atmospheres (Gräfener et al., 2002; Hainich et al., 2019; Hamann & Gräfener, 2003, 2004; Sander et al., 2015). For the WN4 SED, we select a model with SMC abundances, a low ($X_{\rm H} \approx 0.2$) hydrogen fraction, a transformed radius of $\log R_t = 0.7$, a temperature of $T_* = 112$ kK, and a wind speed of $v_\infty = 1,700$ km s^{-1}. For the O6 star, we select a model with SMC abundances, a moderate mass loss rate (corresponding to $\log Q = -13$), a temperature of $T_* = 36$ kK, surface gravity $\log g = 3.6$ cm s^{-2}, and luminosity of $\log L = 5.6$ L$_\odot$. We use these parameters to match the values found by Shenar et al. (2016). We scale the SEDs by the

[2] `http://www.astro.physik.uni-potsdam.de/PoWR.html`

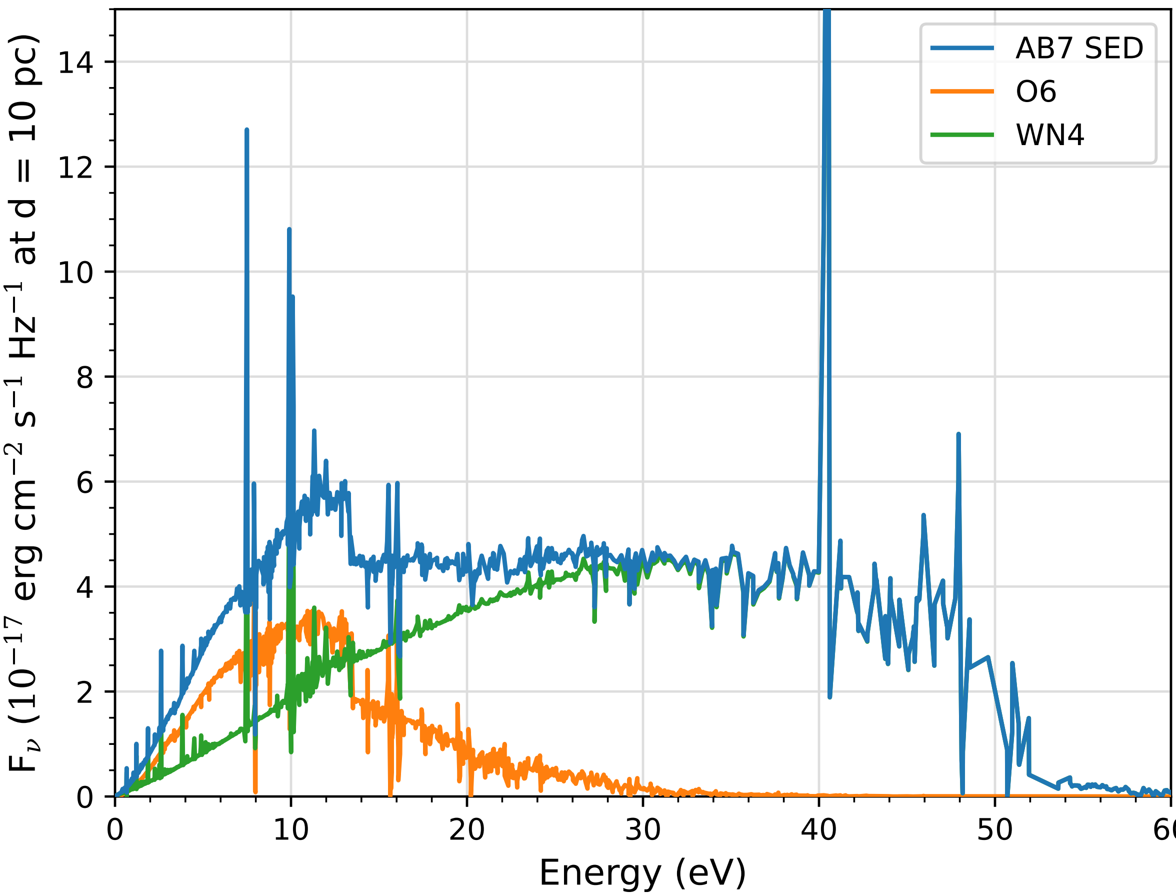

Figure 3.3: The SED of the AB7 system for `Cloudy` input. We use the Potsdam Wolf Rayet database models for the WN Wolf Rayet (Hamann & Gräfener, 2004; Todt et al., 2015) and O6 (Hainich et al., 2019) stars in the AB7 binary and combine them into one input SED. The full SED for AB7 is in blue, the WR is green, and the O star is orange.

Table 3.1: Adopted SMC Abundances

Element	Abundance (X/H)	Reference
He	8.13×10^{-2}	2
C	1.45×10^{-5}	1
N	4.27×10^{-6}	2
O	1.07×10^{-4}	2
Ne	1.86×10^{-5}	2
Al	2.51×10^{-6}	2
Si	4.88×10^{-6}	3,4
S	3.89×10^{-6}	2

References are (1) Dufour (1984) (2) Russell & Dopita (1992), (3) Tchernyshyov et al. (2015), and (4) Jenkins & Wallerstein (2017).

reported luminosities of $\log(L_\odot) = 6.1$ for the WN4 and $\log(L_\odot) = 5.5$ for the O6 components. We then add the luminosity weighted WN and O6 SEDs together to produce a total SED for the AB7 binary system, shown in Figure 3.3. The feature at 40 eV in the spectrum is due to a strong FeV emission line at 305.31 Å.

Elemental abundances: Instead of scaling gas-phase Milky Way abundances to the metallicity of SMC, we employ the best gas-phase abundances available for SMC HII regions. Relative abundances of elements are different in the Magellanic Clouds and the Milky Way due to different nucleosynthesis histories (Russell & Dopita, 1992). Since our focus is to model the ionized gas, we adopt the values provided in Dufour (1984) and Russell & Dopita (1992) for HII regions. For elements where only a photospheric abundance is given, we searched the literature for elemental depletion studies in the SMC and calculated the median gas phase abundance for each element (Jenkins & Wallerstein, 2017; Tchernyshyov et al., 2015). This turns out to be particularly important for predicting [SiII] (see discussion in §3.4.4). Our adopted abundances and the references used are in Table 3.1.

Stopping criteria: We are interested in modeling the ionized gas properties of N76 and do not run the `Cloudy` model through the PDR. We use a range of stopping conditions, but find that an electron temperature cutoff of 2000 K accurately probes the ionized gas to the edge of the ionization front.

Geometry: We assume a spherical geometry to approximate the geometry of N76. The sphere command in `Cloudy` sets the geometry to be closed and assumes that the gas fully covers the ionization source.

Inner radius: The inner radius is defined as the distance between the gas and the ionization source. As we discuss in §3.4.2.1, the region closest to AB7 has been shocked by the wind and is occupied by a tenuous very hot plasma. For the purposes of our modeling, this effect is best reproduced by a central cavity in the gas. We will vary the gas inner radius to best reproduce the observed emission lines.

Hydrogen density: The density input in `Cloudy` is the total hydrogen density. This parameter is varied from $\mathrm{n_H} = 1 - 50\ \mathrm{cm^{-3}}$ in order to best constrain the density in N76 with the observed emission lines. The range of hydrogen densities between $\mathrm{n_H} = 4 - 12\ \mathrm{cm^{-3}}$ that fit the data best are presented in this work.

Since the binary at the center of N76 is well-studied, most of the inputs in the `Cloudy` model are using *a priori* knowledge of the ionization source, abundances, and geometry.

3.3.2 Calculating predicted radial profiles

N76 is an approximately spherical shell, also known as a bubble nebula, with a radius of about 40 pc. Because of the approximately symmetric nature of the nebula, we compare the

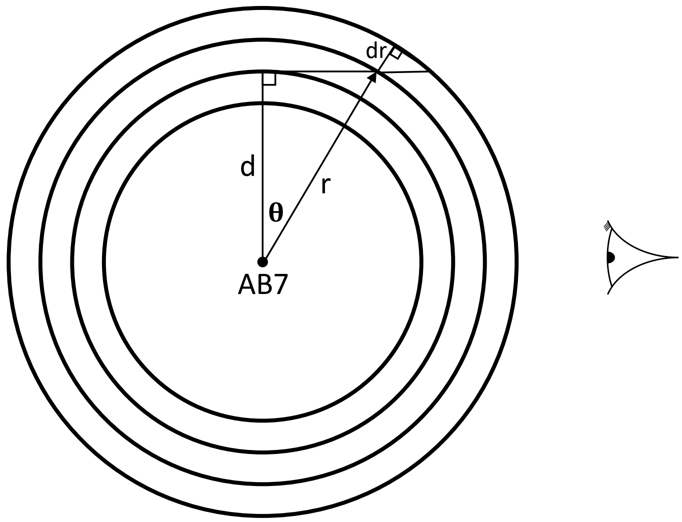

Figure 3.4: Schematic showing the geometry of calculating the projected intensity from `Cloudy` models where d is the projected distance, r is the physical distance, and dr is the differential distance between shells.

`Cloudy` models and the observations using radial profiles. `Cloudy` models report the volume emissivity of each transition as a function of depth into the nebula. In other words, they provide the radial profile of emissivity in a sphere. To compare with the observations, we need to appropriately project these profiles to compute the azimuthal average surface brightness as a function of projected distance from AB7 for each of the emission lines. A point that is at a distance d from the source in projection has contributions from shells that have radii between d and infinity in proportion to their emissivity and projected thickness. Figure 3.4 shows the geometry of the N76 `Cloudy` model and the relationship between different shells, the projected distance d, and the physical distance r. The projected surface brightness for the `Cloudy` model then is:

$$I(d) = \frac{1}{4\pi} \int_{d}^{\infty} \frac{\epsilon(r)}{\sin\theta} dr \ , \tag{3.5}$$

where r is the physical 3D distance from AB7, $\epsilon(r)$ is the radial dependence of the line volume emissivity, d is projected distance from AB7, and θ is the angle between d and r. We convert Equation 3.5 to eliminate θ resulting in

$$I(d) = \frac{1}{4\pi} \int_d^\infty \frac{\epsilon(r)}{\sqrt{1 - d^2/r^2}} dr \ , \tag{3.6}$$

and calculate the surface brightness predicted from the `Cloudy` model, $I(d)$, as a function of the projected distance in order to compare to the observed data.

The `Cloudy` models use AB7 as the only ionization source, but there may be contributions of low ionization ionized gas from the warm ionized medium to our observed emission lines (e.g. Haffner et al., 2009). To account for this, we add a background level described in §3.2.3 to each `Cloudy` model. This background is typically very low representing $\lesssim 5\%$ of the total surface brightness. Lastly, the final `Cloudy` profiles are convolved with a Gaussian kernel with a FWHM of 12″ to make an equal comparison to the 12″ PSF matched emission line images.

3.4 Results

3.4.1 Comparison of models to observations

Figure 3.5 shows the results of the constant density `Cloudy` model with hydrogen densities $n_H = 4 - 12$ cm^{-3}. We compare the models projected on the plane of the sky (§3.3.2) with the measured emission line radial profiles (§3.2.5). Therefore we compare not only the integrated intensity of the emission line, but also how well its predicted distribution matches the data. The emission lines we sample are at a variety of ionization energies and therefore trace the different ionization zones in the nebula. For example, the [OIV] line ($E_{ion} = 55$ eV) peaks at 10 pc while

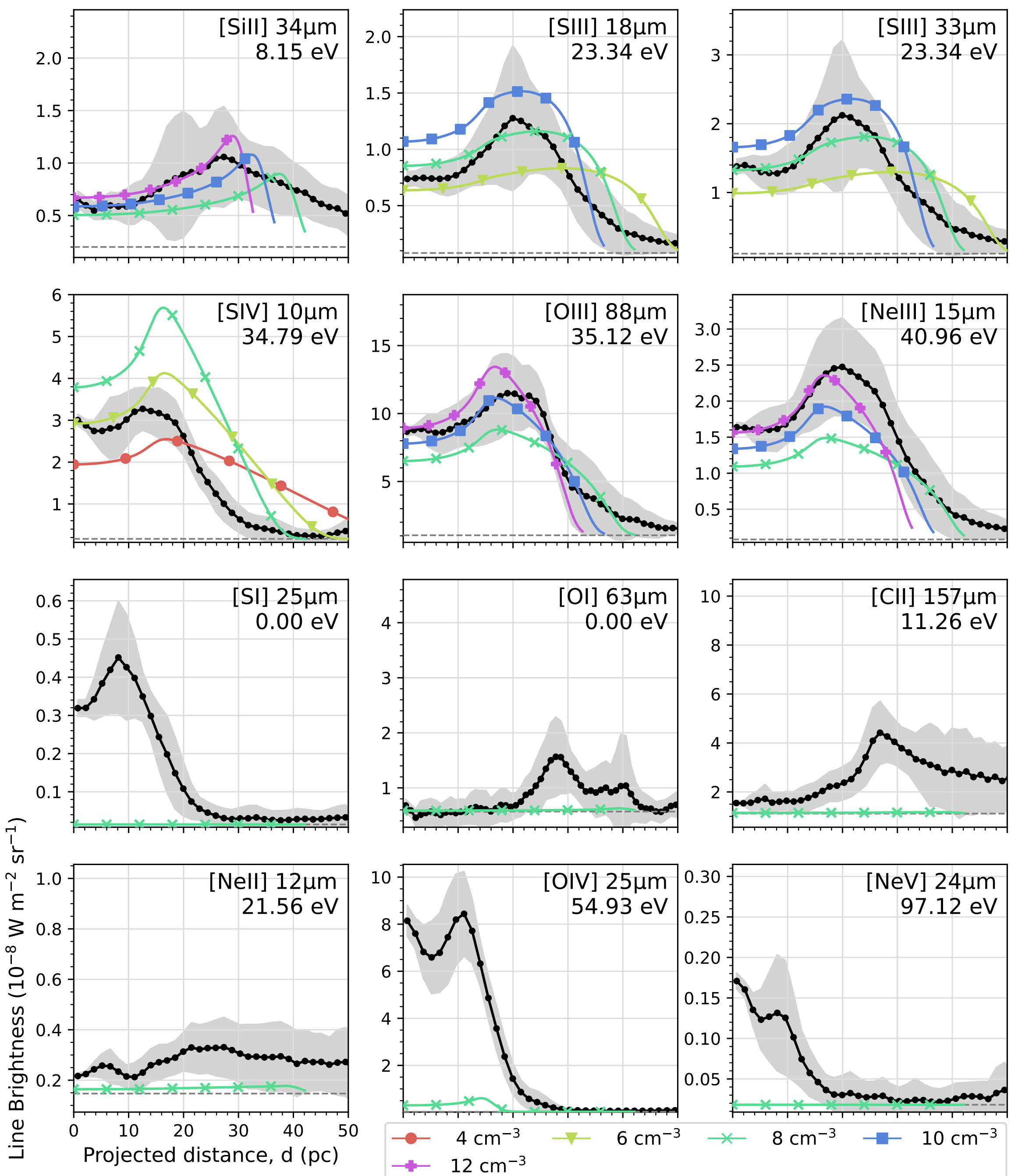

Figure 3.5: Radial profiles of observed emission line brightness and Cloudy photoionization models. The black circles represent the average line brightness of a given emission line as a function of distance away from AB7, the gray region is the standard deviation in a given bin, and the dotted line represents the background diffuse contribution to the emission line (see §3.2.3). The Cloudy models vary with hydrogen density and are represented by the colored lines and symbols. The ions that originate from the dense photoionized gas (excluding emission lines that can be produced through neutral material ([CII], [OI]), shocks ([OIV], [NeV], [SI]), see section 3.4.2, or the diffuse ionized gas, §3.4.3) are well predicted by the Cloudy models that range in density from $n_H \sim 4$ cm^{-3} $-$ 12 cm^{-3}. Both the surface brightness and the shape of the radial profiles are well predicted in these cases.

the [SIII] line ($E_{ion} = 23$ eV) peaks at 20 pc. A model that predicts an emission line well will have a similar peak, spatial gradient, and ending position as the observed radial profile

There is not a single constant density model that is able to predict the shape and intensity of all of the emission lines, but the density range of $n_H = 4$ cm^{-3} to $n_H = 12$ cm^{-3} does a very satisfactory job at matching the majority of the ionized emission lines. In some cases, the spatial distribution of the profile is better matched by a model that does not predict the intensity as well. For example, in the [SIII] profile, the 10 cm^{-3} model predicts the shape very well but is about 50% more luminous than the observations. Similarly, in [NeIII], `Cloudy` predicts that Ne^{++} should peak about 5 pc earlier in the nebula than is observed. These small discrepancies are likely due to our constant density and spherical symmetry simplifying assumptions. While there are small differences between the models and observed emission line profiles, overall `Cloudy` predicts the emission from ionized gas very well with simple models in a narrow density range, except for a few transitions that we will discuss in detail.

In addition to the projected surface brightness profiles from the `Cloudy` models, we also report the predicted total intensities in the `Cloudy` models in Table 3.2 for the $4\ \mathrm{cm}^{-3}$ and $12\ \mathrm{cm}^{-3}$ models. Overall the radial profiles of the surface brightness provide a much more precise way of differentiating between the constant density `Cloudy` models than examining the integrated intensity. For example, the integrated intensity of [NeIII] varies between the $4\ \mathrm{cm}^{-3}$ and $12\ \mathrm{cm}^{-3}$ models by 29.08 to 29.37 $\mathrm{W\ m}^{-2}$, a $< 1\%$ difference. In contrast, the radial profile of the $4\ \mathrm{cm}^{-3}$ model peaks 20 pc after the $12\ \mathrm{cm}^{-3}$ does, clearly showing it does not match the spatial distribution of the [NeIII] emission. Thus a comparison between the spatial resolved radial profiles provides much more information than using just integrated intensities.

To produce both the `Cloudy` models and the measured radial profiles we assume that

Table 3.2: Line properties and intensities

Line	λ (μm)	Ionization Potential (eV)	n_{crit} (cm^{-3})	FWHM ($''$)	Instrument	I_{obs} (10^{-15} W m^{-2}) Total	I_{cloudy} (10^{-15} W m^{-2}) Orig	$n_H = 4$ cm^{-3}	$n_H = 12$ cm^{-3}
[SiII]	34.80	8.2	2×10^3	7.61	LL1	14.75 ± 0.01	...	16.87	14.22
[SIII]	18.71	23.3	2×10^4	4.15	LL2	11.28 ± 0.73	...	25.90	25.88
[SIII]	33.47	23.3	7×10^3	7.17	LL1	18.93 ± 0.00	...	41.18	40.53
[SIV]	10.51	34.8	5×10^4	2.40	SL1	17.58 ± 2.35	...	69.19	77.03
[OIII]	88.33	35.1	5×10^2	5.35	PACS	111.68 ± 2.25	50.21 ± 1.01	144.13	147.19
[NeIII]	15.55	41.0	3×10^5	3.51	LL2	22.05 ± 0.70	...	29.08	29.37
[SI]	25.25	0.0	1×10^5	5.44	LL1	1.04 ± 0.14	...	0.00	0.00
[OI]	63.17	0.0	9×10^5	3.63	PACS	15.74 ± 3.37	4.49 ± 0.90	1.24	0.96
[CII]	157.64	11.3	5×10^1	9.43	PACS	60.35 ± 1.20	16.70 ± 0.33	1.92	1.23
[NeII]	12.81	21.6	7×10^5	2.83	SL1	4.52 ± 1.70	...	0.93	0.74
[OIV]	25.88	54.9	1×10^4	5.66	LL1	20.35 ± 0.04	...	2.78	1.97
[NeV]	24.32	97.1	1×10^5	5.22	LL1	0.20 ± 0.06	...	0.00	0.00

Description of the spectral lines modeled, including the integrated intensities measured and the predicted integrated intensities with two densities from Cloudy. The Ionization Potential is the photon energy required to produce the observed ionization state from the lower ionization state. The critical density is for collisions with electrons. The lines observed with *Herschel*/PACS, and given as I_{obs} Orig, do not cover the full nebula (see Figure 3.1); I_{obs} Total contains the total intensity corrected for this missing flux.

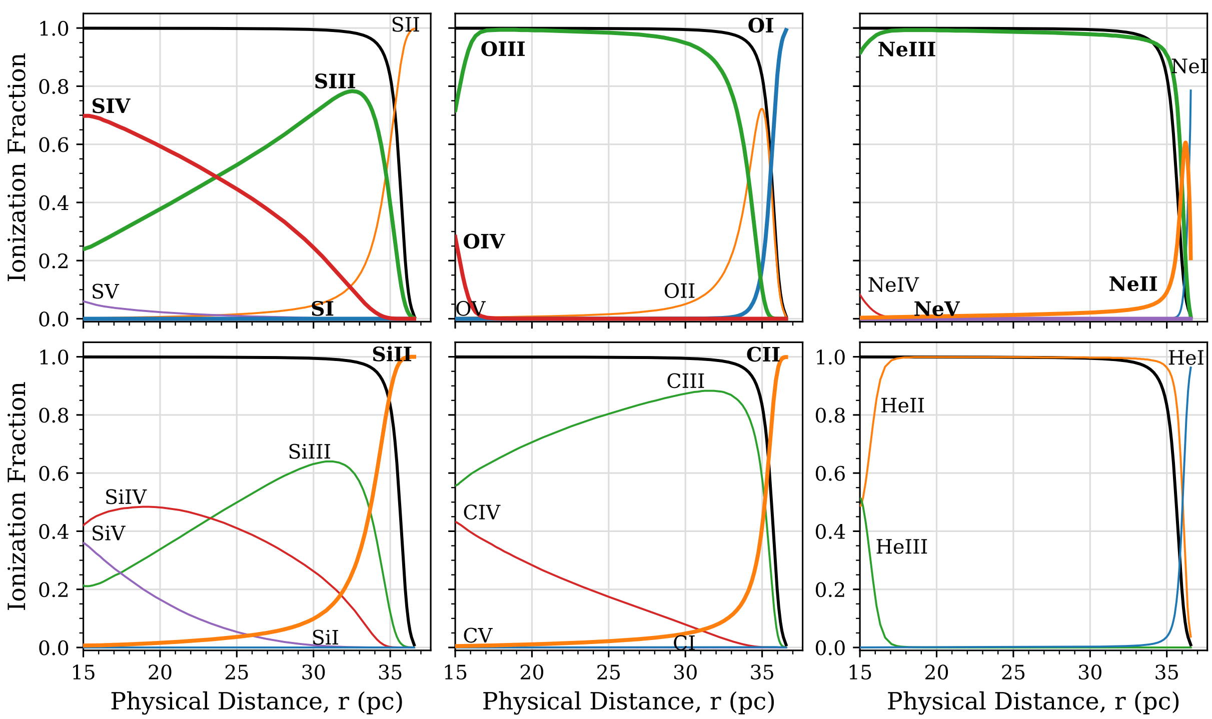

Figure 3.6: The ionization structure of sulphur, oxygen, neon, silicon, carbon, and helium from the 10 cm^{-3} constant density `Cloudy` model beginning at the photoionized region (r = 15pc). Ions that are presented in this paper are bold, and we also show the structure of ionized hydrogen in black. The various ionization zones can be seen throughout these elements in physical distance, similar to the projected distance seen in Figure 3.1.

N76 is spherically symmetric with AB7 in the center of the nebula. This is approximately true, but not precisely correct. Figure 3.1 shows that AB7 appears offset in the eastern direction. Additionally, there is an overall trend for the ionized gas lines to be much brighter on the eastern edge of the nebula in comparison to some of the neutral gas lines ([CII] especially) that have brighter emission on the western edge. We explore the effects of the asymmetries on our results in Appendix A. Images of the H_2 S(1) transition and ancillary ALMA CO data (Figure 3.7) confirm that there is a molecular cloud complex on the western side of N76. Therefore, there are likely internal density gradients as well as a wall of dense gas on the western side of the nebula breaking the symmetry assumption. For example, because AB7 is slightly offset from the center, the radial averaging produces flatter slopes with respect to the models. We have attempted to account for some of this offset by showing the profiles as a strip instead of radially in Appendix A. These show the structure in the different sides of the nebula and how a particular density is a slightly better predictor for one side compared to the other.

We also report the ionization structure predicted by `Cloudy` of each element in Figure 3.6 to complement the projected profiles of surface brightness. The panels show the ionization state of the relevant elements as a function of the physical distance from AB7. In addition to the ions that are studied in this paper, we also plot the ionization structure of helium. As the most abundant element after hydrogen, helium can have a significant impact on the ionization equilibrium of HII regions. This impact is most pronounced in HII regions illuminated by hard radiation fields, due to the fact that their central sources produce a lot of photons capable of ionizing and doubly ionizing helium: the ionization potentials of He^0 and He^+ are 24.6 eV and 54.4 eV respectively. Ionization cross-sections are sharply peaked at the ionization energy: the cross-section of He^0 to 24.6 eV photons is ten times higher than that of H^0, therefore these photons will preferentially

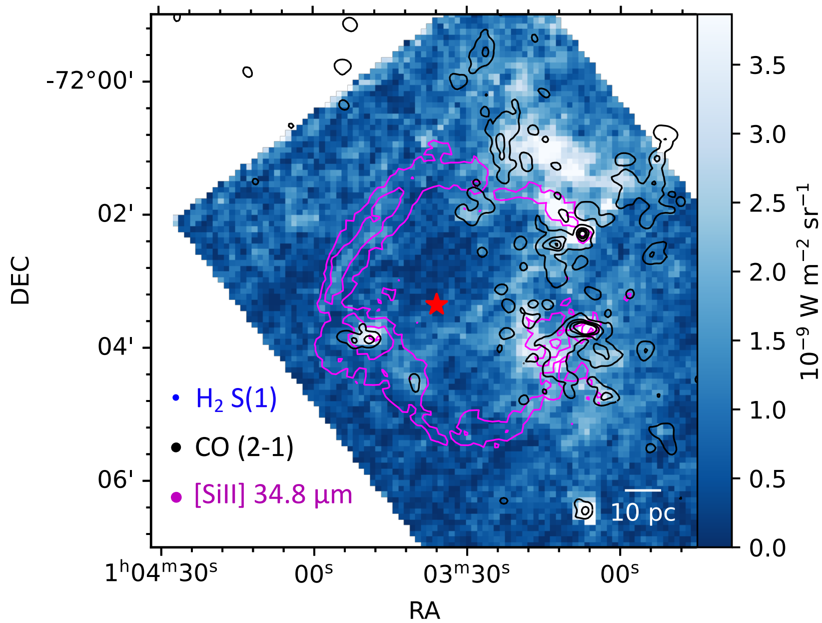

Figure 3.7: The neutral gas tracers in N76, with the H_2 S(1) quadrupole transition in the blue color scale, CO contours from Tokuda et al. (2021) in black (in levels of 1, 6, 11, 16 Jy/beam), and the [SiII] emission in magenta contours (in levels of 1, 1.5, and 3×10^{-8} $\mathrm{W\ m^{-2}\ sr^{-1}}$). The beam/PSF size of each map is in the bottom left corner. The [SiII] emission primarily traces the outer shell of N76, suggesting [SiII] originates mostly from the ionized gas. The CO and H_2 emission is brightest when AB7 illuminates the molecular ridge north and north-east of N76.

ionize helium over hydrogen. For sources with a hard enough spectrum, characterized by the ratio of the rate of production of He-ionizing photons (Q_1) to H-ionizing photons (Q_0), this can lead to the He^+ region extending slightly past the H^+ region. In fact, $Q_1/Q_0 \sim 0.15$ is needed for the HII and HeII regions to be equivalent sizes (Draine, 2011), while for N76 $Q_1/Q_0 \sim 0.55$ matches the slightly larger HeII emitting region. A similar effect is seen in the ionization structure of neon, where the [NeII] emission extends slightly past the hydrogen ionization front.

3.4.2 The high ionization lines: [NeV] and [OIV]

One of the largest discrepancies between models and observations are the very high ionization lines. As seen in Figure 3.5, the highest ionization lines [NeV] and [OIV], with ionization potentials of 97 eV and 55 eV respectively, are severely underpredicted by the photoionization models. There are two main explanations for this: either these species are produced by photoionization and the WR SED is considerably harder than the PoWR models predict, or the high ionization species are shock ionized by the fast stellar winds.

Note that Nazé et al. (2003) report narrow-band optical imaging of N76 and find a similar excess of emission in HeII that cannot be explained by the hottest WR atmospheric model. It is very likely that the whatever causes our [NeV] and [OIV] emission is also causing the excess He II emission.

The ionizing spectrum of WR stars at energies greater than 13.6 eV is uncertain due to the absorption from intervening neutral hydrogen (e.g., Martins, 2011). Nevertheless, bright [OIV] emission has been seen in the stellar winds around WR stars (Ardila et al., 2010; Morris et al., 2004). It is possible that the SED for AB7 is much harder than predicted by the PoWR models. Reproducing the intensities we observe would require extending the SED of the WN4 star to ~ 100 eV at approximately constant luminosity integrated over all wavelengths. This model, however, would still require a ∼10 pc wind-blown bubble to explain the size and distribution of the [OIV] and [NeV] emission.

Photoionization models of the galaxies NGC 5253 and II Zw 40 show that the observed [OIV] emission can be produced through hot, low metallicity WR stars (Schaerer & Stasińska, 1999; Schaerer & Vacca, 1998). Further, Crowther et al. (1999) suggest that WNE-w stars, a special class of WR stars that have weak spectral lines, can produce substantial [NeV] emission. It is possible that AB7 should be reclassified as a WNE-w star and may be able to reproduce the observed emission of these high ionization lines. An alternative explanation, which we outline below, is the high ionization lines are produced in the stellar wind blown bubble of the WR nebula.

3.4.2.1 A wind-blown nebula and shock-heated gas

There are two possible sources of shocks in the AB7/N76 system: the colliding stellar winds from the WR and O star or the shock from the winds interacting with the ambient medium. There is ample evidence of shocks originating from colliding wind systems, such as the winds produced by the WN4 and O6 star in AB7 (e.g. Parkin & Pittard, 2008; Stevens et al., 1992; Tuthill et al., 1999). In order to determine whether the wind collisions from AB7 can produce shocks that can create the O^{3+} and Ne^{4+} ions, we compute the physical scale of the wind collision zone. From Usov (1991), the wind collision zone of AB7 occurs $\sim 10^{-6}$ pc away from the O6 star. The X-ray emitting gas from AB7 attributed to the colliding winds is ~3.5 pc in radius, much smaller than the full extent of the [OIV] and [NeV] (Guerrero & Chu, 2008). The [NeV] and [OIV] emission extend out to $10-20$ pc, much further than other effects due to wind collision, suggesting that their source is not the shock associated with colliding winds.

Early-type stars, like the WR and O star in AB7, create stellar wind-blown bubbles in the surrounding ISM. The resulting nebula consists of an onion like structure (see Figure 1 in Freyer et al., 2003; Weaver et al., 1977) with four layers, including (1) an innermost, free-flowing supersonic wind that travels into (2) a hot ($\sim 10^6 - 10^8$ K), shocked gas region that will expand into (3) the photoionized shell of swept up interstellar gas, and finally into (4) the ambient interstellar medium. The hot, shocked material in shell 2 is typically at much higher pressures than shell 3, and will expand as a function of time. Assuming a uniform density spherical shell with equal pressure throughout and that the thermal energy contained within shell 2 is much higher than the kinetic energy, Weaver et al. (1977) derived a relationship between the radius of hot, shocked gas bubble (shell 2) as a function of time, such that

$$r_{s2}(t) = \left(\frac{125}{154\pi}\right)^{1/5} L_w^{1/5} \rho_0^{-1/5} t^{3/5} \,, \tag{3.7}$$

where $\rho_0 = n_0 m_H$ is the density of the ambient medium and $L_w = \frac{1}{2}\dot{M}_w v_w^2$ is the stellar wind luminosity where $\dot{M}_w$ is the mass loss rate and v_w is the terminal velocity of the stellar wind. We calculate the size of the bubble blown by the WR star in AB7 through the values characterized by Shenar et al. (2016), $\dot{M} = 10^{-5}$ $\mathrm{M_\odot\ yr^{-1}}$, $v_w = 1.7 \times 10^3$ $\mathrm{kms^{-1}}$, and assume $n_0 = 10\ \mathrm{cm^{-3}}$. Using these parameters, a 15 pc radius bubble (the size of the [OIV] and [NeV] emitting region) is created after 0.4 Myr of free expansion. Thus it is reasonable that the high ionization lines are produced by shocks throughout the wind blown bubble and do not originate from photoionization.

In order to test whether the [NeV] emission can be produced from the shocked, hot plasma in zone 2, we calculate the velocity and postshock temperature needed to ionize $\mathrm{Ne^{+3}}$ into $\mathrm{Ne^{+4}}$. We estimate a temperature of $\mathrm{T} \sim \mathrm{E_{ion}/k_B} \sim 10^6$ K by taking the ionization energy of [NeV]. Using the relationship between the postshock temperature (equation 36.28 of Draine, 2011) and the shock velocity, we find the minimum velocity for the shock is $\mathrm{v} \approx 290\ \mathrm{km\,s^{-1}}$. Toalá et al. (2017) study the Wolf–Rayet Nebula NGC 3199 in the Milky Way and find diffuse X-ray emission that corresponds to a plasma temperature of $\mathrm{T} \approx 1.2 \times 10^6$ K, very similar to the temperature required to produce the [NeV] emission observed in N76. Further, the models of a stellar wind blown bubble from Freyer et al. (2003) show expansion velocities of the hot bubble shortly after creation that range from 250 - 500 $\mathrm{km\,s^{-1}}$, agreeing with the estimated shock velocity needed to produce the [NeV] emission.

3.4.3 Production of [NeII] in N76

The `Cloudy` models predict a modest amount of [NeII], about 20% of the observed [NeII]. At an ionization potential of 21.56 eV, [NeII] traces lower energy photons. Figure 3.6 shows how the ionization state of Neon transitions to Ne^{+} at the very edge of N76, suggesting that the bulk of the Neon is in higher ionization states, mostly [NeIII] which is well predicted by the `Cloudy` model. The excess of observed [NeII] emission could be associated with other ionization sources besides AB7, such as smaller HII regions. A density contrast between the gas in the WR nebula ($n_e \sim 10~\mathrm{cm}^{-3}$) and the diffuse ionized gas ($n_e \lesssim 0.1~\mathrm{cm}^{-3}$) may also produce the excess [NeII] emission. In the nearby dwarf galaxy IC 10, Polles et al. (2019) find that their models underpredict the [NeII] observations by a factor between three and four, suggesting that [NeII] may be a tracer of the diffuse ionized gas in low metallicity galaxies.

3.4.4 The neutral-dominated lines: [OI], [CII], and [SiII]

We define the neutral-dominated lines as ions or atoms that can come from neutral gas, i.e. those ions that have an ionization potential less than that of hydrogen. Most of these neutral-dominated emission lines are under-predicted by the `Cloudy` models. The `Cloudy` models were designed to model the ionized gas and do not probe farther than the ionization front after the transition from ionized to neutral material. Further, Figure 3.6 shows the ionization structure of carbon and oxygen, suggesting that the radiation field of AB7 is too hard for O^{0} and C^{+} to exist in the interior of the HII region where oxygen and carbon are in higher ionization states. Thus the bulk of emission from [OI] and [CII] comes from the neutral phases; future photo-dissociation region (PDR) modeling is needed to understand the nature of these neutral lines, which is beyond the scope of this study.

The fine-structure transition of silicon, [SiII], however, is reasonably well predicted by the ionized gas `Cloudy` models. With an ionization potential of 8.15 eV for Si^0, [SiII] can come from the neutral gas. However, `Cloudy` modeling of just the HII region reproduces both the total intensity and the surface brightness distribution of the [SiII] line (see Table 3.2 and Figure 3.5), unlike for the other neutral gas tracers. Figure 3.6 shows that the modeled abundance of Si^+ grows faster toward the edge of the HII region than that of C^+.

Why are there dominant PDR contributions for [CII] and [OI] but not [SiII]? The [SiII] 34 μm fine-structure transition is at shorter wavelengths, and its excitation requires higher temperatures than [OI] 63 μm or [CII] 158 μm. Further, the [CII] and [OI] lines are also major coolants in the Warm and Cold Neutral Medium (Wolfire et al., 1995, 2003) and contributions from that can increase the total intensity of these lines by peering through the atomic gas in projection towards the SMC. In contrast, the cooling from [SiII] is two orders of magnitude lower than that from the [CII] and [OI] lines, which leads to a much fainter neutral gas contribution for the [SiII] emission. The intensity of the [SiII] emission is also highly dependent on the silicon gas abundance. Silicon is depleted heavily into dust, and in order to determine its gas phase abundance we used depletion studies in the SMC (Jenkins & Wallerstein, 2017; Tchernyshyov et al., 2015). The dust depletion of gas phase silicon with respect to the photospheric abundances in the SMC (Russell & Dopita, 1992) has a large range, factors from 1.25 to 0.05 (0.1 to -1.3 dex, our preferred abundance corresponds to 0.4, or -0.4 dex). While we assume some silicon depletion in the ionized gas, our results suggest that even more silicon is depleted in the neutral phase, especially when compared to carbon or oxygen. These combined effects likely explain the much smaller contribution of PDRs toward the observed [SiII] emission.

We present images of the other neutral gas tracers in N76 in Figure 3.7. The *Spitzer* IRS covers the quadrupole transitions of molecular hydrogen, H_2. Our PAHFIT pipeline simultaneously fits these lines and we show the brightest H_2 line, S(1) at 17 μm, in Figure 3.7. This line has $E/k \sim 1000$ K, traces H_2 at $T > 300$ K, and its presence indicates molecular material that is heated by a strong FUV field or through shocks from the central WR star. We compare the H_2 S(1) and [SiII] lines to the ACA CO(2-1) data presented in Tokuda et al. (2021). Interestingly, these neutral gas species are not always spatially coincident. As discussed above, the [SiII] emission originates mostly from the ionized gas and therefore traces the the outer shell of N76. The H_2 and CO emission is brightest where AB7 illuminates the molecular ridge region that is north and north-west of N76.

3.4.5 How changes in the model affect the inferred conditions

Besides the density, for which we produce a grid of models, a variety of other `Cloudy` inputs can affect the final results of the modeling. The `Cloudy` models are most sensitive to the input luminosity and SED.

For example, decreasing the luminosity of the WR by 50% leads to a 56% reduction in the total intensity of the spectral lines at a constant density of $n_H = 10\,\mathrm{cm}^{-3}$. Naively, this reduction in the total intensity provides a slightly better fit for some lines, but it is at the cost of producing emission over a region with a smaller radius and a spectral line radial profile that does not match the data. Thus the strength of comparing the `Cloudy` models to the spatially resolved data shines through; using the *a priori* values for the spectrum and luminosity provide an overall better fit than if one were to directly match the total intensities.

We also experimented with using different stopping conditions, starting radii, abundances, and the presence of dust. All of these parameters have a negligible impact on the overall results of the model, except for the abundances which we fixed in the manner described in §3.3.1 and Table 3.1.

3.4.6 Presence of [SI] in the center of N76

One peculiar detection from *Spitzer* IRS is a spectral line at 25.25 μm in the center of N76 that we tentatively identify as [SI]. The spectrum of this line can be seen in Figure 3.2 and the image in Figure 3.1. Our fitting procedure from PAHFIT identifies a spectral line between 25.2 and 25.3 μm throughout the central region of N76. The neutral sulphur line is directly in the middle of this range, at 25.245 μm. Using the NIST atomic spectral database, the nearest possible spectral lines correspond to Mg II at 25.05 μm and Si I at 25.38 μm. The redshift of these wavelengths due to the systemic velocity of the SMC is 0.01 μm. The average uncertainty PAHFIT reports on this spectral line wherever there are detections is 0.017 μm, which corresponds to $\sim 10\%$ of the wavelength step between spectral pixels in this region of the LL1 map (0.178 μm).

The existence of neutral sulphur (or for that matter any line corresponding to ions found in neutral gas, such as Mg II and Si I) in the center of such a high ionization HII region is a mystery. If the line is confirmed as [SI], then it is the first detection of such a feature in the center of the highly irradiated environment of a WR nebula. Previous observations show [SI] resides in dense, neutral gas and can be produced through fast, dissociative J-shocks (Haas et al., 1991; Rosenthal et al., 2000). These observations, however, consistently show the presence of other neutral lines, such as H_2 and [OI]. In N76, there is no corresponding neutral emission where we observe [SI], making the production of this line a mystery. We explore possible explanations for this emission in §3.5.2.

3.5 Discussion

3.5.1 Ionized gas contributions to the neutral lines: [SiII], [CII], and [OI]

The ions and atoms that can exist in the neutral gas, Si^+, C^+, and O^0, all have ionization potentials less than that of hydrogen, but their next ionization stage is above or close to 13.6 eV. The emission from these ions can therefore be present in both the neutral and ionized gas phases. Although this work is focused on modeling only the ionized gas, understanding the proportion the ionized gas contributes to the overall intensity of the neutral-dominated lines is of interest for using these lines as neutral gas tracers. Our `Cloudy` simulations were designed to end after the ionization front, the position where the ionized gas transitions into fully neutral gas. Similar to Cormier et al. (2019), we compute the contribution the neutral gas has on [SiII], [CII], and [OI] by defining a more conservative "end" of the ionized gas region as the point in which the electron fraction and neutral fraction are equal to 0.5. We use this value to define the end of the ionized gas region.

As described in §3.4.4, the `Cloudy` models underpredict the emission from [OI] and [CII] that is observed in the direction of the nebula, because the neutral gas regions that surround the ionized gas but are not included in our `Cloudy` models contribute the bulk of the emission in these lines. In contrast, the [SiII] intensity is well matched to the predicted emission from ionized gas in the `Cloudy` models, suggesting a substantial amount of [SiII] is produced in the HII region itself. We quantify this by calculating the fraction of the intensity originating from the ionized gas for these lines in our models. We find that for N76 96% of the [SiII] emission originates from the ionized gas while the [OI] and [CII] have an ionized gas contribution of 4% and 2%, respectively. Cormier et al. (2019) use their `Cloudy` models of the Dwarf Galaxy Survey (DGS) to perform a similar calculation and report that $\lesssim$10% of the [CII] and $\lesssim$40% of [SiII] emission originates from the HII regions. Although we see a much higher HII region contribution to the [SiII] emission in N76 than in the galaxy-wide integrated measurements in the DGS, keep in mind that N76 is a Wolf-Rayet nebula and thus not representative of most HII regions.

3.5.2 Production of [SI] in the center of N76

We discussed in §3.4.6 the surprising identification of a line in the central regions of N76 as neutral sulphur. Below we go over some possible ideas about the origin of this transition.

Velocity shifted [OIV] emission: The nearest emission line in wavelength to our possible [SI] emission that is bright and clearly identified in N76 is [OIV] at 25.93 μm. We considered whether the line we identify as [SI] could be high velocity [OIV] emission. The velocity required to shift [OIV] to the observed wavelength of 25.25 μm is 7,600 km s^{-1}. While the WR and O stars in AB7 produce stellar winds, the speed of these winds is below 2,000 km s^{-1} (Shenar et al., 2016). The X-ray emission observed in N76, resulting from the colliding WR and O star winds, also implies a wind speed of 2,000 km s^{-1} (Guerrero & Chu, 2008). Thus it is extremely unlikely that the emission is [OIV] shifted to 25.25 μm. Further, the wind would have to be asymmetric, since we do not see a corresponding redshifted component. Moreover, instead of discrete components we would expect a symmetric, broadened [OIV] profile because the emission should be optically thin.

Dust destruction through stellar winds: The main mystery of the origin of [SI] at the center of this nebula is how sulphur can remain in a neutral state where we also observe ionized species caused by >55 eV photons. It is possible that the winds and radiation from AB7 can interact with the surrounding dust, destroy dust grains, and move their constituent atoms, including neutral sulphur, into the gas phase. We then observe the [SI] emission before neutral sulphur is ionized into higher states. We evaluate whether this is possible by performing a back-of-the-envelope calculation. First, we estimate the timescale it would take to ionize sulphur in the hard radiation field of AB7. We integrate the ionizing spectrum over the ionization potential of sulphur (10.36 eV) to find the rate of sulphur-ionizing photons at a given distance of the [SI] emitting region. We calculate a timescale of 1.7 years to ionize sulphur after assuming a cross-section of $3 \times 10^{-18}\ \mathrm{cm^{-3}}$ (Draine, 2011) and a radius of 10 pc. We next calculate the mass of neutral sulphur that must be replenished within this time. From the observed [SI] intensity we find the column density by assuming collisional excitation and use the equation given in Crawford et al. (1985), a critical density for collisions with $\mathrm{e^{-}}$ of $\mathrm{n} = 1.55 \times 10^{5}\ \mathrm{cm^{-3}}$ (Draine, 2011), a spontaneous decay rate of $\mathrm{A} = 1.40 \times 10^{-3}\ \mathrm{s^{-1}}$ (Froese Fischer et al., 2006), a temperature of $\mathrm{T} = 1.4 \times 10^{4}$ K, an abundance of 3.89×10^{-6} (Russell & Dopita, 1992), and a density of $\mathrm{n} = 40\ \mathrm{cm^{-3}}$. The density is chosen by assuming a strong shock wave will have four times the density of the pre-shocked medium of $10\ \mathrm{cm^{-3}}$(e.g., Draine, 2011). We calculate a column density of $\mathrm{N_{S^0}} = 4.9 \times 10^{14}\ \mathrm{cm^{-2}}$ and consequently a mass of $\mathrm{M_{S^0}} = 3.7 \times 10^{-2}\ \mathrm{M_\odot}$ over a 10 pc radius. Thus our estimate suggests that $3.7 \times 10^{-2}\ \mathrm{M_\odot}$ of sulphur will need to be lifted off of destroyed dust grains every 1.7 years. Given the low abundance of sulphur relative to other elements that make the bulk of the dust mass (C, Si, O), this represents a very large dust mass destroyed every year, and it seems impossible this reservoir would exist over the life of the nebula (or be in some way replenished by the central source mass loss rate).

Unidentified spectral line: We used the NIST atomic spectral database to search for lines near the 20.0-20.5 μm range and did not identify any possible candidates besides [SI] (see discussion in §3.4.6). It is possible that the 25.25 μm emission originates from a molecular compound, but a molecule would have similar difficulties surviving the intense radiation field of AB7. Instead of [SI], however, this line could be an unidentified spectral line that corresponds to a very high ionization state not in the NIST catalog. Clearly more investigation is needed to determine the origin of this line.

3.5.3 Quantifying the escape of ionizing photons from HII regions

Previous studies use a variety of methods to determine the escape of ionizing radiation from HII regions. In Polles et al. (2019), the authors calculate the ionization front as the depth where the hydrogen ionization fraction (H^+/H^{tot}) is below 0.01. They run `Cloudy` models with the stopping depth as a free parameter in order to determine regions where ionizing photons escape. Radiation-bound regions are defined as regions wherein `Cloudy` models end at the ionization front while matter-bound regions end before the front, allowing ionizing photons to escape. Across IC10, Polles et al. (2019) find a depth ranging from 0.75 to 0.90, suggesting a large portion of ionizing photons are escaping the HII regions in this galaxy.

Pellegrini et al. (2012) use optical maps of the [SII]/[OIII] ratio in the Magellanic Clouds to determine the optical depth throughout the HII regions in the LMC and SMC. The authors classify regions as optically thin, optically thick, or blister (showing features of both optically thin and thick) and assign each region an escape fraction of Lyman-continuum (LyC) photons. After luminosity weighting and integrating across the LMC and SMC, they find escape fractions of 42% and 40%, respectively. These authors classify N76 as an optically thin HII region, suggesting that N76 has a non-negligible photon escape fraction.

The models of N76 presented here are radiation-bounded, suggesting that few ionizing photons escape the HII region. When we run a matter-bounded model by stopping the `Cloudy` model before the ionization front, the predicted surface brightness for the lower ionization lines like [SIII] decreases and does not represent well the radial profiles seen in Figure 3.5. However, the `Cloudy` models all assume spherical symmetry. It is clear through Figure 3.1 and in Appendix A that the western side of N76 is denser than the eastern. It is possible that a portion of the ionizing radiation from AB7 may escape through this edge, leading to its diffuse morphology. A similar morphology is seen in N76's HII region neighbor, the supergiant HII region N66 (Geist et al., 2022). Nevertheless, the exact escape fraction of ionizing photons is difficult to quantify due to the spherically symmetric nature of the `Cloudy` models and the limited field of view of the IRS and PACS measurements.

3.5.4 Physical conditions in N76

Figure 3.8 presents how the electron temperature and electron density vary for each constant density model as a function of physical distance from AB7. The electron density is slightly higher at the center of N76, due to the contribution from the He^{++} region that forms around very hot WR stars (see also sixth panel in Figure 3.6). In our constant density modeling $\mathrm{n_e}$ stays constant up to the ionization front, where the gas transitions from ionized to neutral hydrogen. The temperature profile is smooth distribution, with a central peak near the edge of the photoionized region reaching 16,000 to 18,000 K, which then stays approximately constant at around 14,800 K until reaching the hydrogen ionization front. Note that the inner regions close to the star are simply a cavity of radius 15 pc in the photoionization models, so the precise details of the transition between shock-ionized and photoionized gas are not accurately represented in these models.

The ratio of [SIII] 18 μm/ [SIII] 33 μm also provides an estimate for n_e of an HII region. However, this ratio is only sensitive to gas with densities $n_e > 100 \text{ cm}^{-3}$ (Dudik et al., 2007), thus it does not probe the diffuse ionized gas in N76. Our photoionization modeling of N76, however, is able to explore a wider region of parameter space than line ratios alone. Figure 3.8 shows how dramatically the size of the HII region changes for small changes in hydrogen density, illustrating the usefulness of spatially resolved data for characterizing HII regions.

We also calculate the ionization parameter, U, defined as the dimensionless ratio of the hydrogen-ionizing photons to the total hydrogen density. This parameter is often used to characterize HII regions, and is defined as:

$$U = \frac{Q(H)}{4\pi r_o^2 n(H) c}\ , \tag{3.8}$$

where r_o is the ionized region radius in units of cm, $n(H)$ is the total hydrogen number density in units of cm^{-3}, c is the speed of light, and $Q(H)$ is the number of hydrogen-ionizing photons emitted by the central source per second. The ionization parameter we measure for N76 ranges from $U = 3 \times 10^{-2}$ for $\mathrm{n_H} = 4 \text{ cm}^{-3}$ to $U = 1 \times 10^{-2}$ for $\mathrm{n_H} = 12 \text{ cm}^{-3}$.

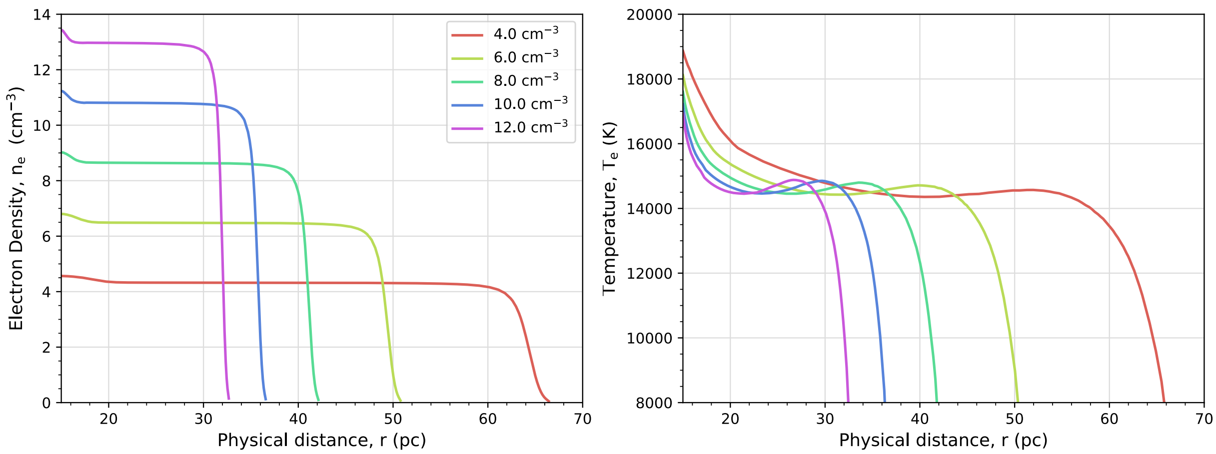

Figure 3.8: The electron temperature and density for the constant density `Cloudy` models as a function of physical distance away from AB7. Colors follow the same scheme as in Figure 3.5.

3.5.5 N76 in context

The N76 nebula is unique for its very luminous central ionizing source, low density ($\sim$10 cm^{-3}), and consequent large ($\sim$40 pc) size. In order to compare it to other HII regions, we examine our results through two difference lenses: observations of the ionized gas in low metallicity dwarf galaxies, and in-depth studies of WR nebulae.

3.5.5.1 Comparison with other low metallicity systems

The largest study focused on understanding the properties of the mid-infrared transitions from gas in low metallicity systems is the Dwarf Galaxy Survey (DGS), which modeled IR observations of 48 nearby galaxies using `Cloudy` (Cormier et al., 2019, 2015). They find electron densities that range $\mathrm{n_e} = 10^{0.5} - 10^{3.0}\ \mathrm{cm}^{-3}$ and ionization parameters of $\log U = -3.0$ to -0.3 with a correlation such that the highest U values are found in the lowest metallicity galaxies. This trend is also seen in the blue compact dwarf (BCD) galaxies analyzed in Hunt et al. (2010), where they report elevated [NeIII]/[NeII], [SIV]/[SIII], and [OIV]/[SiII] ratios when compared to higher metallicity counterparts, indicative of harder radiation fields at low metallicities. Additionally, Hunt et al. (2010) report electron densities ranging from $\mathrm{n_e} = 30 - 600\ \mathrm{cm^{-3}}$ through the [SIII] 18 μm/ [SIII] 33 μm ratio. These two programs focused on analyzing spatially unresolved infrared spectroscopy of galaxy-wide measurements in order to form conclusions about the global ionized gas properties in dwarf galaxies. With a metallicity of 12 + log(O/H) $\sim$ 8.0, N76, as part of the SMC, falls at the median of the metallicity ranges investigated in these studies. Interestingly, our resolved measurements of a single HII region are well in the range of the globally integrated properties determined by these surveys, although the electron density in N76 is at the lower boundary found in these studies.

We also compare N76 to photoionization modeling studies of nearby dwarf galaxies that are more spatially resolved than those in the previous paragraph. To be consistent, all of these studies are done using similar IR spectroscopic observations and modeled with the `Cloudy` photoionization code. Indebetouw et al. (2009) model 30 Doradus in the Large Magellanic Cloud (LMC), the largest supergiant HII region in the nearby universe. They find a relatively high electron density, $n_e = 10^{2.4} - 10^{2.7}\ \mathrm{cm^{-3}}$, and a hard radiation field with $\log U = -1.7 \text{ to} - 1.3$. Similarly, Polles et al. (2019) investigates the ionized gas in five individual star-forming clumps in IC10, and their `Cloudy` modeling indicates $n_e = 10^{2.0} - 10^{2.6}\ \mathrm{cm^{-3}}$ and $\log U = -3.8 \text{ to} - 1.0$. Lastly, Dimaratos et al. (2015) focus their study on NGC 4214 and identify a separate central and southern star forming region, calculating lower densities of $n_e = 440$ and $n_e = 170$, respectively, and ionization parameters of $U = -2.3$ and $U = 170$. Taken as a whole, N76 has a lower electron density than found in those objects, but a comparable ionization parameter.

In order to summarize the infrared `Cloudy` modeling results across these different surveys and studies, we plot the [NeIII] 15 μm/ [NeII] 12 μm and the `Cloudy` model ionization parameter, U, in Figure 3.9. This ratio traces the intensity of the radiation field and, in principle for a single main sequence star hardness should correlate well with U. We also plot a summary of the [NeIII] 15 μm/ [NeII] 12 μm ratio from a sample of high metallicity galaxies (Dale et al., 2009; Inami et al., 2013). While these analyses did not produce an ionization parameter, we do show their range in [NeIII] 15 μm/ [NeII] 12 μm line ratio. We confirm that the higher metallicity galaxies have a much lower [NeIII] 15 μm/ [NeII] 12 μm line ratio than the low metallicity systems. N76 and 30 Doradus are at the upper end of the observed line ratio, with [NeIII] 15 μm/ [NeII] 12 μm $\sim$ 10-15, indicating hard radiation fields in these HII regions. Two galaxies with integrated measurements, IIZw40 and UM461, have radiation fields that may be harder, with a [NeIII] 15 μm/ [NeII] 12 μm $\sim$ 20-25. When examining scales of $\sim$200 pc, (Cormier et al., 2019) find evidence of additional, low ionization components of ionized gas from their `Cloudy` models. Similarly, Polles et al. (2019) and Dimaratos et al. (2015) find excess emission of [NeII] that they attribute to a diffuse ionized gas component. In N76, our `Cloudy` models also underpredict [NeII], providing more evidence for an additional low ionization source that fuels the diffuse ionized gas in these galaxies.

3.5.5.2 Comparison with other Wolf-Rayet nebulae

Most well-studied WR nebula are defined as bubble nebulae, characterized by thin ionized shell covering a large cavity, excavated by the strong stellar winds of the central WR star. Optical IFU measurements of the Milky Way WR nebula NGC 6888 show a three-shell structure centered around a 400 pc evacuated cavity: an elliptical inner broken shell formed by shocks from interactions between the WR and supergiant winds, an outer spherical shell that represents

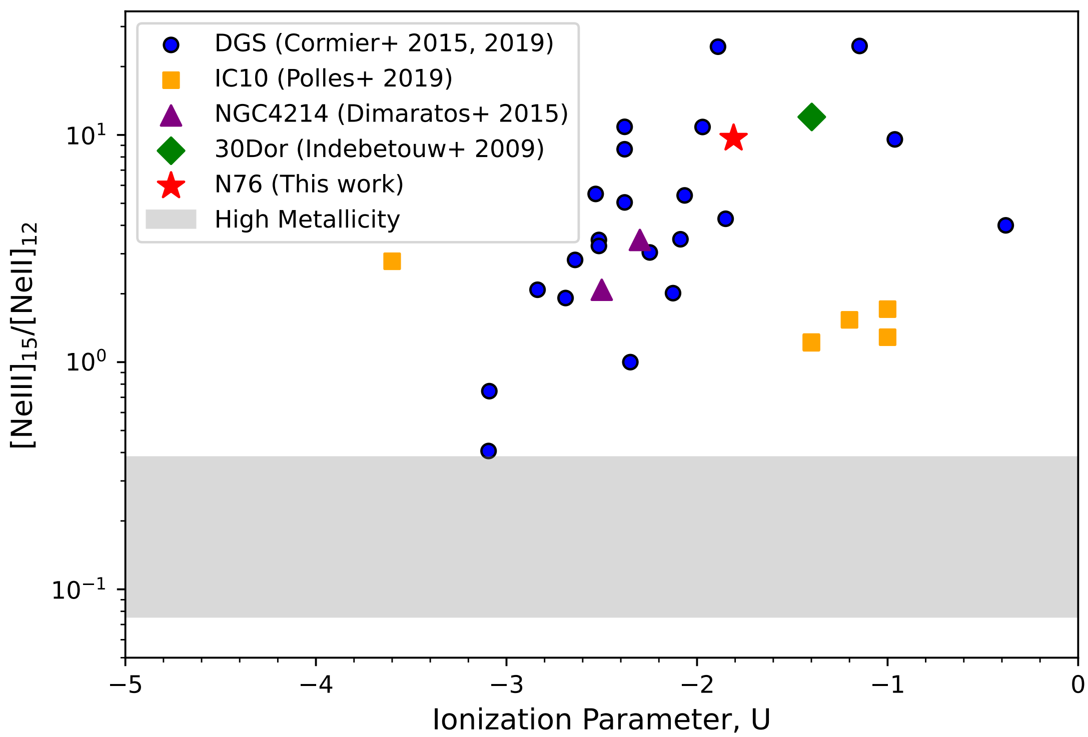

Figure 3.9: Comparing the [NeIII] 15 μm/ [NeII] 12 μm ratio to the ionization parameter of a variety of low metallicity systems, including the Dwarf Galaxy Survey (Cormier et al., 2019, 2015), IC10 (Polles et al., 2019), NGC 4214 (Dimaratos et al., 2015), 30 Doradus (Indebetouw et al., 2009), and N76 (this work). These studies include a mixture of integrated data from entire galaxies (DGS), to individual measurements in divided regions of these galaxies (IC10 and NGC 4214), to single HII regions (N76 and 30 Dor). Overall, the [NeIII] 15 μm/ [NeII] 12 μm ratio shows that the low metallicity systems plotted have much harder radiation fields than the averages shown for the higher metallicity galaxies from Dale et al. (2009) and Inami et al. (2013).

the wind-blown bubble, and a skin of ISM material surrounding the nebula (Fernández-Martín et al., 2012). Through photoionization modeling, Fernández-Martín et al. (2012) calculate an electron density of $n_e = 400\ \mathrm{cm}^{-3}$ for the outer wind-blown bubble shell. Infrared spectroscopy described in Rubio et al. (2020) characterize NGC 6888 further, corroborating the density found for the outer shell in Fernández-Martín et al. (2012) and identifying the density of the ISM skin as $n_e = 180\ \mathrm{cm}^{-3}$.

The overall morphological picture of NGC 6888 is not dissimilar to that of N76: a wind-shocked inner cavity caused by the powerful stellar winds of the WR star that transitions into a photoionized gas region and the surrounding ISM. However, N76 has a much smaller cavity (15 pc in our models compared to 400 pc), a lower density photoionized region with $n_e = 10\ \mathrm{cm}^{-3}$, and this photoionized shell is rather thick compared to the cavity size (35 pc). These differences may be related to the age of N76. Shenar et al. (2016) estimates that AB7 is 5.4 Myr old, and the size of a stellar wind-blown bubble directly correlates with its age (Freyer et al., 2003, 2006; Weaver et al., 1977). Observations of WR nebulae in the LMC show the traditional bubble structure, i.e. a large cavity with a thin, photoionized shell of material in the majority of nebulae (Hung et al., 2021). Future investigation of N76 and a larger sample size of well-studied comparison WR nebulae are needed in order to understand the significance of these measurements.

Since the regions around WR nebulae contain material blown off by the powerful stellar winds of the star, their abundances can be enhanced, yielding elevated nitrogen abundances in those with a central a WN star (e.g. Fernández-Martín et al., 2012; Stock & Barlow, 2014). AB7 contains a WN4 type star, but we do not have a nitrogen spectral line to probe the nitrogen abundance. The abundances described in Table 3.1 do a satisfactory job of predicting the emission line surface brightness so we do not have evidence of elemental enhancement in N76. Optical spectroscopy of N76 by Nazé et al. (2003), however, show a 40% elevated N/O ratio compared to global SMC values, suggesting that the chemical make up of N76 is influenced by AB7.

3.6 Summary and Conclusions

We use *Spitzer* IRS spectroscopic maps of mid-infrared transitions and `Cloudy` to model the photoionization in the HII region N76 in the Small Magellanic Cloud. The ionization source is AB7, a binary composed of a WN4 nitrogen-rich Wolf-Rayet and an O6 I supergiant star, and we use PoWR models (Todt et al., 2015) to estimate its SED and luminosity (Shenar et al., 2016). AB7 contains one of the hottest WR stars in the SMC. We assume the N76 nebula is spherically shaped and project the predicted `Cloudy` line surface brightness as a function of distance to the source on the plane of the sky. We only consider emission from the ionized gas. The results from the photoionization models match the spatially resolved images of intermediately ionized emission lines measured from *Spitzer* IRS and *Herschel* PACS observations fairly well, with just density as the free parameter. Our conclusions are as follows:

1. Comparing the models to the observed spatial distribution of the measured emission line brightness allows us to determine much more precise densities than just using the total line intensity (Figure 3.5 and Table 3.2).
2. Constant density `Cloudy` photoionization models reproduce most of the ionized gas emission line intensity distributions ([SIII], [NeIII], [SIV], and [OIII]) for a narrow hydrogen density between $\mathrm{n_H} = 4\ \mathrm{cm^{-3}} - 12\ \mathrm{cm^{-3}}$ (Figure 3.1).
3. The intensities of the high ionization lines, [OIV] and [NeV], cannot be explained by pho-

toionization. We postulate that these ions are produced by shock ionization in the wind-blown portion of the WR nebula (see also Freyer et al., 2003, 2006; Weaver et al., 1977) or a harder ionizing SED for the central source (e.g. Crowther et al., 1999; Schaerer & Stasińska, 1999; Schaerer & Vacca, 1998). To explain the observations requires a 15 pc in radius wind shocked cavity in the center of N76.

4. The neutral-dominated emission lines (lines coming from ionic species with an ionization potential less than hydrogen, 13.6 eV), can originate from both the ionized gas and the neutral gas. Our modeling finds that very little of the observed [CII] and [OI] emission comes from the ionized gas ($< 5\%$), while most (96%) of the [SiII] emission can be produced in the HII region.

5. The [NeII] line is under-predicted in our `Cloudy` models, suggesting the excess emission may arise from the diffuse ionized gas not associated with N76 (e.g. Cormier et al., 2019; Dimaratos et al., 2015; Polles et al., 2019).

6. We observe a line at 25.25 μm that we identify as [SI] in the high ionization zone of the N76 nebula (see Figure 3.1). We explore possible causes for [SI] and alternative possibilities for the line in §3.5.2, including the possibility of producing neutral sulphur from dust destruction. None of these satisfactorily explains the line.

7. Low metallicity galaxies have harder radiation fields than their higher metallicity counterparts. The N76 region has a harder radiation source than most other low-metallicity regions with analyzed mid-IR spectroscopy, although its ionization parameter falls close to the center of the observed range (see Figure 3.9).

Chapter 4: ALMA/ACA Mapping of the Northern Molecular Ridge in the LMC

4.1 Introduction

Molecular clouds host the bulk of molecular gas in galaxies and are the sites of star formation. The evolution and collapse of molecular clouds into stars is a complex process that is related to the kinematics and turbulence in the cloud (McKee & Ostriker, 2007). The properties of molecular clouds, such as their sizes, velocity dispersions, and masses, are described by scaling relations over several orders of magnitude (Larson, 1981). Solomon et al. (1987) found that the radius of a molecular clouds in the Milky Way, R, and their velocity dispersions, σ_v, follow a powerlaw distribution of $\sigma_v \propto R^{0.5}$. Repeated observations of giant molecular clouds (GMCs) outside of the Milky Way find similar correlations with only slight variations of the normalization factor and powerlaw index, suggesting the universality of these scaling relations (e.g., Bolatto et al., 2007; Hughes et al., 2010; Rosolowsky et al., 2021; Schruba et al., 2017; Wong et al., 2019).

Later follow up observations of Milky Way clouds that include the optically thin $^{13}\mathrm{CO}(1-0)$ emission in Heyer et al. (2009) find a related correlation between the normalization of the size-linewidth relation, $\sigma_v/R^{1/2}$, and the mass surface density calculated through the ^{13}CO optical depth, $\Sigma = M/R^2$. This linear relationship is interpreted as the clouds being in virial equilibrium where the kinematic mass, $\Sigma_{\rm vir} \propto \sigma_v/R^{1/2}$, is approximately equal to the luminous mass Σ (Roman-Duval et al., 2010). Some of these clouds have elevated $\Sigma = M/R^2$ values that Field et al. (2011) suggests are due to an external pressure exerted on the clouds. In order to stay in equilibrium, the external pressure can drive additional kinematic turbulence for a given mass density. An alternative explanation proposed by Ballesteros-Paredes et al. (2011) is that the clouds are in free-fall instead of virial equilibrium, which would increase $\sigma_v/R^{1/2}$ by a factor of two and is more in-line with the observations. Of course, there may also be systematic uncertainties in the observations and the clouds are physically virialized.

Nevertheless, characterizing the properties of molecular clouds and determining their $\Sigma_{\rm vir}$ and Σ is used to establish whether external pressures are exerted on molecular clouds. The pressure may originate from stellar feedback due to expanding HII regions, stellar winds, or supernovae (see Krumholz et al., 2019, for a recent review). For example, multiple CO observations in the supergiant HII region 30 Doradus in the Large Magellanic Cloud show elevated linewidths, indicating energy injection into the molecular clouds from the surrounding star formation (Indebetouw et al., 2013, 2020; Nayak et al., 2016; Wong et al., 2022). Further, observations of molecular gas in the interacting antennae galaxies suggest an external pressure of $P/k \gtrsim 10^8$ K cm^{-3}, many orders of magnitude higher than typical interstellar pressures (Finn et al., 2019; Johnson et al., 2015). Most of these studies, however, have focused on small fields of view in highly energetic environments. In order to understand the role of stellar feedback on the properties of extragalactic molecular clouds a large, high resolution map is needed.

Our target for this study is the northern-most region of the molecular ridge in the Large Magellanic Cloud. This region hosts the largest accumulation of CO in the LMC (Cohen et al., 1988; Fukui et al., 2008; Kutner et al., 1997; Mizuno et al., 2001) and at a distance of ~50 pc (Pietrzyński et al., 2019), the molecular ridge provides an ideal environment to study the interaction between star formation and molecular cloud properties. The northern most portion of this $\sim$ 2kpc feature hosts three bright HII regions from north to south $-$N158, N160, and N159$-$ while the southern portion is quiescent with little high mass star formation (see Figure 4.1, Finn et al., 2021; Indebetouw et al., 2008). The three HII regions in the northern molecular ridge are just south of the supergiant HII region 30 Dor (Figure 4.1). de Boer et al. (1998) suggests that these HII regions have a combined origin triggered by ram pressure compression between the interaction of the LMC and the hot Galactic halo. Alternatively, high resolution ALMA CO observations near the N159 region show evidence that colliding filaments produce high mass protostars in this area (Fukui et al., 2015, 2019; Saigo et al., 2017; Tokuda et al., 2022) and there is some evidence that HI gas flows triggering star formation exist on large scales (Fukui et al., 2017).

We present a large ($10' \times 26'$, 150×380 pc^2), high resolution (1.7 pc) ALMA ACA ^{12}CO$(2-1)$ and ^{13}CO$(2-1)$ maps of the northern molecular ridge in the LMC to study the properties of the molecular clouds and determine whether feedback from the surrounding star formation impacts the kinematics of the clouds. In §4.2, we present the ^{12}CO$(2-1)$ and ^{13}CO$(2-1)$ ALMA ACA data and describe how we image the data and stitch together the large mosaic of the northern molecular ridge. We then outline how we calculated the molecular gas column density through the ^{13}CO line and describe our methods for decomposing the molecular gas into discrete structures in §4.3. We present the size-linewidth correlation and the mass surface density boundedness relation in §4.4. We determine whether the clouds are bound in §4.5 and compare their virial parameters to the 8 μm flux that tracers the star formation. Lastly, in §4.6 we summarize our results and outline our conclusions.

4.2 Observations

4.2.1 ALMA $^{12}\mathrm{CO}(2-1)$ and $^{13}\mathrm{CO}(2-1)$ Data

The northern molecular ridge was observed with the Atacama Large Millimeter/Submillimeter Array (ALMA) Atacama Compact Array (ACA), also known as the Morita array. These observations were part of Cycle 7, under project code 2018.A.00061.S (PI: Bolatto, A). The map covers a region of 10’$'\times$ 26$'$ (150 $\times$ 380 pc) across the northern tip of the molecular ridge in the LMC, overlapping with three HII regions: N158, N160, and N159 (see Figure 4.1 for placement of region within the LMC). The map is comprised of sixteen individual 10’ $\times$ 2.3’ overlapping tiles of separate observations. One frequency setting was configured to cover the $^{12}\mathrm{CO}(2-1)$ line at 230.538 GHz with a bandwidth of 125 MHz and a channel width of 61 kHz. The second frequency setting covered both $^{13}\mathrm{CO}(2-1)$ at 220.399 GHz and $\mathrm{C}^{18}\mathrm{O}(2-1)$ at 219.560 GHz with bandwidths of 62.5 MHz and a channel width of 61 kHz. We also included a broader continuum frequency set up centered at 232.6 GHz with a bandwidth of 2 GHz. These observations include total power ALMA data corresponding to the full rectangular region covering the interferometric map produced on October 15th, 2019, providing short spacings information.

4.2.1.1 Imaging the Combined ACA and TP Data

We use version 6.5.1 of the Common Astronomy Software Applications (The CASA Team et al., 2022) and the standard system calibration to image the northern molecular ridge data. We image each of the sixteen individual tiles that comprise the final map separately and stitch them together in a separate step (see §4.2.1.2). Imaging each tile separately provides higher

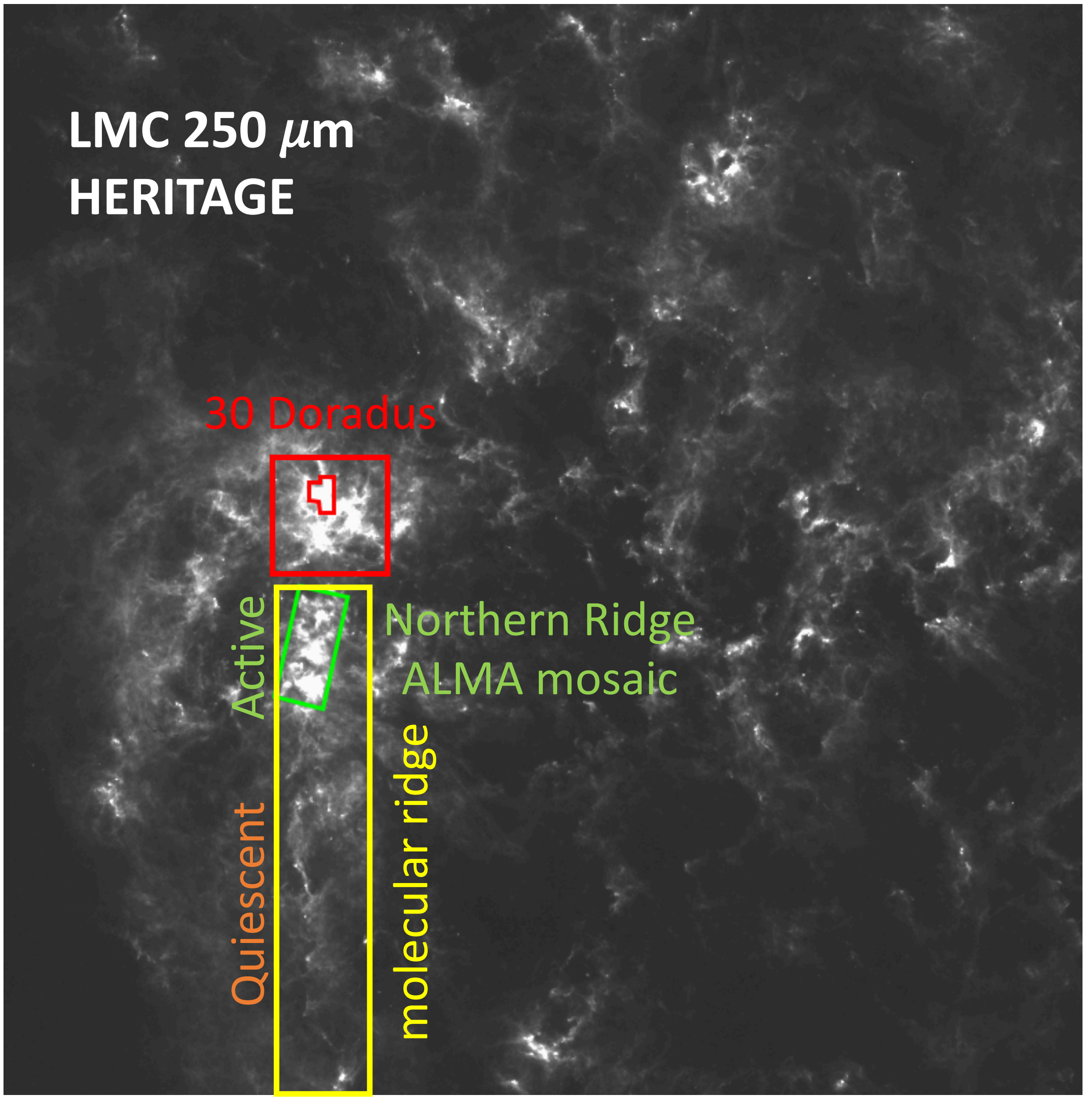

Figure 4.1: The LMC with the molecular ridge highlighted in yellow and the supergiant HII region, 30 Doradus (30 Dor) outlined in red. The ALMA ACA mosaic of the active, northern molecular ridge is in green. The gray scale background is the *Herschel* PACS 250 μm emission from the HERITAGE survey (Meixner et al., 2013). The molecular ridge contains the largest accumulation of gas in the LMC. We study the active region to determine how the properties of molecular clouds are affected by the surrounding star formation.

stability and convergence in the deconvolution algorithm (see also Leroy et al., 2021). For the spectral line data, we use the CASA task `sdint` to image and combine the ACA and TP data. The *sdint* algorithm is a joint deconvolution algorithm that simultaneously images and combines interferometric and single dish data (Rau et al., 2019). We find that the *sdint* algorithm produces better results than the traditional `tclean` and `feather` method. Each tile has a square pixel cell size of $1''.2$, a velocity channel of 0.25 $\mathrm{km\,s^{-1}}$, and a total size of 600 $\times$ 300 pixels. We choose 320 channels which corresponds to the maximum size of the bandwidth for the $^{13}\mathrm{CO}(2-1)$ and $\mathrm{C^{18}O}(2-1)$ data. We use a cleaning threshold of 0.3 Jy/beam and a *cyclefactor=5* in order to make sure the cleaning algorithm doesn't diverge before it reaches the threshold. We use the mosaic gridder, hogbom deconvolver, and briggs weighting with *robust = 0.5*, which provides the bet combination of resolution and signal-to-noise. We mask the data for cleaning through the `auto-multithresh` and the default parameters. The interferometric data are combined with the total power data using an *sdgain=3*, which preserves the flux information from the total power data while mantaining the high resolution structure. We convolved the datacubes to a common restoring beam of $7''$ (1.7 pc).

4.2.1.2 Stitching of the Northern Molecular Ridge Tiles

Due to the large size of the northern molecular ridge map and the limitations of ALMA scheduling, the full map needed to be separated into sixteen individual observations that are stitched together. ALMA observed these tiles in a different times of the year and they consequently have different $u-v$ coverage, weather conditions, and synthesized beams, making it challenging to image the full mosaic at once. After imaging and combining each tile with the TP data in §4.2.1.1, we stitch these tiles together using the Python `astropy` package `reproject`[1] and following the procedure in Leroy et al. (2021). First, we identify an astronomical grid that covers the full mosaic map of the northern molecular ridge and regrid each tile onto this template. We then combine all of the components of the mosaic into a single image by weighting the primary beam response and the rms noise to the intensity:

$$I = \frac{\sum_{i=0}^{n} (B_i^2 \sigma_i^{-2}) \times I_i}{\sum_{i=0}^{n} B_i^2 \sigma_i^{-2}}. \tag{4.1}$$

The total intensity for the full map is given by I and the sum over i represents the sum over all overlapping positions on the mosaic. The primary beam response is given as B and the rms noise is σ. Since each tile has different weather conditions, the rms noise varies based on position on the map from 0.12 - 0.22 Jy beam^{-1}. We compute a noise map for each tile individually by calculating the rms of a spectrum in the first and last 30 channels of the cube where there is no emission. Lastly, the final map of the northern molecular ridge is combined through the `reproject_and_coadd` function.

4.2.1.3 Continuum subtraction

In addition to the spectral line cubes, we also produce a continuum image at 1.3 mm (230 GHz). We use the procedure described above to image the continuum except we do not combine the TP data with the interferometric continuum data. Instead, we use the CASA task `tclean` in MFS mode, a threshold value of 2mJy, and a central reference frequency of 232.6 GHz. The map of the continuum emission in the northern molecular ridge is reported in Appendix B.

[1]`https://reproject.readthedocs.io/en/stable/`

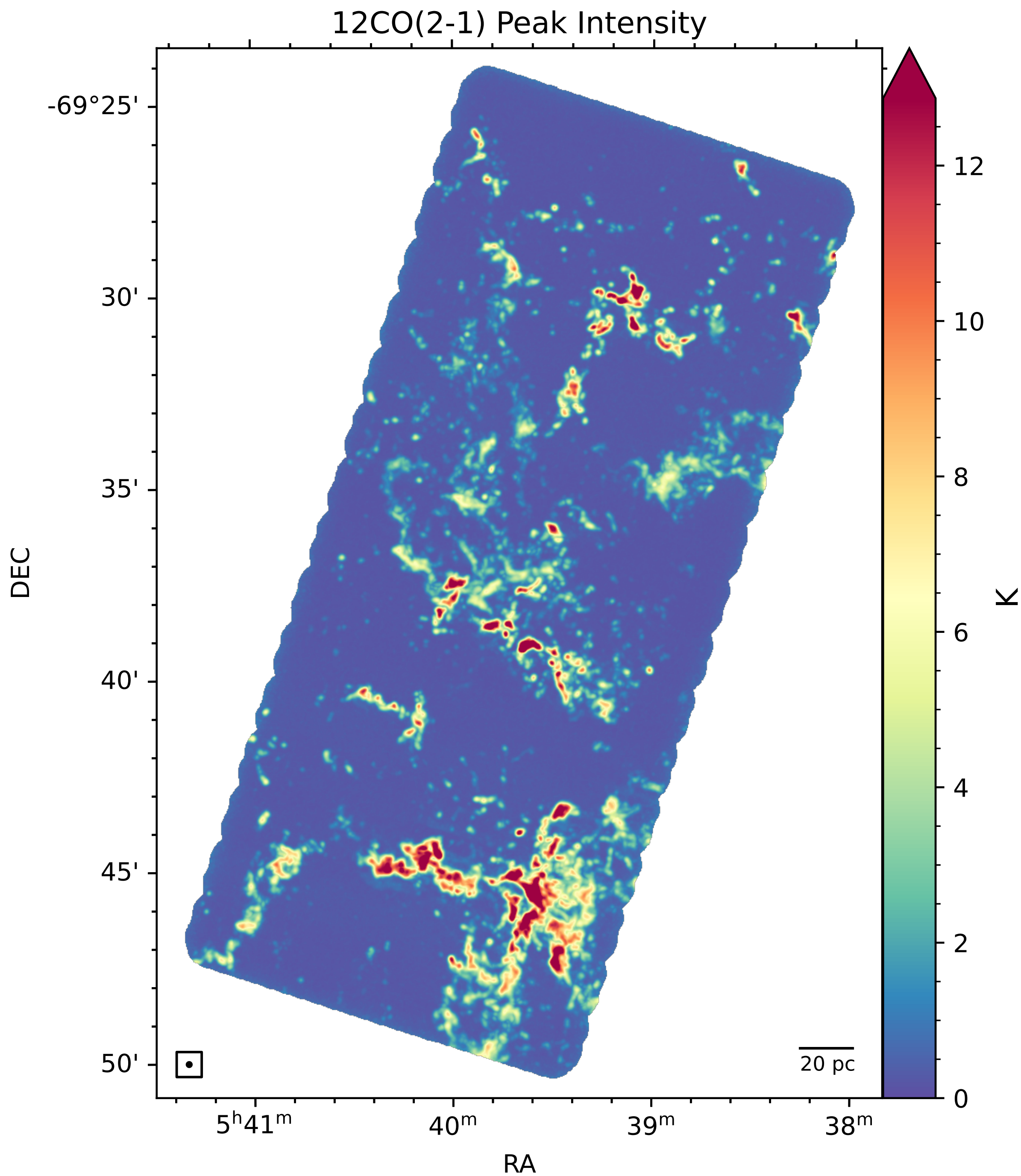

Figure 4.2: The peak intensity map of our ALMA ACA mosaic of the northern molecular ridge in $^{12}\mathrm{CO}(2-1)$. The physical scale of the map is 10' × 26' (150 × 380 pc) and the beam size, pictured in the bottom left corner, is 7″ (1.7 pc). The molecular gas as traced by $^{12}\mathrm{CO}(2-1)$ contains substantial structure, many hundreds of molecular clouds, and large filament-like features.

The continuum sources in the northern molecular ridge are very faint and contain emission from a combination of dust and free-free emission (e.g. Brunetti & Wilson, 2019). Separating out the dominant source of emission requires continuum observations at another frequency and goes beyond the scope of this work. These faint continuum sources may contribute to flux in our emission line datacubes, however. In order to isolate and remove this contribution, we create a mask that includes all of the continuum sources and apply it to our $^{12}\mathrm{CO}(2-1)$, $^{13}\mathrm{CO}(2-1)$, and $\mathrm{C}^{18}\mathrm{O}(2-1)$ datacubes. For the spaxels that overlap with continuum sources, we fit a first order polynomial to the baseline and subtract it from the datacube image.

These continuum subtracted datacubes of the northern molecular ridge are used for the rest of the analysis in this paper. The peak brightness temperature of the $^{12}\mathrm{CO}(2-1)$ mosaic is presented in Figure 4.2. These data contain large scale structure and thousands of individual molecular clouds that we will analyze further in this chapter. This work focuses on the $^{12}\mathrm{CO}(2-1)$ and $^{13}\mathrm{CO}(2-1)$ data.

4.2.2 IR 8μm data

We use previously published 8 μm data from the *Spitzer* Legacy program Spitzer Survey of the Large Magellanic Cloud (SAGE, Meixner et al., 2006) as a measure of the star formation activity in the molecular clouds traced by the ALMA data. We use the 2″-pixel, point source subtracted residual images. The point source subtraction lead to some undefined values in the mosaic which we interpolated over to have pixel values for each point. We download the 2″ IRAC 8 μm PSF[2] and match it to a 7″ Gaussian to match the pixel scale of the northern molecular ridge

[2] https://irsa.ipac.caltech.edu/data/SPITZER/docs/irac/calibrationfiles/psfprf/

CO data.

4.3 Methods

4.3.1 Line Intensity Maps

The integrated intensity maps of $^{13}\mathrm{CO}(2-1)$ and $^{12}\mathrm{CO}(2-1)$ are presented in Figures 4.3 and 4.4, respectively. We also present contours of the $^{12}\mathrm{CO}$ integrated intensity overlayed on top of a 3-color RGB optical image in Figure 4.5. We generate masks for the integrated intensity images by requiring a 3σ detection in three adjacent channels across the map. The rms noise, σ, is defined as a function of spatial position due to the variation in tiles (see §4.2.1.2) and ranges from 0.07 K - 0.11 in the centers of the tiles, increasing to an RMS of 0.2 K at the edges. The intensity images are produced by summing the masked data across the velocity axis. The masking procedure consistently rejects emission due to noise while also preserving extended, diffuse structures.

The $^{12}\mathrm{CO}$ and $^{13}\mathrm{CO}$ images of the northern molecular ridge contain a wealth of structure and filamentary features. While many of the clouds are loosely associated with the HII regions pictured in Figure 4.5, some of the filamentary features correspond to areas of extinction and areas that have not yet formed stars.

4.3.2 HII Region Boundaries

The northern molecular ridge encompasses three active HII regions in addition to gas clouds that appear unassociated with these active areas of star formation. Dividing our analysis based on the the molecular gas that is spatially coincident with these active regions can provide insight

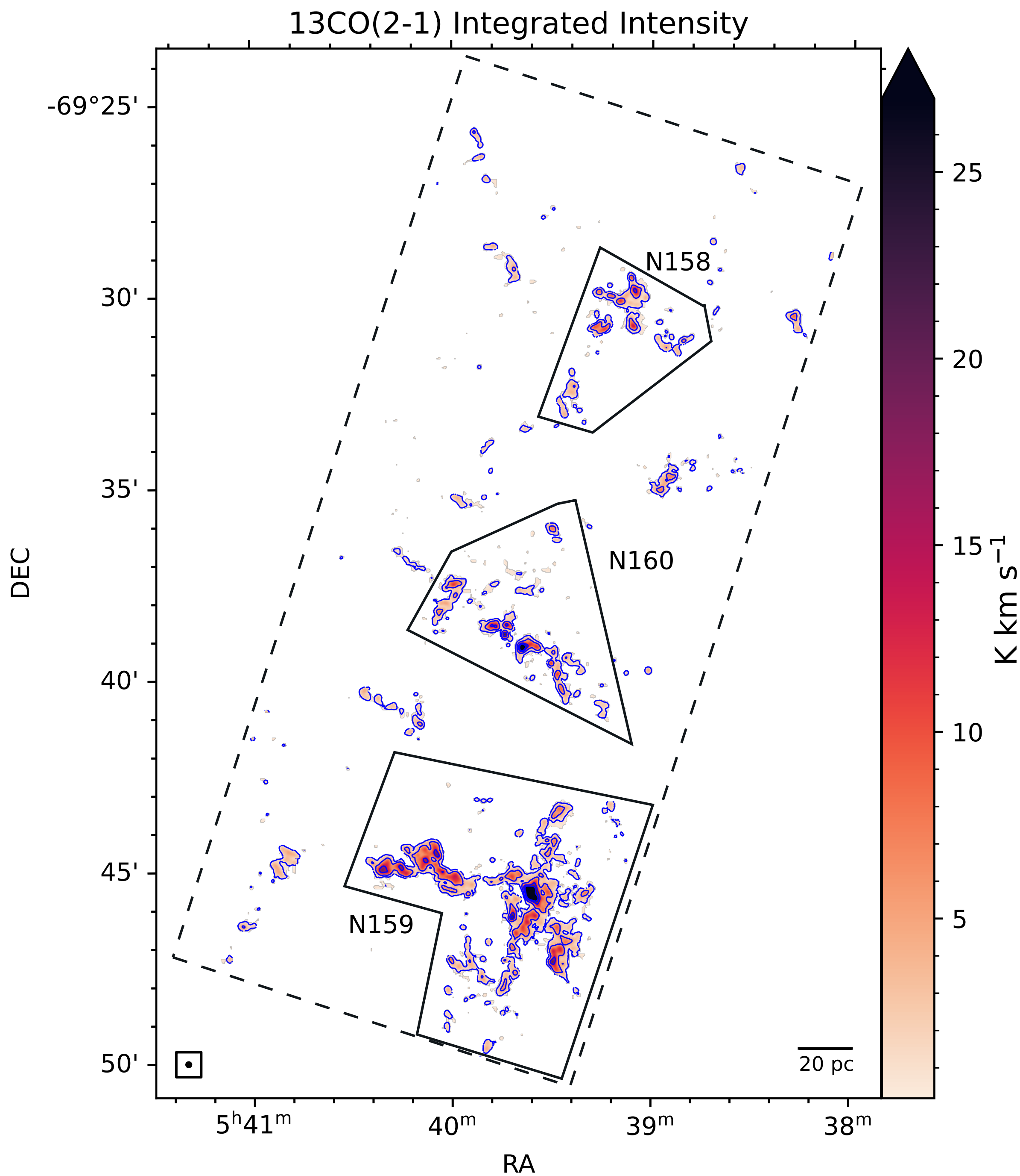

Figure 4.3: The $^{13}\mathrm{CO}(2-1)$ masked integrated intensity map with contour levels of 1, 5, 15, and 25 K $\mathrm{km\,s^{-1}}$. The beam size is given in the lower left and the outline of the mosaic is shown in the dashed black line. The outline of molecular gas associated with the three HII regions, N158, N160, and N159 are reported and defined through identifying the bulk molecular gas surrounding an HII region and including clumps of gas that have similar velocity centroids.

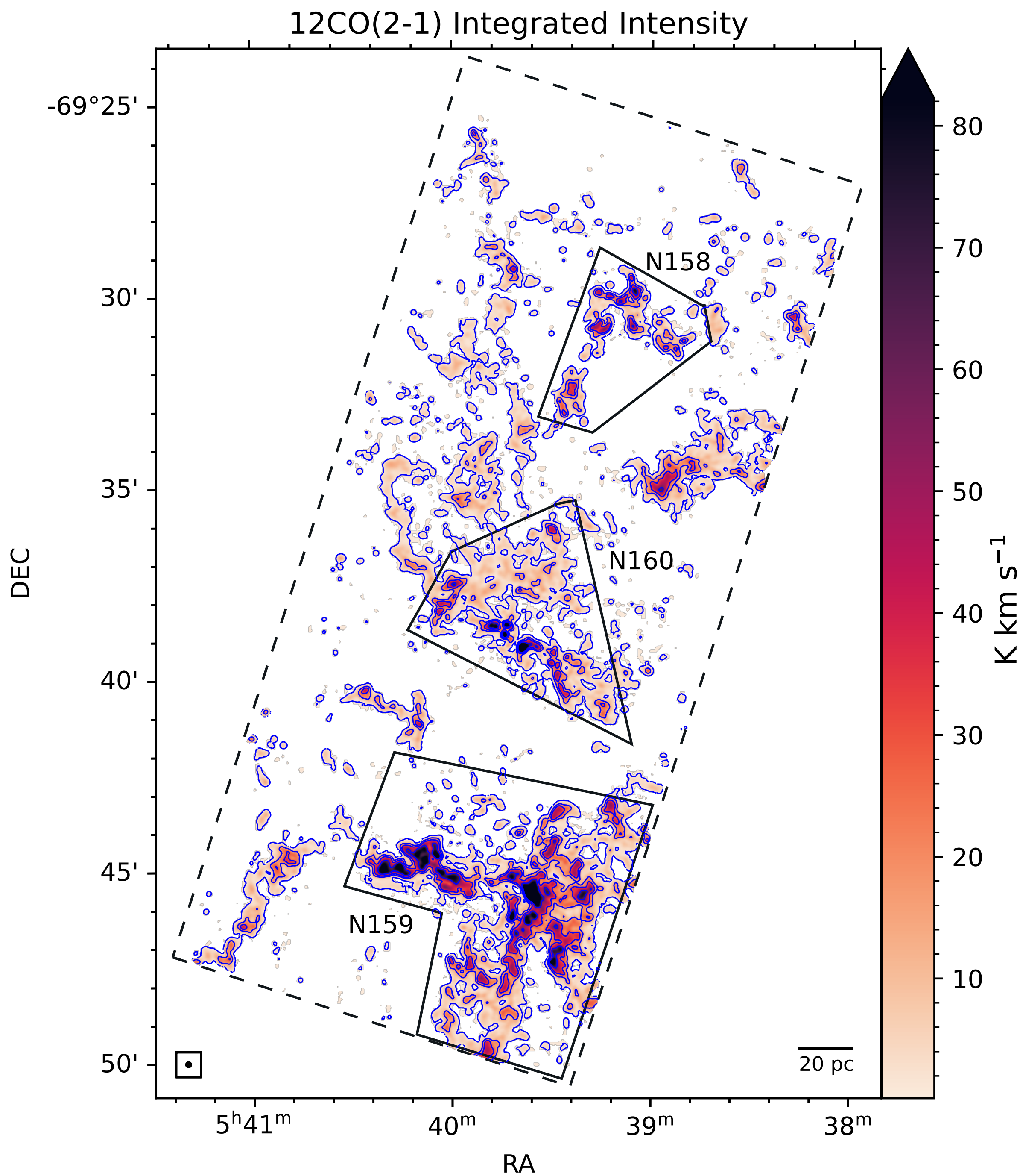

Figure 4.4: The $^{12}\mathrm{CO}(2-1)$ masked integrated intensity map with contour levels of 1.5, 15, 30, 60 K km s^{-1}. The plot symbols are the same as in Figure 4.3.

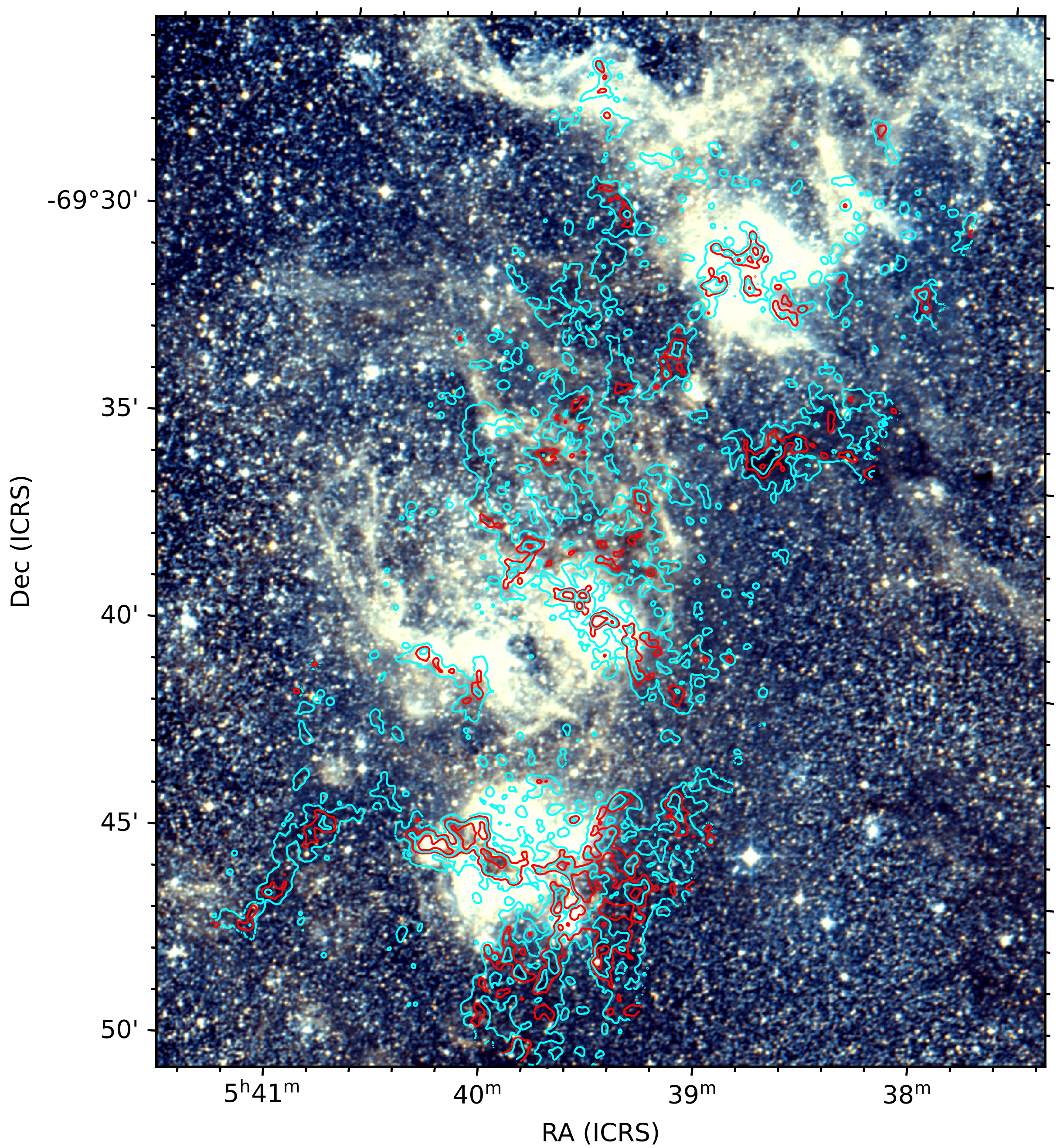

Figure 4.5: The Digitized Sky Survey (DSS, Lasker, 1994) image of the northern molecular ridge, which features the three HII regions, N158, N160, and N159. We present the $^{12}\mathrm{CO}(2-1)$ contour levels from Figure 4.4 in alternating cyan and red contours to increase contrast for the viewer. Most of the molecular gas is loosely associated with these HII regions.

on how the environmental conditions may be affecting the molecular clouds. Because we have an abundant amount of molecular clouds throughout the map, defining discrete boundaries for the HII regions is subjective. We define the boundaries by examining the HII region location in Figure 4.5 and identifying the overlapping bulk of the molecular material. We also include nearby structures that have similar velocity centroids, indicative of gas that is also associated with the HII region. The boundaries we use for the HII region are given by the black polygons in Figures 4.3 and 4.4. We refer to molecular gas that is outside of these regions as belonging in the "Ridge".

4.3.3 Column Densities and LTE Analysis

We assume local thermal equilibrium (LTE) to calculate column densities of the molecular gas that have significant ^{13}CO emission. We use the 3σ in three adjacent channels mask described in §4.3.1 to calculate the ^{13}CO line opacity and subsequent column density. This analysis assumes that the ^{12}CO line is optically thick at its center, the ^{13}CO line traces optically thin molecular gas, and that both lines have a similar excitation temperature that is characterized by the ^{12}CO emission (e.g., Nishimura et al., 2015). Following the analysis in Wong et al. (2019), the $^{12}\mathrm{CO}(2-1)$ peak temperature, $T_{12,\mathrm{pk}}$, is related to the excitation temperature, T_{ex} through (Bourke et al., 1997):

$$J(T_{\mathrm{ex}}) = f_{\mathrm{bm}}^{-1} T_{12,\mathrm{pk}} + J(T_{\mathrm{CMB}}) \tag{4.2}$$

where the beam filling fraction, f_{bm}^{-1}, is assumed to be 1 for a negligible beam dilution. The planck function is:

$$J(T) = \frac{h\nu/k}{\exp(h\nu/kT) - 1}. \tag{4.3}$$

Using the frequency of the $^{12}\mathrm{CO}(2-1)$ line and a temperature of 2.7 K for the CMB, the excitation temperature is calculated to be:

$$T_{\mathrm{ex}}[K] = 11.06 \left[\ln \left(1 + \frac{11.06}{T_{12,\mathrm{pk}} + 0.187} \right) \right]. \tag{4.4}$$

The brightness temperature of the $^{13}\mathrm{CO}(2-1)$ line is related to the $^{13}\mathrm{CO}$ optical depth through:

$$T_{13} = f_{\mathrm{bm}}[J(T_{\mathrm{ex}}) - J(T_{\mathrm{CMB}})][1 - \exp(-\tau_{13})]. \tag{4.5}$$

We assume a negligible beam dilution factor ($f_{\mathrm{bm}} = 1$) and Equation 4.2 to solve for the optical depth of the $^{13}\mathrm{CO}$ line at each position and velocity in the cube:

$$\tau_{13} = -\ln \left[1 - \frac{T_{13}}{T_{12,\mathrm{pk}}} \right]. \tag{4.6}$$

With this formalism, the $^{13}\mathrm{CO}$ optical depth can become undefined for certain combinations of T_{13} and T_{ex}. We assume that the beam dilution factor $f_{\mathrm{bm}} = 1$, but that is not always the case. A smaller beam dilution factor, $f_{\mathrm{bm}} < 1$, can lead to faint $^{13}\mathrm{CO}$ and undefined τ_{13}. Therefore, we impose a minimum floor value for the excitation temperature: $T_{\mathrm{ex,floor}} = 6$ K. The excitation temperatures rarely fall below this level and imposing this floor cutoff affects only 7% of pixels in the map. In the areas it does affect, imposing this floor value corrects for artifacts that correspond to artificially high column densities.

With the determination of T_{ex} and τ_{13} across the datacube, we can now calculate the total

^{13}CO column density in cm^{-2} (Garden et al., 1991):

$$N(^{13}\mathrm{CO}) = \frac{3k}{8\pi^3 B\mu^2} \exp\left[\frac{hBJ(J+1)}{kT_{\mathrm{ex}}}\right] \times \frac{T_{\mathrm{ex}} + hB/3k}{1 - \exp(-h\nu/kT_{\mathrm{ex}})} \frac{\int \tau_{13} dv}{J+1} \tag{4.7}$$

where J is the rotational quantum number of the lower state ($J = 1$), B is the rotational constant for ^{13}CO (55.1 GHz), μ is the dipole moment of ^{13}CO (0.113 debye), and $\int \tau_{13} dv$ is the velocity integrated τ_{13} datacube calculated in Equation 4.6. We derive a molecular hydrogen column density by assuming a constant abundance ratio between ^{13}CO and H_2 of:

$$\frac{N(\mathrm{H}_2)}{N(^{13}\mathrm{CO})} = 3 \times 10^6 \tag{4.8}$$

in order to be consistent with Wong et al. (2019). While the ^{13}CO abundance in the LMC is not well constrained by observations and may vary throughout the galaxy, our chosen value is consistent with those adopted in previous works (Fujii et al., 2014; Heikkilä et al., 1999; Mizuno et al., 2010; Wong et al., 2019, 2022). The molecular hydrogen column density derived from the ^{13}CO optical depth is presented in Figure 4.6. We compare the column density we calculate in N159 to the high resolution (0.3 $''$ $\sim$ 0.07 pc) observations of this region in Fukui et al. (2019) where they find a range of central H_2 column densities of $5 - 30 \times 10^{22}$ cm^{-2}. The column densities we calculate in N159 are slightly lower, with a max column density of 1.3×10^{23} cm^{-2}, which are consistent but lower due to the lower angular resolution of our data.

The molecular clouds of course may not be in LTE and deviations from LTE are a source of systematic uncertainty. Analysis of non-LTE RADEX models by Indebetouw et al. (2020) and O'Neill et al. (2022b) find that the LTE method can underestimate the true ^{13}CO column density by up to a factor of 2 in very cold clouds ($T_k < 10$ K) or overestimate it by a factor of 2 for very dense ($n_{\rm H} > 5000$ cm^{-3}) and warm clouds ($T_k > 10$ K). However, the LTE method is accurate within 25% for column densities that range between $N(\rm H_2) \sim 10^{22} - 10^{24}$, within the parameter space that we explore in this work.

4.3.4 Structural Decomposition

The images of the molecular gas in Figures 4.4 and 4.3 show complex structure and hundreds of molecular clouds. While the molecular gas generally has hierarchical structure across spatial scales, it is very useful to decompose the emission into discrete clouds in order to compare and understand their properties. There are multiple approaches to decompose the molecular gas emission, such as the `clumpfind` algorithm (Williams et al., 1995, 2011), which identifies clouds through local maximum, or through dendrogram structures (Rosolowsky et al., 2008), which assigns isointensity surfaces to a set of hierarchical structures. In this work, we use the python version of `cprops`, originally described in Rosolowsky & Leroy (2006), and contains an updated implementation in python `pycprops`[3] described in detail in Rosolowsky et al. (2021). We briefly summarize the cloud identification algorithm in `pycprops` below.

The `pycprops` code inputs are the molecular gas datacube, a mask that defines the areas of emission in the datacube, and a noise map. The algorithm identifies clouds by searching for local maxima and determines whether the maxima are significant with respect to noise fluctuations. The maxima are compared to the neighboring maximum to see whether they are distinct structures. Emission from the original datacube is then assigned to the local maxima that are defined as unique from their surroundings. The `pycprops` code finds the properties of each cloud, such as the size or linewidth, by calculating the second moment of the emission. The reported

[3]`https://github.com/PhangsTeam/pycprops`

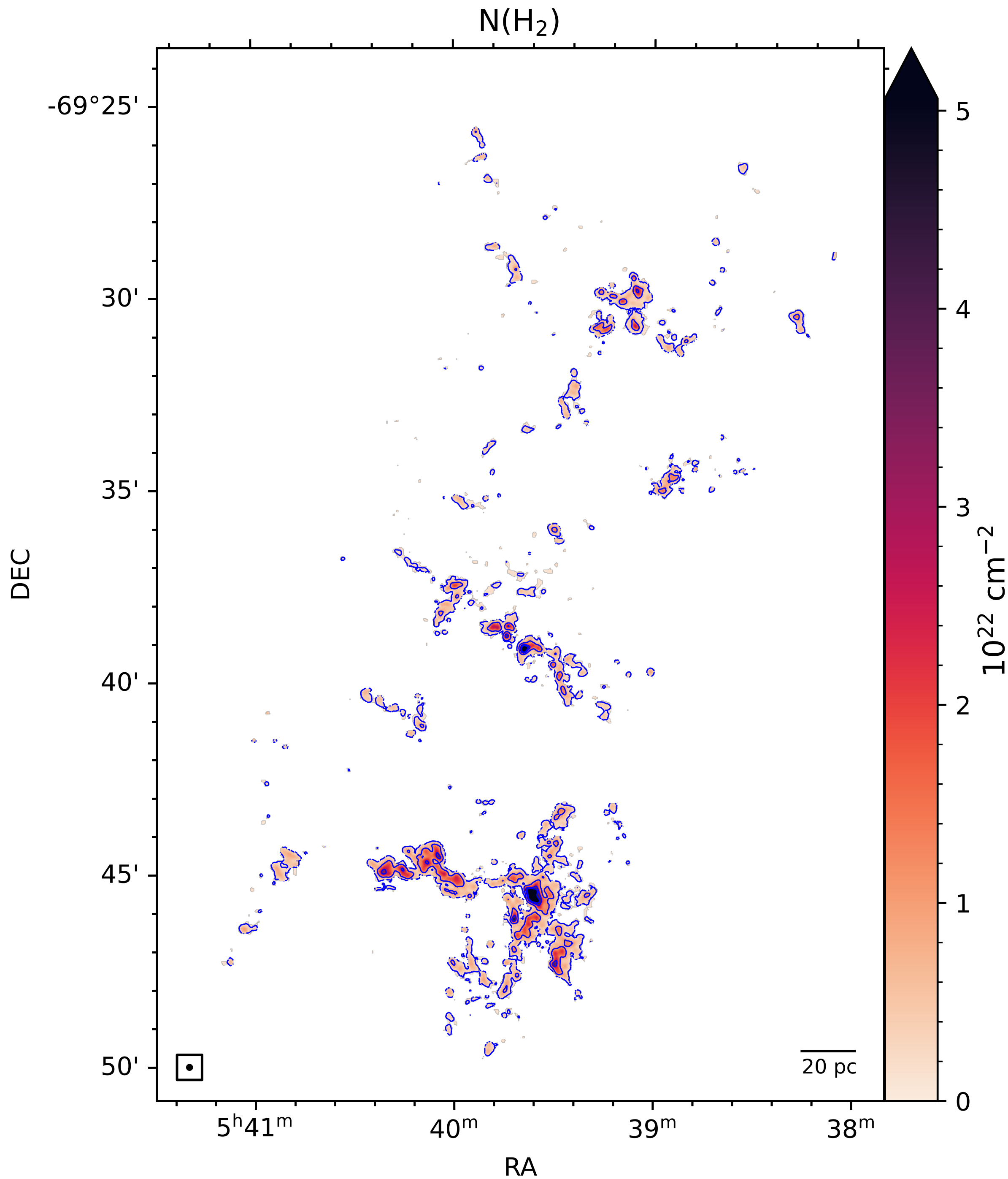

Figure 4.6: The map molecular hydrogen column density, $N(\mathrm{H_2})$, calculated through the optically thin $^{13}\mathrm{CO}$ line and assuming LTE. The contour levels are in 0.2, 1, 3, 5 $\times\ 10^{22}\ \mathrm{cm^{-2}}$. The densest region is near N159 and N160, where $N(\mathrm{H_2}) \sim 10^{23}\ \mathrm{cm^{-2}}$. Given the lower resolution of our data, $N(\mathrm{H_2})$ agrees well with previous observations of N159 and N160 (Bolatto et al., 2000; Fukui et al., 2019).

properties are deconvolved from the Gaussian beam and channel width. The clouds and properties are defined based off of the limited sensitivity of the observations, which can introduce a bias since no clouds can be less than the rms noise. To account for this, the pycprops extrapolates from the measured cloud properties to what would be expected for a 0 K threshold. Lastly, the uncertainties on the properties are given through bootstrapping the data.

For all calculations, we assume a spherical volume density distribution, $\rho(r) = r^{-1}$, that is used by Solomon et al. (1987) and across the molecular cloud literature. The deconvolved radius of each cloud is then:

$$R = 1.91\sqrt{\sigma_{\mathrm{maj,d}}\sigma_{\mathrm{min,d}}} \tag{4.9}$$

where $\sigma_{\mathrm{maj,d}}$ and $\sigma_{\mathrm{min,d}}$ are the beam deconvovled major and minor axes of the cloud. Virial equilibrium is defined by clouds where twice their internal kinetic energy equals their potential energy: $2K + U = 0$. The virial mass is then calculated by Equation 8 in Bolatto et al. (2011):

$$M_{\mathrm{vir}} = \frac{3(5-2k)}{G(3-k)}R\sigma^2 \tag{4.10}$$

where R is the projected radius in pc, σ is the 1D velocity dispersion in $\mathrm{km\,s^{-1}}$, G is the gravitational constant, and k is the power law index for the volume density distribution ($k = 1$ for a spherical density distribution of $\rho(r) = r^{-1}$). Therefore, the virial mass for our clouds is: $M_{\mathrm{vir}} = 1040R\sigma^2$.

The luminosity-based mass is calculated through the ^{12}CO luminosity:

$$\frac{M_{\rm CO}}{\rm M_{\odot}} = \alpha_{CO} \frac{L_{CO}}{\rm K\ km\ s^{-1}\ pc^2} \tag{4.11}$$

where $\alpha_{CO} = 4.3$ for the Galactic CO to H_2 conversion factor (Bolatto et al., 2013). Through a virial analysis of LMC molecular clouds, Hughes et al. (2010) calculate an α_{CO} for the CO(1-0) line that is 2.4 times larger than the Galactic value. After assuming a CO(2-1)/CO(1-0) line ratio of 0.8 (similar to what Wong et al. (2019) follow), we use an $\alpha_{CO} = 12.9$ for the molecular clouds in this work.

We decompose the molecular gas emission from the $^{12}\mathrm{CO}(2-1)$ and $^{13}\mathrm{CO}(2-1)$ data separately, reporting properties for the ^{12}CO and ^{13}CO defined structures. We use the mask that required a 3σ detection in 3 consecutive channels described in §4.3.1. We use the default parameters in `pycprops`, except we require an area equal to the beam size to define a cloud. The reported uncertainties are found through a bootstrap method that randomly samples from the pixels that makeup the cloud to calculate cloud properties and use the variance of the properties as the uncertainty. For these parameters, the `pycprops` code reports 494 individual clouds for the ^{13}CO structures and 1948 clouds for the ^{12}CO structures. After excluding clouds that are unresolved (i.e. clouds that have a major axis smaller than a beam) and clouds that have fractional uncertainties that are greater then 30%, we are left with 206 and 1067 ^{13}CO and ^{12}CO clouds, respectively. We calculate the virial and CO luminosity based mass of each cloud through Equations 4.10 and 4.11. For the ^{13}CO structures, we calculate the LTE based mass described in §4.3.3 through:

$$M_{\rm LTE} = (2m_H)(1.36) \int N(\mathrm{H_2}) dA \tag{4.12}$$

Table 4.1: 13CO(2-1) Structures: Cloud Properties

Cloud	Region	Radius pc	Linewidth km s^{-1}	$\Sigma_{\rm virial}$ M$_\odot$ pc^{-2}	$\Sigma_{\rm LTE}$ M$_\odot$ pc^{-2}	$\alpha_{\rm virial}$	$L_{8\ \mu{\rm m}}$ MJy sr^{-1}
1	Ridge	1.39 ± 0.25	0.78 ± 0.18	146.01 ± 89.89	59.93	2.44	6.45
2	Ridge	0.96 ± 0.21	1.06 ± 0.29	383.98 ± 281.79	111.42	3.45	10.12
3	Ridge	2.12 ± 0.54	0.86 ± 0.17	115.68 ± 79.39	27.94	4.14	8.16
4	Ridge	2.49 ± 0.37	0.97 ± 0.12	125.74 ± 51.31	54.67	2.30	6.35
5	Ridge	2.10 ± 0.28	1.00 ± 0.09	156.04 ± 53.88	100.00	1.56	7.63
6	N160	2.09 ± 0.19	1.13 ± 0.08	203.43 ± 50.13	175.36	1.16	28.28
7	Ridge	2.08 ± 0.59	0.88 ± 0.15	123.28 ± 88.76	33.19	3.71	12.34
8	Ridge	1.59 ± 0.32	0.67 ± 0.08	92.36 ± 46.79	105.72	0.87	10.44
9	Ridge	1.23 ± 0.19	0.59 ± 0.13	93.55 ± 53.41	70.77	1.32	10.62
10	N160	2.30 ± 0.59	0.54 ± 0.14	42.78 ± 32.69	16.98	2.52	12.20

where m_p is the mass of a hydrogen atom, 1.36 is the correction factor for helium, and we integrate the molecular column density from equations Equation 4.8 and Equation 4.7 over the projected area of the structure. Lastly, we convert each mass to a mass surface density through:

$$\Sigma = \frac{M}{\pi R^2}. \tag{4.13}$$

The resulting properties are reported in Tables 4.1 and 4.2 for the ^{13}CO and ^{12}CO structures, respectively. We also present an example of the decomposed cloud structures for ^{13}CO in the N159 region in Figure 4.7. Note that there are some areas of emission that were too small to be pulled as clouds given the size limit we imposed in our analysis. The cloud structures also overlap with one another on this 2D representation because the cloud boundaries are defined in the 3D cube. Nevertheless, this 2D view of N159 illustrates of how the `pycprops` algorithm decomposes the emission.

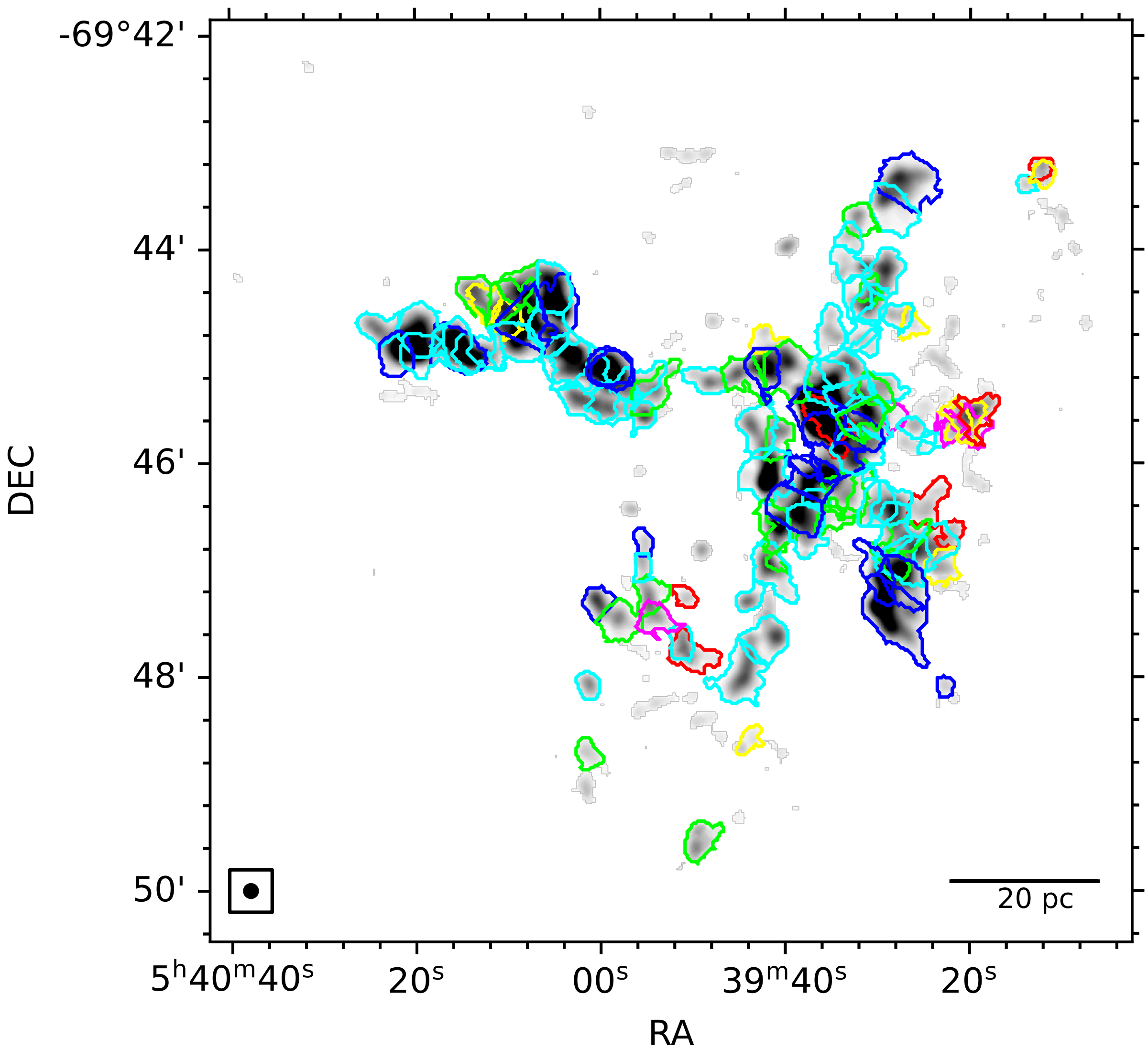

Figure 4.7: Example of the pycprops identification of ^{13}CO projected cloud boundaries near N159. The grayscale represents the masked integrated ^{13}CO emission presented in Figure 4.3. Clouds that are more red have high $\alpha_{\rm vir} \sim 4$, representing clouds that are unbound, while those in blue are bound ($\alpha_{\rm vir} \sim 1$, see §4.5 for more discussion). There is no clear spatial correlation between the bound and unbound clouds. The cloud boundaries overlap because they are defined in 3 dimensions, with the velocity axis as the third. The instances where there is ^{13}CO emission not covered by a cloud are due to those clouds being unresolved and removed from analysis.

Table 4.2: 12CO(2-1) Structures: Cloud Properties

Cloud	Region	Radius pc	Linewidth km s^{-1}	Σ_{virial} $M_{\odot}$ pc^{-2}	Σ_{mol} $M_{\odot}$ pc^{-2}	α_{virial}	$L_{8\ \mu m}$ MJy sr^{-1}
1	N159	1.08 ± 0.18	0.64 ± 0.12	125.09 ± 52.46	31.07	4.03	6.17
2	Ridge	0.64 ± 0.14	0.62 ± 0.11	200.97 ± 81.95	171.11	1.17	5.79
3	Ridge	1.46 ± 0.33	0.94 ± 0.16	199.00 ± 79.55	34.77	5.72	5.82
4	Ridge	0.60 ± 0.11	0.77 ± 0.09	329.89 ± 97.31	167.04	1.97	12.42
5	Ridge	0.72 ± 0.10	0.54 ± 0.10	133.09 ± 50.92	94.04	1.42	8.42
6	Ridge	1.29 ± 0.26	0.73 ± 0.09	134.78 ± 43.98	81.86	1.65	5.12
7	Ridge	0.58 ± 0.10	0.71 ± 0.09	285.98 ± 89.57	285.15	1.00	4.56
8	Ridge	2.07 ± 0.31	0.74 ± 0.06	88.57 ± 18.31	83.79	1.06	4.90
9	Ridge	2.49 ± 0.26	1.50 ± 0.13	298.71 ± 61.05	36.50	8.18	4.99
10	Ridge	2.29 ± 0.58	0.94 ± 0.07	128.39 ± 37.27	58.55	2.19	4.72

4.4 Results

4.4.1 CO and 8μm correlation

Mid-infrared (MIR) continuum emission is mostly attributed to dust grains reprocessing the surrounding local radiation field (e.g., Draine, 2011). At 8 μm, there is a distinctive spectral feature attributed to compounds called polycyclic aromatic hydrocarbons (PAHs) in addition to the continuum emission of small dust grains. The underlying continuum and PAH features at 8 μm are due to dust reprocessing of the incident UV radiation and the band is used as a tracer of star formation (e.g., Calzetti, 2013; Kennicutt & Evans, 2012). At the same time, star formation and cold gas correlate with one another (Kennicutt, 1998). Accordingly, there is also a correlation between the direct observables: the 8 μm and CO fluxes. Leroy et al. 2023 compile a large data set of modestly resolved ($17'' \sim 1.3$ kpc) MIR and CO data in nearby galaxies. They investigate the scaling relations between 8 μm and ^{12}CO (2-1) and indeed find a tight correlation.

The 1.7 pc resolution in the LMC combined with our large scale map (150×380 pc) enable us to test this relation on a completely different spatial scale. We plot the 8 μm and ^{12}CO (2-1) correlation in Figure 4.8 and compare to the Leroy et al. 2023 extrapolated fit in yellow. We fit a powerlaw relation to the data:

$$\log I_{12\mathrm{CO}(2-1)} = a_1 \log I_{8\mu\mathrm{m}} + a_0 \tag{4.14}$$

and find a slope of $a_1 = 0.67 \pm 0.07$ and an intercept of $a_0 = 2.08 \pm 0.08$. We also perform a Spearman correlation test and find a positive correlation with $r_\mathrm{s} = 0.22$ and $p = 2.3 \times 10^{-13}$. Remarkably, our $\sim 100\times$ higher resolution data of the LMC provide a similar correlation to that seen in the nearby galaxies. There is an offset in the intercept, where Leroy et al. 2023 find $a_0 = -0.19 \pm 0.05$, but the slopes are quite close at $a_1 = 1.17 \pm 0.08$. The shallower slope in the higher resolution data may be due to the breakdown of the Kennicutt-Schmidt relation at resolved, molecular cloud scales or a breakdown of the 8 μm as a star formation rate tracer (e.g., Onodera et al., 2010; Schruba et al., 2010). Further, Leroy et al. 2023 find their higher resolution JWST data have flatter slopes compared to their *Spitzer* observations, likely due to the PAH emission at the 8 μm band including contributions from non-CO-emitting gas, and we may be seeing the same effects in the LMC data.

4.4.2 Size-linewidth Relations

The correlation between size and linewidth of molecular clouds and their substructures has been extensively studied since the 1980s (Larson, 1981; Solomon et al., 1987). The correlation is a powerlaw in log-space:

$$\log \sigma_v = a_1 \log R + a_0 \tag{4.15}$$

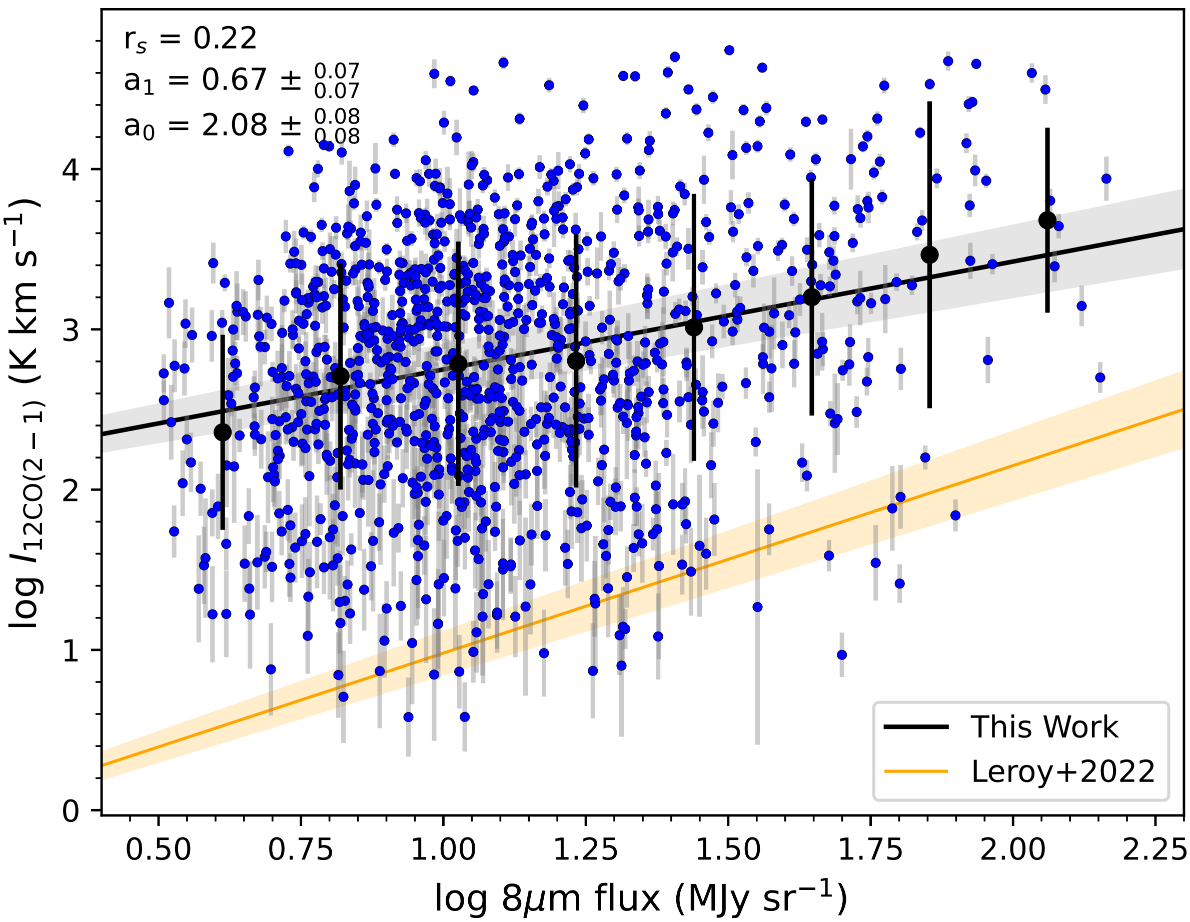

Figure 4.8: The correlation between the median 8 μm flux of a clump and its $^{12}\mathrm{CO}(2-1)$ flux. The fit is represented by a black line with the 1σ error in the grayed region. We bin the data to see the correlation more clearly and present them as the black points with the standard deviation in a given bin represented by the errorbar. The fit for 350 nearby galaxies from Leroy et al. 2023 is in orange has a slope that is similar to the correlation found in $\sim 100\times$ better resolution in the northern molecular ridge.

where σ_v is the velocity dispersion of a structure and R is its radius as defined in Equation 4.9. The parameters for Milky Way clouds are $a_1 = 0.5$ and $a_0 = -0.14$ (Heyer et al., 2009; Solomon et al., 1987). The size-linewidth relation can be interpreted as a measure of the equilibrium turbulence conditions in molecular clouds, likely originating from star formation (Bolatto et al., 2007; McKee & Ostriker, 2007).

We present the size-linewidth relation for the ^{13}CO and ^{12}CO structures in the northern molecular ridge in Figure 4.9. We fit Equation 4.15 on the ^{12}CO and ^{13}CO structures through the `scipy` package `ODR` (orthogonal distance regression) to account for uncertainties in both R and σ_v. The reported errors are from fitting the data through bootstrapping, repeatedly fitting the randomly sampled data with replacement. We do 500 trials of random samples of the cloud structures and report the mean and 1σ confidence interval for a_1 and a_0 as the gray region in the plot. The powerlaw fit for Milky Wilky way from Solomon et al. (1987) is shown in purple and the results for the six molecular clouds analyzed in Wong et al. (2019) are the orange dashed lines.

Overall, the clouds in the northern molecular ridge follow similar relations seen in the Milky Way and LMC. The reported slopes for the ^{12}CO line from Wong et al. (2019) are in the range of $a_1 = 0.32 - 0.97$, suggesting the 0.68 slope we find for the ^{12}CO structures lies in the median of those found throughout the LMC. The slope of the ^{12}CO structures is also comparable to that of Milky Way clouds ($a_0 \sim 0.5$, Heyer et al., 2009; Solomon et al., 1987) and extragalactic local dwarf galaxies ($a_0 \sim 0.6$, Bolatto et al., 2007).

The normalization of the size-linewidth relation (a_0, the intercept in Equation 4.15) is related to the kinetic energy of a cloud at a 1 pc size scale. For our data, a 1 pc cloud in both the ^{12}CO and ^{13}CO structures corresponds to a linewidth of ~ 0.7 km s^{-1}, which is very similar to

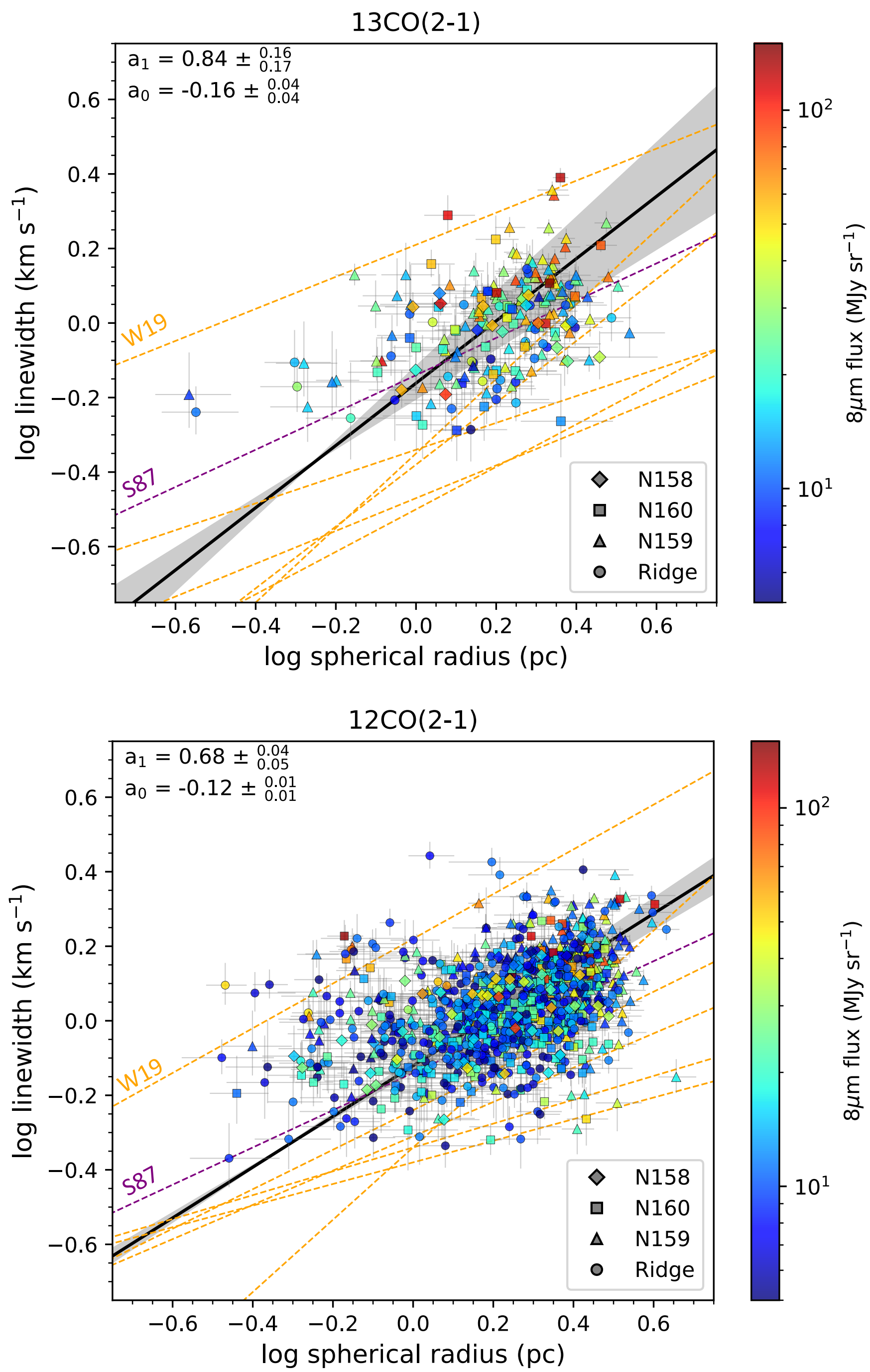

Figure 4.9: Size-linewidth for the ^{13}CO (top) and ^{12}CO (bottom) structures. The symbols are defined in the right corner, with gas associated with N158 a diamond, N160 a square, N159 a triangle, and clouds that are not associated with the HII regions (labeled "Ridge") are circles. The colorscale is the median 8 μm flux of each cloud, which tracks the approximate star formation rate. The fit of Equation 4.15 for these data is in black, with the 1σ confidence interval shown in the shading. For comparison, we present the fit for the Milky Way clouds (Solomon et al., 1987) in purple dashed lines and the fits for the sample of LMC clouds Wong et al. (2019) studied in orange. The northern molecular ridge clouds are very similar to Milky Way clouds and the median of the LMC clouds. There does not appear to be strong trends with the region the clouds are associated with or the 8 μm flux.

the Milky Way clouds at 0.72 km s^{-1}. It is also intermediate between those linewidths observed in the active (30 Dor $\sim 1.2 - 1.5$ km s^{-1}, Nayak et al., 2016; Wong et al., 2017, 2019, 2022) and inactive (PCC $\sim$ 0.3 km s^{-1}, Wong et al., 2017, 2019) regions of the LMC. We also compare our normalization of $\sim$ 0.7 km s^{-1} in the star forming, northern part of the molecular ridge to the quiescent southern portion. Finn et al. (2022) find a linewidth normalization of 0.44 km s^{-1}, indicating structures that reside south of our map have less kinetic energy, as expected for the more quiescent region. Overall, the linewidth we compute for a 1 pc cloud in the northern portion of the molecular ridge indicates moderate kinetic activity that is consistent with average clouds in the Milky Way and LMC.

We do not see a substantial difference in the size-linewidth relation between molecular gas that is associated with the three HII regions in this sample. Further, there are no clear correlations between the median 8 μm flux in the cloud and the size-linewidth relation. In contrast, the six regions across the LMC that Wong et al. (2017) observes have significant variation in the normalization of the size-linewidth relation between region and find a correlation where clouds with brighter 8 μm emission tend to have higher linewidths. The similarity across region in our data may indicate that the molecular clouds have similar kinetic energy densities, regardless of the surrounding star formation rate indicated by the 8 μm flux.

4.4.3 Mass Surface Density and Virial Relations

A method to examine the balance between the kinetic energy in a clump and its gravitational potential energy is through comparison of the virial mass surface density, Σ_{vir} (Equation 4.10) and the luminous mass surface density, Σ_{lum}. For the ^{13}CO structures, we use the LTE based mass for $\Sigma_{\rm lum}$ (see §4.3.3 and Equation 4.12) which is a more direct estimation of the luminous mass that calculates the $N(\rm H_2)$ column density. For the ^{12}CO structures, we use the CO based mass estimate (see Equation 4.11) that relies on an assumption of a α_{CO} value and is susceptible to systematic uncertainties. We present the mass surface densities for the ^{13}CO and ^{12}CO structures in Figure 4.10.

The virial surface density is directly proportional to the normalization of the size-linewidth relation, $\Sigma_{\rm vir} \propto \sigma_v^2/R$ and is analogous to the "boundedness plots" discussed in Heyer et al. (2009) and Field et al. (2011). If $\Sigma_{\rm vir} = \Sigma_{\rm lum}$, then the cloud is in simple virial equilibrium (SVE). When $\Sigma_{\rm vir} = 2\Sigma_{\rm lum}$, the cloud is in equipartition equilibrium and the cloud is considered marginally bound. In instances where the kinetic energy of the cloud is much greater than its gravitational binding energy, $\Sigma_{\rm vir} \gg \Sigma_{\rm lum}$, the cloud is unbound. Alternatively, the cloud may be in equilibrium with an additional external pressure exerted upon it parameterized as:

$$\Sigma_{\rm vir} - \Sigma_{\rm lum} = \frac{20}{3\pi G}\frac{P_{\rm ext}}{\Sigma_{\rm lum}}. \tag{4.16}$$

We plot lines of constant pressure, $P_{\rm ext}$ on Figure 4.10, in addition to the SVE (blue) and equipartition equilibrium cases (black).

We consider a cloud to be bound when their 1σ uncertainty is within the definition of SVE or equipartition equilibrium. For the ^{13}CO structures, only 5% of the total clouds are potentially unbound. For these clouds, there is not a single value of the external pressure that would confine them as they vary between $P_{\rm ext} = 10^4 - 10^6$ K cm^{-3}. Interestingly, these unbound clouds all reside near the HII regions N159 or N160. For the ^{12}CO structures, there are significantly more unbound clouds: 45% of the total clouds are greater than 1σ away from equipartition equilibrium.

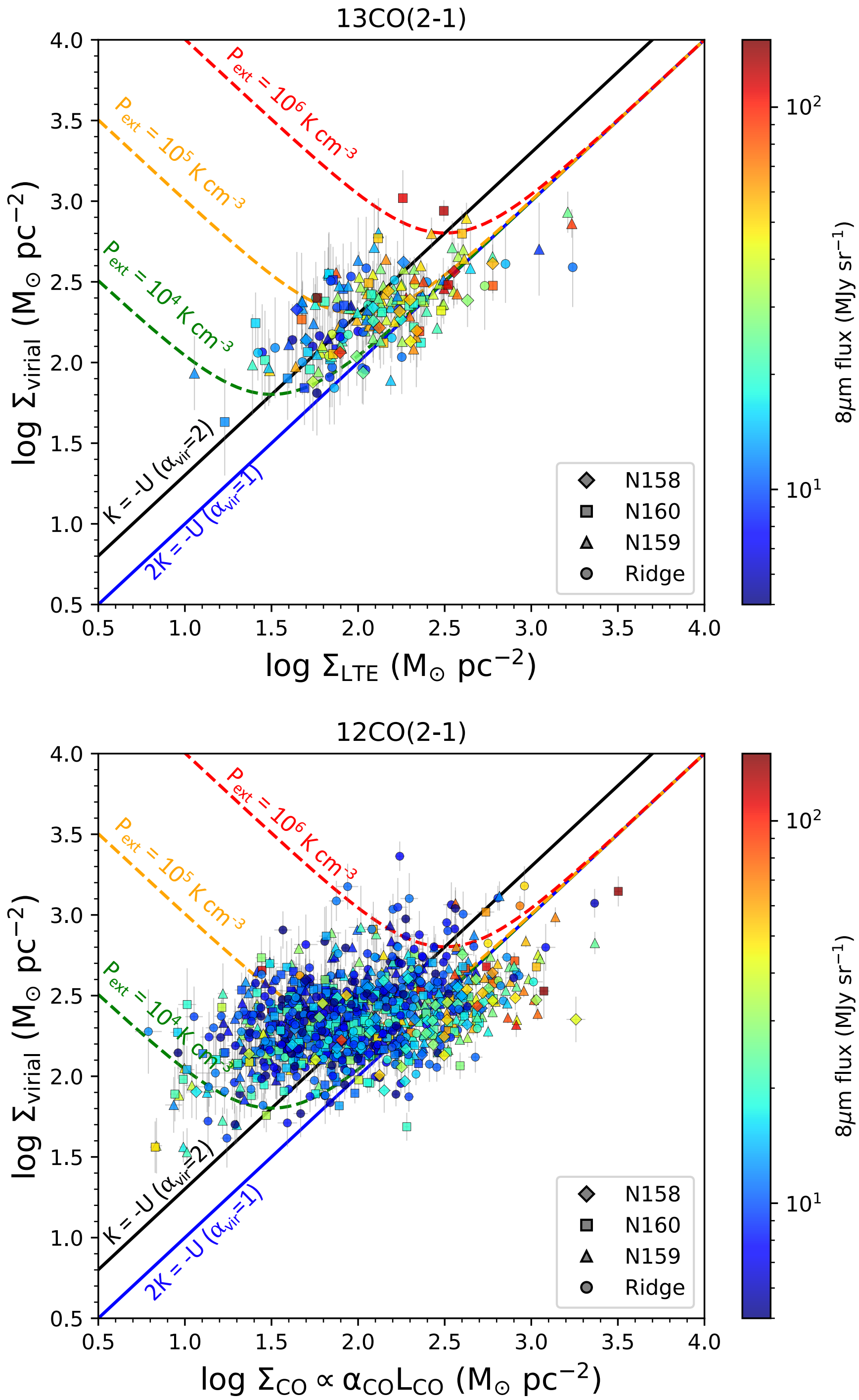

Figure 4.10: Comparison of the virial mass surface density ($\Sigma_{\rm virial}$) and the luminous mass surface density ($\Sigma_{\rm lum}$) for the ^{13}CO (top) and ^{12}CO structures (bottom). The ^{13}CO structures use the more accurate LTE approximation from the optically thin ^{13}CO line to for $\Sigma_{\rm lum} = \Sigma_{\rm LTE}$ while the ^{12}CO structures use an assumed $\alpha_{\rm CO}$ and the ^{12}CO luminosity for $\Sigma_{\rm lum}$. The symbols and colors are the same as in Figure 4.9. The curves on the plot show virial equilibrium (blue), equipartition equlibrium (black), and pressure-bounded equlibrium (green, yellow, red; see Equation 4.16). Most of the ^{13}CO structures are in virial or equipartition equilibrium while the ^{12}CO structures, especially those with lower mass surface densities, tend to more unbound.

The unbound clouds are spatially distributed about evenly throughout the map, with the exception that the the molecular gas near N158 encompasses only 2% of the total unbound clouds. Similar to the ^{13}CO structures, the unbound clouds are inconsistent with a singular external pressure exerted on the clouds.

We also find a trend where higher surface density clouds (as measured by $\Sigma_{\rm lum}$) tend to be closer to SVE or equipartition equilibrium than lower surface density clouds. This trend can partially explain why many of the ^{12}CO structures are considered unbound. The ^{13}CO emission is more optically thin compared to the ^{12}CO emission and consequently structures with lower ^{12}CO surface brightness are less likely to be detected in ^{13}CO. This will bias the ^{12}CO observations to contain fainter clouds than the ^{13}CO data. Since clouds with lower surface density tend to be less bound, the ^{12}CO structures will contain fainter, unbound, lower mass clouds when compared to the ^{13}CO structures. Further, in order to calculate $\Sigma_{\rm CO}$, we assume an $\alpha_{\rm CO}$ factor (see Equation 4.11) based off of previous work in the LMC (Hughes et al., 2010) and CO(1-0)/CO(2-1) ratio of 0.8. This ratio, however, is known to vary across the LMC, with a value of 0.5 in the outskirts of the galaxy and rising to ∼1.2 in 30 Dor (Sorai et al., 2001). A factor of two increase on $\alpha_{\rm CO}$ results in only $\sim 15\%$ of the ^{12}CO structures being unbound. Combined with the ^{12}CO bias towards lower surface density clouds, the 15% unbound fraction for the ^{12}CO structures is reasonable.

4.5 Discussion

We quantify whether the clouds are bound through the virial parameter defined as the ratio between the virial mass and the luminous mass of a cloud (Bertoldi & McKee, 1992):

$$\alpha_{\rm vir} = \frac{2K}{U} = \frac{M_{\rm vir}}{M_{\rm lum}} = \frac{\Sigma_{\rm vir}}{\Sigma_{\rm lum}}. \tag{4.17}$$

A virial parameter of $\alpha_{\rm vir} \sim 1$ corresponds to clouds in SVE, an $\alpha_{\rm vir} \sim 2$ signify clouds in equipartition equilibrium, and unbound clouds have $\alpha_{\rm vir} \gg 2$. As mention in §4.4.3, clouds that are unbound can be in equilibrium with an excess external pressure. Stellar feedback from star formation can heat the surrounding gas and inject turbulence through outflows, giving rise to turbulent pressures. We investigate whether there are trends between the median 8 μm flux in a cloud, our tracer of star formation, and $\alpha_{\rm vir}$ in Figure 4.11 to understand whether feedback from star formation impacts the stability of molecular clouds. On the right-hand panels, we show box plots of the distribution of α_{vir} for the regions defined in §4.3.2.

Overall, both the ^{13}CO and ^{12}CO structures show no positive correlation of $\alpha_{\rm vir}$ vs. 8 μm flux, indicating that there is no evidence of pressures on the clouds driven by star formation feedback. Instead, there is a slight negative correlation (Spearman rank of $r_{\rm s} = -0.22$ and -0.27 for the ^{13}CO and ^{12}CO structures, respectively). This is likely due to a secondary effect: higher mass surface density clouds tend to be more bound and are associated with higher star formation rates.

We do see a slight trend in $\alpha_{\rm vir}$ and the different HII regions traced across the northern molecular ridge. As mentioned in §4.4.3, the ^{13}CO structures that are furthest away from equilibrium are clouds that are associated with N159 and N160. This trend is also seen in the histograms of Figure 4.11, where the median $\alpha_{\rm vir} = 0.9$ for N158 and $\alpha_{\rm vir} = 1.2 - 1.3$ for the N159, N160, and the other regions throughout the northern molecular ridge. The ^{12}CO structures associated with N158 also tend to have lower $\alpha_{\rm vir}$, although there are large uncertainties in the determina-

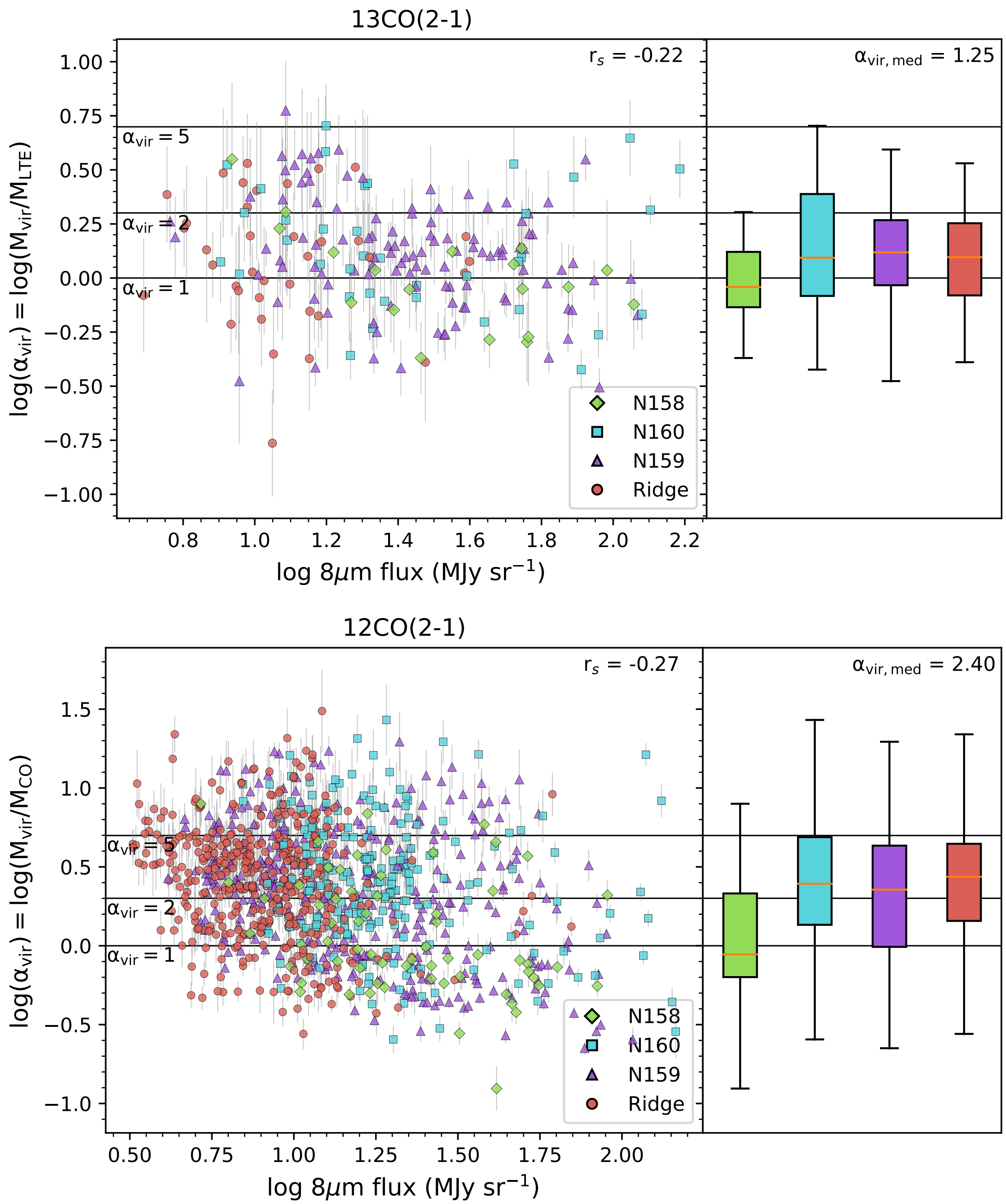

Figure 4.11: Virial parameter, $\alpha_{\rm vir}$ (see Equation 4.17), of the ^{13}CO (top) and ^{12}CO (bottom) structures vs the 8 μm flux. We also present box plots of the distribution of $\alpha_{\rm vir}$ for the designated four regions in the sample on the right hand panels. The Spearman rank correlation coefficient is given in the top right corner of the left panel. There is no positive correlation between the virial parameter and the 8 μm flux, indicating that the measure of boundness of a cloud has no relation to the surrounding star formation rate. There is tentative evidence that clouds associated with the N158 region are more bound than the other regions.

tion of $\Sigma_{\rm CO}$ for the ^{12}CO structures. Work from de Boer et al. (1998) suggests that the string of HII regions from 30 Dor to N159 are produced through bow shock induced star formation from motion of the LMC through the galactic halo. They predict that the HII regions will decrease in age from north to south direction. Through analysis of O star and YSO populations, there is some evidence of this north-south age gradient in N158 (Testor & Niemela, 1998) as well as N160 and N159 (Gordon et al., 2017; Nakajima et al., 2005). Our virial analysis of the molecular clouds suggest that the bound clouds are more associated with the older HII region N158, possibly due to star formation clearing out of molecular material in shorter timescales and leaving only the bound clouds.

The lower surface density clouds in our sample tend to be more unbound, a trend that's also seen throughout clouds in the LMC (Finn et al., 2022; Wong et al., 2017, 2019, 2022). With a lower gravitational potential, these clouds may be more susceptible to disruption, resulting in elevated $\Sigma_{\rm vir}$ for a given $\Sigma_{\rm lum}$. Although there are no clear correlations between $\alpha_{\rm vir}$ and the 8 μm flux, there may be large scale kinetic energy injection that the lower mass clouds are more sensitive to, as is seen in 30 Dor (Lopez et al., 2011; Nayak et al., 2016; Wong et al., 2022). Alternatively, there is evidence of a large scale, 1 kpc HI flow that drives the star formation activity from 30 Dor to N159 due to the interaction between the LMC and SMC (Fukui et al., 2019, 2017). It is possible that these converging gas flows may stir up turbulence throughout the northern molecular ridge region. A simpler explanation, however, is that the lower mass density structures may be transient molecular gas density fluctuations that are not in equilibrium (e.g., Dib et al., 2007). Therefore, these structures are not coherent clouds in equilibrium and consequently have higher $\alpha_{\rm vir}$ values.

Since the LMC is at a metallicity about half solar, there is also a possibility that CO-dark gas may be influencing our results. The CO-dark gas is defined as molecular gas that is not traced by CO observations due to the dissociation of the CO molecule in low dust environments (e.g., Jameson et al., 2018). Compensating for the CO-dark gas in both low metallicity and highly irradiated environments can lead to an enhancement of the $\alpha_{\rm CO}$ factor on order of 4-20 compared to galactic values (Chevance et al., 2020). If there is a substantial envelope of CO-dark gas surrounding the CO-bright material in our clouds, it is possible that clouds may be in virial equilibrium with the extra luminous mass. However, $\Sigma_{\rm vir}$ may also decrease proportionately due to underestimation of R and σ_v. Analysis by O'Neill et al. (2022a) shows a complex relationship between the fraction of CO-dark gas and the adopted density and velocity profiles of the clumps. For the assumed density and velocity profiles in our work, a large fraction of CO-dark gas could decrease $\Sigma_{\rm vir}$, leading to more bound clumps. We caution that there are many systematic uncertainties through our assumptions− such as spherical symmetry, LTE approximation for calculating $\Sigma_{\rm LTE}$, the $\alpha_{\rm CO}$ factor for $\Sigma_{\rm vir}$, and the accuracy of the clump finding algorithm− that may modify the calculated values of α_{vir}. Considering these systematic uncertainties, the majority of our clumps are bound and likely not affected by external pressures due to star formation.

4.6 Summary and Conclusions

We present a large mosaic (10' $\times$ 26', 150 $\times$ 380 pc) of ^{12}CO and ^{13}CO in the northern molecular ridge, a region in the LMC that hosts three well-studied HII regions: N158, N160, and N159 as well as the largest concentration of CO emission in the galaxy. Our goal is to determine the properties (e.g., size, linewidth, mass density) of the molecular clouds to discern whether there are trends with the surrounding star formation that may indicate a source of stellar feedback disrupting the cloud. We decompose our data into structures and calculate their properties through the pycprops package (Rosolowsky et al., 2021; Rosolowsky & Leroy, 2006), finding ~ 1000 molecular clouds in this region. The main conclusions of our analysis follow:

1. We calculate the column density of molecular hydrogen, $N(\mathrm{H_2})$, using the optically thin ^{13}CO line and assuming LTE (§4.3.3). We report a map of $N(\mathrm{H_2})$ throughout the northern molecular ridge in Figure 4.6 and find a peak column density of $N(\mathrm{H_2} = 1.4 \times 10^{23}\ \mathrm{cm}^{-2}$ near N159, consistent with previous observations of the northern molecular ridge (Bolatto et al., 2000; Fukui et al., 2019).
2. After decomposing the ^{12}CO and ^{13}CO data into cloud structures with pycrops (Rosolowsky et al., 2021; Rosolowsky & Leroy, 2006), we find a powerlaw correlation between the $^{12}\mathrm{CO}(2-1)$ intensity of the clouds and their median 8 μm intensity (Figure 4.8). The correlation is not as tight as the results of a large sample of nearby galaxies (Leroy et al. 2022), likely due to the higher resolution of these data.
3. The size-linewidth relation of both the ^{12}CO and ^{13}CO clouds is remarkably similar to the relation found in Milky Way Clouds (Figure 4.9, §4.4.2, Solomon et al., 1987). The clouds in the northern molecular ridge exhibit intermediate kinetic energies between the quiescent and active regions in the LMC (Finn et al., 2022; Nayak et al., 2016; Wong et al., 2017, 2019, 2022).
4. We determine whether the clouds are bound by comparing the virial mass surface density (Σ_{vir}) to the luminous mass surface density (Σ_{lum}) in Figure 4.10 (§4.4.3). For the ^{13}CO structures, Σ_{lum} is calculated through the LTE analysis while the ^{12}CO structures rely on assuming an α_{CO} factor. The vast majority of the ^{13}CO clouds ($\sim$ 95%) are bound or marginally bound. There are more unbound ^{12}CO clouds, but the uncertainty of the α_{CO}

may artificially increase the number of bound clouds. The clouds we identify as unbound are not consistent with being in equilibrium with a constant external pressure.

5. In order to identify whether the surrounding star formation disrupts the molecular clouds through stellar feedback, we compare $\alpha_{\rm vir} = \Sigma_{\rm vir}/\Sigma_{\rm lum}$, a measure of the boundedness of clouds, to the median 8 μm flux, an estimate of the star formation associated with the clouds (Figure 4.11). There is not a positive correlation between $\alpha_{\rm vir}$ and the 8 μm flux, indicating that there is no evidence of external pressure on the clouds driven by star formation feedback.

6. The molecular clouds associated with the N158 HII region have consistently lower $\alpha_{\rm vir}$ than the other regions, suggesting that N158 may host clouds that are more bound. As oldest of the HII regions (Gordon et al., 2017; Nakajima et al., 2005; de Boer et al., 1998), N158 may have cleared away the unbound clouds earlier in its lifetime.

7. The clouds with the lowest masses tend to be more unbound than the more massive clouds, likely because the molecular clouds may be transient clumps of material that are not coherent structures.

Chapter 5: Future Work

In this thesis, I show how spectroscopic observations can reveal the physical conditions and nature of the multi-phase ISM. In chapter 2, I present velocity-resolved [CII] spectroscopy of the nearby galaxies M101 and NGC 6946 and determine that [CII] is associated with the atomic and molecular gas about equally. Using the [CII] cooling function, I calculate the thermal pressure of the CNM and find that it is consistent with predictions from analytical theory that high star-formation rates can drive larger thermal pressures (Wolfire et al., 1995, 2003). Chapter 3 uses infrared spectroscopy to model the ionized gas in the Wolf-Rayet nebula N76, which contains one of the hottest WR stars in the SMC. Our `Cloudy` (Ferland et al., 2017) photoionization models of N76 match the spatial distribution of the moderately ionized lines, [SIII], [OIII], [NeIII], [SIV], very well, but do not predict the intensities of the high ionization lines, [OIV] and [NeV]. We suggest that these lines can be produced through shock ionization from the powerful stellar winds of the WR star. Lastly, chapter 4 explores the properties of molecular clouds at 1.7 pc resolution in a large, 170×350 pc map of the an active star forming region called the northern molecular ridge in the LMC. Using $^{12}\mathrm{CO}(2-1)$ and $^{13}\mathrm{CO}(2-1)$ observations from the ALMA ACA, we decompose the emission into individual coherent structures and determine their sizes, linewidths, mass surface densities, and virial parameters. Almost all of the clouds are bound or marginally bound and are very similar to molecular clouds in the Milky Way (Heyer et al., 2009; Solomon et al., 1987). We also do not find evidence of stellar feedback influencing the kinematic properties of the clouds.

There are many possible directions that the research in this thesis can move towards in the future. Below, I outline the future work I am interested in pursuing that builds off of my research in each thesis chapter.

5.1 What is the nature of [CII] emission?

As discussed in chapter 2, [CII] is an important line since it is bright (e.g. Crawford et al., 1985; Stacey et al., 1991) and a tracer of star formation (Boselli et al., 2002; De Looze et al., 2014; Herrera-Camus et al., 2015, 2018; Smith et al., 2017; Stacey et al., 1991). At redshifts of $z \sim 2 - 6$, the [CII] line falls into the ALMA bands and has been used as a molecular gas tracer (Dessauges-Zavadsky et al., 2020; Le Fèvre et al., 2020; Yan et al., 2020; Zanella et al., 2018). The multi-phase nature of [CII], however, makes it challenging to interpret its observations. In chapter 2 and Tarantino et al. (2021), we find that the [CII] emission is associated with the molecular and atomic gas about equally. Other observations of nearby galaxies on 50 - 500 pc scales also suggest that the atomic gas has a non-negligible component to the overall [CII] emission (Contursi et al., 2002; Fahrion et al., 2017; Mookerjea et al., 2016). Thus more investigation on the atomic component of the [CII] emission is needed in order to determine whether [CII] is an effective molecular gas tracer.

Further, since [CII] can probe regions where the CO molecular dissociated but the state of the gas is still molecular, it may also be good tracer of "CO-dark" gas (Cormier et al., 2015; Jameson et al., 2018; Madden et al., 2020). In order to use [CII] as a CO-dark gas tracer, the components associated with the atomic and ionized phases need to be removed. It is therefore clear that investigation of the multi-phase nature of [CII] is necessary. Unfortunately, the only observatory that could observe [CII] in the nearby universe, SOFIA, had its last flight on September, 30th 2022 due to budgetary constraints. Nevertheless, there is still a rich archival database and potential new observatories coming up in the next decade that can study [CII] in the nearby universe.

For example, SOFIA projects 03_0120 & 05_0210 (PI: R. Herrera-Camus) contain velocity resolved spectroscopy of [CII] and [OI] emission throughout five different star forming regions in the SMC. Figure 5.1 presents an example spectrum of the [CII] and [OI] emission, along with ancillary CO and HI, of the SW bar region. The [CII] is incredibly bright, suggesting a large contribution of CO-dark gas in this region. Precise decomposition of the [CII] emission in this area is challenging, however, due to the larger beam (98″) of the HI data compared to the [CII] data at 15″. Future ASKAP observations will improve on this resolution. In the future, we will implement a multi-component decomposition method outlined in Lebouteiller et al. (2019) to understand the multi-phase origin and CO-dark gas content in the SMC.

I am also a member of the team for the SOFIA Legacy project: "SOFIA Joint Legacy Survey of [CII] in the LMC: LMC+" (Project: 09_0036, PI: S. Madden). This project contains [CII] and [OIII] observations of the northern molecular ridge in the LMC and aims to determine the role of metallicity on the physical conditions of the molecular, atomic, and ionized ISM. Preliminary comparison of the [CII] map from LMC+ and the CO map from chapter 4 of this thesis show some spatial agreement, but there are significant areas of the map that show little correspondence between the [CII] and CO emission. I will contribute my expertise of [CII] and the molecular ridge to help determine the lack of connection between CO and and the [CII]. It is

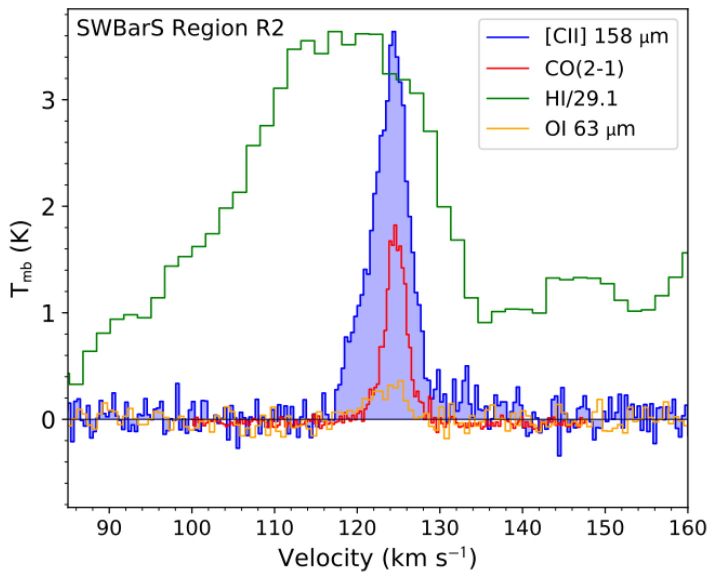

Figure 5.1: SOFIA GREAT Spectrum of [CII] and [OI] in the southwest Bar region with ancillary CO and HI spectra. The [CII] line is very bright in comparison to the CO, suggesting a substantial component of CO-dark gas. The HI data are at much lower resolutions (98″) compared to that of the [CII] (15″), making a direct [CII] decomposition more complex.

possible that the multi-phase nature of [CII] may be playing a larger role than previously thought or the CO-dark gas that the [CII] traces may be significantly spatially offset from the CO.

Although there will be no new [CII] observations from SOFIA, the 2020 Decadal survey recommended the creation of a "probe" class mission designed to bridge the gap between small explorer missions and flagships. The infrared community is actively pursuing proposals for this probe mission, one of which is called PRIMA (PRobe far-Infrared Mission for Astrophysics), which will have extensive spectroscopic capabilities from $\sim 25 - 250\ \mu$m. One key science goal for PRIMA is to use the FIR fine structure lines, many of which that are featured in this thesis, to determine the conditions of gas in nearby galaxies.

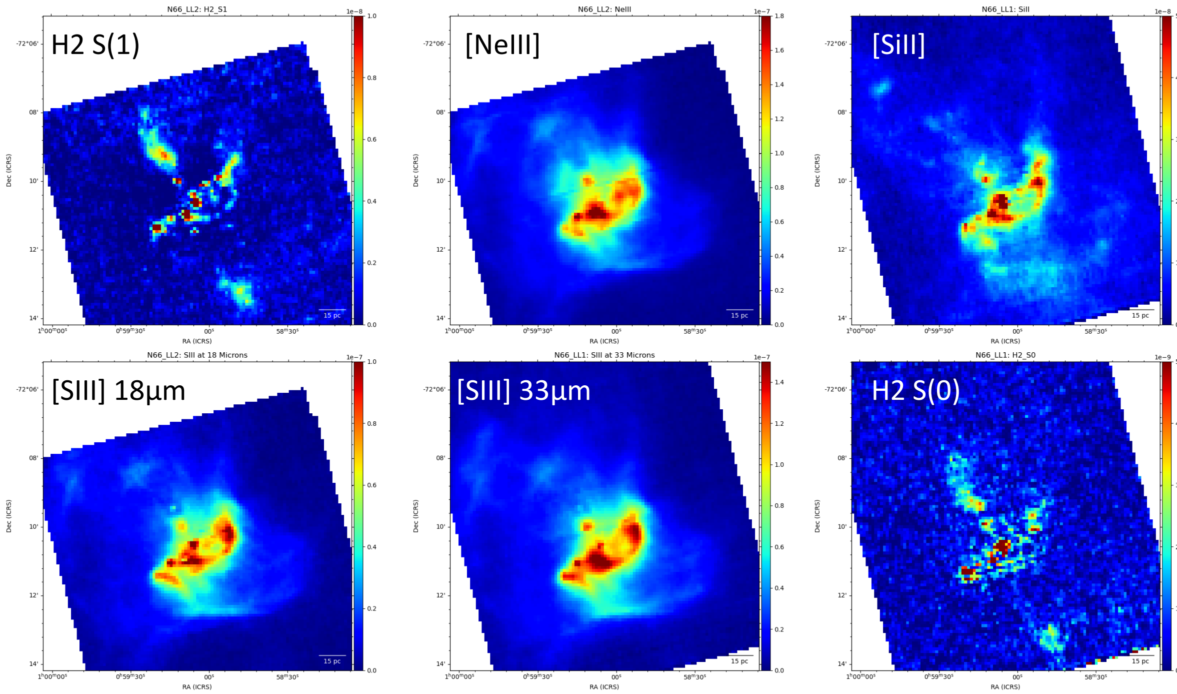

Figure 5.2: *Spitzer*IRS emission line images of the supergiant HII region N66 in the SMC. The ionized gas in N66 is quite complex but concentrated towards the location of the NGC 346 cluster.

5.2 How do the properties of ionized gas vary across the SMC?

Chapter 3 discusses modeling the ionized gas at low metallicities in a Wolf-Rayet nebula. Due to the extreme temperatures and intensity of the WR star powering N76, the environment of this nebula is very unique and may not well represent the ionized gas conditions across the SMC. In addition to N76, we also have *Spitzer* IRS and *Herschel* PACS observations of five other star-forming regions in the SMC. Among these is the N66 supergiant HII region that is ionized by cluster NGC 346. I advised an undergraduate student, Daniel Stapleton, to reduce the IRS data for N66 and run preliminary `Cloudy` models on these data.

Figure 5.2 presents the *Spitzer* IRS line images of N66 (Stapleton et al. , in prep). The ionized gas structure in N66 is quite complex, but is generally concentrated towards the NGC 346 cluster. Similar to N76, the [SiII] emission is spatially more associated with the other ionized gas lines instead of the H_2 quadrupole emission. By searching the literature, we catalogued the ionization sources for N66 and found 37 O-type stars that may contribute to the ionizing flux in N66 (Bonanos et al., 2010; Dufton et al., 2019; Massey et al., 1989). We then constructed an SED for the ionization of N66 by combing the individual PoWR model SEDs of each star. The preliminary `Cloudy` models predict N66 has a hydrogen density $n_{\rm H} \sim 30\ {\rm cm}^{-3}$, consistent with the low [SIII] 18 μm/ [SIII] 33 μm ratio, but lower than the $n_e \sim 140\ {\rm cm}^{-3}$ prediction from optical lines in Peimbert et al. (2000). In the future we will investigate the uncertainties of our assumptions in the Cloudy model. For example, a spherical model with a single ionization source works well for cases such as N76, but it is clear through images of N66 that the HII region is not spherical and that the ionization sources are spread throughout the nebula.

After much anticipation, the James Webb Space Telescope (JWST) launched on December 25th, 2021. The bandpass of JWST covers many of the infrared emission lines studied in this work, including [SIII], [NeII], and [NeIII]. I am involved in the project "Dissecting the Prototypical Starbursts NGC 253 and M 82 and Their Cool Galactic Winds" (GO 1701, PI: A. Bolatto) where I will help aid in the interpretation of the mid-infrared spectral lines to determine the radiation field strength and ionized gas properties near the center of the NGC 253 super star clusters that power its starburst.

5.3 Understanding the filamentary nature of molecular gas in the LMC

In chapter 4, we identify the properties of molecular clouds in the LMC and find that the clouds are mostly bound and similar to clouds in the Milky Way. Previous measurements near the HII region N159 in the northern molecular ridge show evidence of colliding filaments

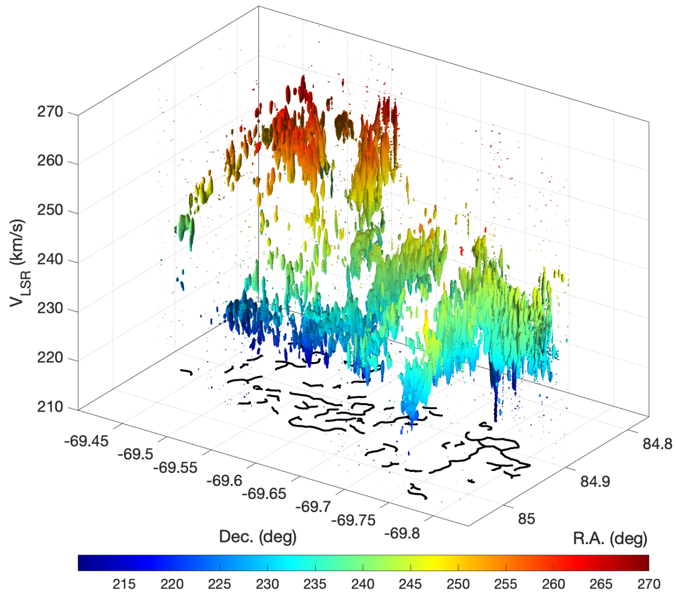

Figure 5.3: Volumetric rendering of the 0.5 K isosurface of the northern molecular ridge. The isosurfaces are colored with the corresponding V_{LSR} velocity (in $\mathrm{km\,s^{-1}}$). Inspection of the cube shows coherent filament-like structures in position-position-velocity space. The black graph projected on the bottom corresponds to the filament skeleton found using the version of FilFinder that works in 2D (Koch & Rosolowsky, 2015)

triggering high-mass star formation (Fukui et al., 2015, 2017; Saigo et al., 2017). Similarly, there is evidence that 30 Dor, just north of the northern molecular ridge, was formed through a large scale gas flow associated with the LMC/SMC interaction (Ochsendorf et al., 2017). Our large scale map of the northern molecular ridge can identify whether these large scale gas flows exist within the molecular gas and are triggering the nearby star formation.

Although the resolution (1.7 pc) of our map will not allow us to resolve traditional filaments that are of order $\lesssim$1 pc, examination of filament-like features can reveal the large scale structure of the molecular gas. In Figure 5.3 we show the 3D structure of the northern molecular ridge and the 2D filament skeleton derived by the Python program FilFinder (Koch & Rosolowsky, 2015). There are significant filamentary features that exist in position-position-velocity space that will need to be investigated by a three-dimensional filament finder in the future. Preliminary, we find a large, $\sim$100 pc feature that extends from the north to south. The $^{12}\mathrm{CO}(2-1)$ clouds in this "filament" also tend to have elevated α_{vir}, an indication of excess kinetic energy. We plan on confirming these results, identifying any other large features, and comparing the molecular gas to associated HI gas from the ASKAP telescope in the future.

Appendix A: Investigating the asymmetries in N76

In order to compare the `Cloudy` models directly to various emission lines in N76, we need to assume spherical symmetry. However, it is clear that the images of the emission lines show spatial asymmetries in Figure 3.1. The eastern side of N76 is brighter in almost every IR line and the western edge is less well-defined, with more diffuse, extended features. To explore how these asymmetries affect the `Cloudy` modeling, we show here the results for a narrow strip that intersects with the AB7 and designate it the central point. We then sample the surface brightness to the left (eastern edge) and right (western edge) of the strip and report it in Figure A.1.

The asymmetric profiles show that the western edge prefers a lower density model in almost all cases (except for [OI], [CII], and [NeII]). The idealized symmetric model presented in the radial profiles in Figure 3.5 is simply an average of these two sides. The difference between these densities is relatively low, however, with the higher density side preferring a model only $4\ \mathrm{cm}^{-3}$ larger. This is typically a $\pm 20 - 30\%$ change in the result of the spherically symmetric modeling.

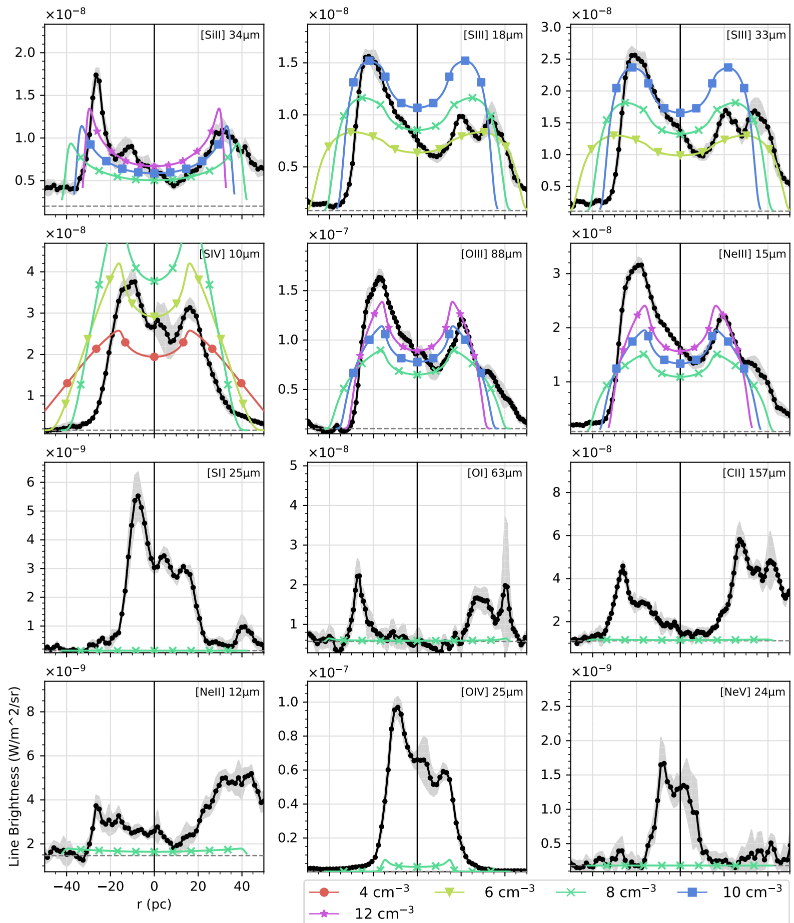

Figure A.1: The surface brightness distribution of emission lines taken as a strip across the nebula with AB7 in the center and the eastern and western edges on the left and right hand of the plot, respectively. This shows the asymmetry of N76, where the eastern edge is brighter than the western side. The `Cloudy` models prefer a slightly lower density for the western side.

Appendix B: 1.3 mm Continuum Observations of the Northern Molecular Ridge

Figure B.1 presents the 1.3 mm continuum emission in the northern molecular ridge from chapter 4. The continuum sources are very faint and contain emission from a combination of dust and free-free emission (e.g. Brunetti & Wilson, 2019). Separating out the dominant source of emission requires continuum observations at another frequency and goes beyond the scope of this work. We do, however, use this map to subtract the possible contamination of continuum on the spectral line data analyzed in chapter 4.

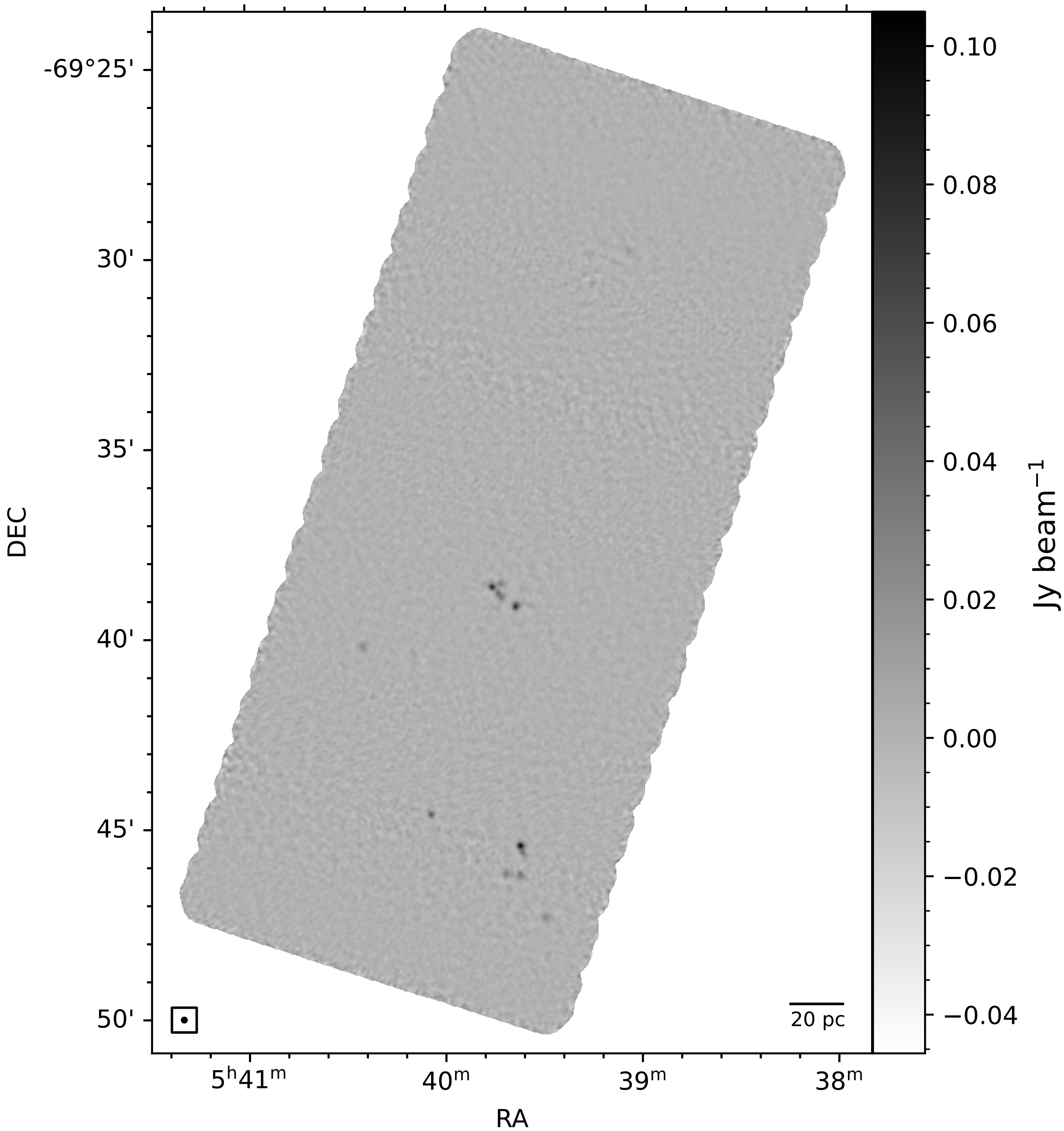

Figure B.1: Continuum image at 1.3 mm of the northern molecular ridge

Appendix C: Facilities and Software used in this Thesis

C.1 Facilities

1. ALMA
2. DSS
3. Herschel/PACS
4. IRAM
5. Spitzer/IRAC
6. Spitzer/IRS
7. SOFIA/GREAT
8. VLA

C.2 Software

1. APLpy (Robitaille & Bressert, 2012)
2. Astropy (The Astropy Collaboration et al., 2018)
3. CASA (The CASA Team et al., 2022)

4. CLASS/GILDAS (Gildas Team, 2013; Pety, 2005)
5. Cloudy (Ferland et al., 2017)
6. CUBISM (Smith et al., 2007a)
7. FilFinder (Koch & Rosolowsky, 2015)
8. MatPlotLib (Barrett et al., 2005)
9. NumPy (Harris et al., 2020)
10. PAHFIT (Smith et al., 2007b)
11. pandas (Reback et al., 2022)
12. PoWR (Gräfener et al., 2002; Hainich et al., 2019; Hamann & Gräfener, 2003, 2004; Sander et al., 2015)
13. pycprops (Rosolowsky et al., 2021; Rosolowsky & Leroy, 2006)
14. SciPy (Virtanen et al., 2020)
15. seaborn (Waskom et al., 2014)
16. scikit-image (van der Walt et al., 2014)
17. SpectralCube (Ginsburg et al., 2019)
18. sTinyTim (Krist, 1995)

Bibliography

Accurso, G., Saintonge, A., Catinella, B., Cortese, L., Davé, R., Dunsheath, S. H., Genzel, R., Gracia-Carpio, J., Heckman, T. M., Jimmy, , Kramer, C., Li, C., Lutz, K., Schiminovich, D., Schuster, K., Sternberg, A., Sturm, E., Tacconi, L. J., Tran, K. V., Wang, J. Deriving a multivariate α_{CO} conversion function using the [C II]/CO (1-0) ratio and its application to molecular gas scaling relations MNRAS. 2017. 470, 4 4750–4766.

Anand, G. S., Rizzi, L., Tully, R. B. A Robust Tip of the Red Giant Branch Distance to the Fireworks Galaxy (NGC 6946) AJ. 2018. 156, 3 105.

Aniano, G., Draine, B. T., Gordon, K. D., Sandstrom, K. Common-Resolution Convolution Kernels for Space- and Ground-Based Telescopes Publications of the Astronomical Society of the Pacific. 2011. 123, 908 1218–1236.

Aniano, G., Draine, B. T., Hunt, L. K., Sandstrom, K., Calzetti, D., Kennicutt, R. C., Dale, D. A., Galametz, M., Gordon, K. D., Leroy, A. K., Smith, J. D. T., Roussel, H., Sauvage, M., Walter, F., Armus, L., Bolatto, A. D., Boquien, M., Crocker, A., De Looze, I., Donovan Meyer, J., Helou, G., Hinz, J., Johnson, B. D., Koda, J., Miller, A., Montiel, E., Murphy, E. J., Relaño, M., Rix, H. W., Schinnerer, E., Skibba, R., Wolfire, M. G., Engelbracht, C. W. Modeling Dust and Starlight in Galaxies Observed by Spitzer and Herschel: The KINGFISH Sample ApJ. 2020. 889, 2 150.

Ardila, D. R., Van Dyk, S. D., Makowiecki, W., Stauffer, J., Song, I., Rho, J., Fajardo-Acosta, S., Hoard, D. W., Wachter, S. The Spitzer Atlas of Stellar Spectra (SASS) ApJS. 2010. 191, 2 301–339.

Atek, H., Siana, B., Scarlata, C., Malkan, M., McCarthy, P., Teplitz, H., Henry, A., Colbert, J., Bridge, C., Bunker, A. J., Dressler, A., Fosbury, R. A. E., Hathi, N. P., Martin, C., Ross, N. R., Shim, H. Very Strong Emission-line Galaxies in the WFC3 Infrared Spectroscopic Parallel Survey and Implications for High-redshift Galaxies ApJ. 2011. 743, 2 121.

Baldwin, J. A., Phillips, M. M., Terlevich, R. Classification parameters for the emission-line spectra of extragalactic objects. PASP. 1981. 93 5–19.

Ballesteros-Paredes, J., Hartmann, L. W., Vázquez-Semadeni, E., Heitsch, F., Zamora-Avilés, M. A. Gravity or turbulence? Velocity dispersion-size relation MNRAS. 2011. 411, 1 65–70.

Barrera-Ballesteros, J. K., Sánchez, S. F., Heckman, T., Wong, T., Bolatto, A., Ostriker, E., Rosolowsky, E., Carigi, L., Vogel, S., Levy, R. C., Colombo, D., Luo, Y., Cao, Y., the EDGE-CALIFA team, . EDGE-CALIFA survey: Self-regulation of Star formation at kpc scales arXiv e-prints. 2021. arXiv:2101.04683.

Barrett, P., Hunter, J., Miller, J. T., Hsu, J.-C., Greenfield, P. matplotlib – A Portable Python Plotting Package Astronomical Data Analysis Software and Systems XIV. 347. 2005. 91. (Astronomical Society of the Pacific Conference Series).

Bennett, C. L., Fixsen, D. J., Hinshaw, G., Mather, J. C., Moseley, S. H., Wright, E. L., Eplee, J. R. E., Gales, J., Hewagama, T., Isaacman, R. B., Shafer, R. A., Turpie, K. Morphology of the Interstellar Cooling Lines Detected by COBE ApJ. 1994. 434 587.

Berg, D. A., Chisholm, J., Erb, D. K., Pogge, R., Henry, A., Olivier, G. M. Intense C IV and He II Emission in z $\sim$ 0 Galaxies: Probing High-energy Ionizing Photons ApJL. 2019. 878, 1 L3.

Bertoldi, F., McKee, C. F. Pressure-confined Clumps in Magnetized Molecular Clouds ApJ. 1992. 395 140.

Bigiel, F., de Looze, I., Krabbe, A., Cormier, D., Barnes, A. T., Fischer, C., Bolatto, A. D., Bryant, A., Colditz, S., Geis, N., Herrera-Camus, R., Iserlohe, C., Klein, R., Leroy, A. K., Linz, H., Looney, L. W., Madden, S. C., Poglitsch, A., Stutzki, J., Vacca, W. D. SOFIA/FIFI-LS Full-disk [CII] Mapping and CO-dark Molecular Gas across the Nearby Spiral Galaxy NGC 6946 arXiv e-prints. 2020. arXiv:2011.02498.

Blitz, L., Rosolowsky, E. The Role of Pressure in GMC Formation II: The H_2-Pressure Relation ApJ. 2006. 650, 2 933–944.

Bolatto, A. D., Jackson, J. M., Israel, F. P., Zhang, X., Kim, S. Carbon in the N159/N160 Complex of the Large Magellanic Cloud ApJ. 2000. 545, 1 234–250.

Bolatto, A. D., Leroy, A. K., Jameson, K., Ostriker, E., Gordon, K., Lawton, B., Stanimirović, S., Israel, F. P., Madden, S. C., Hony, S., Sandstrom, K. M., Bot, C., Rubio, M., Winkler, P. F., Roman-Duval, J., van Loon, J. T., Oliveira, J. M., Indebetouw, R. The State of the Gas and the Relation between Gas and Star Formation at Low Metallicity: The Small Magellanic Cloud ApJ. 2011. 741, 1 12.

Bolatto, A. D., Simon, J. D., Stanimirović, S., van Loon, J. T., Shah, R. Y., Venn, K., Leroy, A. K., Sand strom, K., Jackson, J. M., Israel, F. P., Li, A., Staveley-Smith, L., Bot, C., Boulanger, F., Rubio, M. The Spitzer Survey of the Small Magellanic Cloud: S^3MC Imaging and Photometry in the Mid- and Far-Infrared Wave Bands ApJ. 2007. 655, 1 212–232.

Bolatto, A. D., Wolfire, M., Leroy, A. K. ARA&A. 2013. 51, 1 207–268.

Bonanos, A. Z., Lennon, D. J., Köhlinger, F., van Loon, J. T., Massa, D. L., Sewilo, M., Evans, C. J., Panagia, N., Babler, B. L., Block, M., Bracker, S., Engelbracht, C. W., Gordon, K. D., Hora, J. L., Indebetouw, R., Meade, M. R., Meixner, M., Misselt, K. A., Robitaille, T. P., Shiao, B., Whitney, B. A. Spitzer SAGE-SMC Infrared Photometry of Massive Stars in the Small Magellanic Cloud AJ. 2010. 140, 2 416–429.

Boselli, A., Gavazzi, G., Lequeux, J., Pierini, D. [CII] at 158 mu m as a star formation tracer in late-type galaxies A&A. 2002. 385 454–463.

Bourke, T. L., Garay, G., Lehtinen, K. K., Köhnenkamp, I., Launhardt, R., Nyman, L.-Å., May, J., Robinson, G., Hyland, A. R. Discovery of a Highly Collimated Molecular Outflow in the Southern Bok Globule BHR 71 ApJ. 1997. 476, 2 781–800.

Braun, R., Walterbos, R. A. M. A solution to the short spacing problem in radio interferometry. A&A. 1985. 143 307–312.

Brunetti, N., Wilson, C. D. An ALMA archival study of the clump mass function in the Large Magellanic Cloud MNRAS. 2019. 483, 2 1624–1641.

Calzetti, D., Kennicutt, R. C., Engelbracht, C. W., Leitherer, C., Draine, B. T., Kewley, L., Moustakas, J., Sosey, M., Dale, D. A., Gordon, K. D., Helou, G. X., Hollenbach, D. J., Armus, L., Bendo, G., Bot, C., Buckalew, B., Jarrett, T., Li, A., Meyer, M., Murphy, E. J., Prescott, M., Regan, M. W., Rieke, G. H., Roussel, H., Sheth, K., Smith, J. D. T., Thornley, M. D., Walter, F. The Calibration of Mid-Infrared Star Formation Rate Indicators ApJ. 2007. 666, 2 870–895.

Calzetti, D. Star Formation Rate Indicators Secular Evolution of Galaxies. 2013. 419.

Chevance, M., Madden, S. C., Fischer, C., Vacca, W. D., Lebouteiller, V., Fadda, D., Galliano, F., Indebetouw, R., Kruijssen, J. M. D., Lee, M.-Y., Poglitsch, A., Polles, F. L., Cormier, D., Hony, S., Iserlohe, C., Krabbe, A., Meixner, M., Sabbi, E., Zinnecker, H. The CO-dark molecular gas mass in 30 Doradus MNRAS. 2020. 494, 4 5279–5292.

Chu, Y. H. Galactic ring nebulae associated with Wolf-rayet stars. I. Introduction and classification. ApJ. 1981. 249 195–200.

Chu, Y. H., Treffers, R. R., Kwitter, K. B. Galactic ring nebulae associated with Wolf-Rayet stars. VIII. Summaryand atlas. ApJS. 1983. 53 937–944.

Cohen, R. S., Dame, T. M., Garay, G., Montani, J., Rubio, M., Thaddeus, P. A Complete Survey of the Large Magellanic Cloud ApJL. 1988. 331 L95.

Contursi, A., Kaufman, M. J., Helou, G., Hollenbach, D. J., Brauher, J., Stacey, G. J., Dale, D. A., Malhotra, S., Rubio, M., Rubin, R. H., Lord, S. D. ISO LWS Observations of the Two Nearby Spiral Galaxies NGC 6946 and NGC 1313 AJ. 2002. 124, 2 751–776.

Cormier, D., Abel, N. P., Hony, S., Lebouteiller, V., Madden, S. C., Polles, F. L., Galliano, F., De Looze, I., Galametz, M., Lambert-Huyghe, A. The Herschel Dwarf Galaxy Survey. II. Physical conditions, origin of [C II] emission, and porosity of the multiphase low-metallicity ISM A&A. 2019. 626 A23.

Cormier, D., Madden, S. C., Lebouteiller, V., Abel, N., Hony, S., Galliano, F., Rémy-Ruyer, A., Bigiel, F., Baes, M., Boselli, A., Chevance, M., Cooray, A., De Looze, I., Doublier, V., Galametz, M., Hughes, T., Karczewski, O. Ł., Lee, M. Y., Lu, N., Spinoglio, L. The Herschel Dwarf Galaxy Survey. I. Properties of the low-metallicity ISM from PACS spectroscopy A&A. 2015. 578 A53.

Crawford, M. K., Genzel, R., Townes, C. H., Watson, D. M. Far-infrared spectroscopy of galaxies : the 158 micron C+ line and the energy balance of molecular clouds. ApJ. 1985. 291 755–771.

Crowther, P. A., Hadfield, L. J. Reduced Wolf-Rayet line luminosities at low metallicity A&A. 2006. 449, 2 711–722.

Crowther, P. A., Beck, S. C., Willis, A. J., Conti, P. S., Morris, P. W., Sutherland, R. S. Properties of hot stars in the Wolf-Rayet galaxy NGC 5253 from ISO-SWS spectroscopy MNRAS. 1999. 304, 3 654–668.

Croxall, K. V., Smith, J. D., Pellegrini, E., Groves, B., Bolatto, A., Herrera-Camus, R., Sand strom, K. M., Draine, B., Wolfire, M. G., Armus, L., Boquien, M., Brandl, B., Dale, D., Galametz, M., Hunt, L., Kennicutt, J. R., Kreckel, K., Rigopoulou, D., van der Werf, P., Wilson, C. The Origins of [C II] Emission in Local Star-forming Galaxies ApJ. 2017. 845, 2 96.

Croxall, K. V., Smith, J. D., Brandl, B. R., Groves, B. A., Kennicutt, R. C., Kreckel, K., Johnson, B. D., Pellegrini, E., Sandstrom, K. M., Walter, F., Armus, L., Beirão, P., Calzetti, D., Dale, D. A., Galametz, M., Hinz, J. L., Hunt, L. K., Koda, J., Schinnerer, E. Toward a Removal of Temperature Dependencies from Abundance Determinations: NGC 628 ApJ. 2013. 777, 2 96.

Dabrowski, I. The Lyman and Werner bands of H_2 Canadian Journal of Physics. 1984. 62 1639.

Dale, D. A., Smith, J. D. T., Schlawin, E. A., Armus, L., Buckalew, B. A., Cohen, S. A., Helou, G., Jarrett, T. H., Johnson, L. C., Moustakas, J., Murphy, E. J., Roussel, H., Sheth, K., Staudaher, S., Bot, C., Calzetti, D., Engelbracht, C. W., Gordon, K. D., Hollenbach, D. J., Kennicutt, R. C., Malhotra, S. The Spitzer Infrared Nearby Galaxies Survey: A High-Resolution Spectroscopy Anthology ApJ. 2009. 693, 2 1821–1834.

De Looze, I., Cormier, D., Lebouteiller, V., Madden, S., Baes, M., Bendo, G. J., Boquien, M., Boselli, A., Clements, D. L., Cortese, L., Cooray, A., Galametz, M., Galliano, F., Graciá-Carpio, J., Isaak, K., Karczewski, O. Ł., Parkin, T. J., Pellegrini, E. W., Rémy-Ruyer, A., Spinoglio, L., Smith, M. W. L., Sturm, E. The applicability of far-infrared fine-structure lines as star formation rate tracers over wide ranges of metallicities and galaxy types A&A. 2014. 568 A62.

Dessauges-Zavadsky, M., Ginolfi, M., Pozzi, F., Béthermin, M., Le Fèvre, O., Fujimoto, S., Silverman, J. D., Jones, G. C., Vallini, L., Schaerer, D., Faisst, A. L., Khusanova, Y., Fudamoto, Y., Cassata, P., Loiacono, F., Capak, P. L., Yan, L., Amorin, R., Bardelli, S., Boquien, M., Cimatti, A., Gruppioni, C., Hathi, N. P., Ibar, E., Koekemoer, A. M., Lemaux, B. C., Narayanan, D., Oesch, P. A., Rodighiero, G., Romano, M., Talia, M., Toft, S., Vergani, D., Zamorani, G., Zucca, E. The ALPINE-ALMA [C II] survey. Molecular gas budget in the early Universe as traced by [C II] A&A. 2020. 643 A5.

Dib, S., Kim, J., Vázquez-Semadeni, E., Burkert, A., Shadmehri, M. The Virial Balance of Clumps and Cores in Molecular Clouds ApJ. 2007. 661, 1 262–284.

Dickey, J. M., Strasser, S., Gaensler, B. M., Haverkorn, M., Kavars, D., McClure-Griffiths, N. M., Stil, J., Taylor, A. R. The Outer Disk of the Milky Way Seen in λ21 cm Absorption ApJ. 2009. 693, 2 1250–1260.

Dimaratos, A., Cormier, D., Bigiel, F., Madden, S. C. Modeling the physical properties in the ISM of the low-metallicity galaxy NGC 4214 A&A. 2015. 580 A135.

Dopita, M. A. A law of star formation in disk galaxies : evidence for sel-regulating feedback. ApJL. 1985. 295 L5–L8.

Draine, B. T. Photoelectric heating of interstellar gas. ApJS. 1978. 36 595–619.

Draine, B. T., Bertoldi, F. Structure of Stationary Photodissociation Fronts ApJ. 1996. 468 269.

Draine, B. T., Dale, D. A., Bendo, G., Gordon, K. D., Smith, J. D. T., Armus, L., Engelbracht, C. W., Helou, G., Kennicutt, J. R. C., Li, A., Roussel, H., Walter, F., Calzetti, D., Moustakas, J., Murphy, E. J., Rieke, G. H., Bot, C., Hollenbach, D. J., Sheth, K., Teplitz, H. I. Dust Masses, PAH Abundances, and Starlight Intensities in the SINGS Galaxy Sample ApJ. 2007. 663, 2 866–894.

Draine, B. T. Physics of the Interstellar and Intergalactic Medium. 2011.

Dudik, R. P., Weingartner, J. C., Satyapal, S., Fischer, J., Dudley, C. C., O'Halloran, B. Mid-Infrared Fine-Structure Line Ratios in Active Galactic Nuclei Observed with the Spitzer IRS: Evidence for Extinction by the Torus ApJ. 2007. 664, 1 71–87.

Dufour, R. J. The composition of H II regions in the Magellanic Clouds. Structure and Evolution of the Magellanic Clouds. 108. 1984. 353–361.

Dufton, P. L., Evans, C. J., Hunter, I., Lennon, D. J., Schneider, F. R. N. A census of massive stars in NGC 346. Stellar parameters and rotational velocities A&A. 2019. 626 A50.

Fahrion, K., Cormier, D., Bigiel, F., Hony, S., Abel, N. P., Cigan, P., Csengeri, T., Graf, U. U., Lebouteiller, V., Madden, S. C., Wu, R., Young, L. Disentangling the ISM phases of the dwarf galaxy NGC 4214 using [C II] SOFIA/GREAT observations A&A. 2017. 599 A9.

Ferland, G. J., Chatzikos, M., Guzmán, F., Lykins, M. L., van Hoof, P. A. M., Williams, R. J. R., Abel, N. P., Badnell, N. R., Keenan, F. P., Porter, R. L., Stancil, P. C. The 2017 Release Cloudy RMxAA. 2017. 53 385–438.

Fernández Arenas, D., Terlevich, E., Terlevich, R., Melnick, J., Chávez, R., Bresolin, F., Telles, E., Plionis, M., Basilakos, S. An independent determination of the local Hubble constant MNRAS. 2018. 474, 1 1250–1276.

Fernández-Martín, A., Martín-Gordón, D., Vílchez, J. M., Pérez Montero, E., Riera, A., Sánchez, S. F. Ionization structure and chemical abundances of the Wolf-Rayet nebula NGC 6888 with integral field spectroscopy A&A. 2012. 541 A119.

Field, G. B., Goldsmith, D. W., Habing, H. J. Cosmic-Ray Heating of the Interstellar Gas ApJL. 1969. 155 L149.

Field, G. B., Blackman, E. G., Keto, E. R. Does external pressure explain recent results for molecular clouds? MNRAS. 2011. 416, 1 710–714.

Finn, M. K., Indebetouw, R., Johnson, K. E., Costa, A. H., Chen, C. H. R., Kawamura, A., Onishi, T., Ott, J., Sewiło, M., Tokuda, K., Wong, T., Zahorecz, S. Structural and Dynamical Analysis of the Quiescent Molecular Ridge in the Large Magellanic Cloud AJ. 2022. 164, 2 64.

Finn, M. K., Indebetouw, R., Johnson, K. E., Costa, A. H., Chen, C. H. R., Kawamura, A., Onishi, T., Ott, J., Tokuda, K., Wong, T., Zahorecz, S. Physical Conditions in the LMC's Quiescent Molecular Ridge: Fitting Non-LTE Models to CO Emission ApJ. 2021. 917, 2 106.

Finn, M. K., Johnson, K. E., Brogan, C. L., Wilson, C. D., Indebetouw, R., Harris, W. E., Kamenetzky, J., Bemis, A. New Insights into the Physical Conditions and Internal Structure of a Candidate Proto-globular Cluster ApJ. 2019. 874, 2 120.

Freyer, T., Hensler, G., Yorke, H. W. Massive Stars and the Energy Balance of the Interstellar Medium. I. The Impact of an Isolated 60 M_{solar} Star ApJ. 2003. 594, 2 888–910.

Freyer, T., Hensler, G., Yorke, H. W. Massive Stars and the Energy Balance of the Interstellar Medium. II. The 35 M_{solar} Star and a Solution to the "Missing Wind Problem" ApJ. 2006. 638, 1 262–280.

Froese Fischer, C., Tachiev, G., Irimia, A. Relativistic energy levels, lifetimes, and transition probabilities for the sodium-like to argon-like sequences Atomic Data and Nuclear Data Tables. 2006. 92, 5 607–812.

Fujii, K., Minamidani, T., Mizuno, N., Onishi, T., Kawamura, A., Muller, E., Dawson, J., Tatematsu, K., Hasegawa, T., Tosaki, T., Miura, R. E., Muraoka, K., Sakai, T., Tsukagoshi, T., Tanaka, K., Ezawa, H., Fukui, Y. Dense Molecular Clumps Associated with the Large Magellanic Cloud Supergiant Shells LMC 4 and LMC 5 ApJ. 2014. 796, 2 123.

Fukui, Y., Kawamura, A., Minamidani, T., Mizuno, Y., Kanai, Y., Mizuno, N., Onishi, T., Yonekura, Y., Mizuno, A., Ogawa, H., Rubio, M. The Second Survey of the Molecular Clouds in the Large Magellanic Cloud by NANTEN. I. Catalog of Molecular Clouds ApJS. 2008. 178, 1 56–70.

Fukui, Y., Harada, R., Tokuda, K., Morioka, Y., Onishi, T., Torii, K., Ohama, A., Hattori, Y., Nayak, O., Meixner, M., Sewiło, M., Indebetouw, R., Kawamura, A., Saigo, K., Yamamoto, H., Tachihara, K., Minamidani, T., Inoue, T., Madden, S., Galametz, M., Lebouteiller, V., Mizuno, N., Chen, C. H. R. High-mass Star Formation Triggered by Collision between CO Filaments in N159 West in the Large Magellanic Cloud ApJL. 2015. 807, 1 L4.

Fukui, Y., Tokuda, K., Saigo, K., Harada, R., Tachihara, K., Tsuge, K., Inoue, T., Torii, K., Nishimura, A., Zahorecz, S., Nayak, O., Meixner, M., Minamidani, T., Kawamura, A., Mizuno, N., Indebetouw, R., Sewiło, M., Madden, S., Galametz, M., Lebouteiller, V., Chen, C. H. R., Onishi, T. An ALMA View of Molecular Filaments in the Large Magellanic Cloud. I. The Formation of High-mass Stars and Pillars in the N159E-Papillon Nebula Triggered by a Cloud-Cloud Collision ApJ. 2019. 886, 1 14.

Fukui, Y., Tsuge, K., Sano, H., Bekki, K., Yozin, C., Tachihara, K., Inoue, T. Formation of the young massive cluster R136 triggered by tidally-driven colliding H i flows PASJ. 2017. 69, 3 L5.

Garden, R. P., Hayashi, M., Gatley, I., Hasegawa, T., Kaifu, N. A Spectroscopic Study of the DR 21 Outflow Source. III. The CO Line Emission ApJ. 1991. 374 540.

Garnett, D. R., Kennicutt, J. Robert C., Chu, Y.-H., Skillman, E. D. He II Emission in Extragalactic H II Regions ApJ. 1991. 373 458.

Geis, N., Lutz, D. Herschel/PACS Modelled Point-Spread Functions. 2010.

Geist, E., Gallagher, J. S., Kotulla, R., Oskinova, L., Hamann, W. R., Ramachandran, V., Sabbi, E., Smith, L., Kniazev, A., Nota, A., Rickard, M. J. Ionization and Star Formation in the Giant H II Region SMC-N66 PASP. 2022. 134, 1036 064301.

Gerin, M., Ruaud, M., Goicoechea, J. R., Gusdorf, A., Godard, B., de Luca, M., Falgarone, E., Goldsmith, P., Lis, D. C., Menten, K. M., Neufeld, D., Phillips, T. G., Liszt, H. [C II] absorption and emission in the diffuse interstellar medium across the Galactic plane A&A. 2015. 573 A30.

Gildas Team, . GILDAS: Grenoble Image and Line Data Analysis Software. 2013. ascl:1305.010.

Ginsburg, A., Koch, E., Robitaille, T., Beaumont, C., Adamginsburg, , Sipőcz, B., ZuHone, J., Patra, S., Jones, C., Lim, P. L., Stern, K., Rosolowsky, E., Earl, N., De Val-Borro, M., Jrobbfed, , Shuokong, , Kepley, A., Sokolov, V., Badger, T. G., Maret, S., Garrido, J., Booker, J., Tollerud, E. radio-astro-tools/spectral-cube: Release v0.4.5. 2019.

Glover, S. C. O., Clark, P. C. Is molecular gas necessary for star formation? MNRAS. 2012. 421, 1 9–19.

Goldsmith, P. F., Langer, W. D., Pineda, J. L., Velusamy, T. Collisional Excitation of the [C II] Fine Structure Transition in Interstellar Clouds ApJS. 2012. 203, 1 13.

Goldsmith, P. F., Pineda, J. L., Neufeld, D. A., Wolfire, M. G., Risacher, C., Simon, R. Velocity-resolved [{{C}}\,{{II}}] Emission from Cold Diffuse Clouds in the Interstellar Medium ApJ. 2018. 856, 2 96.

Gordon, M. S., Jones, T. J., Gehrz, R. D., Helton, L. A. Massive Star Formation in the LMC. I. N159 and N160 Complexes ApJ. 2017. 834, 2 122.

Graczyk, D., Pietrzyński, G., Thompson, I. B., Gieren, W., Zgirski, B., Villanova, S., Górski, M., Wielgórski, P., Karczmarek, P., Narloch, W., Pilecki, B., Taormina, M., Smolec, R., Suchomska, K., Gallenne, A., Nardetto, N., Storm, J., Kudritzki, R.-P., Kałuszyński, M., Pych, W. A Distance Determination to the Small Magellanic Cloud with an Accuracy of Better than Two Percent Based on Late-type Eclipsing Binary Stars ApJ. 2020. 904, 1 13.

Gräfener, G., Koesterke, L., Hamann, W. R. Line-blanketed model atmospheres for WR stars A&A. 2002. 387 244–257.

Grenier, I. A., Casandjian, J.-M., Terrier, R. Unveiling Extensive Cl ouds of Dark Gas in the Solar Neighborhood Science. 2005. 307, 5713 1292–1295.

Guan, X., Stutzki, J., Graf, U. U., Güsten, R., Okada, Y., Requena-Torres, M. A., Simon, R., Wiesemeyer, H. GREAT/SOFIA atmospheric calibration A&A. 2012. 542 L4.

Guerrero, M. A., Chu, Y.-H. An X-Ray Survey of Wolf-Rayet Stars in the Magellanic Clouds. I. The Chandra ACIS Data Set ApJS. 2008. 177, 1 216–237.

Haas, M. R., Hollenbach, D., Erickson, E. F. Observations of [Si ii] (35 Micron) and [S i] (25 Micron) in Orion: Evidence for a Wind Shock near IRc2 ApJ. 1991. 374 555.

Haffner, L. M., Dettmar, R. J., Beckman, J. E., Wood, K., Slavin, J. D., Giammanco, C., Madsen, G. J., Zurita, A., Reynolds, R. J. The warm ionized medium in spiral galaxies Reviews of Modern Physics. 2009. 81, 3 969–997.

Hainich, R., Ramachandran, V., Shenar, T., Sander, A. A. C., Todt, H., Gruner, D., Oskinova, L. M., Hamann, W. R. PoWR grids of non-LTE model atmospheres for OB-type stars of various metallicities A&A. 2019. 621 A85.

Hamann, W. R., Gräfener, G. A temperature correction method for expanding atmospheres A&A. 2003. 410 993–1000.

Hamann, W. R., Gräfener, G. Grids of model spectra for WN stars, ready for use A&A. 2004. 427 697–704.

Harris, C. R., Millman, K. J., van der Walt, S. J., Gommers, R., Virtanen, P., Cournapeau, D., Wieser, E., Taylor, J., Berg, S., Smith, N. J., Kern, R., Picus, M., Hoyer, S., van Kerkwijk, M. H., Brett, M., Haldane, A., Fernández del Río, J., Wiebe, M., Peterson, P., Gérard-Marchant, P., Sheppard, K., Reddy, T., Weckesser, W., Abbasi, H., Gohlke, C., Oliphant, T. E. Array Programming with NumPy Nature. 2020. 585 357–362.

Hayward, C. C., Hopkins, P. F. How stellar feedback simultaneously regulates star formation and drives outflows MNRAS. 2017. 465, 2 1682–1698.

Heikkilä, A., Johansson, L. E. B., Olofsson, H. Molecular abundance variations in the Magellanic Clouds A&A. 1999. 344 817–847.

Heiles, C. On the Origin of the Diffuse C + 158 Micron Line Emission ApJ. 1994. 436 720.

Heiles, C., Troland, T. H. The Millennium Arecibo 21 Centimeter Absorption-Line Survey. II. Properties of the Warm and Cold Neutral Media ApJ. 2003. 586, 2 1067–1093.

Henize, K. G. Catalogues of Hα-emission Stars and Nebulae in the Magellanic Clouds. ApJS. 1956. 2 315.

Herrera-Camus, R., Bolatto, A., Wolfire, M., Ostriker, E., Draine, B., Leroy, A., Sandstrom, K., Hunt, L., Kennicutt, R., Calzetti, D., Smith, J. D., Croxall, K., Galametz, M., de Looze, I., Dale, D., Crocker, A., Groves, B. Thermal Pressure in the Cold Neutral Medium of Nearby Galaxies ApJ. 2017. 835, 2 201.

Herrera-Camus, R., Bolatto, A. D., Wolfire, M. G., Smith, J. D., Croxall, K. V., Kennicutt, R. C., Calzetti, D., Helou, G., Walter, F., Leroy, A. K., Draine, B., Brandl, B. R., Armus, L., Sand strom, K. M., Dale, D. A., Aniano, G., Meidt, S. E., Boquien, M., Hunt, L. K., Galametz, M., Tabatabaei, F. S., Murphy, E. J., Appleton, P., Roussel, H., Engelbracht, C., Beirao, P. [C II] 158 μm Emission as a Star Formation Tracer ApJ. 2015. 800, 1 1.

Herrera-Camus, R., Sturm, E., Graciá-Carpio, J., Lutz, D., Contursi, A., Veilleux, S., Fischer, J., González-Alfonso, E., Poglitsch, A., Tacconi, L., Genzel, R., Maiolino, R., Sternberg, A., Davies, R., Verma, A. SHINING, A Survey of Far-infrared Lines in Nearby Galaxies. II. Line-deficit Models, AGN Impact, [C II]-SFR Scaling Relations, and Mass-Metallicity Relation in (U)LIRGs ApJ. 2018. 861, 2 95.

Heyer, M., Krawczyk, C., Duval, J., Jackson, J. M. Re-Examining Larson's Scaling Relationships in Galactic Molecular Clouds ApJ. 2009. 699, 2 1092–1103.

Heyminck, S., Graf, U. U., Güsten, R., Stutzki, J., Hübers, H. W., Hartogh, P. GREAT: the SOFIA high-frequency heterodyne instrument A&A. 2012. 542 L1.

Hollenbach, D. J., Tielens, A. G. G. M. Photodissociation regions in the interstellar medium of galaxies Reviews of Modern Physics. 1999. 71, 1 173–230.

Hoopes, C. G., Walterbos, R. A. M., Bothun, G. D. Far-Ultraviolet and Hα Imaging of Nearby Spiral Galaxies: The OB Stellar Population in the Diffuse Ionized Gas ApJ. 2001. 559, 2 878–891.

Hughes, A., Wong, T., Ott, J., Muller, E., Pineda, J. L., Mizuno, Y., Bernard, J. P., Paradis, D., Maddison, S., Reach, W. T., Staveley-Smith, L., Kawamura, A., Meixner, M., Kim, S., Onishi, T., Mizuno, N., Fukui, Y. Physical properties of giant molecular clouds in the Large Magellanic Cloud MNRAS. 2010. 406, 3 2065–2086.

Hung, C. S., Ou, P.-S., Chu, Y.-H., Gruendl, R. A., Li, C.-J. A Multiwavelength Survey of Wolf-Rayet Nebulae in the Large Magellanic Cloud ApJS. 2021. 252, 2 21.

Hunt, L. K., Thuan, T. X., Izotov, Y. I., Sauvage, M. The Spitzer View of Low-Metallicity Star Formation. III. Fine-Structure Lines, Aromatic Features, and Molecules ApJ. 2010. 712, 1 164–187.

Hurley, J. R., Pols, O. R., Tout, C. A. Comprehensive analytic formulae for stellar evolution as a function of mass and metallicity MNRAS. 2000. 315, 3 543–569.

Inami, H., Armus, L., Charmandaris, V., Groves, B., Kewley, L., Petric, A., Stierwalt, S., Díaz-Santos, T., Surace, J., Rich, J., Haan, S., Howell, J., Evans, A. S., Mazzarella, J., Marshall, J., Appleton, P., Lord, S., Spoon, H., Frayer, D., Matsuhara, H., Veilleux, S. Mid-infrared Atomic Fine-structure Emission-line Spectra of Luminous Infrared Galaxies: Spitzer/IRS Spectra of the GOALS Sample ApJ. 2013. 777, 2 156.

Indebetouw, R., Whitney, B. A., Kawamura, A., Onishi, T., Meixner, M., Meade, M. R., Babler, B. L., Hora, J. L., Gordon, K., Engelbracht, C., Block, M., Misselt, K. The Large Magellanic Cloud's Largest Molecular Cloud Complex: Spitzer Analysis of Embedded Star Formation AJ. 2008. 136, 4 1442–1454.

Indebetouw, R., de Messières, G. E., Madden, S., Engelbracht, C., Smith, J. D., Meixner, M., Brandl, B., Smith, L. J., Boulanger, F., Galliano, F., Gordon, K., Hora, J. L., Sewilo, M., Tielens, A. G. G. M., Werner, M., Wolfire, M. G. Physical Conditions in the Ionized Gas of 30 Doradus ApJ. 2009. 694, 1 84–106.

Indebetouw, R., Brogan, C., Chen, C. H. R., Leroy, A., Johnson, K., Muller, E., Madden, S., Cormier, D., Galliano, F., Hughes, A., Hunter, T., Kawamura, A., Kepley, A., Lebouteiller, V., Meixner, M., Oliveira, J. M., Onishi, T., Vasyunina, T. ALMA Resolves 30 Doradus: Sub-parsec Molecular Cloud Structure near the Closest Super Star Cluster ApJ. 2013. 774, 1 73.

Indebetouw, R., Wong, T., Chen, C. H. R., Kepley, A., Lebouteiller, V., Madden, S., Oliveira, J. M. Structural and Dynamical Analysis of 0.1 pc Cores and Filaments in the 30 Doradus-10 Giant Molecular Cloud ApJ. 2020. 888, 2 56.

Jameson, K. E., Bolatto, A. D., Wolfire, M., Warren, S. R., Herrera-Camus, R., Croxall, K., Pellegrini, E., Smith, J.-D., Rubio, M., Indebetouw, R., Israel, F. P., Meixner, M., Roman-Duval, J., van Loon, J. T., Muller, E., Verdugo, C., Zinnecker, H., Okada, Y. First Results from the Herschel and ALMA Spectroscopic Surveys of the SMC: The Relationship between [C II]-bright Gas and CO-bright Gas at Low Metallicity ApJ. 2018. 853, 2 111.

Jenkins, E. B., Tripp, T. M. The Distribution of Thermal Pressures in the Diffuse, Cold Neutral Medium of Our Galaxy. II. An Expanded Survey of Interstellar C I Fine-structure Excitations ApJ. 2011. 734, 1 65.

Jenkins, E. B., Wallerstein, G. Interstellar Gas-phase Element Depletions in the Small Magellanic Cloud: A Guide to Correcting for Dust in QSO Absorption Line Systems ApJ. 2017. 838, 2 85.

Johnson, K. E., Leroy, A. K., Indebetouw, R., Brogan, C. L., Whitmore, B. C., Hibbard, J., Sheth, K., Evans, A. S. The Physical Conditions in a Pre-super Star Cluster Molecular Cloud in the Antennae Galaxies ApJ. 2015. 806, 1 35.

Kaufman, M. J., Wolfire, M. G., Hollenbach, D. J. [Si II], [Fe II], [C II], and H_2 Emission from Massive Star-forming Regions ApJ. 2006. 644, 1 283–299.

Kennicutt, J. Robert C. The Global Schmidt Law in Star-forming Galaxies ApJ. 1998. 498, 2 541–552.

Kennicutt, J. Robert C., Armus, L., Bendo, G., Calzetti, D., Dale, D. A., Draine, B. T., Engelbracht, C. W., Gordon, K. D., Grauer, A. D., Helou, G., Hollenbach, D. J., Jarrett, T. H., Kewley, L. J., Leitherer, C., Li, A., Malhotra, S., Regan, M. W., Rieke, G. H., Rieke, M. J., Roussel, H., Smith, J.-D. T., Thornley, M. D., Walter, F. SINGS: The SIRTF Nearby Galaxies Survey PASP. 2003. 115, 810 928–952.

Kennicutt, J. Robert C., Hao, C.-N., Calzetti, D., Moustakas, J., Dale, D. A., Bendo, G., Engelbracht, C. W., Johnson, B. D., Lee, J. C. Dust-corrected Star Formation Rates of Galaxies. I. Combinations of Hα and Infrared Tracers ApJ. 2009. 703, 2 1672–1695.

Kennicutt, J. Robert C., Lee, J. C., Funes, J. G., J., S., Sakai, S., Akiyama, S. An Hα Imaging Survey of Galaxies in the Local 11 Mpc Volume ApJS. 2008. 178, 2 247–279.

Kennicutt, R. C., Calzetti, D., Aniano, G., Appleton, P., Armus, L., Beirão, P., Bolatto, A. D., Brandl, B., Crocker, A., Croxall, K., Dale, D. A., Donovan Meyer, J., Draine, B. T., Engelbracht, C. W., Galametz, M., Gordon, K. D., Groves, B., Hao, C. N., Helou, G., Hinz, J., Hunt, *L. K., Johnson, B., Koda, J., Krause, O., Leroy, A. K., Li, Y., Meidt, S., Montiel, E., Murphy, E. J., Rahman, N., Rix, H. W., Roussel, H., Sandstrom, K., Sauvage, M., Schinnerer, E., Skibba, R., Smith, J. D. T., Srinivasan, S., Vigroux, L., Walter, F., Wilson, C. D., Wolfire, M., Zibetti, S.* KINGFISH—Key Insights on Nearby Galaxies: A Far-Infrared Survey with Herschel: Survey Description and Image Atlas PASP. 2011. 123, 910 1347.

Kennicutt, R. C., Evans, N. J. Star Formation in the Milky Way and Nearby Galaxies ARA&A. 2012. 50 531–608.

Kim, C.-G., Kim, W.-T., Ostriker, E. C. Regulation of Star Formation Rates in Multiphase Galactic Disks: Numerical Tests of the Thermal/Dynamical Equilibrium Model ApJ. 2011. 743, 1 25.

Kim, S., Reach, W. T. The Origin of Far-Infrared [C II] Emission in the Large Magellanic Cloud ApJ. 2002. 571, 1 288–292.

Koch, E. W., Rosolowsky, E. W. Filament identification through mathematical morphology MNRAS. 2015. 452, 4 3435–3450.

Kramer, C., Abreu-Vicente, J., García-Burillo, S., Relaño, M., Aalto, S., Boquien, M., Braine, J., Buchbender, C., Gratier, P., Israel, F. P., Nikola, T., Röllig, M., Verley, S., van der Werf, P., Xilouris, E. M. Gas and dust cooling along the major axis of M 33 (HerM33es). ISO/LWS [C ii] observations A&A. 2013. 553 A114.

Kreckel, K., Ho, I. T., Blanc, G. A., Glover, S. C. O., Groves, B., Rosolowsky, E., Bigiel, F., Boquíen, M., Chevance, M., Dale, D. A., Deger, S., Emsellem, E., Grasha, K., Kim, J. J., Klessen, R. S., Kruijssen, J. M. D., Lee, J. C., Leroy, A. K., Liu, D., McElroy, R., Meidt, S. E., Pessa, I., Sanchez-Blazquez, P., Sandstrom, K., Santoro, F., Scheuermann, F., Schinnerer, E., Schruba, A., Utomo, D., Watkins, E. J., Williams, T. G. Measuring the mixing scale of the ISM within nearby spiral galaxies MNRAS. 2020. 499, 1 193–209.

Krist, J. E. WFPC2 Ghosts, Scatter and PSF Field Dependence Calibrating Hubble Space Telescope. Post Servicing Mission. 1995. 311.

Krumholz, M. R. Star Formation in Atomic Gas ApJ. 2012. 759, 1 9.

Krumholz, M. R., McKee, C. F., Bland-Hawthorn, J. Star Clusters Across Cosmic Time ARA&A. 2019. 57 227–303.

Kulkarni, S. R., Heiles, C. The Atomic Component Interstellar Processes, Proceedings of a symposium, held at Grand Teton National Park, Wyo., July, 1986, Dordrecht: Reidel, 1987, edited by David J. Hollenbach, and Harley A. Thronson. Astrophysics and Space Science Library, Vol. 134, p.87. 134. 1987. 87.

Kutner, M. L., Rubio, M., Booth, R. S., Boulanger, F., de Graauw, T., Garay, G., Israel, F. P., Johansson, L. E. B., Lequeux, J., Nyman, L. A. Results of the ESO-SEST key programme: CO in the Magellanic Clouds. VI. The 30 DOR Complex A&AS. 1997. 122 255–266.

Langer, W. D., Velusamy, T., Pineda, J. L., Willacy, K., Goldsmith, P. F. A Herschel [C ii] Galactic plane survey. II. CO-dark H_2 in clouds A&A. 2014. 561 A122.

Langer, W. D., Penzias, A. A. 12C/ 13C Isotope Ratio across the Galaxy from Observations of 13C 18O in Molecular Clouds ApJ. 1990. 357 477.

Larson, R. B. Turbulence and star formation in molecular clouds. MNRAS. 1981. 194 809–826.

Lasker, B. M. Digitization Programs at STScI Astronomy from Wide-Field Imaging. 161. 1994. 167.

Le Fèvre, O., Béthermin, M., Faisst, A., Jones, G. C., Capak, P., Cassata, P., Silverman, J. D., Schaerer, D., Yan, L., Amorin, R., Bardelli, S., Boquien, M., Cimatti, A., Dessauges-Zavadsky, M., Giavalisco, M., Hathi, N. P., Fudamoto, Y., Fujimoto, S., Ginolfi, M., Gruppioni, C., Hemmati, S., Ibar, E., Koekemoer, A., Khusanova, Y., Lagache, G., Lemaux, B. C., Loiacono, F., Maiolino, R., Mancini, C., Narayanan, D., Morselli, L., Méndez-Hernàndez, H., Oesch, P. A., Pozzi, F., Romano, M., Riechers, D., Scoville, N., Talia, M., Tasca, L. A. M., Thomas, R., Toft, S., Vallini, L., Vergani, D., Walter, F., Zamorani, G., Zucca, E. The ALPINE-ALMA [CII] survey. Survey strategy, observations, and sample properties of 118 star-forming galaxies at 4 ¡ z ¡ 6 A&A. 2020. 643 A1.

Lebouteiller, V., Cormier, D., Madden, S. C., Galametz, M., Hony, S., Galliano, F., Chevance, M., Lee, M. Y., Braine, J., Polles, F. L., Requeña-Torres, M. A., Indebetouw, R., Hughes, A., Abel, N. Physical conditions in the gas phases of the giant H II region LMC-N 11. II. Origin of [C II] and fraction of CO-dark gas A&A. 2019. 632 A106.

Lee, J. C., Gil de Paz, A., Tremonti, C., Kennicutt, J. Robert C., Salim, S., Bothwell, M., Calzetti, D., Dalcanton, J., Dale, D., Engelbracht, C., Funes, S. J. J. G., Johnson, B., Sakai, S., Skillman, E., van Zee, L., Walter, F., Weisz, D. Comparison of Hα and UV Star Formation Rates in the Local Volume: Systematic Discrepancies for Dwarf Galaxies ApJ. 2009. 706, 1 599–613.

Lequeux, J., Le Bourlot, J., Pineau des Forets, G., Roueff, E., Boulanger, F., Rubio, M. Results of the ESO-SEST Key Programme: CO in the Magellanic Clouds. IV. Physical properties of molecular clouds in the Small Magellanic Cloud. A&A. 1994. 292 371–380.

Leroy, A., Bolatto, A., Stanimirovic, S., Mizuno, N., Israel, F., Bot, C. The Spitzer Survey of the Small Magellanic Cloud: Far-Infrared Emission and Cold Gas in the Small Magellanic Cloud ApJ. 2007. 658, 2 1027–1046.

Leroy, A. K., Bigiel, F., de Blok, W. J. G., Boissier, S., Bolatto, A., Brinks, E., Madore, B., Munoz-Mateos, J.-C., Murphy, E., Sandstrom, K., Schruba, A., Walter, F. Estimating the Star Formation Rate at 1 kpc Scales in nearby Galaxies AJ. 2012. 144, 1 3.

Leroy, A. K., Hughes, A., Liu, D., Pety, J., Rosolowsky, E., Saito, T., Schinnerer, E., Schruba, A., Usero, A., Faesi, C. M., Herrera, C. N., Chevance, M., Hygate, A. P. S., Kepley, A. A., Koch, E. W., Querejeta, M., Sliwa, K., Will, D., Wilson, C. D., Anand, G. S., Barnes, A., Belfiore, F., Bešlić, I., Bigiel, F., Blanc, G. A., Bolatto, A. D., Boquien, M., Cao, Y., Chandar, R., Chastenet, J., Chiang, I.-D., Congiu, E., Dale, D. A., Deger, S., den Brok, J. S., Eibensteiner, C., Emsellem, E., García-Rodríguez, A., Glover, S. C. O., Grasha, K., Groves, B., Henshaw, J. D., Jiménez Donaire, M. J., Kim, J., Klessen, R. S., Kreckel, K., Kruijssen, J. M. D., Larson, K. L., Lee, J. C., Mayker, N., McElroy, R., Meidt, S. E., Mok, A., Pan, H.-A., Puschnig, J., *Razza, A., Sánchez-Bl'azquez, P., Sandstrom, K. M., Santoro, F., Sardone, A., Scheuermann, F., Sun, J., Thilker, D. A., Turner, J. A., Ubeda, L., Utomo, D., Watkins, E. J., Williams, T. G.* PHANGS-ALMA Data Processing and Pipeline ApJS. 2021. 255, 1 19.

Leroy, A. K., Walter, F., Bigiel, F., Usero, A., Weiss, A., Brinks, E., de Blok, W. J. G., Kennicutt, R. C., Schuster, K.-F., Kramer, C., Wiesemeyer, H. W., Roussel, H. Heracles: The HERA CO Line Extragalactic Survey AJ. 2009. 137, 6 4670–4696.

Leroy, A. K., Walter, F., Sandstrom, K., Schruba, A., Munoz-Mateos, J.-C., Bigiel, F., Bolatto, A., Brinks, E., de Blok, W. J. G., Meidt, S., Rix, H.-W., Rosolowsky, E., Schinnerer, E., Schuster, K.-F., Usero, A. Molecular Gas and Star Formation in nearby Disk Galaxies AJ. 2013. 146, 2 19.

Lopez, L. A., Krumholz, M. R., Bolatto, A. D., Prochaska, J. X., Ramirez-Ruiz, E. What Drives the Expansion of Giant H II Regions?: A Study of Stellar Feedback in 30 Doradus ApJ. 2011. 731, 2 91.

Lopez, L. A., Krumholz, M. R., Bolatto, A. D., Prochaska, J. X., Ramirez-Ruiz, E., Castro, D. The Role of Stellar Feedback in the Dynamics of H II Regions ApJ. 2014. 795, 2 121.

Madden, S. C., Cormier, D., Hony, S., Lebouteiller, V., Abel, N., Galametz, M., De Looze, I., Chevance, M., Polles, F. L., Lee, M. Y., Galliano, F., Lambert-Huyghe, A., Hu, D., Ramambason, L. Tracing the total molecular gas in galaxies: [CII] and the CO-dark gas A&A. 2020. 643 A141.

Madden, S. C., Geis, N., Genzel, R., Herrmann, F., Jackson, J., Poglitsch, A., Stacey, G. J., Townes, C. H. 158 Micron [C ii] Mapping of NGC 6946: Probing the Atomic Medium ApJ. 1993. 407 579.

Madden, S. C., Poglitsch, A., Geis, N., Stacey, G. J., Townes, C. H. [C II] 158 Micron Observations of IC 10: Evidence for Hidden Molecular Hydrogen in Irregular Galaxies ApJ. 1997. 483, 1 200–209.

Makiuti, S., Shibai, H., Nakagawa, T., Okuda, H., Okumura, K., Matsuhara, H., Hiromoto, N., Doi, Y. Diffuse far-infrared [C II] line emission from high Galactic latitude A&A. 2002. 382 600–609.

Maloney, P., Black, J. H. I CO/N(H 2) Conversions and Molecular Gas Abundances in Spiral and Irregular Galaxies ApJ. 1988. 325 389.

Martín-Hernández, N. L., Vermeij, R., Tielens, A. G. G. M., van der Hulst, J. M., Peeters, E. The stellar content, metallicity and ionization structure of H II regions A&A. 2002. 389 286–294.

Martins, F. UV, optical and near-IR diagnostics of massive stars Bulletin de la Societe Royale des Sciences de Liege. 2011. 80 29–41.

*Maseda, M. V., van der Wel, A., da Cunha, E., Rix, H.-W., Pacifici, C., Momcheva, I., Brammer, G. B., Franx, M., van Dokkum, P., Bell, E. F., Fumagalli, M., Grogin, N. A., Kocevski, D. D., Koekemoer, A. M., Lundgren, B. F., Marchesini, D., Nelson, E. J., Patel, S. G., Skelton, R. E., *Straughn, A. N., Trump, J. R., Weiner, B. J., Whitaker, K. E., Wuyts, S.* Confirmation of Small Dynamical and Stellar Masses for Extreme Emission Line Galaxies at z ~2 ApJL. 2013. 778, 1 L22.

Massey, P., Parker, J. W., Garmany, C. D. The Stellar Content of NGC 346: A Plethora of O Stars in the SMC AJ. 1989. 98 1305.

McKee, C. F., Ostriker, E. C. Theory of Star Formation ARA&A. 2007. 45, 1 565–687.

McLeod, A. F., Dale, J. E., Evans, C. J., Ginsburg, A., Kruijssen, J. M. D., Pellegrini, E. W., Ramsay, S. K., Testi, L. Feedback from massive stars at low metallicities: MUSE observations of N44 and N180 in the Large Magellanic Cloud MNRAS. 2019. 486, 4 5263–5288.

Meixner, M., Panuzzo, P., Roman-Duval, J., Engelbracht, C., Babler, B., Seale, J., Hony, S., Montiel, E., Sauvage, M., Gordon, K., Misselt, K., Okumura, K., Chanial, P., Beck, T., Bernard, J. P., Bolatto, A., Bot, C., Boyer, M. L., Carlson, L. R., Clayton, G. C., Chen, C. H. R., Cormier, D., Fukui, Y., Galametz, M., Galliano, F., Hora, J. L., Hughes, A., Indebetouw, R., Israel, F. P., Kawamura, A., Kemper, F., Kim, S., Kwon, E., Lebouteiller, V., Li, A., Long, K. S., Madden, S. C., Matsuura, M., Muller, E., Oliveira, J. M., Onishi, T., Otsuka, M., Paradis, D., Poglitsch, A., Reach, W. T., Robitaille, T. P., Rubio, M., Sargent, B., Sewiło, M., Skibba, R., Smith, L. J., Srinivasan, S., Tielens, A. G. G. M., van Loon, J. T., Whitney, B. The HERSCHEL Inventory of The Agents of Galaxy Evolution in the Magellanic Clouds, a Herschel Open Time Key Program AJ. 2013. 146, 3 62.

Meixner, M., Gordon, K. D., Indebetouw, R., Hora, J. L., Whitney, B., Blum, R., Reach, W., Bernard, J.-P., Meade, M., Babler, B., Engelbracht, C. W., For, B.-Q., Misselt, K., Vijh, U., Leitherer, C., Cohen, M., Churchwell, E. B., Boulanger, F., Frogel, J. A., Fukui, Y., Gallagher, J., Gorjian, V., Harris, J., Kelly, D., Kawamura, A., Kim, S., Latter, W. B., Madden, S., Markwick-Kemper, C., Mizuno, A., Mizuno, N., Mould, J., Nota, A., Oey, M. S., Olsen, K., Onishi, T., Paladini, R., Panagia, N., Perez-Gonzalez, P., Shibai, H., Sato, S., Smith, L., Staveley-Smith, L., Tielens, A. G. G. M., Ueta, T., van Dyk, S., Volk, K., Werner, M., Zaritsky, D. Spitzer Survey of the Large Magellanic Cloud: Surveying the Agents of a Galaxy's Evolution (SAGE). I. Overview and Initial Results AJ. 2006. 132, 6 2268–2288.

Mendenhall, W., Sincich, T. A Second Course in Statistics: Regression Analysis. 2011.

Meyer, D. M., Cardelli, J. A., Sofia, U. J. The Abundance of Interstellar Nitrogen ApJL. 1997. 490, 1 L103–L106.

Mizuno, N., Yamaguchi, R., Mizuno, A., Rubio, M., Abe, R., Saito, H., Onishi, T., Yonekura, Y., Yamaguchi, N., Ogawa, H., Fukui, Y. A CO Survey of the LMC with NANTEN: II. Catalog of Molecular Clouds PASJ. 2001. 53, 6 971–984.

Mizuno, Y., Kawamura, A., Onishi, T., Minamidani, T., Muller, E., Yamamoto, H., Hayakawa, T., Mizuno, N., Mizuno, A., Stutzki, J., Pineda, J. L., Klein, U., Bertoldi, F., Koo, B.-C., Rubio, M., Burton, M., Benz, A., Ezawa, H., Yamaguchi, N., Kohno, K., Hasegawa, T., Tatematsu, K., Ikeda, M., Ott, J., Wong, T., Hughes, A., Meixner, M., Indebetouw, R., Gordon, K. D., Whitney, *B., Bernard, J.-P., Fukui, Y.* Warm and Dense Molecular Gas in the N 159 Region: ^{12}CO J = 4-3 and ^{13}CO J = 3-2 Observations with NANTEN2 and ASTE PASJ. 2010. 62, 1 51–67.

Mookerjea, B., Israel, F., Kramer, C., Nikola, T., Braine, J., Ossenkopf, V., Röllig, M., Henkel, C., van der Werf, P., van der Tak, F., Wiedner, M. C. Velocity resolved [C II] spectroscopy of the center and the BCLMP 302 region of M 33 (HerM 33es) A&A. 2016. 586 A37.

Morris, P. W., Crowther, P. A., Houck, J. R. Spitzer Space Telescope Infrared Spectrograph (IRS) Spectroscopy of the Prototype Wolf-Rayet Star EZ Canis Majoris (HD 50896) ApJS. 2004. 154, 1 413–417.

Muñoz-Mateos, J. C., Gil de Paz, A., Zamorano, J., Boissier, S., Dale, D. A., Pérez-González, P. G., Gallego, J., Madore, B. F., Bendo, G., Boselli, A., Buat, V., Calzetti, D., Moustakas, J., Kennicutt, J. R. C. Radial Distribution of Stars, Gas, and Dust in SINGS Galaxies. I. Surface Photometry and Morphology ApJ. 2009. 703, 2 1569–1596.

Murphy, J. W., Khan, R., Williams, B., Dolphin, A. E., Dalcanton, J., Díaz-Rodríguez, M. The Progenitor Age and Mass of the Black Hole Formation Candidate N6946-BH1 ApJ. 2018. 860, 2 117.

Nakajima, Y., Kato, D., Nagata, T., Tamura, M., Sato, S., Sugitani, K., Nagashima, C., Nagayama, T., Iwata, I., Ita, Y., Tanabe, T., Kurita, M., Nakaya, H., Baba, D. Near-Infrared Imaging Observations of the N159/N160 Complex in the Large Magellanic Cloud: Large Clusters of Herbig Ae/Be Stars and Sequential Cluster Formation AJ. 2005. 129, 2 776–789.

National Academies, . Pathways to Discovery in Astronomy and Astrophysics for the 2020s. 2021.

Nayak, O., Meixner, M., Indebetouw, R., De Marchi, G., Koekemoer, A., Panagia, N., Sabbi, E. A Study of the Relation between Star Formation and Molecular Clumps on Subparsec Scales in 30 Doradus ApJ. 2016. 831, 1 32.

Nazé, Y., Rauw, G., Manfroid, J., Chu, Y. H., Vreux, J. M. WR bubbles and He II emission A&A. 2003. 408 171–186.

Nicholls, D. C., Sutherland, R. S., Dopita, M. A., Kewley, L. J., Groves, B. A. Abundance scaling in stars, nebulae and galaxies MNRAS. 2017. 466, 4 4403–4422.

Niemela, V. S., Massey, P., Testor, G., Giménez Benítez, S. The massive Wolf-Rayet binary SMC WR7 MNRAS. 2002. 333, 2 347–352.

Nieva, M. F., Przybilla, N. Present-day cosmic abundances. A comprehensive study of nearby early B-type stars and implications for stellar and Galactic evolution and interstellar dust models A&A. 2012. 539 A143.

Nishimura, A., Tokuda, K., Kimura, K., Muraoka, K., Maezawa, H., Ogawa, H., Dobashi, K., Shimoikura, T., Mizuno, A., Fukui, Y., Onishi, T. Revealing the Physical Properties of Molecular Gas in Orion with a Large-scale Survey in J = 2-1 Lines of ^{12}CO, ^{13}CO, and C^{18}O ApJS. 2015. 216, 1 18.

O'Neill, T. J., Indebetouw, R., Bolatto, A. D., Madden, S. C., Wong, T. Effects of CO-dark Gas on Measurements of Molecular Cloud Stability and the Size-Linewidth Relationship ApJ. 2022a. 933, 2 179.

O'Neill, T. J., Indebetouw, R., Sandstrom, K., Bolatto, A. D., Jameson, K. E., Carlson, L. R., Finn, M. K., Meixner, M., Sabbi, E., Sewiło, M. Sequential Star Formation in the Young SMC Region NGC 602: Insights from ALMA ApJ. 2022b. 938, 1 82.

Oberst, T. E., Parshley, S. C., Stacey, G. J., Nikola, T., Löhr, A., Harnett, J. I., Tothill, N. F. H., Lane, A. P., Stark, A. A., Tucker, C. E. Detection of the 205 μm [N II] Line from the Carina Nebula ApJL. 2006. 652, 2 L125–L128.

Ochsendorf, B. B., Zinnecker, H., Nayak, O., Bally, J., Meixner, M., Jones, O. C., Indebetouw, R., Rahman, M. The star-forming complex LMC-N79 as a future rival to 30 Doradus Nature Astronomy. 2017. 1 784–790.

Okada, Y., Güsten, R., Requena-Torres, M. A., Röllig, M., Stutzki, J., Graf, U. U., Hughes, A. Velocity profiles of [C_{II}], [C_I], CO, and [O_I] and physical conditions in four star-forming regions in the Large Magellanic Cloud A&A. 2019. 621 A62.

Okada, Y., Requena-Torres, M. A., Güsten, R., Stutzki, J., Wiesemeyer, H., Pütz, P., Ricken, O. Velocity resolved [C ii], [C i], and CO observations of the N159 star-forming region in the Large Magellanic Cloud: a complex velocity structure and variation of the column densities A&A. 2015. 580 A54.

Olivier, G. M., Berg, D. A., Chisholm, J., Erb, D. K., Pogge, R. W., Skillman, E. D. Characterizing Extreme Emission Line Galaxies. II. A Self-consistent Model of Their Ionizing Spectrum ApJ. 2022. 938, 1 16.

Olivier, G. M., Lopez, L. A., Rosen, A. L., Nayak, O., Reiter, M., Krumholz, M. R., Bolatto, A. D. Evolution of Stellar Feedback in H II Regions ApJ. 2021. 908, 1 68.

Onodera, S., Kuno, N., Tosaki, T., Kohno, K., Nakanishi, K., Sawada, T., Muraoka, K., Komugi, S., Miura, R., Kaneko, H., Hirota, A., Kawabe, R. Breakdown of Kennicutt-Schmidt Law at Giant Molecular Cloud Scales in M33 ApJL. 2010. 722, 2 L127–L131.

Ostriker, E. C., McKee, C. F., Leroy, A. K. Regulation of Star Formation Rates in Multiphase Galactic Disks: A Thermal/Dynamical Equilibrium Model ApJ. 2010. 721, 2 975–994.

Pabst, C., Higgins, R., Goicoechea, J. R., Teyssier, D., Berne, O., Chambers, E., Wolfire, M., Suri, S. T., Guesten, R., Stutzki, J., Graf, U. U., Risacher, C., Tielens, A. G. G. M. Disruption of the Orion molecular core 1 by wind from the massive star θ^1 Orionis C Nature. 2019. 565, 7741 618–621.

Parkin, E. R., Pittard, J. M. A 3D dynamical model of the colliding winds in binary systems MNRAS. 2008. 388, 3 1047–1061.

Peimbert, M., Peimbert, A., Ruiz, M. T. The Chemical Composition of the Small Magellanic Cloud H II Region NGC 346 and the Primordial Helium Abundance ApJ. 2000. 541, 2 688–700.

Pellegrini, E. W., Oey, M. S., Winkler, P. F., Points, S. D., Smith, R. C., Jaskot, A. E., Zastrow, J. The Optical Depth of H II Regions in the Magellanic Clouds ApJ. 2012. 755, 1 40.

Pereira-Santaella, M., Diamond-Stanic, A. M., Alonso-Herrero, A., Rieke, G. H. The Mid-infrared High-ionization Lines from Active Galactic Nuclei and Star-forming Galaxies ApJ. 2010. 725, 2 2270–2280.

Pérez-Beaupuits, J. P., Stutzki, J., Ossenkopf, V., Spaans, M., Güsten, R., Wiesemeyer, H. Detection of a large fraction of atomic gas not associated with star-forming material in M17 SW$\star$ A&A. 2015. 575 A9.

Pety, J. Successes of and Challenges to GILDAS, a State-of-the-Art Radioastronomy Toolkit SF2A-2005: Semaine de l'Astrophysique Francaise. 2005. 721.

Pietrzyński, G., Graczyk, D., Gallenne, A., Gieren, W., Thompson, I. B., Pilecki, B., Karczmarek, P., Górski, M., Suchomska, K., Taormina, M., Zgirski, B., Wielgórski, P., Kołaczkowski, Z., Konorski, P., Villanova, S., Nardetto, N., Kervella, P., Bresolin, F., Kudritzki, R. P., Storm, J., Smolec, R., Narloch, W. A distance to the Large Magellanic Cloud that is precise to one per cent Nature. 2019. 567, 7747 200–203.

Pilyugin, L. S., Grebel, E. K., Zinchenko, I. A., Kniazev, A. Y. The Abundance Properties of Nearby Late-Type Galaxies. II. the Relation between Abundance Distributions and Surface Brightness Profiles AJ. 2014. 148, 6 134.

Pineda, J. L., Langer, W. D., Goldsmith, P. F. A Herschel [C II] Galactic plane survey. III. [C II] as a tracer of star formation A&A. 2014. 570 A121.

Pineda, J. L., Langer, W. D., Velusamy, T., Goldsmith, P. F. A Herschel [C ii] Galactic plane survey. I. The global distribution of ISM gas components A&A. 2013. 554 A103.

Pineda, J. L., Langer, W. D., Goldsmith, P. F., Horiuchi, S., Kuiper, T. B. H., Muller, E., Hughes, A., Ott, J., Requena-Torres, M. A., Velusamy, T., Wong, T. Characterizing the Transition from Diffuse Atomic to Dense Molecular Clouds in the Magellanic Clouds with [C II], [C I], and CO ApJ. 2017. 839, 2 107.

Poglitsch, A., Krabbe, A., Madden, S. C., Nikola, T., Geis, N., Johansson, L. E. B., Stacey, G. J., Sternberg, A. A Multiwavelength Study of 30 Doradus: The Interstellar Medium in a Low-Metallicity Galaxy ApJ. 1995. 454 293.

Polles, F. L., Madden, S. C., Lebouteiller, V., Cormier, D., Abel, N., Galliano, F., Hony, S., Karczewski, O. Ł., Lee, M. Y., Chevance, M., Galametz, M., Lianou, S. Modeling ionized gas in low-metallicity environments: the Local Group dwarf galaxy IC 10 A&A. 2019. 622 A119.

Rau, U., Naik, N., Braun, T. A Joint Deconvolution Algorithm to Combine Single-dish and Interferometer Data for Wideband Multiterm and Mosaic Imaging AJ. 2019. 158, 1 3.

Reback, J., jbrockmendel, , McKinney, W., Van den Bossche, J., Augspurger, T., Roeschke, M., Hawkins, S., Cloud, P., gfyoung, , Sinhrks, , Hoefler, P., Klein, A., Petersen, T., Tratner, J., She, C., Ayd, W., Naveh, S., Darbyshire, J., Garcia, M., Shadrach, R., Schendel, J., Hayden, A., Saxton, D., Gorelli, M. E., Li, F., Zeitlin, M., Jancauskas, V., McMaster, A., Wörtwein, T., Battiston, P. pandas-dev/pandas: Pandas 1.4.2. 2022.

Requena-Torres, M. A., Israel, F. P., Okada, Y., Güsten, R., Stutzki, J., Risacher, C., Simon, R., Zinnecker, H. Carbon gas in SMC low-metallicity star-forming regions A&A. 2016. 589 A28.

Rigby, J. R., Bayliss, M. B., Gladders, M. D., Sharon, K., Wuyts, E., Dahle, H., Johnson, T., Peña-Guerrero, M. C III] Emission in Star-forming Galaxies Near and Far ApJL. 2015. 814, 1 L6.

Risacher, C., Güsten, R., Stutzki, J., Hübers, H. W., Aladro, R., Bell, A., Buchbender, C., Büchel, D., Csengeri, T., Duran, C., Graf, U. U., Higgins, R. D., Honingh, C. E., Jacobs, K., Justen, M., Klein, B., Mertens, M., Okada, Y., Parikka, A., Pütz, P., Reyes, N., Richter, H., Ricken, O., Riquelme, D., Rothbart, N., Schneider, N., Simon, R., Wienold, M., Wiesemeyer, H., Ziebart, M., Fusco, P., Rosner, S., Wohler, B. The upGREAT Dual Frequency Heterodyne Arrays for SOFIA Journal of Astronomical Instrumentation. 2018. 7, 4 1840014.

Risacher, C., Güsten, R., Stutzki, J., Hübers, H. W., Bell, A., Buchbender, C., Büchel, D., Csengeri, T., Graf, U. U., Heyminck, S., Higgins, R. D., Honingh, C. E., Jacobs, K., Klein, B., Okada, Y., Parikka, A., Pütz, P., Reyes, N., Ricken, O., Riquelme, D., Simon, R., Wiesemeyer, H. The upGREAT 1.9 THz multi-pixel high resolution spectrometer for the SOFIA Observatory A&A. 2016. 595 A34.

Robitaille, T., Bressert, E. APLpy: Astronomical Plotting Library in Python. 2012. ascl:1208.017.

Röllig, M., Simon, R., Güsten, R., Stutzki, J., Israel, F. P., Jacobs, K. [C II] 158 μm and [N II] 205 μm emission from IC 342. Disentangling the emission from ionized and photo-dissociated regions A&A. 2016. 591 A33.

Roman-Duval, J., Jackson, J. M., Heyer, M., Rathborne, J., Simon, R. Physical Properties and Galactic Distribution of Molecular Clouds Identified in the Galactic Ring Survey ApJ. 2010. 723, 1 492–507.

Rosenthal, D., Bertoldi, F., Drapatz, S. ISO-SWS observations of OMC-1: H_2 and fine structure lines A&A. 2000. 356 705–723.

Rosolowsky, E. W., Pineda, J. E., Kauffmann, J., Goodman, A. A. Structural Analysis of Molecular Clouds: Dendrograms ApJ. 2008. 679, 2 1338–1351.

Rosolowsky, E., Hughes, A., Leroy, A. K., Sun, J., Querejeta, M., Schruba, A., Usero, A., Herrera, C. N., Liu, D., Pety, J., Saito, T., Bešlić, I., Bigiel, F., Blanc, G., Chevance, M., Dale, D. A., Deger, S., Faesi, C. M., Glover, S. C. O., Henshaw, J. D., Klessen, R. S., Kruijssen, J. M. D., Larson, K., Lee, J., Meidt, S., Mok, A., Schinnerer, E., Thilker, D. A., Williams, T. G. Giant molecular cloud catalogues for PHANGS-ALMA: methods and initial results MNRAS. 2021. 502, 1 1218–1245.

Rosolowsky, E., Leroy, A. Bias-free Measurement of Giant Molecular Cloud Properties PASP. 2006. 118, 842 590–610.

Rubio, G., Toalá, J. A., Jiménez-Hernández, P., Ramos-Larios, G., Guerrero, M. A., Gómez-González, V. M. A., Santamaría, E., Quino-Mendoza, J. A. Unveiling the stellar origin of the Wolf-Rayet nebula NGC 6888 through infrared observations MNRAS. 2020. 499, 1 415–427.

Russell, S. C., Dopita, M. A. Abundances of the Heavy Elements in the Magellanic Clouds. III. Interpretation of Results ApJ. 1992. 384 508.

Saigo, K., Onishi, T., Nayak, O., Meixner, M., Tokuda, K., Harada, R., Morioka, Y., Sewiło, M., Indebetouw, R., Torii, K., Kawamura, A., Ohama, A., Hattori, Y., Yamamoto, H., Tachihara, K., Minamidani, T., Inoue, T., Madden, S., Galametz, M., Lebouteiller, V., Chen, C. H. R., Mizuno, N., Fukui, Y. Kinematic Structure of Molecular Gas around High-mass YSO, Papillon Nebula, in N159 East in the Large Magellanic Cloud: A New Perspective with ALMA ApJ. 2017. 835, 1 108.

Sander, A., Shenar, T., Hainich, R., Gímenez-García, A., Todt, H., Hamann, W. R. On the consistent treatment of the quasi-hydrostatic layers in hot star atmospheres A&A. 2015. 577 A13.

Sandstrom, K. M., Bolatto, A. D., Bot, C., Draine, B. T., Ingalls, J. G., Israel, F. P., Jackson, J. M., Leroy, A. K., Li, A., Rubio, M., Simon, J. D., Smith, J. D. T., Stanimirović, S., Tielens, A. G. G. M., van Loon, J. T. The Spitzer Spectroscopic Survey of the Small Magellanic Cloud (S^4MC): Probing the Physical State of Polycyclic Aromatic Hydrocarbons in a Low-metallicity Environment ApJ. 2012. 744, 1 20.

Sandstrom, K. M., Bolatto, A. D., Draine, B. T., Bot, C., Stanimirović, S. The Spitzer Survey of the Small Magellanic Cloud (S^3MC): Insights into the Life Cycle of Polycyclic Aromatic Hydrocarbons ApJ. 2010. 715, 2 701–723.

Sandstrom, K. M., Bolatto, A. D., Stanimirović, S., van Loon, J. T., Smith, J. D. T. Measuring Dust Production in the Small Magellanic Cloud Core-Collapse Supernova Remnant 1E 0102.2-7219 ApJ. 2009. 696, 2 2138–2154.

Schaerer, D., Stasińska, G. On the origin of [O iv] emission in Wolf-Rayet galaxies A&A. 1999. 345 L17–L21.

Schaerer, D., Vacca, W. D. New Models for Wolf-Rayet and O Star Populations in Young Starbursts ApJ. 1998. 497, 2 618–644.

Schlegel, D. J., Finkbeiner, D. P., Davis, M. Maps of Dust Infrared Emission for Use in Estimation of Reddening and Cosmic Microwave Background Radiation Foregrounds ApJ. 1998. 500, 2 525–553.

Schöier, F. L., van der Tak, F. F. S., van Dishoeck, E. F., Black, J. H. An atomic and molecular database for analysis of submillimetre line observations A&A. 2005. 432, 1 369–379.

Schruba, A., Leroy, A. K., Kruijssen, J. M. D., Bigiel, F., Bolatto, A. D., de Blok, W. J. G., Tacconi, L., van Dishoeck, E. F., Walter, F. Physical Properties of Molecular Clouds at 2 pc Resolution in the Low-metallicity Dwarf Galaxy NGC 6822 and the Milky Way ApJ. 2017. 835, 2 278.

Schruba, A., Leroy, A. K., Walter, F., Sandstrom, K., Rosolowsky, E. The Scale Dependence of the Molecular Gas Depletion Time in M33 ApJ. 2010. 722, 2 1699–1706.

Senchyna, P., Stark, D. P., Vidal-García, A., Chevallard, J., Charlot, S., Mainali, R., Jones, T., Wofford, A., Feltre, A., Gutkin, J. Ultraviolet spectra of extreme nearby star-forming regions - approaching a local reference sample for JWST MNRAS. 2017. 472, 3 2608–2632.

Shenar, T., Hainich, R., Todt, H., Sander, A., Hamann, W. R., Moffat, A. F. J., Eldridge, J. J., Pablo, H., Oskinova, L. M., Richardson, N. D. Wolf-Rayet stars in the Small Magellanic Cloud. II. Analysis of the binaries A&A. 2016. 591 A22.

Shibai, H., Okuda, H., Nakagawa, T., Matsuhara, H., Maihara, T., Mizutani, K., Kobayashi, Y., Hiromoto, N., Nishimura, T., Low, F. J. Large-Scale [C ii] 158 Micron Emission from the Galaxy ApJ. 1991. 374 522.

Simón-Díaz, S., Stasińska, G. The chemical composition of the Orion star forming region. II. Stars, gas, and dust: the abundance discrepancy conundrum A&A. 2011. 526 A48.

Smith, J. D. T., Armus, L., Dale, D. A., Roussel, H., Sheth, K., Buckalew, B. A., Jarrett, T. H., Helou, G., Kennicutt, J. R. C. Spectral Mapping Reconstruction of Extended Sources PASP. 2007a. 119, 860 1133–1144.

Smith, J. D. T., Armus, L., Dale, D. A., Roussel, H., Sheth, K., Buckalew, B. A., Jarrett, T. H., Helou, G., Kennicutt, J. R. C. Spectral Mapping Reconstruction of Extended Sources PASP. 2007b. 119, 860 1133–1144.

Smith, J. D. T., Croxall, K., Draine, B., De Looze, I., Sandstrom, K., Armus, L., Beirão, P., Bolatto, A., Boquien, M., Brandl, B., Crocker, A., Dale, D. A., Galametz, M., Groves, B., Helou, G., Herrera-Camus, R., Hunt, L., Kennicutt, R., Walter, F., Wolfire, M. The Spatially Resolved [CII] Cooling Line Deficit in Galaxies ApJ. 2017. 834, 1 5.

Smith, J. D. T., Rudnick, L., Delaney, T., Rho, J., Gomez, H., Kozasa, T., Reach, W., Isensee, K. Spitzer Spectral Mapping of Supernova Remnant Cassiopeia a ApJ. 2009. 693, 1 713–721.

Sofia, U. J., Lauroesch, J. T., Meyer, D. M., Cartledge, S. I. B. Interstellar Carbon in Translucent Sight Lines ApJ. 2004. 605, 1 272–277.

Sokal, K. R., Johnson, K. E., Indebetouw, R., Massey, P. The Prevalence and Impact of Wolf-Rayet Stars in Emerging Massive Star Clusters ApJ. 2016. 826, 2 194.

Solomon, P. M., Rivolo, A. R., Barrett, J., Yahil, A. Mass, Luminosity, and Line Width Relations of Galactic Molecular Clouds ApJ. 1987. 319 730.

Sorai, K., Hasegawa, T., Booth, R. S., Rubio, M., Morino, J. I., Bronfman, L., Handa, T., Hayashi, M., Nyman, L. Å., Oka, T., Sakamoto, S., Seta, M., Usuda, K. S. The CO J=2-1/J=1-0 Ratio in the Large Magellanic Cloud ApJ. 2001. 551, 2 794–802.

Stacey, G. J., Geis, N., Genzel, R., Lugten, J. B., Poglitsch, A., Sternberg, A., Townes, C. H. The 158 Micron [C ii] Line: A Measure of Global Star Formation Activity in Galaxies ApJ. 1991. 373 423.

Stacey, G. J., Viscuso, P. J., Fuller, C. E., Kurtz, N. T. The 157-micron forbidden C II luminosity of ghe Galaxy. II - The presence of knotlike features in the forbidden C II emission ApJ. 1985. 289 803–806.

Stevens, I. R., Blondin, J. M., Pollock, A. M. T. Colliding Winds from Early-Type Stars in Binary Systems ApJ. 1992. 386 265.

Stock, D. J., Barlow, M. J. Herschel-PACS measurements of nitrogen enrichment in nebulae around Wolf-Rayet stars MNRAS. 2014. 441, 4 3065–3074.

Strömgren, B. The Physical State of Interstellar Hydrogen. ApJ. 1939. 89 526.

Sutter, J., Dale, D. A., Croxall, K. V., Pelligrini, E. W., Smith, J. D. T., Appleton, P. N., Beirão, P., Bolatto, A. D., Calzetti, D., Crocker, A., De Looze, I., Draine, B., Galametz, M., Groves, B. A., Helou, G., Herrera-Camus, R., Hunt, L. K., Kennicutt, R. C., Roussel, H., Wolfire, M. G. Using [C II] 158 μm Emission from Isolated ISM Phases as a Star Formation Rate Indicator ApJ. 2019. 886, 1 60.

Tarantino, E., Bolatto, A. D., Herrera-Camus, R., Harris, A. I., Wolfire, M., Buchbender, C., Croxall, K. V., Dale, D. A., Groves, B., Levy, R. C., Riquelme, D., Smith, J. D. T., Stutzki, J. Characterizing the Multiphase Origin of [C II] Emission in M101 and NGC 6946 with Velocity-resolved Spectroscopy ApJ. 2021. 915, 2 92.

Tayal, S. S. Electron impact excitation collision strength for transitions in C II A&A. 2008. 486, 2 629–636.

Tayal, S. S. Electron Excitation Collision Strengths for Singly Ionized Nitrogen ApJS. 2011. 195, 2 12.

Tchernyshyov, K., Meixner, M., Seale, J., Fox, A., Friedman, S. D., Dwek, E., Galliano, F. Elemental Depletions in the Magellanic Clouds and the Evolution of Depletions with Metallicity ApJ. 2015. 811, 2 78.

Testor, G., Niemela, V. The OB associations LH 101 and LH 104 in the HII region N158 of the LMC A&AS. 1998. 130 527–538.

The Astropy Collaboration, , Price-Whelan, A. M., Sipőcz, B. M., Günther, H. M., Lim, P. L., Crawford, S. M., Conseil, S., Shupe, D. L., Craig, M. W., Dencheva, N., Ginsburg, A., VanderPlas, J. T., Bradley, L. D., Pérez-Suárez, D., de Val-Borro, M., Aldcroft, T. L., Cruz, K. L., Robitaille, T. P., Tollerud, E. J., Ardelean, C., Babej, T., Bachetti, M., Bakanov, A. V., Bamford, S. P., Barentsen, G., Barmby, P., Baumbach, A., Berry, K. L., Biscani, F., Boquien, M., Bostroem, K. A., Bouma, L. G., Brammer, G. B., Bray, E. M., Breytenbach, H., Buddelmeijer, H., Burke, D. J., Calderone, G., Cano Rodríguez, J. L., Cara, M., Cardoso, J. V. M., Cheedella, S., Copin, Y., Crichton, D., DÁvella, D., Deil, C., Depagne, É., Dietrich, J. P., Donath, A., *Droettboom, M., Earl, N., Erben, T., Fabbro, S., Ferreira, L. A., Finethy, T., Fox, R. T., Garrison, L. H., Gibbons, S. L. J., Goldstein, D. A., Gommers, R., Greco, J. P., Greenfield, P., Groener, A. M., Grollier, F., Hagen, A., Hirst, P., Homeier, D., Horton, A. J., Hosseinzadeh, G., Hu, L., Hunkeler, J. S., Ivezić, Ž., Jain, A., Jenness, T., Kanarek, G., Kendrew, S., Kern, N. S., Kerzendorf, W. E., Khvalko, A., King, J., Kirkby, D., Kulkarni, A. M., Kumar, A., Lee, A., Lenz, D., Littlefair, S. P., Ma, Z., Macleod, D. M., Mastropietro, M., McCully, C., Montagnac, S., Morris, B. M., Mueller, M., Mumford, S. J., Muna, D., Murphy, N. A., Nelson, S., Nguyen, G. H., Ninan, J. P., Nöthe, M., Ogaz, S., Oh, S., Parejko, J. K., Parley, N., Pascual, S., Patil, R., Patil, A. A., Plunkett, A. L., Prochaska, J. X., Rastogi, T., Reddy Janga, V., Sabater, J., Sakurikar, P., Seifert, M., Sherbert, L. E., Sherwood-Taylor, H., Shih, A. Y., Sick, J., Silbiger, M. T., Singanamalla, S., Singer, L. P., Sladen, P. H., Sooley, K. A., Sornarajah, S., Streicher, O., Teuben, P., Thomas, S. W., Tremblay, G. R., Turner, J. E. H., Terrón, V., van Kerkwijk, M. H., de la Vega, A., Watkins, L. L., Weaver, B. A., Whitmore, J. B., Woillez, J., Zabalza, V.* The Astropy Project: Building an inclusive, open-science project and status of the v2.0 core package ArXiv e-prints. 2018.

The CASA Team, , Bean, B., Bhatnagar, S., Castro, S., Donovan Meyer, J., Emonts, B., Garcia, E., Garwood, R., Golap, K., Gonzalez Villalba, J., Harris, P., Hayashi, Y., Hoskins, J., Hsieh, M., Jagannathan, P., Kawasaki, W., Keimpema, A., Kettenis, M., Lopez, J., Marvil, J., Masters, J., McNichols, A., Mehringer, D., Miel, R., Moellenbrock, G., Montesino, F., Nakazato, T., Ott, J., Petry, D., Pokorny, M., Raba, R., Rau, U., Schiebel, D., Schweighart, N., Sekhar, S., Shimada, K., Small, D., Steeb, J.-W., Sugimoto, K., Suoranta, V., Tsutsumi, T., van Bemmel, I. M., Verkouter, M., Wells, A., Xiong, W., Szomoru, A., Griffith, M., Glendenning, B., Kern, J. CASA, the Common Astronomy Software Applications for Radio Astronomy arXiv e-prints. 2022. arXiv:2210.02276.

Tielens, A. G. G. M., Hollenbach, D. Photodissociation regions. I. Basic model. ApJ. 1985. 291 722–746.

Toalá, J. A., Guerrero, M. A., Ramos-Larios, G., Guzmán, V. WISE morphological study of Wolf-Rayet nebulae A&A. 2015. 578 A66.

Toalá, J. A., Marston, A. P., Guerrero, M. A., Chu, Y. H., Gruendl, R. A. Hot Gas in the Wolf-Rayet Nebula NGC 3199 ApJ. 2017. 846, 1 76.

Todt, H., Sander, A., Hainich, R., Hamann, W. R., Quade, M., Shenar, T. Potsdam Wolf-Rayet model atmosphere grids for WN stars A&A. 2015. 579 A75.

Tokuda, K., Kondo, H., Ohno, T., Konishi, A., Sano, H., Tsuge, K., Zahorecz, S., Goto, N., Neelamkodan, N., Wong, T., Sewiło, M., Fukushima, H., Takekoshi, T., Muraoka, K., Kawamura, A., Tachihara, K., Fukui, Y., Onishi, T. An Unbiased CO Survey toward the Northern Region of the Small Magellanic Cloud with the Atacama Compact Array. I. Overview: CO Cloud Distributions ApJ. 2021. 922, 2 171.

Tokuda, K., Minami, T., Fukui, Y., Inoue, T., Nishioka, T., Tsuge, K., Zahorecz, S., Sano, H., Konishi, A., Rosie Chen, C. H., Sewiło, M., Madden, S. C., Nayak, O., Saigo, K., Nishimura, A., Tanaka, K. E. I., Sawada, T., Indebetouw, R., Tachihara, K., Kawamura, A., Onishi, T. An

ALMA Study of the Massive Molecular Clump N159W-North in the Large Magellanic Cloud: A Possible Gas Flow Penetrating One of the Most Massive Protocluster Systems in the Local Group ApJ. 2022. 933, 1 20.

Tuthill, P. G., Monnier, J. D., Danchi, W. C. A dusty pinwheel nebula around the massive star WR104 Nature. 1999. 398, 6727 487–489.

Usov, V. V. Stellar wind collision and dust formation in long-period, heavily interacting Wolf-Rayet binaries. MNRAS. 1991. 252 49.

Velusamy, T., Langer, W. D., Goldsmith, P. F., Pineda, J. L. Thermal Pressure in Diffuse H2 Gas Measured by Herschel [C II] Emission and FUSE UV H2 Absorption ApJ. 2017. 838, 2 165.

Vink, J. S., de Koter, A., Lamers, H. J. G. L. M. Mass-loss predictions for O and B stars as a function of metallicity A&A. 2001. 369 574–588.

Virtanen, P., Gommers, R., Burovski, E., Oliphant, T. E., Weckesser, W., Cournapeau, D., alexbrc, , Peterson, P., Reddy, T., Wilson, J., Haberland, M., Mayorov, N., endolith, , Nelson, A., van der Walt, S., Laxalde, D., Brett, M., Polat, I., Larson, E., Millman, J., Lars, , van Mulbregt, P., eric-jones, , Carey, C., Moore, E., Kern, R., Leslie, T., Perktold, J., Striega, K., Feng, Y. scipy/scipy: SciPy 1.5.3. 2020.

Walter, F., Brinks, E., de Blok, W. J. G., Bigiel, F., Kennicutt, J. Robert C., Thornley, M. D., Leroy, A. THINGS: The H I Nearby Galaxy Survey AJ. 2008. 136, 6 2563–2647.

Waskom, M., Botvinnik, O., Hobson, P., Cole, J. B., Halchenko, Y., Hoyer, S., Miles, A., Augspurger, T., Yarkoni, T., Megies, T., Coelho, L. P., Wehner, D., cynddl, , Ziegler, E., diego0020, , Zaytsev, Y. V., Hoppe, T., Seabold, S., Cloud, P., Koskinen, M., Meyer, K., Qalieh, A., Allan, D. Seaborn: V0.5.0 (November 2014). 2014.

Weaver, R., McCray, R., Castor, J., Shapiro, P., Moore, R. Interstellar bubbles. II. Structure and evolution. ApJ. 1977. 218 377–395.

Welty, D. E., Lauroesch, J. T., Wong, T., York, D. G. Thermal Pressures in the Interstellar Medium of the Magellanic Clouds ApJ. 2016. 821, 2 118.

Williams, J. P., Blitz, L., Stark, A. A. The Density Structure in the Rosette Molecular Cloud: Signposts of Evolution ApJ. 1995. 451 252.

Williams, J. P., de Geus, E. J., Blitz, L. Clumpfind: Determining Structure in Molecular Clouds. 2011. ascl:1107.014.

Wolfire, M. G., Hollenbach, D., McKee, C. F., Tielens, A. G. G. M., Bakes, E. L. O. The Neutral Atomic Phases of the Interstellar Medium ApJ. 1995. 443 152.

Wolfire, M. G., Hollenbach, D., McKee, C. F. The Dark Molecular Gas ApJ. 2010. 716, 2 1191–1207.

Wolfire, M. G., Hollenbach, D., Tielens, A. G. G. M. The Correlation of C II 158 Micron and CO (J = 1–0) Line Emission ApJ. 1989. 344 770.

Wolfire, M. G., McKee, C. F., Hollenbach, D., Tielens, A. G. G. M. Neutral Atomic Phases of the Interstellar Medium in the Galaxy ApJ. 2003. 587, 1 278–311.

Wolfire, M. G., Vallini, L., Chevance, M. Photodissociation and X-Ray-Dominated Regions ARA&A. 2022. 60 247–318.

Wong, T., Hughes, A., Tokuda, K., Indebetouw, R., Bernard, J.-P., Onishi, T., Wojciechowski, E., Bandurski, J. B., Kawamura, A., Roman-Duval, J., Cao, Y., Chen, C. H. R., Chu, Y.-h., Cui, C., Fukui, Y., Montier, L., Muller, E., Ott, J., Paradis, D., Pineda, J. L., Rosolowsky, E., Sewiło, M. ALMA Observations of a Quiescent Molecular Cloud in the Large Magellanic Cloud ApJ. 2017. 850, 2 139.

Wong, T., Hughes, A., Tokuda, K., Indebetouw, R., Onishi, T., Bandurski, J. B., Chen, C. H. R., Fukui, Y., Glover, S. C. O., Klessen, R. S., Pineda, J. L., Roman-Duval, J., Sewiło, M., Wojciechowski, E., Zahorecz, S. Relations between Molecular Cloud Structure Sizes and Line Widths in the Large Magellanic Cloud ApJ. 2019. 885, 1 50.

Wong, T., Oudshoorn, L., Sofovich, E., Green, A., Shah, C., Indebetouw, R., Meixner, M., Hacar, A., Nayak, O., Tokuda, K., Bolatto, A. D., Chevance, M., De Marchi, G., Fukui, Y., Hirschauer, A. S., Jameson, K. E., Kalari, V., Lebouteiller, V., Looney, L. W., Madden, S. C., Onishi, T., Roman-Duval, J., Rubio, M., Tielens, A. G. G. M. The 30 Doradus Molecular Cloud at 0.4 pc Resolution with the Atacama Large Millimeter/submillimeter Array: Physical Properties and the Boundedness of CO-emitting Structures ApJ. 2022. 932, 1 47.

Wright, E. L., Mather, J. C., Bennett, C. L., Cheng, E. S., Shafer, R. A., Fixsen, D. J., Eplee, J. R. E., Isaacman, R. B., Read, S. M., Boggess, N. W., Gulkis, S., Hauser, M. G., Janssen, M., Kelsall, T., Lubin, P. M., Meyer, S. S., Moseley, J. S. H., Murdock, T. L., Silverberg, R. F., Smoot, G. F., Weiss, R., Wilkinson, D. T. Preliminary Spectral Observations of the Galaxy with a 7 degrees Beam by the Cosmic Background Explorer (COBE) ApJ. 1991. 381 200.

Yan, L., Sajina, A., Loiacono, F., Lagache, G., Béthermin, M., Faisst, A., Ginolfi, M., Fèvre, O. L., Gruppioni, C., Capak, P. L., Cassata, P., Schaerer, D., Silverman, J. D., Bardelli, S., Dessauges-Zavadsky, M., Cimatti, A., Hathi, N. P., Lemaux, B. C., Ibar, E., Jones, G. C., Koekemoer, A. M., Oesch, P. A., Talia, M., Pozzi, F., Riechers, D. A., Tasca, L. A. M., Toft, S., Vallini, L., Vergani, D., Zamorani, G., Zucca, E. The ALPINE-ALMA [C II] Survey: [C II] 158 μm Emission Line Luminosity Functions at z $\sim$ 4-6 ApJ. 2020. 905, 2 147.

Zanella, A., Daddi, E., Magdis, G., Diaz Santos, T., Cormier, D., Liu, D., Cibinel, A., Gobat, R., Dickinson, M., Sargent, M., Popping, G., Madden, S. C., Bethermin, M., Hughes, T. M., Valentino, F., Rujopakarn, W., Pannella, M., Bournaud, F., Walter, F., Wang, T., Elbaz, D., Coogan, R. T. The [C II] emission as a molecular gas mass tracer in galaxies at low and high redshifts MNRAS. 2018. 481, 2 1976–1999.

de Blok, W. J. G., Walter, F., Smith, J. D. T., Herrera-Camus, R., Bolatto, A. D., Requena-Torres, M. A., Crocker, A. F., Croxall, K. V., Kennicutt, R. C., Koda, J., Armus, L., Boquien, M., Dale, D., Kreckel, K., Meidt, S. Comparing [C II] , HI, and CO Dynamics of Nearby Galaxies AJ. 2016. 152, 2 51.

de Boer, K. S., Braun, J. M., Vallenari, A., Mebold, U. Bow-shock induced star formation in the LMC? A&A. 1998. 329 L49–L52.

van der Walt, S., Schönberger, J. L., Nunez-Iglesias, J., Boulogne, F., Warner, J. D., Yager, N., Gouillart, E., Yu, T., scikit-image Contributors, . scikit-image: Image processing in Python PeerJ. 2014. 2 e453.